



This is to certify that the
dissertation entitled

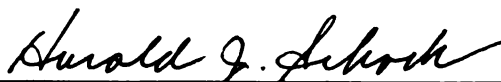
NUMERICAL MODELS FOR THE ASSESSMENT OF THE
CYLINDER-KIT PERFORMANCE OF FOUR-STROKE INTERNAL
COMBUSTION ENGINES

presented by

ANDREAS PETROU PANAYI

has been accepted towards fulfillment
of the requirements for the

Ph.D. degree in Mechanical Engineering



Major Professor's Signature

4/30/09

Date

PLACE IN RETURN BOX to remove this checkout from your record.
TO AVOID FINES return on or before date due.
MAY BE RECALLED with earlier due date if requested.

DATE DUE	DATE DUE	DATE DUE

**NUMERICAL MODELS FOR THE ASSESSMENT OF THE
CYLINDER-KIT PERFORMANCE OF FOUR-STROKE INTERNAL
COMBUSTION ENGINES**

By

Andreas Petrou Panayi

A DISSERTATION

**Submitted to
Michigan State University
in partial fulfillment of the requirements
for the degree of**

DOCTOR OF PHILOSOPHY

Mechanical Engineering

2009

ABSTRACT

NUMERICAL MODELS FOR THE ASSESSMENT OF THE CYLINDER-KIT PERFORMANCE OF FOUR-STROKE INTERNAL COMBUSTION ENGINES

By

Andreas Petrou Panayi

Governments across the globe are introducing more stringent emission standards, setting targets for higher engine efficiencies and looking into alternative fuels. At the same time the consumer demands have to be met: low cost, high fuel efficiency, long trouble-free life, low emissions and low noise and vibration. In order to meet all of these demands, a vast amount of design and testing is needed. This is where the numerical models for the assessment of cylinder-kit performance apply. Such models greatly reduce the amount of time from conception to launch of a new product. They reduce the number of expensive prototypes required to complete a design, and they allow for multiple design iterations to be tested in virtual space.

In this dissertation, numerical models for the assessment of cylinder-kit performance of four-stroke internal combustion engines are explored. A novel 3-D numerical model for predicting piston dynamics was developed. This model deviates from conventional ones, as in addition to the axial and thrust plane motions of the piston it also considers the secondary motion in the wrist-pin plane. It is shown that the motion in this additional dimension becomes important with the new generation pistons, especially when faced with asymmetric and eccentric cylinder bore deformations. The

model is used to investigate piston dynamics for both gasoline and diesel engines, and the predicted results are compared with the actual operating pistons.

Also, a method for the optimization of piston skirt profiles used in internal combustion engine piston design is proposed. The method is based on a response surface approximation of standard performance measures used in piston design, namely, the RMS values of the piston's transverse and angular accelerations, used as indicators of piston slap and noise, and the friction work on the skirt. The method is intended to be used in conjunction with computationally-intensive piston simulation tools. As such, it can be used also as a paradigm for strategies to solve optimization problems that rely on computationally expensive simulation models. An example illustrates the capabilities of the method and the significant enhancements in performance that result from an optimized piston skirt profile.

Finally, the ring-pack performance of a newly developed gasoline engine is benchmarked against that of a similar production engine using CASE, a commercial ring dynamics simulation program. Some limitations of such models that perform the calculations at one cross-section of the ring-pack are identified, and an introduction is made to the initial developments of an advanced 3-D ring dynamics numerical model.

Copyright by
ANDREAS PETROU PANAYI
2009

"It is an art to design an engine that revs up to 19000 RPM and yields a power beyond the 950 bhp horizon for a lifespan of one race weekend. The real art though is to design an engine that is fuel-efficient, reliable with a lifespan beyond 150,000 miles, and has a light footprint on the environment. It even becomes a masterpiece when you can harness some of the waste energy."

Andreas P. Panayi, 2009

for my wife, Darioulla

for my parents, Petros and Panayiota

ACKNOWLEDGEMENTS

First I would like to give my sincere thanks to my advisor, Dr. Harold Schock, for giving me the opportunity to work as a research assistant at the Automotive Research Experiment Station. These years have not only enriched my engineering knowledge, but also developed me as a researcher and a person, preparing me for the next step in life.

Under his tutelage I have been motivated to strive for and achieve exceptionally high standards in engineering. He provided me with the opportunity to attend and present at multiple conferences, while working with him on several research projects. This has established my professional network which will be an invaluable asset in my future job hunt. In many areas, both personally and professionally, Dr. Schock has taught and encouraged me to meet challenges that I had never before thought possible. Most important of all he led me to understand the art of the production internal combustion engine.

Second, I would like to thank the members of my Guidance Committee. Their advice and input along the way led me to the completion of this dissertation. Namely I would like to thank Dr. Farhad Jaber. He was the first one to expose me to all the glory of numerical modeling from my first semester here at Michigan State University. I thank Dr. Ronald Averill, who advised me on finite element modeling throughout my Masters and continued to do so through my PhD; and Dr. Alejandro Diaz who introduced me to optimization methods through his Optimal Design of Mechanical Systems class. His ability to motivate and challenge me resulted in a collaboration beyond the class which led to the development of the pseudo-Adaptive Response Surface Methodology which

will be described later in this dissertation. Finally, I thank Dr. Mikhail Ejakov of Ford Motor Company, who advised me from the early stages of my research on the numerical modeling of pistons and later piston rings. I would also like to extend to him my sincere appreciation for making it possible for me to intern at Ford Motor Company last summer. The experiences I acquired from that industry exposure will be invaluable in my future career.

In turn I would like to thank Mulyanto Poort of Mid Michigan Research for his support and friendship all these years. We have spent quite a few hours together exchanging ideas for modeling approaches. Also, the support of Mid Michigan Research allowed for the development of these numerical models.

I would like to thank Dr. Dan Richardson of Cummins Inc. for all his input month after month regarding the modeling efforts in both piston dynamics and ring dynamics. I would also like to express my appreciation to him for giving me the opportunity to get involved with the Internal Combustion Engine Division of ASME and allowing me to assist in the organization of two technical conferences. Many thanks to Andy Flack of Cummins Inc. also, for all his inputs in the piston modeling efforts.

Furthermore I would like to thank all the people at the Automotive Research Experiment Station who made these years more pleasant through lunch breaks, fishing trips or just hanging out.

Finally, I would like to thank and express my gratitude to my wife Daria and to my parents, Petros and Panayiota, for their love, support and patience, even when I am so far away. In order to achieve this, we had to spend considerable amounts of time apart on opposite sides of the Atlantic, however, they were always there.

To conclude, I would like to extend my apologies to the future researchers that will end up reading this work on microfiche, as some of the images in this dissertation are presented in color.

TABLE OF CONTENTS

LIST OF TABLES	xiii
LIST OF FIGURES	xv
KEY TO SYMBOLS.....	xxiii
INTRODUCTION.....	1
CHAPTER 1. NUMERICAL MODELS FOR THE ASSESSMENT OF CYLINDER-KIT PERFORMANCE	3
1.1 Motivation.....	3
1.2 Objectives	4
1.3 Previous Efforts	5
1.3.1 Piston Dynamics.....	6
1.3.2 Skirt Profile Optimization	9
1.3.3 Ring Dynamics	12
1.4 Structure of the Dissertation	13
CHAPTER 2. THE CYLINDER-KIT	15
2.1 Introduction.....	15
2.2 The Piston	18
2.2.1 Piston Design.....	20
2.2.2 Piston Mass	22
2.2.3 Piston Crown	23
2.2.4 Top Land	23
2.2.5 Second and Third Lands.....	24
2.2.6 Piston Pin-boss	26
2.2.7 Wrist-pin.....	26
2.2.8 Piston Skirt	27
2.2.9 Piston Skirt Design.....	30
2.2.10 Piston Strength	31
2.2.11 Piston Deformation	32
2.2.12 Thermal Expansion Control	33
2.2.13 Skirt Lubrication and Friction.....	34
2.2.14 Piston Profile.....	35
2.2.15 Piston Ovality.....	37
2.3 The Ring-pack.....	38
2.3.1 Top Compression Ring.....	41
2.3.2 Second Compression Ring	43
2.3.3 Oil Control Ring.....	43
2.3.4 Pressure Loading	44

2.3.5	Heat Transfer.....	46
2.3.6	Ring Friction	48
2.3.7	Engine Speed.....	49
2.4	Cylinder Liner.....	49
 CHAPTER 3. PISTON FINITE ELEMENT ANALYSIS AND DYNAMICS		
	MODEL.....	52
3.1	Introduction.....	52
3.2	Overview of the PIFEAD.....	53
3.2.1	Skirt Compliance.....	54
3.3	Piston Dynamics	58
3.3.1	Coordinate Systems.....	59
3.3.2	Piston Coordinate System	60
3.3.3	Skirt	61
3.3.4	Axial Dynamics.....	62
3.3.5	Piston Eccentricity.....	64
3.3.6	Equations of Motion.....	67
3.4	Hydrodynamic Pressure	74
3.5	Oil Film Thickness.....	77
3.6	Squeeze Film Velocity	78
3.7	Oil Dynamic Viscosity.....	79
3.8	Hydrodynamic Forces and Moments.....	80
3.9	Contact Pressure.....	81
3.9.1	Contact Forces and Moments	83
3.10	Wrist-pin Friction.....	84
3.11	Wear	84
3.12	Numerical Procedure	85
3.13	Remarks	91
 CHAPTER 4. APPROXIMATION OF THE ASPERITY CONTACT		
	PRESSURE.....	92
4.1	Introduction.....	92
4.2	Background of the Greenwood-Tripp Asperity Contact Model	93
4.3	The Greenwood-Tripp Model Equations	94
4.4	Approximations.....	96
4.4.1	Power Law.....	96
4.4.2	Sixth Order Polynomial.....	96
4.4.3	Proposed Approximation.....	97
4.5	Comparison of the Approximations.....	98
4.5.1	Quality of Fit	98
4.5.2	Computation Time.....	102
 CHAPTER 5. PISTON DYNAMICS SIMULATIONS		
5.1	New Generation Piston: A Comparison between 2-D and 3-D Numerical Models	104
5.1.1	Numerical Experiments.....	104

5.1.2	Predictions by 2-D and 3-D Models.....	109
5.1.3	2-D/Land and 3-D/Land Models, Fully Flooded Land Lubrication	114
5.1.4	Dry and Fully Flooded Second Land Conditions.....	117
5.1.5	Analytical Results	120
5.1.6	Remarks.....	121
5.2	High-speed Piston	123
5.2.1	Cyclic Stress Recovery.....	123
5.2.2	Progressive Wear.....	131
5.3	Assessing the Piston Performance of a Development Engine Relative to a Production Engine.....	140
5.4	Wear Prediction for a Heavy-duty Diesel Engine Piston.....	148
5.4.1	Skirt Compliance.....	152
5.4.2	Investigations on Skirt Wear	153
5.4.3	Remarks.....	174
 CHAPTER 6. AN OPTIMIZATION ALGORITHM FOR PISTON SKIRT PROFILES..... 175		
6.1	Introduction.....	175
6.2	Overview of Piston Modeling and Performance.....	176
6.3	Optimization Problem.....	180
6.3.1	Design Variables In Piston Skirt Design.....	180
6.4	Geometric Constraints	181
6.4.1	Problem Formulation.....	182
6.4.2	Skirt Profiles Described by Other Equations	184
6.5	The Surrogate Model	188
6.5.1	Adjustment of Regression Coefficients by IRLS	189
6.5.2	Generation of the Initial Set of Design Points.....	190
6.5.3	Adding a Point to an Existing Set	192
6.6	The Pseudo-Adaptive Response Surface Method.....	193
6.7	Selecting the Interpolation Model in Piston Skirt Design	196
6.8	Skirt Profile Optimization.....	198
6.8.1	Robustness of pARSM.....	205
6.8.2	Effects of IRLS.....	208
6.8.3	Optimal Profiles at Different Operating Conditions	211
6.9	Final Remarks	213
 CHAPTER 7. RING-PACK PRESSURES AND BLOW-BY 215		
7.1	Introduction.....	215
7.2	The Leakage Coefficient.....	215
7.3	Ring-pack Pressures.....	216
7.4	Ring-pack Blow-by.....	225
7.4.1	Tuning the CASE Model for Blow-by	229
 CHAPTER 8. AN INTRODUCTION TO 3-D NUMERICAL MODELING OF PISTON RING DYNAMICS 241		

8.1	Background	241
8.2	Finite Element Model in RING.....	244
8.3	Finite Element Model for a 3-D Ring.....	245
8.4	Ring Discretization and Coordinate Transformation.....	252
8.5	Bore Deformation	256
8.6	Gap Location.....	257
8.7	Ring-bore Conformability - Methodology.....	257
	8.7.1 The Fix-and-release Strategy.....	261
8.8	Choosing the Penalty Number	261
8.9	Validating the Ring Finite Element Model.....	264
8.10	Choosing the Number of Nodes.....	265
8.11	Sample Numerical Results.....	268
8.12	Incorporating the Groove	279
	8.12.1 Constrained Ring Results	282
8.13	Further Developments.....	286
CHAPTER 9. FINAL REMARKS.....		288
9.1	Lessons Learned.....	288
9.2	Limitations and Recommendations.....	289
9.3	Conclusions.....	291
APPENDIX A PARSM - PERFORMANCE MEASURES OF THE SURROGATE MODEL QUALITY.....		294
APPENDIX B PARSM - COEFFICIENTS FOR THE QUARTIC POLYNOMIAL SKIRT PROFILE		296
BIBLIOGRAPHY		297

LIST OF TABLES

Table 2.1:	Engine components in Figure 2.1	16
Table 2.2:	Piston features in Figure 2.4.....	20
Table 2.3:	Piston mass to diameter ratios	22
Table 2.4:	Coefficients of thermal expansion for different materials.....	34
Table 4.1:	Tabulated values for (4.6)	96
Table 4.2:	Statistics for the three approximations	100
Table 4.3:	Computation times	103
Table 5.1:	Engine and piston properties	106
Table 5.2:	High speed piston dimensions and properties	124
Table 5.3:	Piston dimensions and properties	142
Table 5.4:	Heavy-duty diesel piston dimensions and properties	149
Table 5.5:	Simulation cases	153
Table 6.1:	Engine and piston data	179
Table 6.2:	Surrogate model statistics.....	197
Table 6.3:	Summary of results.....	202
Table 6.4:	Summary of optimization results at 3000 RPM	207
Table 6.5:	Summary of optimization results at 1000 RPM	210
Table 6.6:	Summary of results at 5000 RPM	212
Table 7.1:	Channel height.....	220
Table 7.2:	Leakage coefficients.....	220
Table 7.3:	Ring-pack channel heights for the two engines	228
Table 7.4:	Ring masses.....	228

Table 7.5:	End gap clearances	229
Table 7.6:	Leakage coefficients and blow-by per cylinder at WOT	230
Table 8.1:	Ring properties	262
Table 8.2:	Effect of number of nodes	267
Table 8.3:	Ring-pack properties	269

LIST OF FIGURES

Figure 2.1:	Cross-section of a V-8 engine	16
Figure 2.2:	The four strokes in a gasoline engine – intake, compression, expansion and exhaust	18
Figure 2.3:	Modes of energy losses at the piston assembly	19
Figure 2.4:	Piston features, light-duty diesel piston	19
Figure 2.5:	Top land crevice	24
Figure 2.6:	Second and third land loads	25
Figure 2.7:	Connecting rod reaction force components during expansion stroke	28
Figure 2.8:	Asymmetric thrust sides	31
Figure 2.9:	Cold and hot piston profiles	36
Figure 2.10:	Piston ovality	38
Figure 2.11:	A typical ring-pack (a) diesel engine and (b) gasoline engine	39
Figure 2.12:	In-cylinder and land pressures	46
Figure 2.13:	Oil film wedge forming during the upstroke	47
Figure 2.14:	Forces generating axial friction at the ring-cylinder liner interface	48
Figure 2.15:	Cylinder liner deformation (a) assembled cold and (b) rated conditions	51
Figure 3.1:	Skirt nodes contributing to compliance matrix	57
Figure 3.2:	Skirt cross-sections for obtaining the skirt compliance	58
Figure 3.3:	Coordinate systems	59
Figure 3.4:	Piston coordinate system (a) X_p - Y_p plane, (b) Y_p - Z_p plane and (c) X_p - Z_p plane	60
Figure 3.5:	Skirt mesh on the local coordinate system	61
Figure 3.6:	Vector diagram of the piston crank assembly	62

Figure 3.7: Reference points (a) in the X_p - Y_p plane and (b) in the X_p - Z_p plane.....	66
Figure 3.8: Eccentricity in (a) the X_p - Y_p and (b) the X_p - Z_p planes with respect to the cylinder center line	66
Figure 3.9: Piston-connecting rod assembly free body diagrams	69
Figure 3.10: Second land mesh, 4 x 90 elements.....	76
Figure 3.11: Schematic of cylinder bore deformation	77
Figure 3.12: Components of pressure on skirt surface	80
Figure 3.13: PIFEAD flow diagram	90
Figure 4.1: Gap between two rough surfaces	94
Figure 4.2: Approximations of (4.6).....	101
Figure 4.3: Approximations of (4.6) in segments	101
Figure 4.4: Residuals of approximations of (4.6)	102
Figure 5.1: Piston mesh	105
Figure 5.2: Skirt profile	107
Figure 5.3: Pressure traces	107
Figure 5.4: Cylinder bore temperature.....	108
Figure 5.5: Cylinder bore deformation	108
Figure 5.6: Eccentricity at wrist-pin level, X_p - Y_p plane	110
Figure 5.7: Piston tilt	110
Figure 5.8: Total force in the X_p - Y_p plane.....	111
Figure 5.9: Eccentricity along the wrist-pin	112
Figure 5.10: Skirt wear (a) minor thrust 2-D model, (b) major thrust 2-D model, (c) minor thrust 3-D model, (d) major thrust 3-D model.....	112
Figure 5.11: Skirt wear on minor thrust side (a) 2-D model, (b) 3-D model.....	113
Figure 5.12: Skirt wear on major thrust side (a) 2-D model, (b) 3-D model.....	113

Figure 5.13: Eccentricity at wrist-pin level, X_p - Y_p plane	115
Figure 5.14: Piston tilt	115
Figure 5.15: Eccentricity along the wrist-pin	116
Figure 5.16: Second land wear predicted by (a) 2-D\Land and (b) 3-D\Land models ..	116
Figure 5.17: Eccentricity at wrist-pin level, X_p - Y_p plane	118
Figure 5.18: Piston tilt	118
Figure 5.19: Eccentricity along the wrist-pin	119
Figure 5.20: Second land wear predicted by (a) 3-D\Land – fully flooded lubrication and (b) 3-D\Land – dry lubrication models.....	119
Figure 5.21: Forces in the X_p - Y_p plane.....	121
Figure 5.22: In-cylinder pressure.....	125
Figure 5.23: Piston axial acceleration.....	125
Figure 5.24: Piston temperature distribution	126
Figure 5.25: Principal stresses at 7500 RPM, 0 cad	128
Figure 5.26: Principal stresses at 7500 RPM, 270 cad	128
Figure 5.27: Principal stresses at 7500 RPM, 369 cad	129
Figure 5.28: Principal stresses at 7500 RPM, 450 cad	129
Figure 5.29: Principal stresses at 9000 RPM, 373 cad	130
Figure 5.30: von Mises yield criterion 7500 RPM, 369 cad.....	130
Figure 5.31: von Mises yield criterion 9000 RPM, 373 cad.....	131
Figure 5.32: Instantaneous skirt wear	134
Figure 5.33: Cumulative skirt wear at 1 hour	135
Figure 5.34: Cumulative skirt wear at 2 hours.....	135
Figure 5.35: Piston secondary motion in thrust plane (a) eccentricity at wrist-pin level and (b) piston tilt	136
Figure 5.36: Piston translation along the wrist-pin.....	137

Figure 5.37: Friction force	137
Figure 5.38: Piston side forces in thrust plane (a) hydrodynamic and contact and (b) total force	139
Figure 5.39: Cylinder bore deformation for the two engines.....	141
Figure 5.40: Piston translation along the wrist-pin.....	143
Figure 5.41: Piston secondary motion in thrust plane (a) eccentricity at wrist-pin level and (b) piston tilt	144
Figure 5.42: Friction force	145
Figure 5.43: Piston side forces in thrust plane (a) hydrodynamic and contact and (b) total force	146
Figure 5.44: Engine block configuration	148
Figure 5.45: In-cylinder pressure at idle (750 RPM) no-load conditions.....	150
Figure 5.46: Cylinder bore deformation (a) three-dimensional and (b) along cylinder bore length at minor and major thrust sides	151
Figure 5.47: Skirt compliance of the heavy duty diesel piston.....	152
Figure 5.48: Symmetric temperature distribution decreasing along cylinder bore length.....	154
Figure 5.49: Asymmetric temperature distribution, hotter imposed on the inboard side of either bank	154
Figure 5.50: Piston secondary motion in thrust plane (a) eccentricity at wrist-pin level and (b) piston tilt, Case 1	156
Figure 5.51: Piston translation along the wrist-pin, Case 1	157
Figure 5.52: Piston total side force, Case 1	157
Figure 5.53: Side force analysis at 380 crank angle degrees	158
Figure 5.54: Typical loading on left bank with the engine run at no load (a) minor thrust side and (b) major thrust side	159
Figure 5.55: Piston secondary motion in thrust plane (a) eccentricity at wrist-pin level and (b) piston tilt, Case 2.....	160
Figure 5.56: Skirt contact forces, Case 2	161

Figure 5.57: Skirt wear, left bank, Case 2.....	162
Figure 5.58: Skirt wear, right bank, Case 2	162
Figure 5.59: Skirt contact forces, Case 3	163
Figure 5.60: Piston secondary motion in thrust plane (a) eccentricity at wrist-pin level and (b) piston tilt, Case 3.....	164
Figure 5.61: Skirt wear, left bank, Case 3.....	165
Figure 5.62: Skirt wear, right bank, Case 3	165
Figure 5.63: Piston secondary motion in thrust plane (a) eccentricity at wrist-pin level and (b) piston tilt, Case 4.....	167
Figure 5.64: Piston translation along the wrist-pin, Case 4	168
Figure 5.65: Skirt contact forces, Case 4	168
Figure 5.66: Skirt wear, left bank Case 4.....	170
Figure 5.67: Piston wear on left bank (a) minor thrust side and (b) major thrust side ..	170
Figure 5.68: Skirt wear, right bank, Case 4	171
Figure 5.69: Piston wear on right bank (a) minor thrust side and (b) major thrust side	171
Figure 5.70: Wear marks on cylinder liner (a) left bank bottom of major thrust side, (b) right bank bottom of minor thrust side	172
Figure 5.71: Piston drop.....	173
Figure 6.1: Representation of skirt profile and oil film thickness	177
Figure 6.2: Skirt profile described by a quartic polynomial (a) skirt profile coordinate system referenced to the piston nominal diameter, (b) design variables	181
Figure 6.3: Skirt profile described by NURBS with (a) three and (b) four control points	186
Figure 6.4: Skirt profile described by the barrel equation	187
Figure 6.5: Skirt profiles, reference (SPI) and optimized (SPO32 and SPO69).....	202
Figure 6.6: Transverse and angular accelerations in the reference (a) and optimized SPO32 (b) profile	203

Figure 6.7:	Total friction forces in the reference and optimized SPO32 profiles.....	204
Figure 6.8:	pARSM iteration history for the SPO32 profile.....	204
Figure 6.9:	Best merit function in design library at each pARSM iteration for the SPO32 profile	205
Figure 6.10:	Skirt profiles	207
Figure 6.11:	Skirt profiles obtained from optimization 3 at 1000 RPM.....	210
Figure 6.12:	Optimal skirt profiles at different engine speeds.....	212
Figure 7.1:	Ring leakage: (a) channel height and (b) leakage height when ring is seated at the bottom of the groove and (c) leakage height when ring is seated at the top of the groove.....	216
Figure 7.2:	Ring-pack pressures	217
Figure 7.3:	In-cylinder pressure at 1500 RPM 2 psi boost	220
Figure 7.4:	Top ring groove pressure.....	221
Figure 7.5:	Second land pressure	221
Figure 7.6:	Second ring groove pressure	222
Figure 7.7:	Third land pressure.....	222
Figure 7.8:	Oil ring groove pressure	223
Figure 7.9:	Top ring location relative to bottom of groove	223
Figure 7.10:	Second ring location relative to bottom of groove	224
Figure 7.11:	Oil ring location relative to bottom of groove.....	224
Figure 7.12:	Blow-by mechanisms, (a) ring floating, (b) ring collapse and (c) through end gap	226
Figure 7.13:	In-cylinder pressure traces for Engine 1 engine at 3000 RPM	227
Figure 7.14:	In-cylinder pressure traces for Engine 1 and Engine 2 engines at 3000 RPM WOT	228
Figure 7.15:	Measured blow-by (average per cylinder).....	229
Figure 7.16:	Predicted and measured blow-by at WOT	231

Figure 7.17: Predicted blow-by for the four cylinders of Engine 1 using Leakage 2....	232
Figure 7.18: Predicted blow-by for the four cylinders of Engine 1 using Leakage 2....	233
Figure 7.19: Predicted blow-by, Engine 1, Cylinder 1, Leakage 1.....	234
Figure 7.20: Predicted blow-by, Engine 1, Cylinder 1, Leakage 3.....	235
Figure 7.21: Predicted blow-by, Engine 2, Cylinder 1, Leakage 2.....	236
Figure 7.22: Predicted ring location, Cylinder 1, Leakage 2, Load WOT, 6500 RPM (a) Engine 1 and (b) Engine 2	238
Figure 7.23: Predicted ring location, Cylinder 1, Leakage 2, Load 25P, 6500 RPM (a) Engine 1 and (b) Engine 2	239
Figure 8.1: Axial cross-section of ring-pack	242
Figure 8.2: Typical groove and land volumes at (a) end of compression stroke (b) beginning of expansion stroke	243
Figure 8.3: Planar frame element.....	244
Figure 8.4: Space frame element	246
Figure 8.5: Principal axis (y-z) rotation, viewed from the positive x-direction	249
Figure 8.6: Beam element.....	251
Figure 8.7: Ring in its global coordinate system (viewed from the negative Y-direction)	253
Figure 8.8: Radial-tangential coordinate system	254
Figure 8.9: Ring end gap.....	255
Figure 8.10: Flow area created due to non-conforming nodes	255
Figure 8.11: Bore deformation.....	256
Figure 8.12: Gap location	257
Figure 8.13: Nodal clearances and displacements	258
Figure 8.14: Radial displacements prediction due to a distributive load with different penalty numbers	263
Figure 8.15: Ring fitted to distorted bore with different penalty numbers	263

Figure 8.16: Half ring subjected to uniform distributive load	264
Figure 8.17: Comparing analytical with finite element model results.....	265
Figure 8.18: Effect of number of nodes on (a) number of iterations (b) on the normalized gas flow area and end gap clearance	267
Figure 8.19: Ring groove pressure.....	269
Figure 8.20: Cylinder bore distortion	270
Figure 8.21: Ring-bore conformability – top ring	271
Figure 8.22: End gap clearance – top ring	272
Figure 8.23: Flow area – top ring	272
Figure 8.24: Non-conforming node – top ring.....	273
Figure 8.25: Ring-bore conformability – second ring	274
Figure 8.26: Ring twist – second ring.....	275
Figure 8.27: End gap clearance – second ring	275
Figure 8.28: Flow area – second ring	276
Figure 8.29: Non-conforming nodes – second ring	276
Figure 8.30: Ring-bore conformability – oil ring segment.....	277
Figure 8.31: End gap clearance – oil ring segment.....	278
Figure 8.32: Flow area – oil ring segment	278
Figure 8.33: Non-conforming nodes – oil ring segment.....	279
Figure 8.34: Groove coordinate system.....	280
Figure 8.35: Ring-bore conformability – constrained second ring.....	283
Figure 8.36: Ring twist – constrained second ring	284
Figure 8.37: End gap clearance – second ring	284
Figure 8.38: Flow area – second ring	285
Figure 8.39: Non-conforming nodes – second ring	285
Figure 8.40: Loads on ring at one cross-section	287

KEY TO SYMBOLS

a_0	profile height at the top of the skirt
a_1	profile height at the bottom of the skirt
a_2	location along the skirt length where the skirt profile height is at maximum
a_3	skirt profile maximum height
a_4	first derivative of the profile at the top of the skirt.
$a_{cm,x}$	acceleration of connecting rod center of mass in X-direction
$a_{cm,y}$	acceleration of connecting rod center of mass in Y-direction
A_{flow}	gas flow area
A_{RMS}	rms acceleration objective function
a_p	piston axial acceleration
B	tuning constant
c	nominal piston-to-cylinder bore clearance
C_h	crown height
D	piston diameter
dA	infinitesimal skirt area
d_{cyl}	cylinder diameter
D_i	ring inside diameter
d_n	piston skirt nominal diameter
D_o	ring outside diameter
d_w	wrist-pin diameter

D_x	piston diameter in the thrust axis
D_z	piston diameter in the wrist-pin axis
E	modulus of elasticity
E'	composite modulus of elasticity
E_1	piston modulus of elasticity
E_2	cylinder bore modulus of elasticity
e_b	eccentricity at the bottom of the piston
e_c	ring end gap clearance
e_{cg}	eccentricity at the center of gravity
e_{lb}	eccentricity at the bottom of the second land
e_{lt}	eccentricity at the top of the second land
e_p	eccentricity at the wrist-pin axis
e_{sb}	eccentricity at the bottom of the skirt
e_{st}	eccentricity at the top of the skirt
e_t	eccentricity at the top of the piston
e_z	eccentricity along the wrist-pin
\mathbf{f}	load vector
F_c	normal contact force
F_{cx}	contact force X_p -direction
F_{cz}	contact force Z_p -direction
F_f	total friction force on the skirt
F_{fc}	contact friction

F_{fh}	hydrodynamic shear
F_{fwz}	wrist-pin friction
F_{fy}	friction force in the Y_p -direction
F_g	combustion gas force
F_{gy}	combustion gas force in the Y_p -direction
F_{hx}	hydrodynamic forces in X_p -direction
F_{hz}	hydrodynamic forces in Z_p -direction
F_{ipx}	piston inertia in the X_p -direction
F_{ipy}	piston inertia in the Y_p -direction
F_{ipz}	piston inertia in the Z_p -direction
F_{irx}	connecting rod inertia in the X_p -direction
F_{iry}	connecting rod inertia in the Y_p -direction
F_{iwx}	wrist-pin inertia in the X_p -direction
F_{iwy}	wrist-pin inertia in the Y_p -direction
\mathbf{f}_L	local load vector
F_{mpx}	piston weight component in the X_p -direction
F_{mpy}	piston weight component in the Y_p -direction
F_{mrx}	connecting rod weight component in the X_p -direction
F_{mry}	connecting rod weight component in the Y_p -direction
F_{mwx}	wrist-pin weight component in the X_p -direction
F_{mwy}	wrist-pin weight component in the Y_p -direction

F_o	crankshaft reaction force
F_{pwx}	reaction at the piston-wrist-pin interface in the X_p -direction
F_{pwy}	reaction at the piston-wrist-pin interface in the Y_p -direction
F_r	radial reaction force
F_{rwx}	reaction at the wrist-pin-connecting rod interface in the X_p -direction
F_{rwy}	reaction at the wrist-pin-connecting rod interface in the Y_p -direction
F_t	force due to ring tension
F_{tx}	total force in the X_p -direction
F_{tz}	total force in the Z_p -direction
g_2	geometric constraint
h	oil film thickness
H	skirt material hardness
\dot{h}	squeeze film velocity
h_i	channel height
h_o	oil film thickness due to the elastohydrodynamic effects
$h_{p,i}$	leakage channel height
H_σ	normalized oil film thickness
I_p	second moment of inertia of the piston about the Z_p -axis
I_r	second moment of inertia of the connecting rod about the Z_p -axis
k	pressure iteration step
\mathbf{K}	global stiffness matrix
\mathbf{K}_L	local stiffness matrix

K_w	skirt wear coefficient
l	element length
L	skirt length
l_{ox}	direction cosine
M_{ic}	piston inertia moment
m_{ox}	direction cosine
m_p	piston mass
m_r	connecting rod mass
M_{rod}	connecting rod inertia moment
M_t	total moment about the wrist-pin
m_w	wrist-pin mass
N	matrix of shape functions
n	number of nodes
N	engine speed in revolutions per minute
n_b	number of regression coefficients
n_d	number of data values
n_{ox}	direction cosines
p	ring groove index
\bar{P}	pressure on the boundary
p_0	distributive load
P_g	combustion gas pressure
P_h	hydrodynamic pressure

\mathbf{q}	global displacement vector
\mathbf{q}_L	local displacement vector
r	radial displacement
R	ring radius
R	piston radius
R_a^2	adjusted coefficient of determination
r_1	crankshaft radius
r_2	length of the connecting rod
R^2	coefficient of determination
r_3	wrist-pin position from the crankshaft axis
R_a	roughness average value
S	distance moved by the skirt
\mathbf{T}	transformation matrix
T_1	high oil temperature
T_2	low oil temperature
\mathbf{T}_a	transformation matrix
\mathbf{T}_b	transformation matrix
T_{oil}	oil temperature
T_{ref}	reference oil temperature
\mathbf{T}_s	transformation matrix
u_x	deformation component in the X_p -direction
u_z	deformation components in the Z_p -direction

V	volume of material removed
v_p	piston axial velocity
w	ring width
W_{fr}	friction work constraint
x_{cg}	X_p -coordinate of the piston's center of mass
X_c - Y_c	cylinder local coordinate system
x_o	X_o -coordinate for the crank offset
X_o - Y_o	global coordinate system
X_{pp} - Y_{pp}	wrist- pin local coordinate system
X_p - Y_p	piston local coordinate system
x_s - y_s	skirt 2-D coordinate system
x_{wp}	X_p -coordinate of the wrist-pin offset
y	set of data
\bar{y}	arithmetic mean of y
y_{cg}	Y_p -coordinate of piston's center of mass
y_p	piston axial position
y_{wp}	Y_p -coordinate of the wrist-pin

Greek symbols

α	coefficient of thermal expansion
α	constant in double ellipse equation
α_2	connecting rod angular acceleration
β	piston tilt
β	constant in double ellipse equation
β	ring twist
Γ	boundary region
γ	cylinder bank angle
δ	piston ovality
δ_c	cylinder bore deformation
δ_p	skirt profile height
δ_s	skirt deformation
Δt	time step
δ_o	piston ovality
ε	residual error
η	asperity density on the skirt
η	scaling factor
θ	crankshaft angle
θ_p	piston angular coordinate
κ	piston mass to diameter ratio
λ	penalty number
$\lambda_{p,i}$	leakage coefficient

μ	oil dynamic viscosity
$\mu_1,$	oil viscosity at T_1
μ_2	oil viscosity at T_2
μ_f	coefficient of friction between the piston skirt and the cylinder liner
μ_{ref}	oil viscosity at T_{ref}
μ_w	wrist-pin friction coefficient
ν_1	piston Poisson ratio
ν_2	cylinder bore Poisson ratio
ξ	asperity radius of curvature on the skirt
Π	potential energy
ρ	distance from the connecting rod big end to its center of mass
σ	composite standard deviation of asperity height distribution
$\hat{\sigma}$	standard deviation of the error
σ_1	standard deviation of asperity height distribution on the surface 1
σ_2	standard deviation of asperity height distribution on the surface 2
φ	connecting rod angle
$\chi(P_h)$	switch function
Ψ	descent (merit) function
ω_1	engine angular speed
ω_2	connecting rod angular speed
ω_r	underrelaxation factor

Abbreviations

ABDC	after bottom dead center
ATDC	after top dead center
BBDC	before bottom dead center
BDC	bottom dead center
BTDC	before top dead center
CAD	computer aided design
CAE	computer aided engineering
FDM	finite differences method
FEM	finite element method
HC	hydrocarbon
LHD	Latin Hypercube Design
NURBS	non-uniform rational basis splines
PIFEAD	Piston Finite Element and Dynamics
RMS	root mean square
TDC	top dead center
WOT	wide open throttle

INTRODUCTION

This past year with its economic crisis has been an awakening to the automotive industry worldwide. It was clearly understood that the old school “muscle engine” was being put aside and the smaller, more fuel-efficient and environmentally friendly engine was stealing consumers’ hearts. The trend started a while back, especially in Europe and Asia, but this year only reinforced it and made this new breed of engines more desirable even in the North American markets. The key to the success of every manufacturer being able to understand and adjust to the current consumer demands. For this to happen, the people who drive these manufacturers have to understand the trends. The author of this dissertation was faced with a similar challenge, adjusting from the search of sheer power to the search of a greener future:

“The internal combustion engine always fascinated me, since a young boy watching the Formula 1 cars circling the track. In the search to understand better the technologies that caused this fascination and with the intention of one day contributing to it, I embarked on my engineering journey. And what better place to enhance the understanding of the internal combustion engine than the front where chemistry meets mechanics, the heart of the engine, the piston and piston rings. A famous Greek poet, Kavafis, once wrote ‘it is the journey that counts, not the destination.’ And indeed all the experiences along this dissertation journey have influenced my thinking. I came in searching for sheer power for the racetrack and I am going out looking to utilize my expertise in improving engine efficiency and life and ultimately contribute to a greener future.”

In recent years there has been an increased awareness of the future of the planet. In response to this, governments across the globe are introducing more stringent emission standards. At the same time, a concern for the quantity of oil reserves fuels the search for higher efficiencies. This search for fuel efficiency is also driven by the most important

factor in the lifecycle of the internal combustion engine, the consumer. Since 2008 when gas prices rose beyond four dollars a gallon, there has been a big jump in demand for more fuel-efficient engines. The manufacturers who could deliver prospered whereas the ones who could not suffered.

As mentioned earlier, the key to every manufacturer's success is to understand and adjust to the consumer demands. What are the demands nowadays though? Low cost, high fuel efficiency, long trouble-free life, low emissions and comfort at operation, that is low noise and vibration. In order to meet all of these demands, a vast amount of design and testing is needed. This is where the numerical models for the assessment of cylinder-kit performance and more generally of the whole engine apply. Such models greatly reduce the amount of time from conception to launch of a new product. They reduce the number of expensive prototypes required to complete a design, they allow for multiple design iterations to be tested in virtual space. As a result, a better final product design that can meet all consumer demands can be achieved in less time, thus making it cheaper. After all, it is cheaper to move electrons than atoms.

CHAPTER 1. NUMERICAL MODELS FOR THE ASSESSMENT OF CYLINDER-KIT PERFORMANCE

1.1 Motivation

In today's automotive market, the ability of a manufacturer to develop a powerful, fuel-efficient, low emission, quiet and durable internal combustion dictates its ability to survive in the years to come. The prime "navigators" in the search of these qualities are computational tools. Such tools allow for a fast and relatively cheap course for a prototype design, but they can also be utilized for troubleshooting and optimization of existing designs.

The internal combustion engine as it is known today has been around since 1876 when Nikolaus Otto, Gottlieb Daimler and Wilhelm Maybach developed the first practical four-stroke internal combustion engine. Despite the fact that nowadays alternatives are being sought, and implemented, to the internal combustion engine, it does not cease to be the prime mover in automobiles and heavy duty machinery. As long as there is oil to be pumped out of the earth, the internal combustion engine will exist. This necessitates continuous efforts in investigating the physics of this machine.

The internal combustion engine is a cyclic machine. Its cyclic behavior represents an unsteady complex system with multiple physical processes occurring simultaneously. The system then is a multidisciplinary one which can be described by combustion, thermodynamics, heat transfer, solid mechanics, fluid mechanics, dynamics, and tribology.

The “heart” of a reciprocating internal combustion engine is the cylinder-kit. It is comprised of the piston, the piston rings, the cylinder bore and the cylinder head. The cylinder bore and cylinder head are stationary, whereas the piston and piston rings reciprocate allowing for the formation of the combustion chamber with a varying volume. The function of the piston is to convert the thermal energy of the combustion gases into the mechanical energy that drives the engine. The piston rings are responsible for sealing the combustion chamber, that is, preventing any gases escaping into the crankcase. They achieve this by sliding over the cylinder bore which acts as a guide for this reciprocating motion. It is generally believed that about half of the mechanical energy losses in an engine occur at the piston assembly [60]. Emissions are also greatly affected by the sealing ability of the piston rings. Therefore piston and piston ring design is a very important factor in engine performance.

The focus of this dissertation will be on the piston, the piston rings and the cylinder bore and their interactions.

1.2 Objectives

The main objective of this work was to develop a piston dynamics numerical model that would utilize the meshed geometry of a piston CAD model and also incorporate advanced numerical techniques in the model. A pre-existing model [7] that used parameterized piston geometry and a methodology of different modes of contact to evaluate piston dynamics proved to have limited capabilities in modeling modern engines and was being phased out. During the development process of this new model, the necessity to consider motion along the wrist-pin was identified and implemented. This

new model has been used in numerous modeling efforts as it is described further on in this dissertation.

Also, along the way, an opportunity to develop an optimization methodology tailored to the piston skirt profile optimization problem was identified and pursued. This methodology complements the piston dynamics numerical model and has been proven to be robust and easy to implement.

Finally, in the last stages, effort was made to understand piston ring dynamics by utilizing a commercial ring dynamics numerical model. This led to the identification of potential limitations in conventional models and the commencement of a new advanced 3-D ring dynamics model.

1.3 Previous Efforts

Mathematical models for the assessment of cylinder-kit performance have been around since the inception of the internal combustion engine. These models started becoming more and more complex by simultaneously accounting for multiple phenomena, with the evolution of computers. They are utilized and independently developed both in academia and in industry. In the recent years, facing all the demands for the optimal engine, special attention is paid to these models.

1.3.1 Piston Dynamics

Over the years several numerical models and computational tools have been developed in an attempt to model piston behavior and estimate its performance and its impact on the efficiency of the internal combustion engine.

In the area of thermal modeling Annand [2] and Woschni [75] pioneered in proposing correlations to calculate the heat transfer coefficient of the combustion gases above the piston crown. Woschni [76] continued to evaluate heat transfer coefficients for a high-speed diesel engine piston. He proposed ranges for heat transfer coefficients describing the different surfaces of the piston. Wu et al. [79] modified Annand's correlation to include radiation effects, and they developed a numerical model for the calculation of the piston's temperature distribution. Li [32] considered the piston's thermoelastic behavior. He assumed that temperature fluctuations during a cycle affect a piston layer only about 2 mm thick. Beyond this layer the temperature is steady, given enough operating time for the engine. Consequently he treated the piston's thermoelastic behavior as a steady state problem. He used experimental temperature measurements to propose a range of heat transfer coefficients for an aluminum gasoline piston.

Li et al. [34] developed an automotive piston lubrication model to study the effects of piston pin location, piston-to-cylinder clearances and lubricant viscosities on piston dynamics and friction. They solved for the particular solutions of the Reynolds equation using finite differences, and used the Newton-Raphson method to solve for the nonlinear equations of motion for the piston. In their model they assumed a rigid piston. Li [33] considered the elastic deformation of the piston skirt; integrating this with hydrodynamic lubrication has formed the elastohydrodynamic lubrication analysis which

is considered by most of the recent efforts [9, 10, 11, 17, 29, 30, 41, 42, 47, 55, 74, 81, 82]. All these have contributed to understanding the elastic deformation of the piston using the finite element method. Oh et al. [47] used the finite element method to solve for the Reynolds equation; however they linearized it, thus solving for a set of linear equations. The other efforts used finite differences to solve for the Reynolds equation. This method, however, requires mapping of nodal information back and forth from the finite element mesh to the finite difference grid. This can result in the loss of crucial numerical information, especially where sharp gradients exist between two nodes. Zhu et al. [81, 82] were the first to consider the elastic deformation of the cylinder bore. They also used the average Reynolds equation developed by Patir and Cheng [54] which accounts for the effect of surface texture on hydrodynamic lubrication. They proposed flow coefficients for the average Reynolds equation that account for the skirt waviness if any. They also solved for the solid-to-solid contact using the Johnson (1985) model for a blunt wedge against a plane. In more recent years Duyar et al. [11] used the mass-conserving Reynolds equation to solve for the hydrodynamic pressure using finite volumes. They predicted lower hydrodynamic pressures compared to the finite difference solution of the Reynolds equation. This allowed for higher transverse motion of the piston and consequently higher contact forces. Chui [7] continued the modeling efforts on an existing numerical model to implement the elastohydrodynamic analysis of the piston skirt. He used oil film thickness measurements from an optical engine to validate his efforts, and he concluded that in-cylinder gas pressure and engine load play significant and independent roles in determining piston secondary motion. McClure [41, 42] developed a numerical model to investigate component friction under both dry and

lubricated conditions. She concluded that the dry model can be used as a fast tool for investigating the influence of system parameters on piston dynamics, as it is computationally less expensive.

All these models, though, employed a common assumption. Piston motion along the wrist-pin was considered negligible, compared to the oscillating motion of the piston in the thrust plane. Consequently the motion along the wrist-pin was ignored. This allowed for the modeling of a half-piston in some of the above models. This assumption in turn led to another assumption; the pressures developed on the skirt surface were symmetric. Consequently a symmetry boundary condition was imposed in the solution of the Reynolds equation. However, this is not the case, especially when bore deformation is considered, which is usually circumferentially asymmetric. Furthermore, assuming no motion along the wrist-pin allows for the incorrect prediction of the location of possible solid-to-solid contact. Thus skirt wear is not accurately captured. Also, the interaction of the piston lands with the cylinder bore was not investigated. Although piston land-cylinder bore interaction is not desirable and piston design engineers try to inhibit it, it does occur under actual operating conditions. These observations imply the need for a new improved computational model for piston dynamics.

Panayi et al. [49, 51] compared the behavior of the parameterized piston used by CASE, a comprehensive cylinder-kit simulation software used to predict piston and ring-pack dynamics, to the behavior of the corresponding CAD piston model under different loading conditions. The two showed very good agreement under both thermal and mechanical loading. However, they demonstrated quantitative disagreement when the deformation due to thermal loading was considered. This led Panayi in search of a

computational tool that would consider the real piston model. The Piston Finite Element Analysis code was developed [50]. This model is a computational tool that uses an externally supplied mesh of a CAD piston model to perform a finite element analysis over a full four-stroke cycle. It estimates the piston's temperature distribution, deformation, strains, and stresses.

The need, posed above, for an improved computational model for piston dynamics led to further developments, yielding the Piston Finite Element Analysis and Dynamics model. This model is a marriage of the methods used in the previous piston modeling efforts and the finite element analysis developed in [50], as well as some of the methods used in bearing dynamic analyses [46]. The model considers translation along the wrist pin as well as second land interactions with the cylinder bore.

1.3.2 Skirt Profile Optimization

The relation between skirt profile and piston performance involves complex, non-linear behavior. Over the years several attempts have been made in the development of piston performance simulation software [29, 41, 53, 74, 81, 82]. These works consider the effects of the skirt profile but treat profile height as prescribed input, usually as 2-D coordinates along the skirt length, and then interpolated over a mapped 2-D skirt domain. These 2-D coordinates are the industry standard in describing skirt profiles on piston CAD drawings. The models are quite effective in analyzing piston performance, but they are complex, computationally intensive, and available to practicing engineers primarily as black-box software packages. A set of coordinates describing the skirt profile typically consists of twenty points. The optimization of such a set would be very expensive and

require highly complex constraints to ensure a barrel-shaped skirt profile. To overcome this obstacle, the 2-D coordinates can be very accurately interpolated with a quartic polynomial. Consequently, the shape of the skirt profile can be defined by five design variables and a geometric constraint can be imposed to ensure the optimization yields a barrel-shaped profile. This makes the optimization far more attractive. The random selection of design variables by standard space-filling techniques, however, would yield some non-barrel-shaped profiles and make the implementation of such techniques troublesome. Tsujiuchi et al. [67] presented the optimization of the piston skirt profile for a generator engine. They showed that an optimized profile (defined by a quartic polynomial) is effective in reducing piston slap.

Since piston performance simulations are performed using black-box software packages, the optimization of skirt profiles needs to be performed on surrogate models. One attractive method for surrogate modeling is the Response Surface Methodology (RSM) where response surfaces are fitted to data collected from the expensive black-box simulations. In turn these surfaces are used for the optimization. This method has been widely used in research. Jones et al. [28] developed an efficient global optimization for black-box functions aiming to model the response of nonlinear functions that typically occur in engineering. Li et al. [35] presented a new approach for the surrogate modeling of multi-response deterministic simulations. These surrogates are built by utilizing the correlation of different responses. This makes them mutually dependent and thus improving the accuracy of the surrogate itself. Both of these efforts used the Kriging model (Sacks et al. [63]) to approximate the responses. Papila and Haftka [52] explored the modeling errors associated with polynomial response surfaces. They demonstrated

that higher-order (cubic) models help reduce noise in the data as well as increase the accuracy of the optimization process.

The two competing response surfaces are the Kriging and polynomial models. It is believed that a Kriging model is more accurate for nonlinear problems and typically requires fewer function evaluations than a traditional second order polynomial response surface. However, it is far more complex to implement, as its parameters are estimated so that they maximize the likelihood of the sample. On the other hand, a polynomial model is easy to construct and use. The interested reader is referred to Simpson et al. [64] and Wang and Shan [72] for a thorough review of surrogate modeling techniques.

An important area of research focuses on methods that iteratively improve the accuracy of RSM. Wujek and Renaud [80] presented a review of such methods and proposed an adaptive strategy for the adjustment of design variable limits.

Wang et al. [71, 70] developed an Adaptive Response Surface Method (ARSM) utilizing LHD. ARSM progressively reduces the design space by finding new bounds for each design variable, inheriting the last optimum, and generating new LHD points to make up for the ones that fall outside the reduced design space. This method, though, requires the solution of two subsidiary optimization problems for each design variable, with nonlinear objective functions at each reduction step. Wang also incorporated a search algorithm to place the new LHD points at the underrepresented regions of the design space.

The findings from these efforts are utilized to develop the pseudo-Adaptive Response Surface Method which is presented in Chapter 6.

1.3.3 Ring Dynamics

Alongside the piston dynamics numerical models, there has been parallel development of ring dynamics models. These models couple the gas dynamics of the combustion gases with the ring motion in an effort to assess the performance of the ring-pack [1, 7, 12, 13, 14, 37, 38, 39, 40, 61, 66]. All these have contributed to better understanding the ring dynamics. Richardson [61] made a comparison between measured and calculated interring gas pressures for a diesel engine using two different ring-pack configurations. The comparison showed good agreement between measured and predicted results. The numerical model helped explain the differences in measurements observed for the two ring packs. These were due to significant differences in ring motion.

Ejakov et al. [13] used a ring dynamics model to generate blow-by maps and compared them to measured ones. The results showed good correlation. In their study they found that blow-by is greatly affected by top ring design and motion. They also concluded that ring-pack performance depends on the ring parameters such as mass and tension. Also, they found that cylinder bore-to-stroke ratio affects ring-pack performance as it influences ring-pack inertia.

Ejakov [14] continued to develop an existing ring dynamics model. He developed the first model to consider ring twist calculated via finite element methods. For his model he considered only a half ring and used that to generate gas flow area maps by applying a range of loads and moments on the ring. These flow area maps would be used to perform the two-dimensional gas flow calculations. He found that ring twist is an important parameter affecting ring-pack performance and necessitates a three-dimensional analysis of the ring motion. He also developed an optimization technique for the ring-pack design.

It was used to show that optimizing ring geometry can lead to significant decrease in blow-by.

Liu et al. [37, 38, 39, 40] developed a static finite element model to facilitate ring design. The model can be used to fit an uncompressed ring into the cylinder bore and predict the induced twist due to the radial loads. The model accounts for half the ring assuming axisymmetric conditions about the cylinder bore axis. He then went on to develop a three-dimensional model for ring and gas dynamics by coupling the dynamics along the ring circumference. It was used to model a heavy-duty diesel engine and showed significant variations along the ring-pack circumference in both interring gas pressure and ring motion predictions.

Following the observations from these researchers and recognizing from experience that asymmetric cylinder bore deformations can have great impacts on the cylinder-kit performance, it was deemed appropriate to develop a new advanced 3-D ring dynamics model. The finite element developments for this model are presented here. The model accounts for the whole ring in order to capture all the variations along the ring circumference.

1.4 Structure of the Dissertation

The rest of this dissertation is organized as follows. An overview of the cylinder-kit and its components is included in Chapter 2. In Chapter 3, the theory behind the piston dynamics numerical model is described. The present approximations in literature for the Greenwood-Tripp asperity contact model are reviewed and a new one is proposed in Chapter 4. In Chapter 5, the piston dynamics numerical model is employed to assess the

performance of different gasoline and diesel pistons. Some of the predicted results are compared and correlated with test results. In Chapter 6, an optimization algorithm tailored for piston skirt profiles is presented. An example for the optimization of a gasoline piston skirt profile is also shown. In Chapter 7, the predicted ring-pack pressures and blow-by for three gasoline engines are discussed, and numerical results are correlated with measurements. An introduction to the finite element model for development of an advanced 3-D ring dynamics model is presented in Chapter 8. The dissertation is concluded in Chapter 9 where limitations of the models are identified, experiences are shared and some recommendations are made.

CHAPTER 2. THE CYLINDER-KIT

2.1 Introduction

The internal combustion engine converts the thermal energy of combustion into mechanical energy. This conversion occurs at the cylinder-kit. The cylinder-kit is comprised of the piston, piston rings, cylinder liner, and cylinder head. The cylinder liner and cylinder head are stationary, whereas the piston and piston rings are movable. The piston converts the thermal energy of combustion into reciprocating motion, which is transferred via the wrist-pin to the connecting rod and finally to the crankshaft where it is converted and output as rotational motion. The reciprocating motion of the piston allows for the formation of the combustion chamber with a varying volume. The piston rings are responsible for sealing the combustion chamber, that is, preventing any gases escaping into the crankcase. They are situated in the ring grooves below the piston crown and create a seal by sliding over the cylinder bore, which acts as a guide for this reciprocating motion.

In this chapter the main components of the cylinder-kit that are of relevance to this dissertation, the piston and piston rings, will be described. The interested reader may refer to [22] for an in-depth description of the other components.

Figure 2.1 shows a schematic of a V-8 pushrod engine with its main components (Table 2.1). The cylinder head shown in this schematic is simplified. It houses the valves, intake and exhaust ports, the camshafts for overhead camshaft engines, and the spark plugs for gasoline engines.

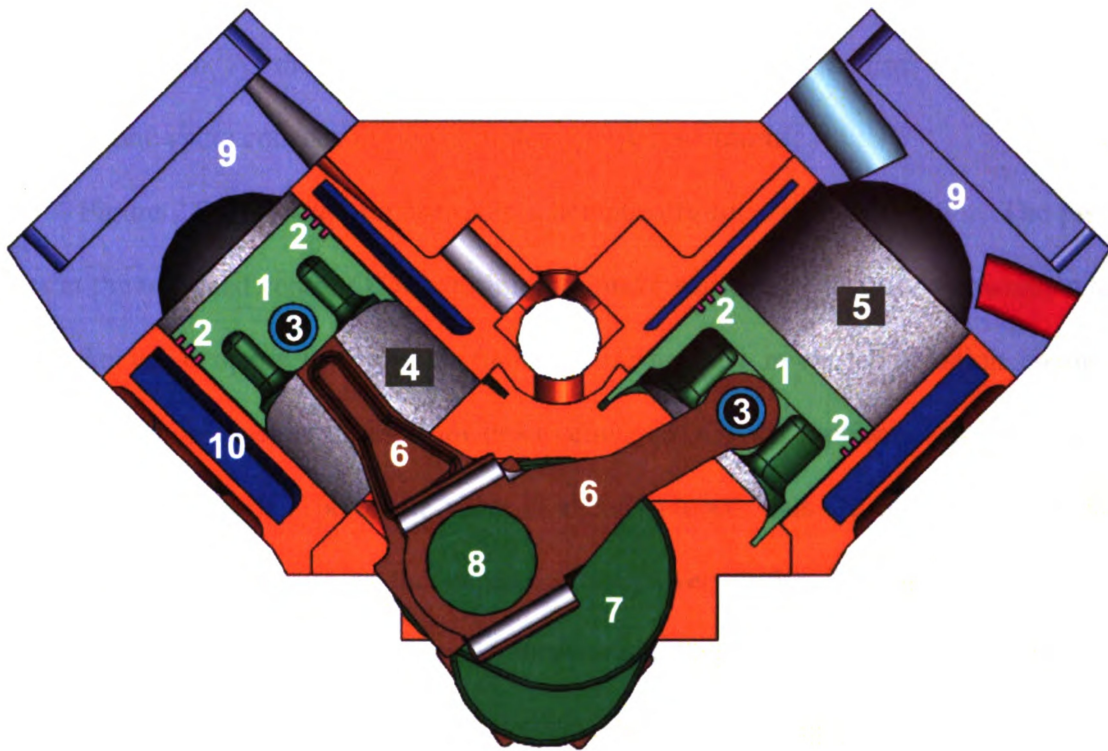


Figure 2.1: Cross-section of a V-8 engine

Table 2.1: Engine components in Figure 2.1

No.	Component
1	Piston
2	Ring-pack
3	Wrist-pin
4	Cylinder liner
5	Combustion chamber
6	Connecting rod
7	Crankshaft
8	Crankshaft bearing
9	Cylinder head
10	Water jacket

The four-stroke internal combustion, on which this dissertation is focused, is the most widely used type of engine in automobiles, heavy-duty machinery and small scale power generation. As the name implies, the four-stroke engine requires four strokes per cycle and one cycle consists of two complete crank revolutions.

Figure 2.2 shows the four strokes schematically for a gasoline engine. The piston starts at the top dead center (TDC) during the intake stroke and moves downwards while the intake valve opens to allow air-fuel mixture to flow in the combustion chamber. When the piston reaches the bottom dead center (BDC) the motion is reversed and it starts moving upwards. The intake valve is already closed; thus the compression begins. The next stroke is known as the expansion or power stroke. The air-fuel mixture is ignited by the spark-plug and the useful work is delivered pushing the piston down. The final stroke is the exhaust where the exhaust valve opens and the exhaust gases are pushed out by the piston. In the case of a diesel engine, the spark plug is not necessary as the air-fuel mixture self-ignites. Also, the fuel is injected directly into the combustion chamber, something that is being adopted in modern gasoline engines as well in an effort to control emissions better and limit cylinder-to-cylinder variability.

The convention in this dissertation is that a cycle begins at 0 cad (crank angle degrees) and ends at 720 cad. Each cycle is subdivided as follows:

- | | |
|-----------------|--------------------|
| • 0 – 180 cad | intake stroke |
| • 180 – 360 cad | compression stroke |
| • 360 – 540 cad | expansion stroke |
| • 540 – 720 cad | exhaust stroke |

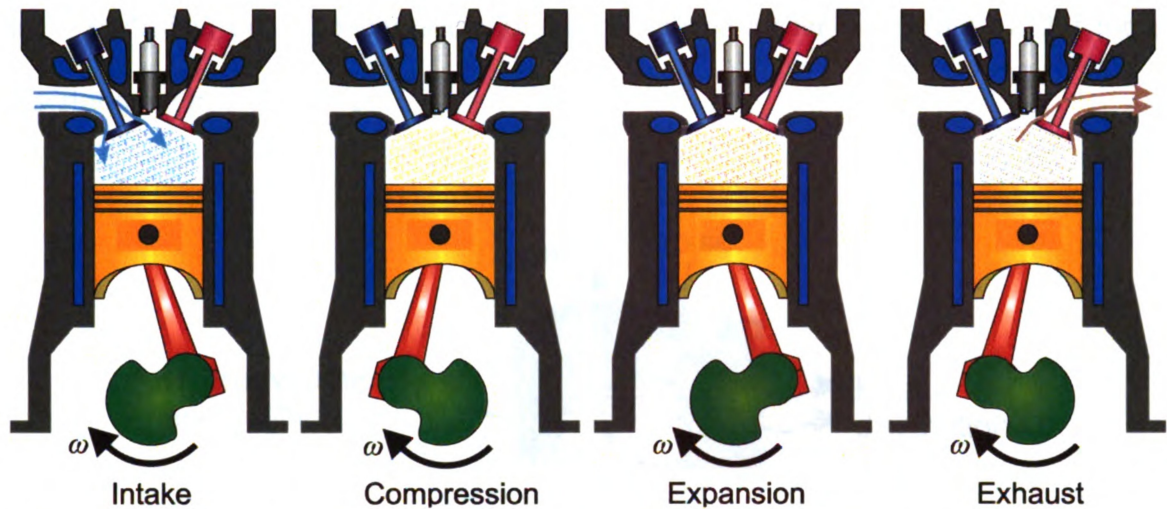


Figure 2.2: The four strokes in a gasoline engine – intake, compression, expansion and exhaust

2.2 The Piston

The piston assembly, even after more than a century of revisited designs, is far from being ideal. While the piston undergoes the reciprocating motion it loses energy by several modes (Figure 2.3) such as inertia losses due to the piston mass, noise due to slapping on the cylinder liner, heat transfer through the ring-pack and the skirt to the cylinder liner, hydrodynamic shear and scuffing at the skirt-cylinder liner interface, and bearing friction at the wrist-pin, connecting rod and crankshaft interfaces. It is generally believed that about half of the mechanical energy losses in an engine occur at the piston assembly [60]. Consequently, assessment and control of these losses requires careful piston design and investigations on piston dynamics in order to understand how piston geometry and material properties affects them.

Figure 2.4 and Table 2.2 show and name respectively the different piston features. The piston external surfaces are comprised of the crown, the ring-pack, the skirt, the under-crown area and the wrist-pin bore. The basic function and design considerations

are described in the following sections. The interested reader is referred to [27] for a description of piston features.

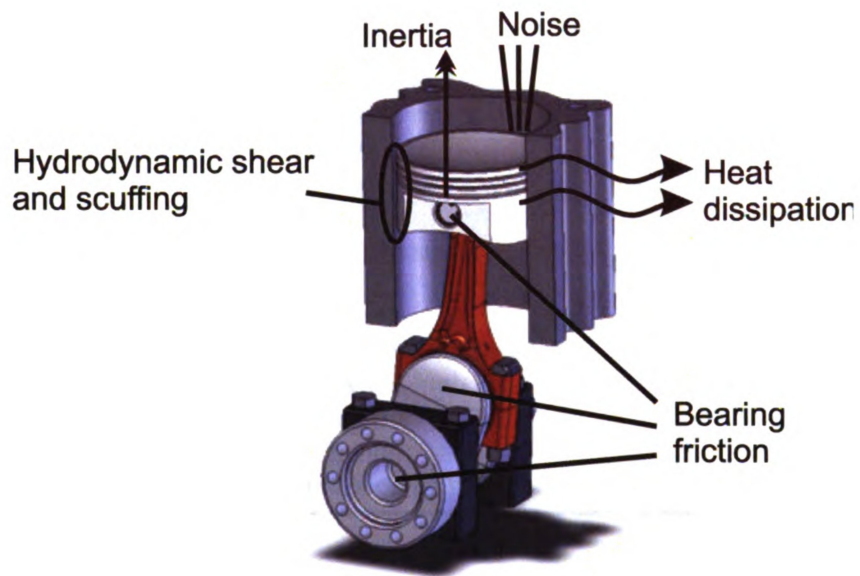


Figure 2.3: Modes of energy losses at the piston assembly

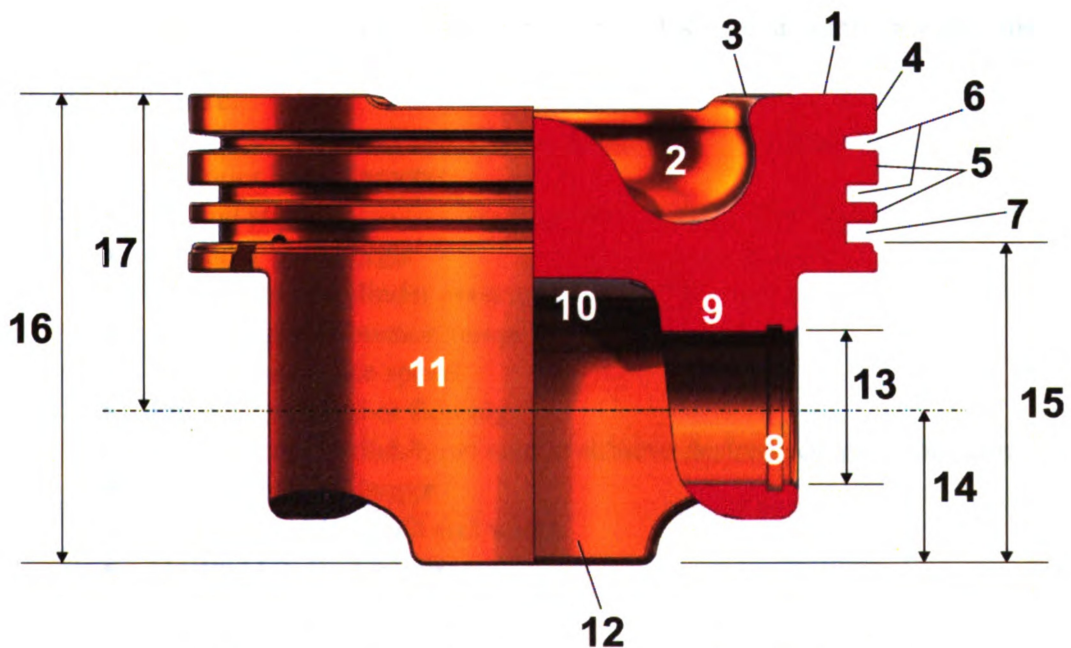


Figure 2.4: Piston features, light-duty diesel piston

Table 2.2: Piston features in Figure 2.4

No.	Feature
1	Crown
2	Bowl
3	Bowl lip
4	Top land
5	2 nd and 3 rd ring lands
6	Compression ring grooves
7	Oil ring groove
8	Pin retainer groove
9	Pin-boss
10	Under-crown surface
11	Skirt
12	Skirt tail
13	Wrist-pin bore diameter
14	Lower skirt length
15	Skirt length
16	Piston height
17	Compression height

2.2.1 Piston Design

In order to design a new piston, several steps have to be followed by the design engineer. The first step is to collect some key engine design characteristics and operating conditions. These are:

- Cylinder bore diameter
- Engine stroke
- Cylinder bore height
- Maximum in-cylinder pressure
- Maximum combustion temperature
- Maximum engine speed
- Pin design, fixed or floating
- Piston dome or dish/bowl size to achieve desired compression ratio
- Connecting rod length
- Connecting rod small end width
- Desired top land width
- Piston ring widths

Once these parameters are obtained, the next step is to calculate the piston pin-boss inside spacing that will allow for minimum clearance with the small end of the connecting rod. Then the wrist-pin outside and inside diameters and length are calculated based on expected loading. The wrist-pin length then dictates the pin-boss outside dimension. The connecting rod small end outside diameter and piston under-crown boundary can then be established based on the wrist-pin outside diameter. Then the second and third land widths are calculated based on the maximum combustion temperature and in-cylinder pressure. With all these known dimensions, the wrist-pin outside diameter and the ring and land widths, and the piston compression height can be calculated. By considering the maximum combustion temperature and in-cylinder pressure, the minimum crown thickness can then be calculated. Next the pin-boss lower area is designed to withstand the inertia forces based on the approximate weight of the piston and wrist-pin.

The next step in the piston design process uses numerical models such the one described in this dissertation. Once engineers have established all the key dimensions of the piston, piston dynamics CAE tools are employed to determine the wrist-pin offset, skirt length, skirt profile, skirt ovality and ring land profiles. The optimal design of these features will ensure the optimal performance of the piston.

The final step in the piston design process is to employ cylinder head CAE tools to determine whether any valve pockets are required on the top of the crown. This is beyond the scope of this dissertation and will not be explored further.

2.2.2 Piston Mass

The inertia of the piston is one of the main modes of energy losses at the piston assembly. The objective in every piston design is to minimize the mass in order to keep inertia losses at a minimum. The piston compression height has the most influence on piston mass. The minimization of mass can be achieved with careful design iterations and the utilization of CAE tools to get the optimal dimensions for the piston features. Also newer, higher-strength aluminum alloys allow for the reduction of mass.

A ratio, κ , similar to density in units, is used to compare different piston designs based on mass,

$$\kappa = \frac{m_p}{D^3} \quad (2.1)$$

where m_p is the piston mass and D is the piston diameter.

Over the years this ratio has been decreasing. Table 2.3 shows these trends. By modern pistons, it implies designs that use high-strength aluminum alloys or use design techniques for uneven thrust sides.

Table 2.3: Piston mass to diameter ratios

Piston	κ (g/cm ³)
Conventional	~ 0.55 – 0.65
Modern	~ 0.50
Target	~ 0.40 – 0.45

2.2.3 Piston Crown

The piston crown forms the combustion chamber geometry together with the cylinder liner and cylinder head. It is the only piston surface that comes in direct contact with the combustion gases. Temperatures at the crown can range between 260 °C to 350 °C in gasoline engines. In diesel engines the crown temperatures can be even higher as combustion temperatures are higher.

The thickness of the crown depends on the in-cylinder peak pressures, and the shape depends on the required compression ratio. The domes are usually employed in gasoline engines to increase compression ratio. However, they increase weight. The bowls/dishes are employed to reduce weight and also enhance mixing of the fuel in direct-injection engines. Traditionally they are used on diesel pistons. These design characteristics of the crown, though, can have adverse effects in the operation of the ring-pack. Domes or bowls/dishes increase the surface area exposed to the combustion gases and thus increase heat transfer to the piston and in turn to the ring-pack.

2.2.4 Top Land

The key question to answer when designing the top land is how close the top ring can be placed to the crown so that temperatures will not have adverse effects on its operation. The desired position is as close to the crown as possible to minimize weight. Also, low ring placement relative to the crown is not desirable for emissions. The crevice between the top land and the cylinder bore (Figure 2.5) traps unburnt gases which are released in the exhaust gases thus increasing hydrocarbon (HC) emissions.

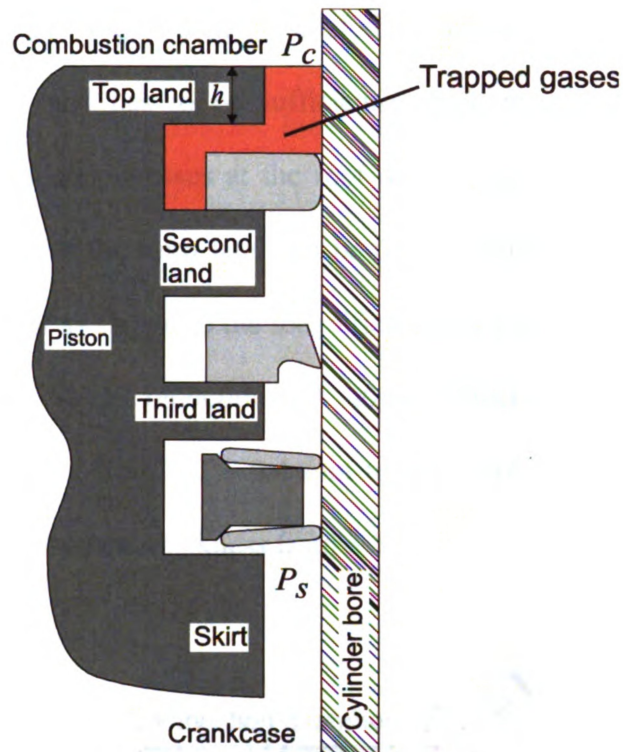


Figure 2.5: Top land crevice

The typical height of the top land in a gasoline engine is about 6.5 – 8 % of the piston diameter. There are some applications, especially in racing, with top lands as low as 3 mm. However, they utilize reinforcement at the top groove, usually a steel insert. The land profile should also be designed carefully in order to account for the thermal expansion of the top land and thus avoid contact with the cylinder liner during operation. Top land contact results in noise and cylinder liner polishing which decreases engine life.

2.2.5 Second and Third Lands

The height of the second and third lands is as important as the height of the top land in reducing piston weight. The second and third lands have to be designed to withstand the load from the combustion gas pressure (Figure 2.6). The combustion gas

pressure acts on the top ring, which most of the time is seated on the second land. Therefore the second land has to be sufficiently thick to withstand the combustion pressure load which creates stresses at the root of the groove. The pressure above the second ring is lower; thus the third land can be thinner than the second land. The fillet radius at the groove root as shown in the magnification in Figure 2.6 is very important as it leads to significant stress reductions. A stress reduction means a thinner land; increasing the fillet radius from 0.2 – 0.4 mm to 0.4 – 0.6 mm yields the same stress reduction as increasing the land thickness from 3.5 mm to 4.0 mm.

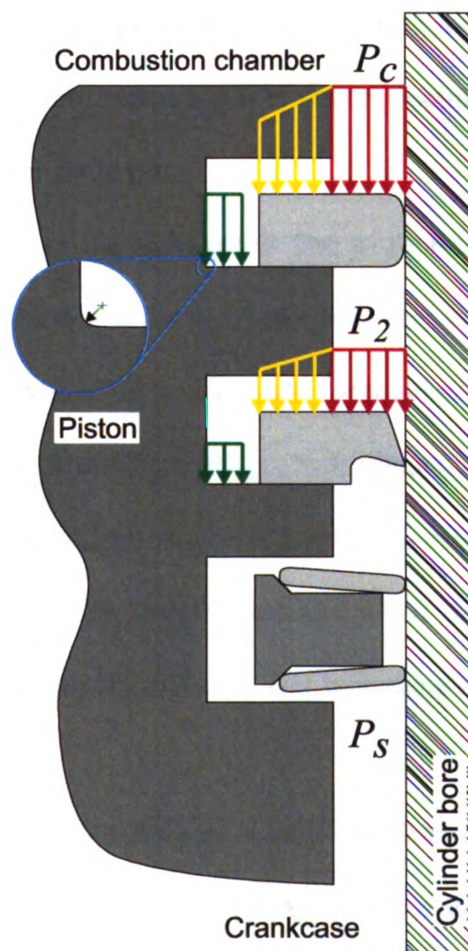


Figure 2.6: Second and third land loads

2.2.6 Piston Pin-boss

The piston pin-boss is one of the most highly loaded areas of the piston as it is responsible for transmitting the loads from the piston to the wrist-pin. Over-designing the pin-boss will result in unnecessary increase in mass, under-designing it will reduce piston life. Therefore the pin-boss design requires finding the right balance between piston life and piston mass.

2.2.7 Wrist-pin

The wrist-pin connects the piston to the connecting rod, and it is the intermediary component in the transmission of piston loads to the connecting rod. The wrist-pin can be of two types, a floating pin or fixed pin.

In a floating pin design the wrist-pin is free to rotate. This rotation is caused by the interaction of moment friction at the wrist-pin piston interface. The bearing surface of such a design is under heavy loading as the loads continuously change direction and also due to the renewal of the oil film which affects hydrodynamic pressures. The benefits of such a design are very good scuff resistance and low wear rates. In some applications the piston wrist-pin assembly is with interference and when the piston reaches operating temperatures and expands thermally it floats. This technique is employed to reduce noise at cold starts.

In a fixed pin design the wrist-pin is with interference fit at the connecting rod small end. This eliminates the need of a bushing at the connecting rod small end. With this design, though, all the oscillatory motion of the connecting rod is transferred at the pin-boss, which results in less favorable lubrication conditions. In such a case, other

techniques are employed to enhance lubrication. One way is to drill passages that will direct oil from the oil ring groove to the pin-boss.

The choice of a wrist-pin design is purely driven by cost. A fixed pin design is the cheapest and the path of choice. However lubrication problems that result in scuffing at the pin-boss will require that one introduces oil passages on the piston or moves to a floating pin design. The piston compression height also affects the wrist-pin design. A low compression height will lead to higher temperatures at the pin-boss, which will require better lubrication conditions and thus a floating pin design. Also high compression ratio engines that experience high loads at the pin-boss bearing require floating pin designs. Finally, the desired engine life will dictate the wrist-pin design. In long life expectancy engines, greater than 150,000 miles, such as track engines, the floating pin design is used as it shows less wear.

2.2.8 Piston Skirt

The piston skirt extends below the piston crown. It is comprised of the major and minor thrust sides, also sometimes referred to as thrust and anti-thrust sides. The major thrust side is the one that experiences the highest loads during the expansion stroke because of the connecting rod orientation (Figure 2.7).

The main function of the skirt is to provide guidance for the piston during its reciprocating motion. The piston is fitted with some clearance to the cylinder bore to account for thermal expansion. Most pistons are made of aluminum alloys with cylinder liners of cast iron, except in heavy-duty diesel engines where one can find steel pistons. Aluminum alloys expand faster and more than cast iron so the design of the piston has to

account for these, hence the piston and cylinder bore are designed with a clearance. Of course nowadays some of the high end engines utilize cylinder blocks made from aluminum or magnesium alloys which allow for much tighter clearances. The transverse components of the combustion gas force and inertia arising due to connecting rod orientation result in tilting about the wrist-pin and transverse movement of the piston. These two motions constitute the piston secondary motion. This motion can greatly impair ring sealing and oil consumption. Also, the secondary motion is responsible for the piston noise which can make an engine uncomfortable to the end user. As the piston move and slaps on the cylinder liner it transfers energy to it which creates noise.

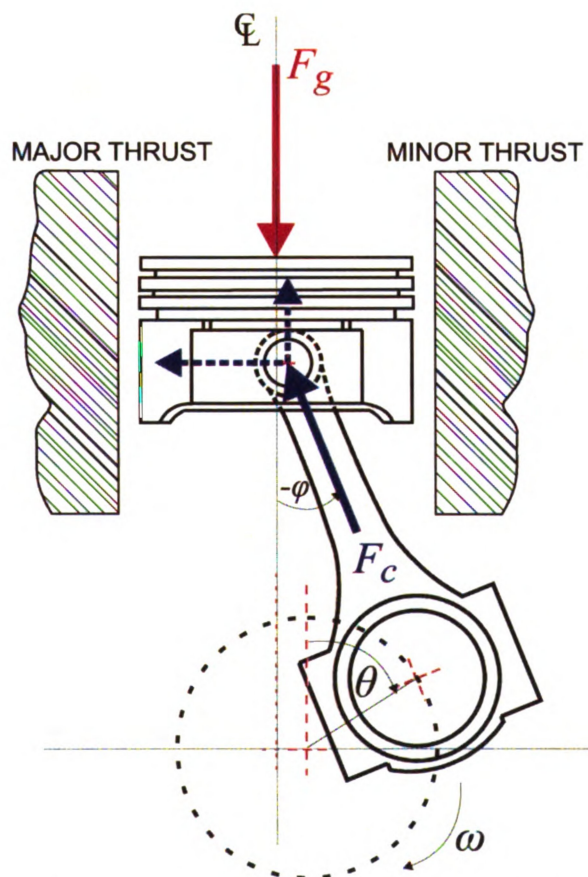


Figure 2.7: Connecting rod reaction force components during expansion stroke

A well-designed skirt will provide optimal control over the piston secondary motion, thus ensuring good ring sealing and minimization of oil consumption and induced noise. Several parameters determine the effectiveness of the skirt in completing these tasks:

- Clearance
- Skirt length
- Skirt profile
- Piston ovality
- Skirt elasticity
- Expansion control
- Position of piston's center of gravity relative to wrist-pin axis
- Wrist-pin offset
- Cylinder liner distortion

In recent years, in the attempt to reduce piston weight, shorter and shorter skirts are being introduced. This necessitates very careful skirt design and skirt profile definition.

The location of the wrist-pin axis relative to the skirt is an important factor dictating the loading on the skirt and the quality of the lubrication conditions. In order to achieve even loading of the skirt and development of optimum lubrication gap, it would require the wrist-pin axis to be located approximately at the middle of the skirt. This would minimize any moment imbalance about the wrist-pin due to hydrodynamic pressures. This, however, shifts the piston center of gravity away from the wrist-pin towards the crown and thus results in unfavorable tilting. In modern piston designs the wrist-pin axis is pushed as close to the crown as possible to minimize compression height and thus weight. This in turn necessitates extremely short skirts to accommodate the wrist-pin axis approximately at the middle of the skirt and thus very careful design of the skirt.

Another function of the skirt is to transmit forces from the piston to the cylinder bore. These forces depend on combustion pressure, inertia, and moment arising from wrist-pin offset and wrist-pin friction.

Also the skirt assists in the control of the piston temperature. It has a limited contribution in transmitting heat to the oil film, which in turn transmits the heat to the cylinder liner to end up in the cooling system.

2.2.9 Piston Skirt Design

All the skirt functions described in Section 2.2.8 together with piston weight and elasticity depend on skirt design. A well-designed skirt will result in the optimal operation of the engine, low friction, low noise, low oil consumption, low emissions and ultimately long engine life.

The skirt design can vary from full skirt, which can be found in some diesel applications where combustion pressures are very high, to the shaved skirts found in lighter duty applications. In gasoline engines the skirt tends to be more flexible as it experiences lower loads. Also, the surfaces are recessed in the pin direction, where there is no bearing function.

Another skirt design characteristic that has been introduced with the modern pistons driven by the difference in thrust side loads is the asymmetric skirt design. This aids in the reduction of piston weight as well as friction at the skirt surface. In such a design the major thrust side is different from the minor thrust side accommodating the loads on each side. This is achieved by the major thrust side being wider than the minor

thrust side, but more often the length and thickness for each side are adjusted according to the loading. In such a case the minor thrust side is shorter and thinner (Figure 2.8).

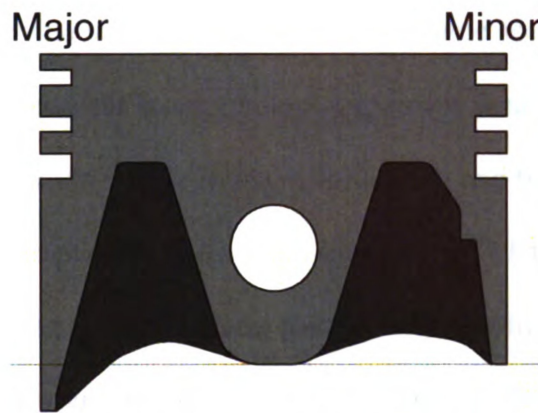


Figure 2.8: Asymmetric thrust sides

2.2.10 Piston Strength

The piston experiences cyclic loading throughout its operation due to combustion gas pressure, inertia, thermal expansion, and thrust side loadings. In order to fulfill its operation cycle after cycle it needs to be stiff in some areas but elastic in others. Its shape and cross-sections must always be matched to the local loading so that the permissible stresses will not be exceeded.

The design process of the skirt requires compromises to be made in regards to stiffness. On one hand the skirt has to be sufficiently stiff, that is achieved by thickness, to avoid large deformations or even fracture. On the other hand the skirt has to be sufficiently elastic to undergo deformations due to external loads from the cylinder liner. This will reduce scuffing and prolong the engine life. In general a more elastic skirt requires less expansion control (Section 2.2.12) but it is more susceptible to permanent

deformation which will degrade its functions. During operation the top part of the minor thrust side is subjected to loading due to the tilting that arises from the wrist-pin offset (usually wrist-pin offset is towards the major thrust side) and the deflection of the lower part of the skirt on the major thrust side. It must be able to withstand the reversing stresses that occur between the compression, expansion and exhaust strokes as the loading moves from minor thrust side to major thrust side and back to minor. The length and strength of the lower part of skirt, more significantly of the major thrust side, is responsible for maintaining the piston axis parallel to the cylinder bore axis. A poorly designed lower skirt part would fail to maintain the axes parallel at operating conditions and could result in land contact with the cylinder bore which would be detrimental to the engine life.

2.2.11 Piston Deformation

The cyclic loading the piston experiences results in a very complex deformation. The crown and skirt are connected, and thus their deformations are interrelated. In numerical modeling the piston deformation is obtained by superimposing the thermal expansion, and the deformations due to combustion gas pressure, inertia and thrust side loading.

The thermal expansion results in the diametral growth of the piston. This growth reduces moving down the skirt as temperatures drop and usually material volume is less. This allows for the barrel shaped skirt profile.

The combustion pressure and inertia loading bend the crown around the wrist-pin, which pushes the skirt downwards. This causes an oval deformation as the diameter in the thrust direction decreases relative to the diameter in the wrist-pin direction.

Over time the piston diameter in the thrust direction tends to reduce slightly. The piston tilt in this direction causes wear and in some cases plastic deformation, called skirt collapse. Skirt collapse can be caused by high mechanical or thermal loading or by unfavorable cylinder bore deformations. A well-designed skirt will minimize skirt collapse as it will lead to noise problems.

2.2.12 Thermal Expansion Control

As most of the pistons are made of aluminum alloys which expand much faster than the traditional cast iron cylinder liners, some effort is required in the design process to control the thermal expansion of the piston.

One method is the use of bimetal pistons. The first successful commercial design was introduced in the 1920's. These pistons usually have a steel (lower coefficient of thermal expansion than aluminum) ring or struts, inserted at the top of the skirt. This reduces the thermal deformation of the skirt in the thrust direction and directs it to the wrist-pin axis direction.

In recent years better understanding of piston design and advances in manufacturing techniques, materials, casting, skirt shaping and bore distortion control allow the mono-metal pistons to achieve most of the functional benefits of the bi-metal pistons.

Also, the introduction of newer aluminum alloys has made the bi-metal pistons less favorable. High silicon, hyper-eutectic aluminum alloys have lower coefficients of thermal expansion which enhances expansion control. Pistons made from these alloys are lighter, and also cheaper as manufacturing is simpler than bi-metal pistons. Table 2.4 shows a comparison of the coefficients of thermal expansion for different types of aluminum alloys and steel. A strutted piston typically would have a coefficient of thermal expansion at around $14.0 \mu\text{m}/\mu\text{m } ^\circ\text{C}$.

Table 2.4: Coefficients of thermal expansion for different materials

Material	α ($\mu\text{m}/\mu\text{m } ^\circ\text{C}$)
Hypo-eutectic aluminum alloy	21.6
Hyper-eutectic aluminum alloy	19.0
Eutectic aluminum alloy	21.0
Steel	11.0
Strutted piston	~ 14.0

2.2.13 Skirt Lubrication and Friction

The piston assembly is responsible for about 50% of the mechanical energy losses in an engine. The piston itself and more specifically the skirt itself contributes about one third of these losses. The major thrust side is heavily pushed towards the cylinder liner wall close to TDC in the expansion stroke. In order to prevent scuffing, lubrication is required. Lubrication necessitates the existence of a gap between the cylinder liner and skirt. The factors that have an important effect on this gap are the skirt profile barrel

shape, the design of the skirt upper and lower edges, and the piston mobility about the wrist-pin.

Lubrication does not eliminate friction. However, it minimizes it. The hydrodynamic pressures developed at the skirt-liner interface result in hydrodynamic shear stresses. The magnitude of these shear stresses depends on the oil viscosity which is temperature dependent, on the piston axial velocity, and on the gap or oil film thickness. As the gap decreases, the shear stresses increase.

The steps employed in the piston design process to reduce friction are the reduction of the skirt surface area, the design for adequate clearances at all operating conditions, the hydrodynamic optimization for the skirt profile and the design for minimum lateral forces. The lateral force can be kept at a minimum by a small compression height and wrist-pin diameter and short skirt.

In order to ensure good lubrication characteristics the skirt surface texture has to be carefully selected as well. A smooth skirt has limited oil retention capabilities, which can impair engine break-in and also lead to scuffing at critical lubrication conditions. A rough skirt, on the other hand, can lead to excessive abrasive wear. A roughness average, R_a , value of 0.8 to 1.4 μm is desirable on the skirt. Such a surface will possess good oil retention capabilities as well low abrasive wear rates.

2.2.14 Piston Profile

The piston temperature distribution varies along the piston height. The temperature decreases moving away from the crown towards the lower skirt. This temperature difference at different levels necessitates the need for a piston profile to

account for the thermal expansion and maintain adequate clearances between the skirt and the cylinder liner at operating conditions. The initial profile is usually selected based on experience and then it is optimized using CAE tools such as the ones described in this dissertation. Figure 2.9 shows a schematic of how a typical piston profile looks at cold conditions and how it becomes at operating hot conditions. The clearances at all levels become tighter.

Usually profiles are added to the top two lands and the skirt. The third land is usually smaller in diameter to maintain lower gas pressures below the second ring; thus, a profile is not needed.

The land profiles are typically tapered. The high combustion pressures and temperatures and the large crown deformation require large clearances at the lands. On the other hand such large clearances increase ring loading and HC emissions, especially at cold conditions when the crevice volumes are large.

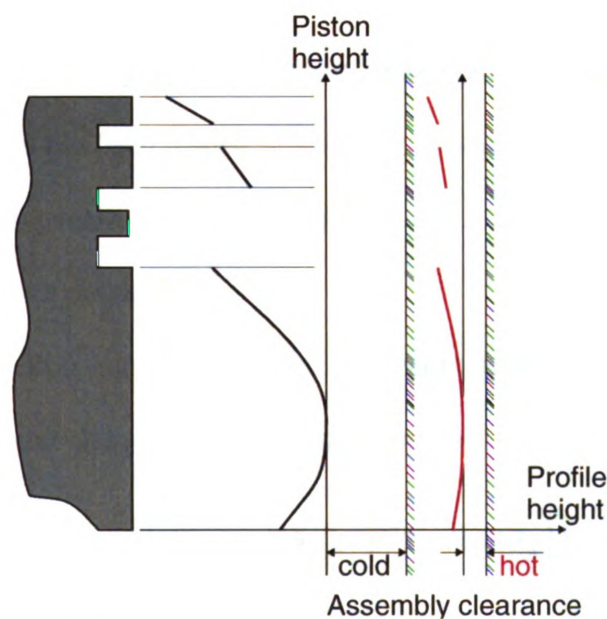


Figure 2.9: Cold and hot piston profiles

The skirt profile is usually a complex barrel shape. It is designed to aid the various skirt functions. It ensures good guidance by supplying the biggest bearing surface area without compromising scuff. Its curvature is increased at the top and bottom to encourage hydrodynamic lubrication.

A properly designed profile allows for smaller clearances at both the skirt and land levels. This results in less noise, limited scuff, improved oil consumption, lower blow-by and HC emissions and ultimately prolonged engine life.

The different equations used to describe skirt profiles will be further discussed in Chapter 6.

2.2.15 Piston Ovality

The loading conditions described in Section 2.2.11 and the volume of material found at the pin-boss necessitate the introduction of piston ovality. Piston ovality refers to the case where the piston diameter in the wrist-pin axis is smaller than the piston diameter in the thrust axis (Figure 2.10). Piston ovality ensures that once the piston has expanded thermally and has been loaded, it is almost cylindrical.

The ovality is usually used only on the skirt. Ovality on the lands is only introduced in the event of contact.

The most common equation to describe ovality is the double ellipse equation, which varies the diameter along the piston circumference,

$$\delta_o = \frac{1}{4} \left[\alpha (1 - \cos 2\theta_p) - \beta (1 - \cos 4\theta_p) \right] \quad (2.2)$$

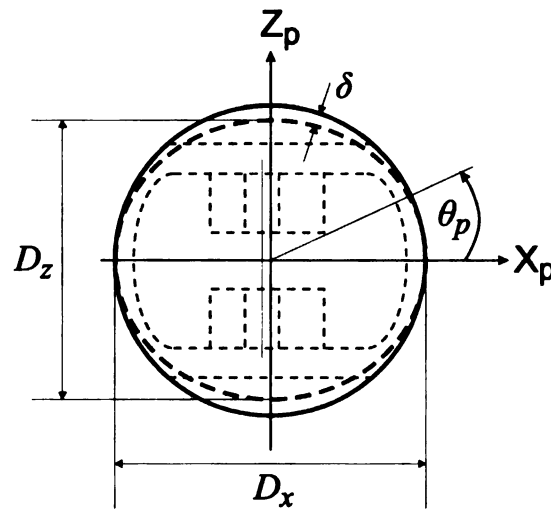


Figure 2.10: Piston ovality

2.3 The Ring-pack

The ring-pack in modern internal combustion engines is usually comprised of two compression rings and an oil control ring. The ring-pack in conjunction with the piston lands and the cylinder bore act as a labyrinth of seals and orifices that control gas and oil flows. The combustion gases and oil share common paths, so leakage of gases to the crankcase should be minimum and existing oil should be directed back to the crankcase.

The primary functions of the ring-pack are:

- i. Blow-by control, that is, controlling the amount of combustion gas flowing from the combustion chamber to the crankcase.
- ii. Oil control, that is, distributing evenly the oil film on the cylinder bore walls and circulating oil through the ring-pack. Effective oil control leads to the minimization of oil losses due to evaporation and burning of leftover oil on the combustion chamber walls.

- iii. Heat transfer; the ring-pack aids in the cooling of the piston. The piston crown is exposed to the combustion gases. The piston rings act as a path for the heat to flow from the piston to the cylinder wall and eventually to the cooling system, thus ensuring operation of the system at normal operating temperatures.

The ring-pack design is driven by the search of reduced oil consumption, blow-by and exhaust emissions; higher power output, lower friction, decreased variability from cycle-to-cycle, prolonged engine life and reduced costs. In the effort to reduce friction and also piston weight, some applications utilize a two-ring ring-pack. The second compression ring is retired, eliminating its contribution to friction and allowing for a shorter crown to decrease piston weight.

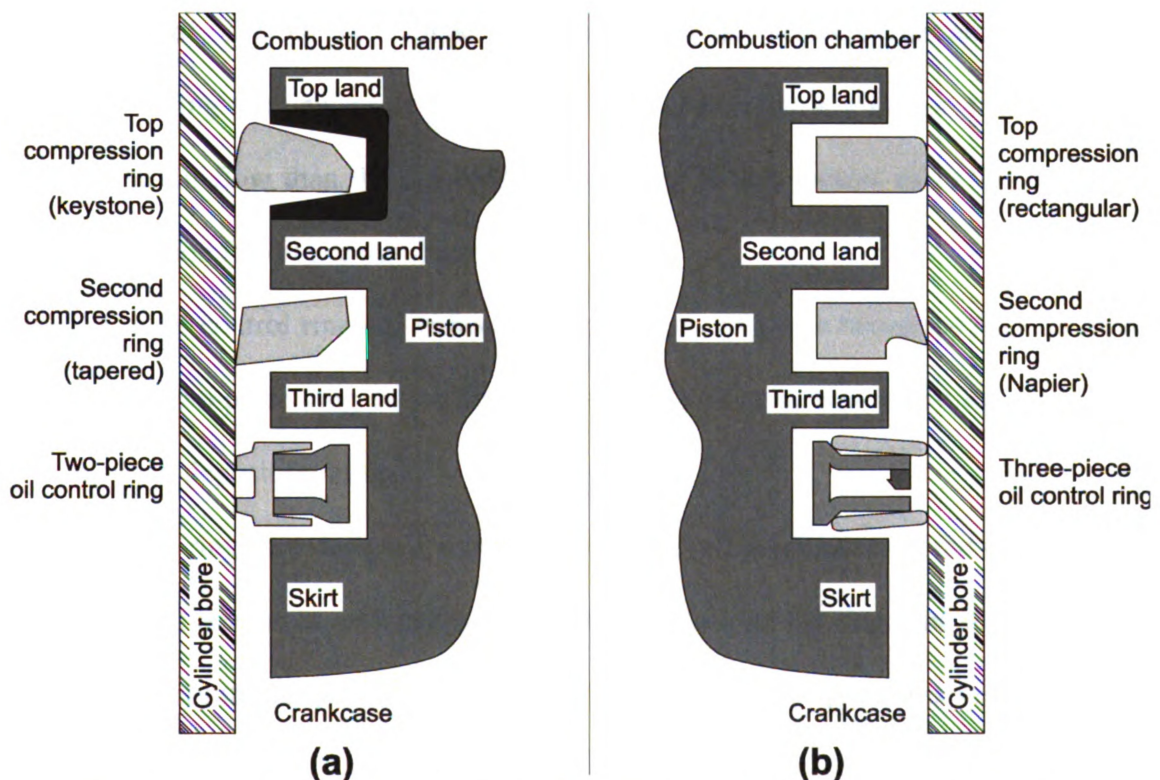


Figure 2.11: A typical ring-pack (a) diesel engine and (b) gasoline engine

Figure 2.11 shows the typical ring-pack configuration for diesel and gasoline engines. The rings are usually made of steel alloys, and different coatings are utilized at the face and sides to increase wear resistance. The diesel ring-pack configuration employs a keystone-type top compression ring as well as a reinforced top groove (higher combustion gas pressures). In cases of turbocharged engines, the second compression ring can also be of keystone type. Diesel combustion results in higher deposits than gasoline combustion. The keystone ring is thus preferred in diesel engines as it is less likely to stick to the piston since it promotes the break-up of deposits due to piston secondary motion. The top ring is usually designed to have a positive twist (front end lifted upwards) when fitted in the cylinder so that when loaded with combustion gas pressure it will have approximately zero twist.

The second compression ring is designed with a tapered face in order to promote the scraping of oil from the cylinder wall during the downward stroke and distribute a thin layer during the upward strokes. The Napier ring design allows for a more natural path for the oil flow than the standard tapered ring. It also creates extra volume in the third land region for oil accumulation.

The oil control ring can either be a three-piece ring or a two-piece ring. In diesel engines the two-piece ring is preferred, again because it is less likely to stick to the groove due to deposit build-up.

Piston rings are designed to exert a uniform radial pressure on the cylinder wall due to internal tension as well as due to gas pressure behind the ring. The oil control ring has the highest internal tension as the gas pressure in the third groove is very low, close

to the crankcase pressure. In order to achieve this high internal tension it utilizes a spring expander, hence the name two-piece or three-piece.

The following sections will describe the main functions and characteristics of the rings. The interested reader is referred to [24, 25, and 26] for a description of the different types of rings.

2.3.1 Top Compression Ring

The top compression ring is responsible for sealing combustion gases in the combustion chamber and preventing them from escaping to the crankcase. The main path of gas flow is through the ring end gap. The end gap flow area is affected by the ring outside diameter, chamfers at the gap edge and land diameter. These clearances should be kept at minimum to reduce blow-by in both directions, from the combustion chamber to the crankcase and vice versa.

During the intake stroke, especially at the beginning, the combination of ring inertia and pressure differentials between the second land and the combustion chamber forces the top ring to reside at the top of the groove. Close to the end of the intake stroke, the ring will start moving toward the bottom of the groove. This transition period will lead to loss of sealing, creating a leak path for gases and increasing blow-by. This requires the clearances to be kept as small as possible, as well as careful selection of ring inertia to maintain this transition period as short as possible. Some axial ring movement is necessary in order to ensure favorable lubrication conditions at the interface between the lower sides of the ring and groove to inhibit wear.

During the expansion stroke high pressures may build up at the second land volume. These high pressures may lift the top ring, especially at the end of the expansion stroke. This lift will allow for reverse blow-by, thus increasing HC emissions as unburnt gases trapped in the second land volume will flow into the exhaust gases. In order to avoid this problem, the ring-pack is designed so that it relieves this pressure in the third land. In doing so it also helps oil control, as the flowing gases to the third land transport with them oil which is ultimately returned to the crankcase. Another remedy to this problem is decreasing the second land diameter or introducing a groove at the second land. This increases the volume at the second land which leads to lower pressure build-up in that region. The decrease of the second land diameter is not usually preferred, as it will increase the flow areas at the end gaps of both the top and second ring.

The face of the top ring is usually barrel-shaped in order to provide good sealing and oil distribution. It maintains better contact with the cylinder liner as the piston tilts, thus tilting the ring. The barrel-face profile also makes the top ring a non-dimensional scraper. However, in high loading conditions where the piston experiences high tilts or the ring high negative twists, this can have adverse effects as the top edge of the ring can end up being a scraper due to top outside diameter contact. This will throw oil into the combustion chamber which will increase oil consumption. The introduction of up-tilted grooves, positive twisted rings, or asymmetric barrel face profiles are utilized to help eliminate this problem.

2.3.2 Second Compression Ring

The main functions of the second ring are to act as a scraper for oil control and to dampen the pressure drop across the top ring.

The tapered face usually found on the second ring acts as a unidirectional scraper. It rides on the oil film on the upward strokes and scrapes the oil on the downward stroke to control oil consumption. The taper face profile is very important as it is determinant to engine life. Engine life is affected by how long it will take for the taper face to wear out. A groove is usually introduced at the bottom of the second ring in order to provide extra volume for the accumulation of oil. It also helps in the control of interring gas pressure. For the same purpose, grooves may be introduced at the third land.

The second ring also controls the pressure differential across the top ring. It achieves this by sealing the dynamic pressure increase in the second land during the compression and expansion strokes and delaying the release into the third land. The timely release of this pressure prevents top ring lift. Also, it enhances the oil-scraping action of the second ring, as the flow carries oil with it.

2.3.3 Oil Control Ring

The main function of the oil control ring is to control oil consumption. It has negligible gas sealing and heat transfer capabilities. It scrapes excessive oil from the cylinder liner to the crankcase and acts as a check valve to prevent oil flow into the combustion chamber.

The expander provides a uniform radial force to push the segment or segments, in the case of a three-piece ring, against the cylinder liner. In the case of the three-piece

ring, the expander also provides an axial force to push the segments against the top and bottom sides of the grooves. This seals the oil passages and prevents reverse oil flow at high engine vacuums. This axial force, though, should not be excessively high so that it can be overcome by gas pressure and scraped oil in the third land to create a crevice for the oil to flow into the crankcase. The radial force determines the oil film thickness that will stay on the cylinder liner, which is important for engine life and oil consumption.

Unlike the second ring, the oil control ring is a multi-directional scraper. It scrapes oil both during the upward and downward strokes. During the downward strokes, the bottom segment scrapes oil directly into the crankcase. During the upward strokes, it scrapes oil into the groove through the expander. This necessitates the introduction of holes at the back of the groove to allow for oil drainage. A cheaper solution is the introduction of cast slots at the bottom of the groove as it does not require drilling. Similarly, the top segment scrapes oil into the groove during the downward stroke. The recovery of oil scraped in the third land by the top segment during the upward stroke becomes more complex. This completely relies on the forces acting on the top segment, which at times throughout the cycle overcome the axial force of the expander and create a crevice for the oil to drain into the third groove. At the same time this relieves pressure from the third land.

2.3.4 Pressure Loading

The three rings across the ring-pack experience different pressure loadings. Figure 2.12 shows typical in-cylinder and land pressures. The upper surface of the top ring is exposed to the high in-cylinder (combustion) pressure. This high pressure puts a moment

about the land on the ring forcing it to twist downwards. This twisting can have several adverse effects. As described in Section 2.3.1, this can lead to oil scraping into the combustion chamber. The pivoting of the top ring about the second land increases the radial force exerted by the ring, which can break the oil film and lead to high wear rates. This twisting also degrades the lower side sealing as the ring back edge lifts away from the groove, thus allowing for gas leakage past the lower side of the ring. These adverse effects can be avoided by careful design of the top ring, groove, and second land.

The second and third rings experience much lower pressure loads. The second land pressure after a point during the expansion stroke exceeds the in-cylinder pressure as both the top and second rings are seated at the bottom of the groove sealing the gases in the second land. This point is known as the crossover point and it is desired to occur at around 120 degrees ATDC. If it happens earlier it can cause the top ring to lift and increase blow-by. At around 120 degrees ATDC ring inertia starts dominating as the piston slows down, thus even though the second land pressure is higher the top ring still remains seated.

The pressure build-up in the third land is necessary to help the transport of oil accumulated there into the crankcase as described in Section 2.3.3.

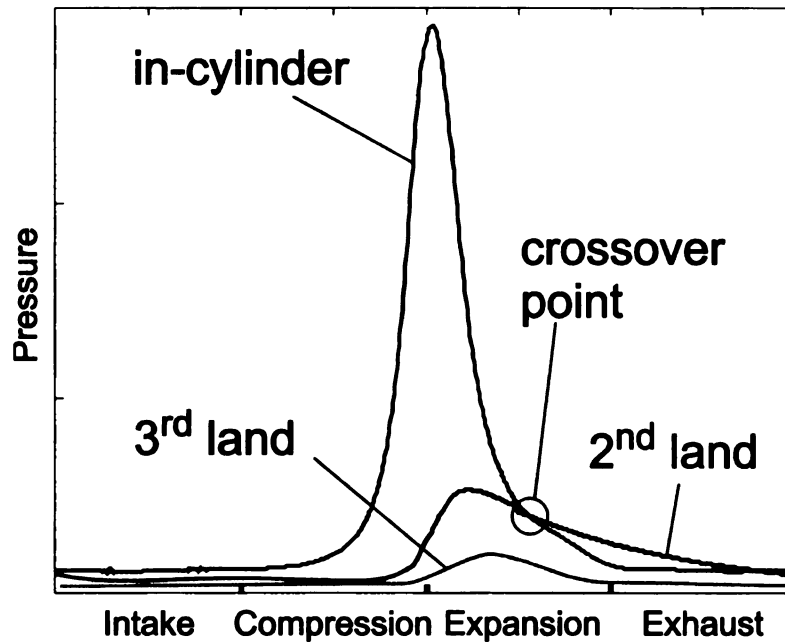


Figure 2.12: In-cylinder and land pressures

2.3.5 Heat Transfer

Other than controlling blow-by and oil consumption, piston rings are very important for maintaining favorable piston temperatures. It is estimated that about 70% of the piston heat is dissipated by the piston rings. The heat flow path is from the piston to the piston rings to the oil film to the cylinder liner and finally to the coolant in the water jackets. The heat flow is dominant in the radial direction from the inside diameter to the outside diameter; thus, any heat flow in the circumferential direction of the ring is ignored in numerical models. The fact that the rings spend most of their time seated at the bottom the groove results in the top part of the groove being hotter.

The formation of the oil film wedge between the ring and the cylinder liner (Figure 2.13) is very important in controlling heat transfer as it increases the ring-to-oil surface contact area. The top ring with the barrel profile benefits from this wedge in both

upward and downward strokes, whereas the tapered second ring benefits only in the upward strokes. The importance and contribution of the second ring in cooling the piston has been noted in experiments, where removing the second ring resulted in increased piston crown temperatures of about 14 °C.

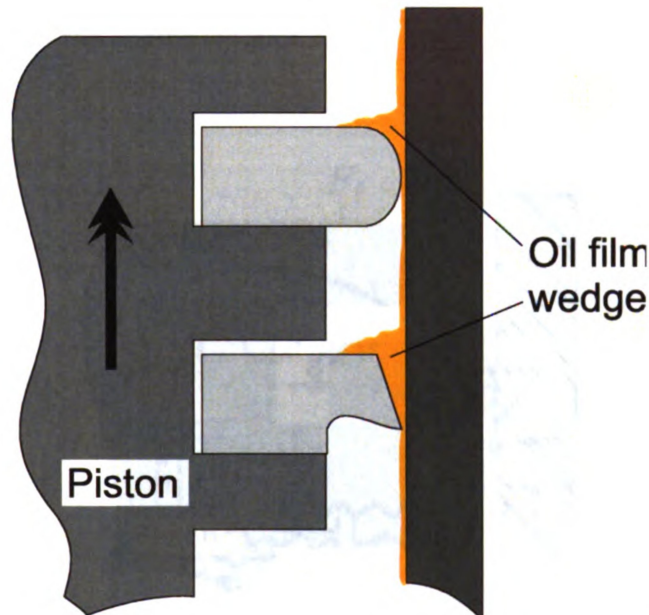


Figure 2.13: Oil film wedge forming during the upstroke

The challenge in the modern trends of engine development becomes how to keep the piston at favorable temperatures. Rings are getting thinner to decrease friction and inertia losses. Also, some applications seek to eliminate completely the second ring. These trends will result in higher thermal loads and higher heat fluxes the rings will have to withstand. Thus numerical modeling of the ring-pack is more crucial than ever to ensure excellent engine performance.

2.3.6 Ring Friction

In order for the rings to seal the combustion chamber, they exert a radial force on the cylinder liner. This radial force arises from the combination of the ring internal tension and the gas force generated due to gas pressure behind the ring. It results in the generation of an axial friction force which resists piston motion and subtracts energy from the useful work of the engine (Figure 2.14).

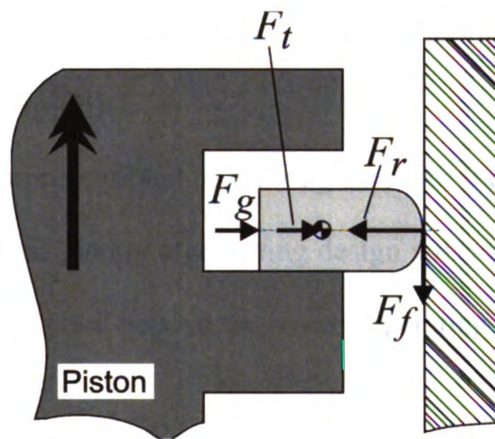


Figure 2.14: Forces generating axial friction at the ring-cylinder liner interface

The piston rings account for about 20-40% of the total engine friction. The axial friction force is directly proportional to the radial tension generated. In recent years this radial tension has been reduced to about 50-60%. This was due to advances in machining processes which allow for better cylinder liner finishes, pistons and piston rings. Also the advancements in lubricant technologies and ring face coatings have contributed. Finally the trends for thinner rings also help reduce friction.

2.3.7 Engine Speed

Engine speed is an important factor influencing the ring sealing properties. The ring inertia is directly proportional to engine speed. Close to the TDC, where piston deceleration increases, inertia tries to lift the ring from its seat at the bottom of the groove. At high loads where the combustion pressure is high, thus the forces acting on top of the ring are high, they dominate inertia and thus the ring remains seated. However, at high engine speeds low engine loads, where inertia is high and combustion pressure is low, the ring can lift and loses its sealing properties, resulting in high blow-by. This is referred to as ring instability [83].

The ring inertia is proportional to the ring mass, to the engine stroke and to the engine speed squared. Consequently a good ring design will account for this relationship and push the ring instability point beyond the normal operating range of the engine.

2.4 Cylinder Liner

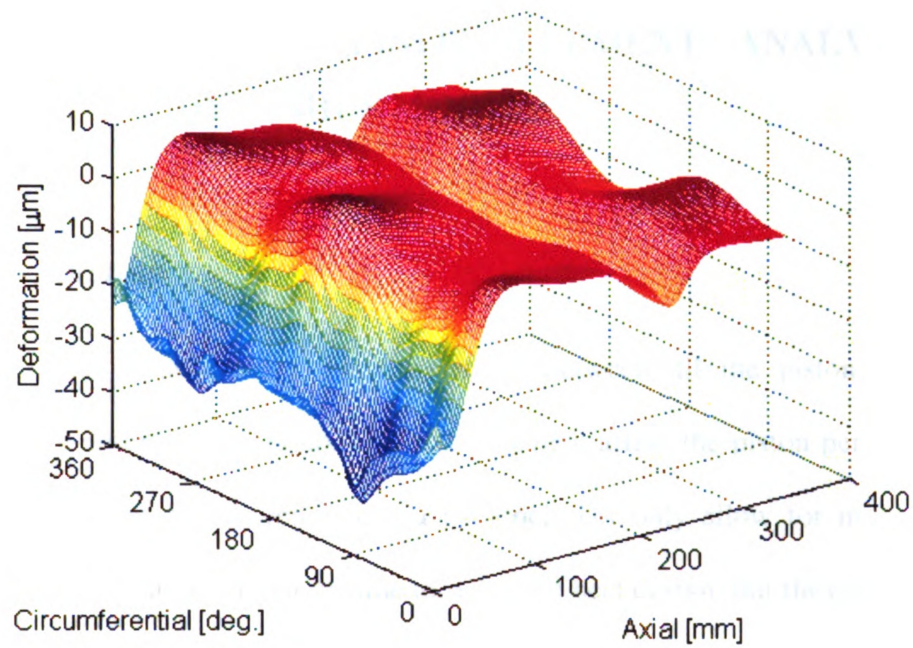
The cylinder liner acts as the guide for the reciprocating motion. It provides the surface where the piston and piston rings slide, thus it has its own role in determining engine performance and engine life.

Like the skirt surface finish described in Section 2.2.13, the cylinder liner has to possess surface finish properties that will yield favorable lubrication conditions, thus minimizing wear, but at the same time minimize oil consumption. A rough cylinder liner has very good oil retention properties; however, the oil between the micro-valleys is not scraped during the downstroke, thus remaining exposed to the combustion flames. This in

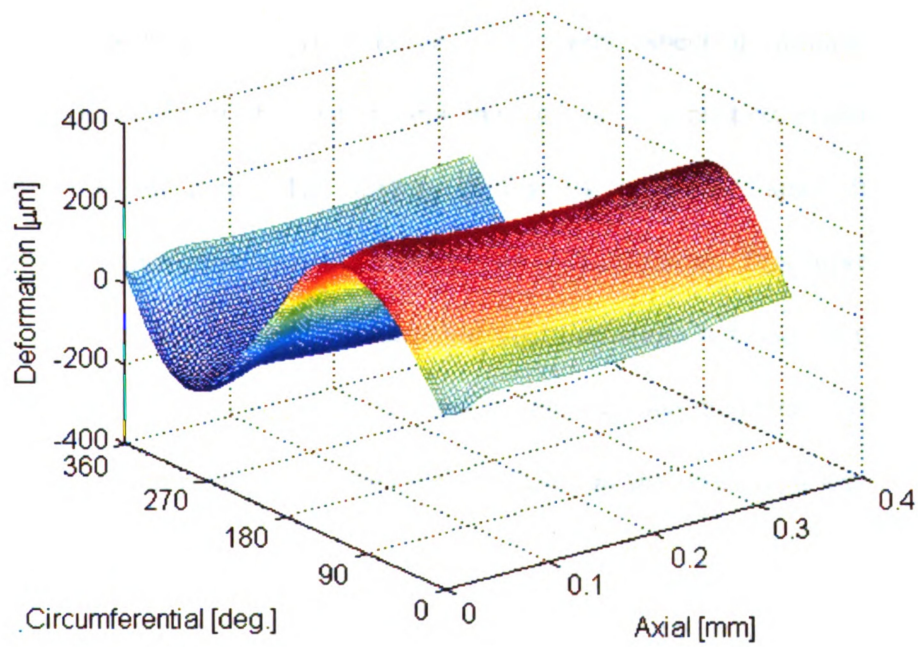
turn will increase oil consumption. Typical values for the cylinder roughness average value are about $0.5\text{ }\mu\text{m}$, and different honing techniques are used to achieve this.

Another challenge faced with the cylinder liner design is its deformation. Once the engine is assembled the cylinder liner will deviate from the round shape (Figure 2.15), both circumferentially and axially. This deformation arises from the bolt loads fitting the cylinder head to the cylinder block. At operating conditions these deformations increase even more due to thermal expansion and loads from the piston. These deformations have adverse effects on engine life and efficiency, as they increase clearances which may result in large amplitudes of piston motion, increased blow-by, and oil consumption. The sequence of peaks and valleys in the axial direction can result in high impact loads on the skirt, thus leading to plastic deformation and premature failure of the piston.

A technique called hot honing may be used to eliminate the effects of thermal expansion; however, it is an expensive process, which makes it infeasible for mass production. This involves bringing the cylinder block to operating temperatures and then honing the round shape of the cylinder liner. Thus the liner will deviate from roundness when the engine is cold and become round at operating temperatures.



(a)



(b)

Figure 2.15: Cylinder liner deformation (a) assembled cold and (b) rated conditions

CHAPTER 3. PISTON FINITE ELEMENT ANALYSIS AND DYNAMICS MODEL

3.1 Introduction

In order to understand the correlations between all the piston features and characteristics described in Section 2.2 and how they affect the piston performance, the use of numerical models is required. Such models not only allow for multiple design iterations in a minimum amount of time to reach the best design, but they also reduce the need of many prototypes, thus decreasing costs. The cost of moving electrons is significantly less than moving atoms.

Numerical models are very important for every aspect of engineering design, so the optimal operation of the piston, and the internal combustion engine as a whole, greatly depends on them. The piston, during its operation, apart from the axial reciprocating motion experiences small transverse oscillations. This represents a highly nonlinear problem, involving the thermoelastohydrodynamic behavior of the piston skirt. The identification of the magnitudes of these oscillations and the ability to control them is crucial, as the piston performance depends on them. In the process of this identification, numerical models are utilized.

This chapter will develop the theory behind the numerical model for the assessment of piston performance developed at the Automotive Research Experiment Station at Michigan State University. The model has been named Piston Finite Element Analysis and Dynamics and from here on it will be referred to as PIFEAD.

3.2 Overview of the PIFEAD

The PIFEAD model is comprised of two modules, the finite element analysis module and the dynamics analysis part (Figure 3.13). Despite the fact that a dynamics analysis can be performed assuming a rigid piston, the finite element analysis is an integral part of elastohydrodynamic lubrication analysis which yields more realistic predictions of piston performance.

A thorough description of the code's finite element analysis is found in [49] and will not be repeated here. In summary, the piston has to be meshed externally via linear tetrahedral elements, obeying the coordinate system convention described in the following section. A data file containing all the mesh information has to be supplied as an input to the model in order to perform a thermal and structural finite element analysis.

The original finite element model described in [49] was written in MATLAB. However, in order to minimize processing time, in this version it was migrated to FORTRAN. Execution of numerically intensive programs developed in FORTRAN is much more efficient than ones developed in MATLAB. Also the version in [49] was accepting mesh data only from COSMOS DesignSTAR. In this version the piston can be meshed in Altair Hypermesh which is the most widely used meshing tool in the automotive industry. PIFEAD then uses the mesh information output (element connectivity and node coordinates).

For the thermal analysis, the piston is assumed to be at steady state over the cycle [31]. A convective boundary is applied to the whole piston, splitting the boundary in five regions: crown, ring-pack, skirt, underside, and pin-hole. The heat transfer coefficients and ambient temperatures are assumed to be constant over the cycle and are carefully

selected to account for the operating conditions and within the ranges archived in [76, 78]. This allows for the estimation of the temperature profile on the skirt. Averaging it with the cylinder bore temperature, the oil viscosity on the skirt can be calculated.

For the structural analysis the piston is constrained at the pin-hole and the principle of minimum potential energy is applied. Inputs for calculating piston deformation are thermal loads, from the thermal analysis above, unit pressure load on the crown, to simulate the combustion gas pressure, and unit body load, to simulate the piston's inertia. The deformations due to the pressure on the crown and due to the body load are scaled to the combustion gas pressure and piston axial acceleration, respectively, at each crank angle. The skirt compliance is also obtained and it is used during the iterative solution to obtain the skirt deformation due to the hydrodynamic and contact pressures developed at the skirt surface. All these deformations allow for the consideration of a fully elastic skirt in the dynamics analysis.

3.2.1 Skirt Compliance

In the piston elastohydrodynamic lubrication problem, the skirt compliance is used to relate the skirt deformation to the skirt hydrodynamic and contact loads. It can be calculated directly from the stiffness matrix, iteratively or experimentally. The concept behind the compliance matrix is to reduce the degrees of freedom of the system just to the ones of interest, in this case, the skirt area. This will eliminate the need of solving a large system of equations at each iteration step to calculate the skirt deformations.

3.2.1.1 Guyan Reduction

One straightforward method of obtaining the compliance matrix is the Guyan reduction or static condensation method [21]. Given a system,

$$\begin{matrix} \mathbf{K} & \mathbf{u} & = & \mathbf{f} \\ n \times n & n \times 1 & & n \times 1 \end{matrix} \quad (3.1)$$

where n is the number of degrees of freedom, decomposing it,

$$\left[\begin{array}{c|c} \mathbf{K}_{11} & \mathbf{K}_{12} \\ \hline \mathbf{K}_{21} & \mathbf{K}_{22} \end{array} \right] \left\{ \begin{array}{c} \mathbf{u}_1 \\ \hline \mathbf{u}_2 \end{array} \right\} = \left\{ \begin{array}{c} \mathbf{f}_1 \\ \hline \mathbf{f}_2 \end{array} \right\} \quad (3.2)$$

$\begin{matrix} p \times p & p \times q \\ q \times p & q \times q \end{matrix}$ $\begin{matrix} p \times 1 \\ q \times 1 \end{matrix}$ $\begin{matrix} p \times 1 \\ q \times 1 \end{matrix}$

with

$$q + p = n \quad (3.3)$$

Now if \mathbf{u}_2 is the vector of unwanted degrees of freedom, then the above system can be reduced to,

$$\left[\mathbf{K}_{11} - \mathbf{K}_{12} \mathbf{K}_{22}^{-1} \mathbf{K}_{21} \right] \mathbf{u}_1 = \mathbf{f}_1 \quad (3.4)$$

where the reduced matrix, \mathbf{K}_{red} , is given by,

$$\mathbf{K}_{red} = \mathbf{K}_{11} - \mathbf{K}_{12} \mathbf{K}_{22}^{-1} \mathbf{K}_{21} \quad (3.5)$$

The compliance matrix, \mathbf{C} is given by,

$$\mathbf{C} = \mathbf{K}_{red}^{-1} \quad (3.6)$$

Also if \mathbf{u}_2 , the deformation of the rest of the body, is needed then,

$$\mathbf{u}_2 = -\mathbf{K}_{22}^{-1} \mathbf{K}_{21} \mathbf{u}_1 \quad (3.7)$$

where the coordinate transformation matrix, \mathbf{T} is defined as,

$$\mathbf{T} = -\mathbf{K}_{22}^{-1} \mathbf{K}_{21} \quad (3.8)$$

When the stiffness matrix of a static problem is reduced, no information is lost. It can be seen from (3.5) that all the elements contribute to the reduced matrix. Also the advantage of this method is that the coordinate transformation matrix (3.8) is readily available to obtain the deformations at all nodes of the system. This is useful when determining the stress concentrations. The disadvantage, though, of this method is that it can be computationally expensive as matrix \mathbf{K}_{22} needs to be inverted. This can lead to computer memory allocation problems if the mesh is very big.

3.2.1.2 Node-by-node Loading

One way to get around this problem is to calculate the compliance matrix iteratively. This eliminates the need of inverting any matrices since algorithms such as the conjugate gradient method can be used to solve the system of equations. This methodology involves loading node i (Figure 3.1) on the skirt with unit force and then calculating the deformation at all the nodes on the skirt. The compliance matrix, \mathbf{C} , can then be built from the skirt deformation vectors, \mathbf{s} , of each loading case.

$$\begin{aligned} \mathbf{K} \mathbf{u}_i &= \mathbf{f}_i \quad i = 1, 2, \dots, n \\ n &= \text{no. of nodes on skirt} \end{aligned} \quad (3.9)$$

$$\mathbf{s}_i \subset \mathbf{u}_i \quad (3.10)$$

$$\mathbf{C} = [\mathbf{s}_1 \quad \mathbf{s}_2 \quad \dots \quad \mathbf{s}_n] \quad (3.11)$$

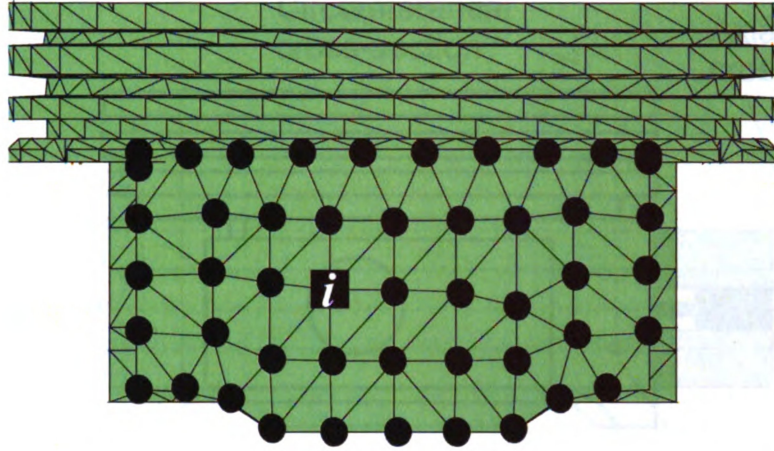


Figure 3.1: Skirt nodes contributing to compliance matrix

3.2.1.3 Compliance by Measurements

Another method for obtaining the skirt compliance is via direct measurement of the skirt deformation subjected to loading. The piston skirt is split into axial and circumferential cross-sections. A load $F_{i,j}$ is applied at the intersection of the cross-sections, and the deformation $s_{i,j}$ is measured at all the intersections (Figure 3.2). The procedure is repeated for all cross-sections, thus allowing for assembly of the compliance matrix. The advantage of this method is that it can be used to capture non-linearities in the skirt compliance. In the two previous methods described above, the compliance matrix is derived from the linear stiffness matrix. In this method, however, the load F can be applied at two magnitudes, e.g. low and high, which will yield two sets of deformations. The load can then be related to the deformations by a higher order polynomial that will account for non-linearities.

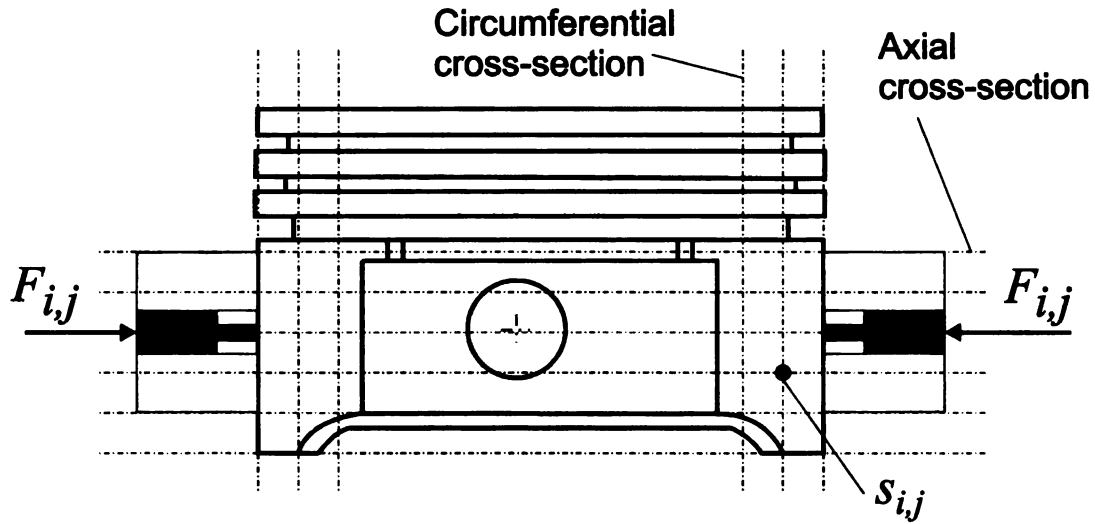


Figure 3.2: Skirt cross-sections for obtaining the skirt compliance

3.3 Piston Dynamics

The piston dynamics analysis requires the solution of a highly nonlinear problem. The piston position within the cylinder affects the oil film thickness, which affects the hydrodynamic and contact pressures, which in turn affect the piston deformation, which again affects the oil film thickness. This problem is solved iteratively via the Newton-Raphson method and underrelaxation of the pressures developed at the skirt surface. The modeling approach and computational methodology for the dynamic analysis are described in the following sections.

3.3.1 Coordinate Systems

The coordinate systems used to describe the engine in the model are shown in Figure 3.3. They consist of one global and three local ones. The local coordinate systems are interrelated by the global coordinate system.

X_O-Y_O is the global coordinate system which is at an angle, γ , from the vertical to accommodate for V-engines. x_o is the X_O -coordinate for the crank offset from the cylinder center line. θ is the crankshaft angle, and ϕ is the connecting rod angle, both with respect to the Y_O -axis. X_C-Y_C is the cylinder local coordinate system. X_P-Y_P is the piston local coordinate system, and $X_{PP}-Y_{PP}$ is the wrist-pin local coordinate system. The third direction Z for these coordinate systems is not shown here. The nominal piston-to-cylinder liner clearance is given by c .

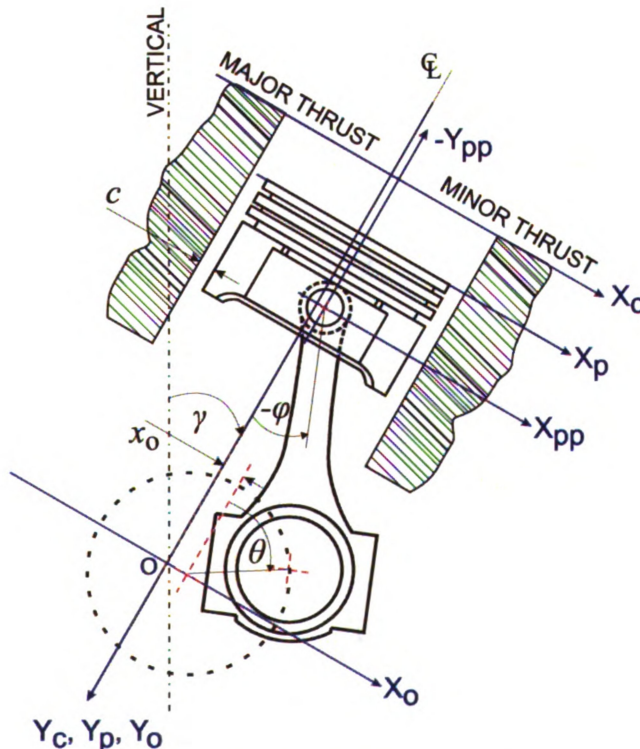


Figure 3.3: Coordinate systems

3.3.2 Piston Coordinate System

The piston local coordinate system is shown in Figure 3.4. The coordinate system is centered at the top of the piston crown and aligned with the piston center axis. The minor thrust side is found in the positive Y_p - Z_p plane, and the major thrust side in the negative. x_{cg} is the X_p -coordinate of the piston's center of mass and x_{wp} is the X_p -coordinate of the wrist-pin offset. y_{cg} and y_{wp} are their respective coordinates in the Y_p -direction. H_p is the piston height, and L is the skirt length. θ_p is the piston's angular coordinate. It is positive in the counterclockwise direction with zero being collinear with the X_p -axis. The piston nominal radius is given by R .

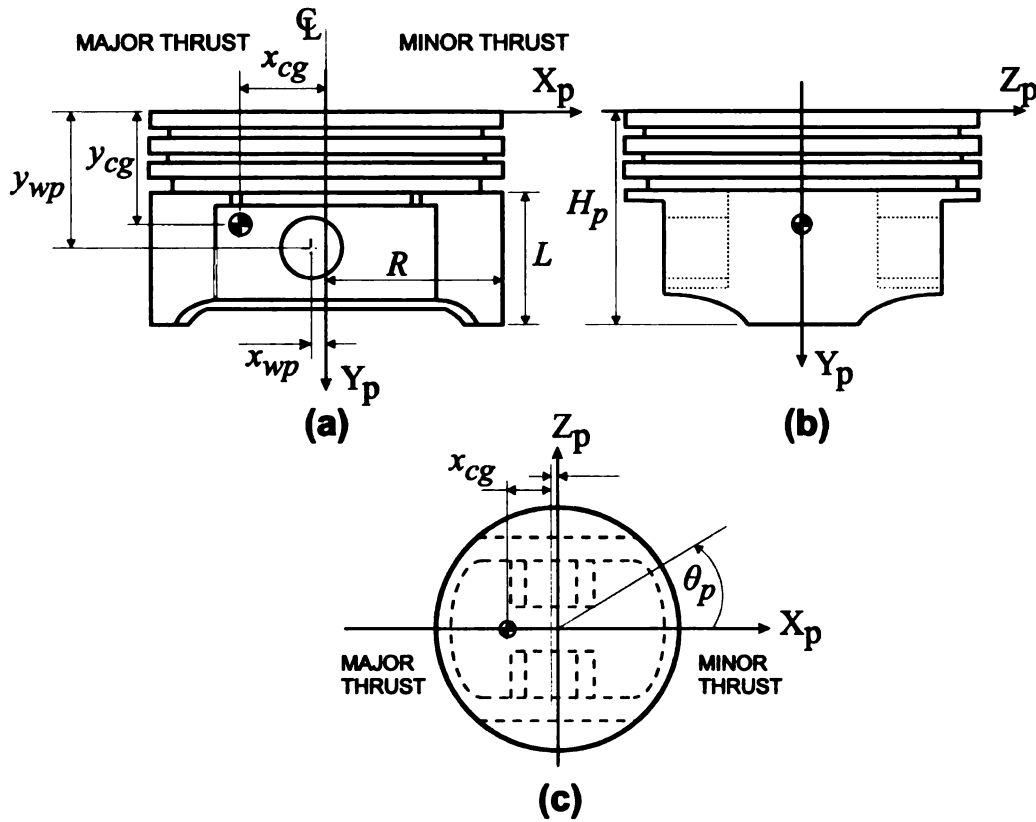


Figure 3.4: Piston coordinate system (a) X_p - Y_p plane, (b) Y_p - Z_p plane and (c) X_p - Z_p plane

3.3.3 Skirt

In order to solve for the hydrodynamic pressure developed on the skirt using the Reynolds lubrication equation, the skirt is mapped to a 2-D coordinate system, x_s - y_s , from the piston 3-D coordinate system, X_p - Y_p - Z_p .

The skirt 2-D coordinates are given by (3.12) and (3.13).

$$x_s = R\theta_p \quad (3.12)$$

$$y_s = Y_p - (H_p - L) \quad (3.13)$$

where, for the minor thrust side, $\theta_p \in [3\pi/2, \pi/2]$, and for the major thrust side, $\theta_p \in [\pi/2, 3\pi/2]$.

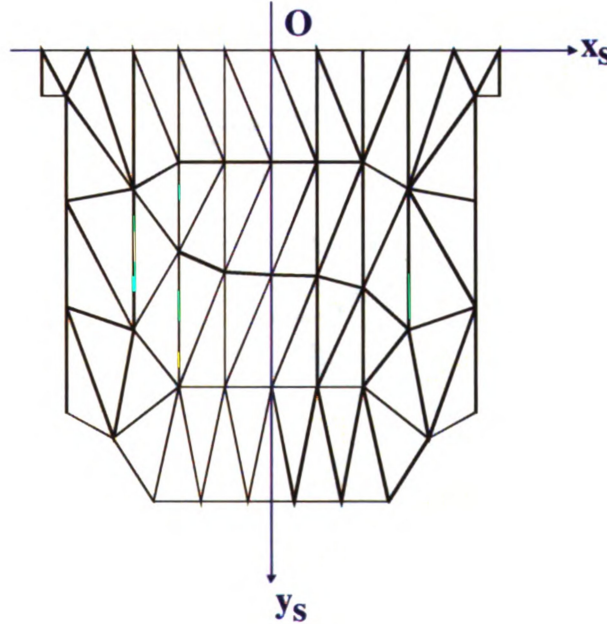


Figure 3.5: Skirt mesh on the local coordinate system

3.3.4 Axial Dynamics

The piston position, velocity, and acceleration along the cylinder bore center line as well as the connecting rod angle φ , and the acceleration of its center of mass, $a_{cm,x}$ and $a_{cm,y}$, can be readily derived using vector mechanics [73]. Figure 3.6 shows a vector diagram of the piston crank assembly. For these derivations the crankshaft is assumed to rotate at a constant angular speed, ω_1 . Also the crankshaft and the connecting rod are assumed to be rigid. r_1 is the crankshaft radius, r_2 is the length of the connecting rod, r_3 is the piston pin position from the crankshaft axis, and ρ is the distance from the connecting rod's big end to its center of mass. ω_2 and α_2 are the connecting rod angular speed and angular acceleration, respectively.

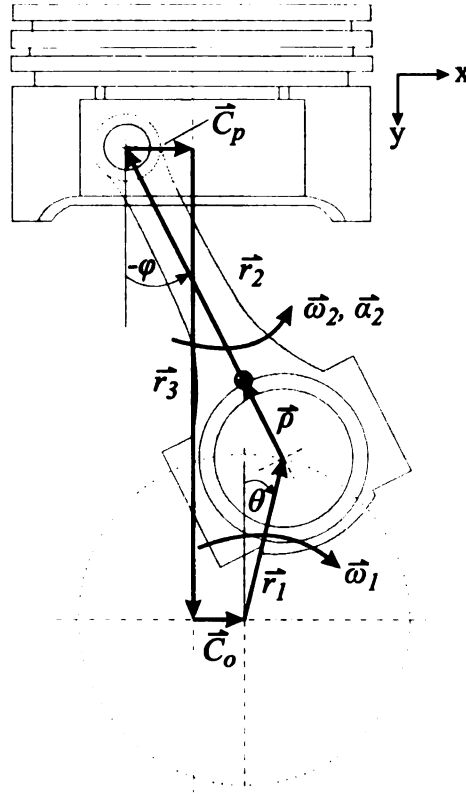


Figure 3.6: Vector diagram of the piston crank assembly

The vector equation describing the assembly of Figure 3.6 is given by,

$$\vec{C}_o + \vec{r}_1 + \vec{r}_2 + \vec{C}_p + \vec{r}_3 = 0 \quad (3.14)$$

Taking the components of (3.14), the piston position is given by,

$$r_3 = -r_1 \cos \theta - r_2 \cos \varphi \quad (3.15)$$

and the connecting rod angle by,

$$\varphi = -\sin^{-1} \left(\frac{r_1 \sin \theta + C_o - C_p}{r_2} \right) \quad (3.16)$$

Now taking the first derivative of (3.14) with respect to time, and recognizing that

$\dot{\vec{C}}_o = \dot{\vec{C}}_p = 0$, $\dot{\vec{r}}_1 = \bar{\omega}_1 \times \vec{r}_1$, and $\dot{\vec{r}}_2 = \bar{\omega}_2 \times \vec{r}_2$ then

$$\bar{\omega}_1 \times \vec{r}_1 + \bar{\omega}_2 \times \vec{r}_2 + \dot{\vec{r}}_3 = 0 \quad (3.17)$$

Again taking the components of (3.17), the piston axial velocity is given by,

$$\dot{r}_3 = \omega_1 r_1 \sin \theta + \omega_2 r_2 \sin \varphi \quad (3.18)$$

and the connecting rod angular speed by,

$$\omega_2 = -\frac{\omega_1 r_1 \cos \theta}{r_2 \cos \varphi} \quad (3.19)$$

Now taking the second derivative of (3.14) with respect to time, and recognizing that

again $\ddot{\vec{C}}_o = \ddot{\vec{C}}_p = 0$, and now $\ddot{\vec{r}}_1 = \bar{\omega}_1 \times \bar{\omega}_1 \times \vec{r}_1$, and $\ddot{\vec{r}}_2 = \bar{\omega}_2 \times \bar{\omega}_2 \times \vec{r}_2 + \bar{\alpha}_2 \times \vec{r}_2$ then

$$\bar{\omega}_1 \times \bar{\omega}_1 \times \vec{r}_1 + \bar{\omega}_2 \times \bar{\omega}_2 \times \vec{r}_2 + \bar{\alpha}_2 \times \vec{r}_2 + \ddot{\vec{r}}_3 = 0 \quad (3.20)$$

From the components of (3.20), the piston axial acceleration is given by,

$$\ddot{r}_3 = \omega_1^2 r_1 \cos \theta + \omega_2^2 r_2 \cos \varphi + \alpha_2 r_2 \sin \varphi \quad (3.21)$$

and the connecting rod angular acceleration by,

$$\alpha_2 = \frac{\omega_1^2 r_1 \sin \theta + \omega_2^2 r_2 \sin \varphi}{r_2 \cos \varphi} \quad (3.22)$$

The acceleration of the center of mass of the connecting rod is given by,

$$\begin{aligned} \bar{a}_{cm} &= a_{cm,x} \hat{i} + a_{cm,y} \hat{j} \\ &= \bar{\omega}_1 \times \bar{\omega}_1 \times \bar{r}_1 + \bar{\omega}_2 \times \bar{\omega}_2 \times \bar{\rho} + \bar{\alpha}_2 \times \bar{\rho} \end{aligned} \quad (3.23)$$

which yields,

$$a_{cm,x} = -\omega_1^2 r_1 \sin \theta - \omega_2^2 \rho \sin \varphi + \alpha_2 \rho \cos \varphi \quad (3.24)$$

and

$$a_{cm,y} = \omega_1^2 r_1 \cos \theta + \omega_2^2 \rho \cos \varphi + \alpha_2 \rho \sin \varphi \quad (3.25)$$

From here on the piston axial position will be referred to as y_p , the piston axial velocity as v_p , and the piston axial acceleration as a_p .

3.3.5 Piston Eccentricity

The piston eccentricity – transverse position relative to the cylinder center axis – is described by the eccentricities at the reference points shown in Figure 3.7,

- T: top of piston
- B: bottom of piston
- Z: piston center axis

Once these primary eccentricities are known, the eccentricities at different piston levels can be calculated. Figure 3.8 shows a translated and tilted piston, confined within

the cylinder liner. The eccentricity at the top of the piston is given by e_t , the eccentricity at the bottom of the piston is given by e_b , and the eccentricity (translation) along the wrist-pin is given by e_z . These can be used to derive the eccentricities at the top and bottom of the second land, e_{lt} and e_{lb} , at the center of gravity, e_{cg} , at the top and bottom of the skirt, e_{st} and e_{sb} , at the piston pin level, e_p , and the piston tilt, β .

$$e_{lt} = e_t - \frac{y_{lt}}{H_p}(e_t - e_b) \quad (3.26)$$

$$e_{lb} = e_t - \frac{y_{lb}}{H_p}(e_t - e_b) \quad (3.27)$$

$$e_{cg} = e_t - \frac{y_{cg}}{H_p}(e_t - e_b) \quad (3.28)$$

$$e_{st} = e_t - \frac{H_p - L}{H_p}(e_t - e_b) \quad (3.29)$$

$$e_{sb} = e_b \quad (3.30)$$

$$e_p = e_t - \frac{y_{wp}}{H_p}(e_t - e_b) \quad (3.31)$$

$$\beta = \sin^{-1} \left(\frac{e_t - e_b}{H_p} \right) \cong \frac{e_t - e_b}{H_p} \quad (3.32)$$

All these quantities are functions of time, and are extremely important although very small, since their evaluation allows for the estimation of the hydrodynamic and contact forces and moments and ultimately the piston performance.

3.3.6 Equations of Motion

In order to calculate the piston eccentricities described in Section 3.3.5 the equations of motion for the piston assembly have to be derived. Figure 3.9 shows the free body diagrams of the piston-connecting rod assembly in the X_p - Y_p - Z_p coordinate system. The system is tilted by an angle γ from the vertical. This angle represents the cylinder bank angle in the case of V-engine configuration. The forces are:

- F_{gy} combustion gas force in the Y_p -direction
- F_{mpy} piston weight component in the Y_p -direction
- F_{mpx} piston weight component in the X_p -direction
- F_{ipy} piston inertia in the Y_p -direction
- F_{ipx} piston inertia in the X_p -direction
- F_{ipz} piston inertia in the Z_p -direction
- F_{fy} friction force in the Y_p -direction: sum of hydrodynamic shear, F_{fh} , and contact friction, F_{fc}
- F_{tx} force in the X_p -direction: sum of hydrodynamic and contact forces, F_{hx} and F_{cx}
- F_{tz} force in the Z_p -direction: sum of hydrodynamic and contact forces, F_{hz} and F_{cz} , hydrodynamic shear and contact friction forces, F_{fhz} and F_{fcz} , and wrist-pin friction F_{fwz}
- F_{pwx} reaction at the piston-wrist-pin interface in the X_p -direction
- F_{pwy} reaction at the piston-wrist-pin interface in the Y_p -direction
- F_{mwy} wrist-pin weight component in the Y_p -direction
- F_{mwx} wrist-pin weight component in the X_p -direction
- F_{iwy} wrist-pin inertia in the Y_p -direction
- F_{iwx} wrist-pin inertia in the X_p -direction
- F_{rwx} reaction at the wrist-pin-connecting rod interface in the X_p -direction
- F_{rwy} reaction at the wrist-pin-connecting rod interface in the Y_p -direction
- F_{mry} connecting rod weight component in the Y_p -direction
- F_{mrx} connecting rod weight component in the X_p -direction
- F_{iry} connecting rod inertia in the Y_p -direction
- F_{irx} connecting rod inertia in the X_p -direction

- F_o crankshaft reaction force
- M_{ic} piston inertia moment
- M_{rod} connecting rod inertia moment
- M_t moments about wrist-pin: sum of hydrodynamic and contact moments, M_{hz} and M_{cz} , hydrodynamic shear and contact friction moments, M_{fhz} and M_{fcz} , and wrist-pin friction moment, M_{fwz}

The equations are derived from Newton's second law of motion and the conservation of angular momentum. The following derivations assume a rigid connecting rod and wrist-pin. Also, the crankshaft reaction force F_o is assumed to be collinear with the connecting rod axis. Clockwise moments are positive.



3.3.6.1 Piston

Sum of forces in the X_p -direction,

$$F_{ipx} + F_{mpx} + F_{tx} + F_{pwx} = 0 \quad (3.33)$$

Sum of forces in the Y_p -direction,

$$F_{ipy} + F_{mpy} + F_{gy} + F_{fy} + F_{pwy} = 0 \quad (3.34)$$

Sum of forces in the Z_p -direction,

$$F_{ipz} + F_{tz} = 0 \quad (3.35)$$

Moments about the wrist-pin,

$$M_{ip} + M_t - F_{gy}x_{wp} + (F_{ipy} + F_{mpy})(x_{cg} - x_{wp}) + (F_{ipx} + F_{mpx})(y_{wp} - y_{cg}) = 0 \quad (3.36)$$

where,

$$F_{tx} = F_{hx} + F_{cx} \quad (3.37)$$

$$F_{fy} = F_{fhy} + F_{fcy} \quad (3.38)$$

$$F_{tz} = F_{hz} + F_{cz} + F_{fhz} + F_{fcz} + F_{fwz} \quad (3.39)$$

$$M_t = M_{hz} + M_{cz} + M_{fz} + M_{fwz} \quad (3.40)$$

3.3.6.2 Wrist-pin:

Sum of forces in the X_p -direction,

$$-F_{pwx} + F_{mwx} + F_{iwx} + F_{rwx} = 0 \quad (3.41)$$

Sum of forces in the Y_p -direction,

$$-F_{pwy} + F_{mwy} + F_{iwy} + F_{rwy} = 0 \quad (3.42)$$

3.3.6.3 Connecting Rod:

Sum of forces in the X_p -direction,

$$-F_{wrx} + F_{irx} + F_{mrx} + F_o \sin(-\varphi) = 0 \quad (3.43)$$

Sum of forces in the Y_p -direction,

$$-F_{wry} + F_{iry} + F_{mry} + F_o \cos(-\varphi) = 0 \quad (3.44)$$

Moments about O,

$$\begin{aligned} M_{rod} + F_{rwy} r_2 \sin(-\varphi) - F_{rwx} r_2 \cos(-\varphi) \\ - (F_{iry} + F_{mry}) \rho \sin(-\varphi) + (F_{irx} + F_{mrx}) \rho \cos(-\varphi) = 0 \end{aligned} \quad (3.45)$$

Equations (3.33), (3.34), (3.41), (3.42) and (3.45) can be rearranged and combined into one equation yielding,

$$\begin{aligned} M_{rod} + (F_{ipy} + F_{iwy} + F_{mpy} + F_{mwy} + F_{gy} + F_{fy}) r_2 \sin(\varphi) \\ - (F_{ipx} + F_{iwx} + F_{mpx} + F_{mwx} + F_{hx} + F_{cx}) r_2 \cos(\varphi) \\ - (F_{iry} + F_{mry}) \rho \sin(-\varphi) + (F_{irx} + F_{mrx}) \rho \cos(\varphi) = 0 \end{aligned} \quad (3.46)$$

Now (3.35), (3.36) and (3.46) will be the basis for solving for the piston secondary motion. The forces constituting these equations are as follows: The combustion force is given by,

$$F_{gy} = P_g \pi R^2 \quad (3.47)$$

where P_g is the combustion gas pressure.

The weight component forces are given by,

$$F_{mpx} = m_p g \sin \gamma \quad (3.48)$$

$$F_{mpy} = m_p g \cos \gamma \quad (3.49)$$

$$F_{mwx} = m_w g \sin \gamma \quad (3.50)$$

$$F_{mwy} = m_w g \cos \gamma \quad (3.51)$$

$$F_{mrx} = m_r g \sin \gamma \quad (3.52)$$

$$F_{mry} = m_r g \cos \gamma \quad (3.53)$$

where m_p is piston mass, m_w is the wrist-pin mass and m_r is the connecting rod mass.

The inertia forces are given by,

$$F_{ipx} = -m_p \ddot{e}_{cg} \quad (3.54)$$

$$F_{ipy} = -m_p a_p \quad (3.55)$$

$$F_{iwx} = -m_w \ddot{e}_p \quad (3.56)$$

$$F_{iwy} = -m_w a_p \quad (3.57)$$

$$F_{irx} = -m_r a_{cm,x} \quad (3.58)$$

$$F_{iry} = -m_r a_{cm,y} \quad (3.59)$$

The inertia moments are given by,

$$M_{ip} = -I_p \ddot{\beta} \quad (3.60)$$

$$M_{rod} = -I_r \alpha_2 \quad (3.61)$$

where I_p and I_r are the second moment of inertias about the Z_p -axis of the piston and connecting rod respectively.

In the above equations the secondary motion accelerations are given by the time derivatives of the secondary motion velocities,

$$\ddot{e}_{cg} = \frac{1}{\Delta t} \left(\dot{e}_t - \frac{y_{cg}}{H_p} (\dot{e}_t - \dot{e}_b) \right) \quad (3.62)$$

$$\ddot{e}_p = \frac{1}{\Delta t} \left(\dot{e}_t - \frac{y_{wp}}{H_p} (\dot{e}_t - \dot{e}_b) \right) \quad (3.63)$$

$$\ddot{\beta} \equiv \frac{1}{\Delta t} \left(\frac{\dot{e}_t - \dot{e}_b}{H_p} \right) \quad (3.64)$$

where Δt is the time step. For a four stroke engine running at N revolutions per minute the time step for each crank angle is given by,

$$\Delta t = \frac{1}{6N} \quad (3.65)$$

The hydrodynamic and contact forces and moments, as well as the shear and contact friction forces and moments, are all functions of the piston secondary motion. Their relationship will be described in detail in the following sections. All these constitute a highly non-linear problem with three equations, (3.35), (3.36) and (3.46), and six unknowns, e_t , e_b , e_z , \dot{e}_t , \dot{e}_b , and \dot{e}_z . In order to solve for the secondary motion, the

secondary velocity at the current time step has be equal to the time derivative of the piston eccentricity at the current time step relative to the previous time step. That is,

$$\dot{e}_t^\theta = \frac{e_t^\theta - e_t^{\theta-1}}{\Delta t} \quad (3.66)$$

$$\dot{e}_b^\theta = \frac{e_b^\theta - e_b^{\theta-1}}{\Delta t} \quad (3.67)$$

$$\dot{e}_z^\theta = \frac{e_z^\theta - e_z^{\theta-1}}{\Delta t} \quad (3.68)$$

These now complete the system of equations which can be solved iteratively for the six unknowns using the Newton-Raphson method.

3.4 Hydrodynamic Pressure

In order to calculate the hydrodynamic pressure developed at the skirt surface, the standard Reynolds equation is used despite the fact that in some of the previous efforts the average Reynolds equation proposed by Patir and Cheng [54] is used. This equation accounts for the effect of surface roughness on the pressure. The scope of this dissertation, though, is to develop a new model which considers piston translation along the wrist-pin. Since it has already been shown in literature that the average Reynolds equation can yield better results, it can be easily implemented with minimal programming effort later on. The standard Reynolds equation employed in the current model is of the form,

$$\frac{\partial}{\partial x_s} \left(\frac{h^3}{12\mu} \frac{\partial P_h}{\partial x_s} \right) + \frac{\partial}{\partial y_s} \left(\frac{h^3}{12\mu} \frac{\partial P_h}{\partial y_s} \right) = \frac{1}{2} \left(\dot{e}_z \frac{\partial h}{\partial x_s} + v_p \frac{\partial h}{\partial y_s} \right) + \dot{h} \quad (3.69)$$

with,

$$P_h = \bar{P} \text{ on } \Gamma \quad (3.70)$$

where P_h is the hydrodynamic pressure, h is the oil film thickness, \dot{h} is the squeeze film velocity, and \bar{P} is the pressure on the boundary, Γ , which is set to zero gauge. It should be noted that the physical wedge term, the first term on the right-hand side of the equation, includes the effects of both the axial velocity of the piston and the velocity along the wrist-pin.

This equation is solved via the finite element method (FEM) as described in [50, 49]. FEM is chosen rather than the traditional finite differences method (FDM) as it allows for direct mapping of pressure and skirt deformations from the 2-D skirt mesh (Figure 3.5) to the 3-D piston mesh. This eliminates the numerical error that would arise from the interpolations between the finite difference grid and the finite element mesh. It can be argued that the finite element mesh can be too coarse to obtain an accurate solution for the Reynolds equation. Panayi [49] showed that by controlling the mesh size with finer mesh on the skirt surface and coarser elsewhere on the piston, the hydrodynamic pressure can be evaluated within desirable accuracy. Of course there is a trade-off here between accuracy and computation time, a dilemma that researchers always face.

Equation (3.69) is solved for both the major and minor thrust sides at each iteration step assuming fully flooded lubrication conditions. The half-Sommerfeld condition, (3.71), is applied to the calculated hydrodynamic pressure, as conventional lubricants used in internal combustion engines cannot withstand negative pressures and cavitate.

$$P_h = P_h \cdot \chi(P_h) \quad (3.71)$$

where $\chi(P_h)$ is a switch function,

$$\chi(P_h) = \begin{cases} 1, & \text{if } P_h \geq 0 \\ 0, & \text{if } P_h < 0 \end{cases} \quad (3.72)$$

In the case that hydrodynamic lubrication is considered at the second land, the same equation, (3.69), is solved on a uniformly generated 2-D finite element mesh (Figure 3.10) of the land. In this case the deformations at each node are interpolated from the 3-D piston solid mesh. The boundary conditions applied to the Reynolds equation when solving for the second land lubrication pressure are,

$$P_h(y_{lt} = 0) = \bar{P} \quad (3.73)$$

$$P_h(y_{lb} = 0) = \bar{P} \quad (3.74)$$

$$P_h(\theta_p = 0) = P_h(\theta_p = 2\pi) \quad (3.75)$$

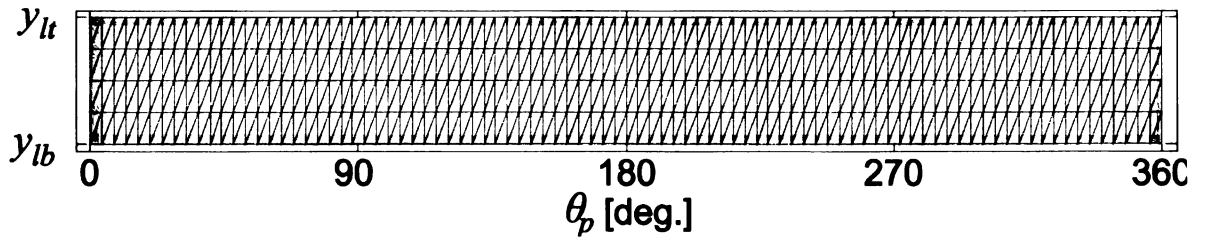


Figure 3.10: Second land mesh, 4 x 90 elements

3.5 Oil Film Thickness

As the eccentricities (Figure 3.8) are much smaller than the skirt length the oil film thickness can be approximated by,

$$h = c - \left[e_{st} + (e_{sb} - e_{st}) \frac{y_s}{L} \right] \cos \theta_p - e_z \sin \theta_p + \delta_c - \delta_s - \delta_o - \delta_p \quad (3.76)$$

where c is the nominal piston to cylinder bore clearance, δ_c is the cylinder bore deformation, δ_s is the skirt deformation, δ_o is the contribution to oil film thickness due to piston ovality if any, and δ_p is the skirt profile height.

The cylinder bore deformation is assumed to be constant over the cycle. The hydrodynamic and contact pressures developed at the interface between the skirt surface and the cylinder bore have negligible effect on it. The cylinder bore deformation is supplied as input data either from experimental measurements or from finite element analysis of the cylinder block. This allows for a shorter computation time. δ_c is positive if the cylinder deformation increases the piston to cylinder bore clearance (Figure 3.11). The cylinder bore deformation is interpolated at each crank angle for each skirt node from the supplied data as shown in Figure 2.15.

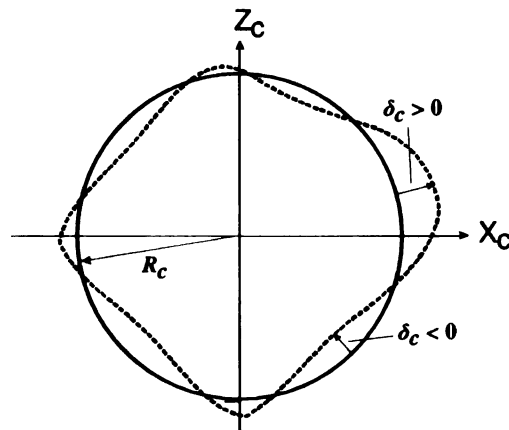


Figure 3.11: Schematic of cylinder bore deformation

The skirt deformation, δ_s , includes the deformations induced on the skirt by the thermal expansion, the combustion gas pressure, the piston inertia, and the hydrodynamic and contact pressures. Given the 3-D deformation components of a node the deformation in the radial direction is obtained by,

$$\delta_s = u_x \cos(\theta_p) + u_z \sin(\theta_p) \quad (3.77)$$

where u_x and u_z are the deformation components in the X_p and Z_p directions respectively. The skirt compliance described in Section 3.2.1 is used here to calculate the contribution of hydrodynamic and contact forces to skirt deformation.

The skirt profile height, δ_p , is the offset of the skirt surface from the nominal skirt diameter. The interested reader is referred to Chapter 6 for a detailed description of skirt profiles. The skirt profile ovality, δ_o , is described in Section 2.2.15 and it is usually calculated by (2.2).

3.6 Squeeze Film Velocity

It should be noted that in (3.76), e_{st} , e_{sb} , e_z , δ_s and δ_c are all functions of time.

The squeeze film velocity is then given by,

$$\dot{h} = - \left[\dot{e}_{st} + (\dot{e}_{sb} - \dot{e}_{st}) \frac{y_s}{L} \right] \cos \theta_p - \dot{e}_z \sin \theta_p + \dot{\delta}_c - \dot{\delta}_s \quad (3.78)$$

where,

$$\dot{\delta}_c = \frac{\delta_c^\theta - \delta_c^{\theta-1}}{\Delta t} \quad (3.79)$$

$$\dot{\delta}_s = \frac{\delta_s^\theta - \delta_s^{\theta-1}}{\Delta t} \quad (3.80)$$

3.7 Oil Dynamic Viscosity

The oil dynamic viscosity, μ , is an important parameter in the Reynolds equation as it can vary with temperature, pressure, or both. In this work the viscosity is assumed to vary with temperature but be invariant to pressure. The Vogel law [69] is used to evaluate the oil viscosity at the interface between the piston skirt and the cylinder bore. The piston temperature is found to decrease along the skirt length, being higher at the top. In a similar way, the temperature of the cylinder bore decreases from top to bottom. Consequently the oil temperature, T_{oil} , in the interface is taken as the average of the two temperatures. The piston temperature is taken from the piston thermal finite element analysis. The cylinder bore temperature, like the cylinder bore deformation, is supplied as input data either from experimental measurements or from finite element analysis of the cylinder block. Both of these temperature distributions are assumed to be constant over the cycle. The viscosity is thus given by,

$$\mu = \mu_{ref} e^{-\kappa (T_{oil} - T_{ref})} \quad (3.81)$$

with,

$$\kappa = \frac{\log(\mu_2/\mu_1)}{T_1 - T_2} \quad (3.82)$$

Here T_1 , T_2 , μ_1 , and μ_2 are the low and high oil temperatures respectively. Their corresponding viscosities are found in the oil data sheets supplied by manufacturers.

These viscosities are usually for temperatures of 40 °C and 100 °C. T_{ref} is the oil temperature in the engine oil sump and μ_{ref} its corresponding viscosity.

3.8 Hydrodynamic Forces and Moments

Once the hydrodynamic pressure is calculated via the Reynolds equation, then the hydrodynamic forces and moments that contribute to the equations of motion can be calculated. The normal hydrodynamic pressure is split into components (Figure 3.12) to calculate the contributions in the X_p and Z_p directions.

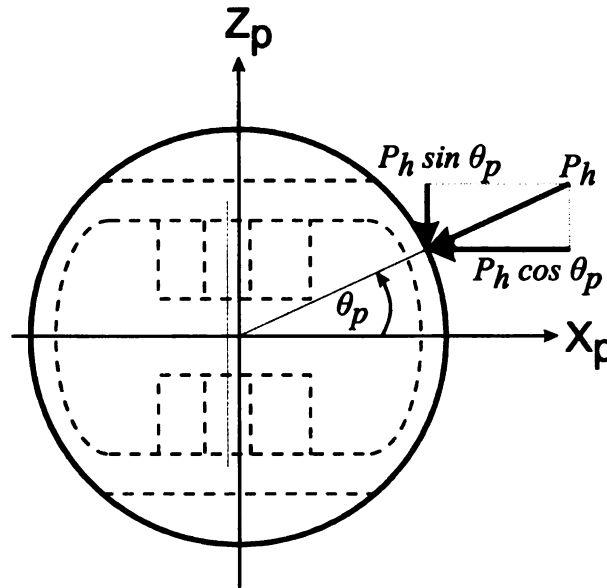


Figure 3.12: Components of pressure on skirt surface

The hydrodynamic forces acting in the X_p and Z_p directions are given by,

$$F_{hx} = \iint_{A_s} P_h \cos \theta_p \, dA \quad (3.83)$$

$$F_{hz} = \iint_{A_s} P_h \sin \theta_p dA \quad (3.84)$$

where dA is the infinitesimal skirt area, given by,

$$dA = R d\theta_p dy_s \quad (3.85)$$

The hydrodynamic moment about the wrist-pin is given by,

$$M_{hz} = \iint_{A_s} P_h \cos \theta_p \cdot (y_{wp} - (H_p - L) - y_s) dA \quad (3.86)$$

The hydrodynamic shear developed on the skirt or land surface can be evaluated by,

$$\tau = -\frac{\mu v_p}{h} + \frac{h}{2} \frac{\partial P_h}{\partial y_s} \quad (3.87)$$

The hydrodynamic shear force and the hydrodynamic shear moment about the wrist-pin are then given by,

$$F_{fh} = \iint_{A_s} \tau dA \quad (3.88)$$

$$M_{fhz} = \iint_{A_s} \tau \cdot (X_p - x_{wp}) dA \quad (3.89)$$

3.9 Contact Pressure

As the piston travels laterally within the cylinder bore, the oil film thickness can become very small, thus allowing for possible solid-to-solid contact. The magnitude of the pressure arising by this contact is calculated via the Greenwood-Tripp model [19],

which assumes that both contacting surfaces are rough with their height distribution being Gaussian. The contact pressure is given by,

$$P_c(h) = K E' F_{5/2}(H_\sigma) \quad (3.90)$$

with,

$$K = \frac{16\sqrt{2}}{15} \pi (\eta \xi \sigma)^2 \sqrt{\frac{\sigma}{\xi}} \quad (3.91)$$

Here, η is the asperity density on the skirt, ξ is the asperity radius of curvature on the skirt, and σ is the composite standard deviation of asperity height distribution, given by,

$$\sigma = \sqrt{\sigma_1^2 + \sigma_2^2} \quad (3.92)$$

where σ_1 and σ_2 are the standard deviations of asperity height distribution for the piston skirt and cylinder bore respectively.

The composite modulus of elasticity, E' , is given by,

$$E' = \frac{1-\nu_1^2}{E_1} + \frac{1-\nu_2^2}{E_2} \quad (3.93)$$

with E_1 and ν_1 being the modulus of elasticity and the Poisson ratio of the piston respectively. Similarly, E_2 and ν_2 are for the cylinder liner.

The normalized oil film thickness, H_σ , is given by,

$$H_\sigma = \frac{h}{\sigma} \quad (3.94)$$

The function $F_{2.5}(H_\sigma)$ is the Gaussian distribution of asperity heights. In order to avoid the numerical integration of this function at each iteration step, it is approximated beforehand with an exponential function, as follows,

$$F_{2.5}(H_{\sigma}) = \begin{cases} \exp\left(\frac{c_1 + c_2 H_{\sigma} + c_3 H_{\sigma}^2}{1 + c_4 H_{\sigma} + c_5 H_{\sigma}^2}\right) + c_6 & H_{\sigma} < 4.0 \\ 0 & H_{\sigma} \geq 4.0 \end{cases} \quad (3.95)$$

A more detailed explanation of the Greenwood-Tripp model and on the approximation of $F_{2.5}(H_{\sigma})$ can be found in Chapter 4.

3.9.1 Contact Forces and Moments

The contact pressure is split into components like the hydrodynamic pressure (Figure 3.12) to obtain the contributions in the X_p and Z_p directions.

The contact forces acting in the X_p and Z_p directions are given by,

$$F_{cx} = \iint_{A_s} P_c \cos \theta_p \, dA \quad (3.96)$$

$$F_{cz} = \iint_{A_s} P_c \sin \theta_p \, dA \quad (3.97)$$

The contact moment about the wrist-pin is given by,

$$M_{cz} = \iint_{A_s} P_c \cos \theta_p \cdot (y_{wp} - (H_p - L) - y_s) \, dA \quad (3.98)$$

The friction developed due to the contact of the piston skirt with the cylinder liner is calculated via the Coulomb friction model as,

$$F_{fc} = -\text{sign}(v_p) \iint_{A_s} \mu_f P_c \, dA \quad (3.99)$$

where μ_f is the coefficient of friction between the piston skirt and the cylinder liner.

Similarly the contact friction moment about the wrist-pin is given by,

$$M_{fc} = \text{sign}(v_p) \iint_{A_s} \mu_f P_c \cdot (X_p - x_{wp}) dA \quad (3.100)$$

3.10 Wrist-pin Friction

The reaction loads developed at the wrist-pin interface result in the generation of frictional moments and forces. At the interface, complex lubrication conditions exist. Specialized computational models are used to investigate the wrist-pin lubrication. In this work it is assumed that the friction developed at the wrist-pin obeys the Coulomb friction model. The friction moment generated about the wrist-pin is given by,

$$M_{fwz} = -\text{sign}(\dot{\beta}) \mu_w \frac{d_w}{2} \sqrt{F_{pwx}^2 + F_{pwy}^2} \quad (3.101)$$

where μ_w is the wrist-pin friction coefficient, and d_w the wrist-pin diameter.

The friction force in the Z_p -direction is given by,

$$F_{fwz} = -\text{sign}(\dot{e}_z) \mu_w \sqrt{F_{pwx}^2 + F_{pwy}^2} \quad (3.102)$$

3.11 Wear

The wear on the skirt is calculated using the Archard wear model [3], which relates the volume of material removed to the ratio of the contact work, $F_c S$, to the material hardness,

$$V = K_w \frac{F_c S}{H} \quad (3.103)$$

Here, V is the volume of material removed, F_c is the normal contact force, S is the distance moved by the skirt, H is the skirt material hardness, and K_w is the skirt wear coefficient. Expressing the model in infinitesimal values yields,

$$dV = dA dh_w = K_w \frac{(P_c dA) dS}{H} \quad (3.104)$$

from which the height of material removed, h_w , can be obtained as,

$$h_w = \int \frac{K_w}{H} P_c dS \quad (3.105)$$

3.12 Numerical Procedure

The equations of motion describing the piston secondary motion constitute an initial value problem for a system of non-linear second order differential equations in e_t , e_b , e_z , \dot{e}_t , \dot{e}_b , and \dot{e}_z with respect to time or crank angle, as the crank angle is directly proportional to time. The equations of motion derived in Section 3.3.6 can be put in a functional vector, $\mathbf{f} \in \mathbb{R}^6$, of the form,

$$\mathbf{f} = \mathbf{0} \quad (3.106)$$

where,

$$\begin{aligned} f_1 = & M_{rod} + (F_{ipy} + F_{iwy} + F_{mpy} + F_{mwy} + F_{gy} + F_{fy}) r_2 \sin(\varphi) \\ & - (F_{ipx} + F_{iwx} + F_{mpx} + F_{mwx} + F_{hx} + F_{cx}) r_2 \cos(\varphi) \\ & - (F_{iry} + F_{mry}) \rho \sin(-\varphi) + (F_{irx} + F_{mrx}) \rho \cos(\varphi) = 0 \end{aligned} \quad (3.107)$$

$$f_2 = F_{ipz} + F_{hz} + F_{cz} + F_{fhz} + F_{fcz} + F_{fwz} = 0 \quad (3.108)$$

$$f_3 = M_{ip} + M_{hz} + M_{cz} + M_{fz} + M_{fwz} - F_{gy}x_{wp} + (F_{ipy} + F_{mpy})(x_{cg} - x_{wp}) + (F_{ipx} + F_{mpx})(y_{wp} - y_{cg}) = 0 \quad (3.109)$$

$$f_4 = \dot{e}_t^\theta - \frac{e_t^\theta - e_t^{\theta-1}}{\Delta t} = 0 \quad (3.110)$$

$$f_5 = \dot{e}_b^\theta - \frac{e_b^\theta - e_b^{\theta-1}}{\Delta t} = 0 \quad (3.111)$$

$$f_6 = \dot{e}_z^\theta - \frac{e_z^\theta - e_z^{\theta-1}}{\Delta t} = 0 \quad (3.112)$$

In order to solve for the six unknowns the Newton-Raphson method is employed. The implementation of the Newton-Raphson algorithm is described in detail in [16] and will not be repeated here. In brief, given the vector $\mathbf{x} = [e_t, e_b, e_z, \dot{e}_t, \dot{e}_b, \dot{e}_z]^T$, the solution to the system of equations in (3.106) is found iteratively via,

$$\mathbf{x}^{\theta, n+1} = \mathbf{x}^{\theta, n} - \lambda \mathbf{J}^{-1} \mathbf{f} \quad (3.113)$$

where θ is the time step, n is the Newton-Raphson iteration, and λ the Newton step calculated by the algorithm in [16]. It is calculated such that it ensures global convergence of the methodology. \mathbf{J} is the Jacobian matrix of vector \mathbf{f} relative to the unknowns given by,

$$\mathbf{J} = \left[\frac{\partial f_i}{\partial x_j} \right] \quad i, j = 1, 2, \dots, 6 \quad (3.114)$$

In order to start the Newton-Raphson iteration, an initial guess is required for vector \mathbf{x} . To start the simulation it is assumed that all the values are zero, ($\mathbf{x} = \mathbf{0}$); that is, the piston is stationary exactly at the center of the cylinder bore. After the first time step

the converged solution for the previous time step is taken as the initial for the current time step ($\mathbf{x}^{\theta,0} = \mathbf{x}^{\theta-1,converged}$).

Once \mathbf{x} is available the transverse accelerations, \ddot{e}_t , \ddot{e}_b , and \ddot{e}_z can then be calculated at each Newton-Raphson iteration via numerical differentiation as,

$$\begin{Bmatrix} \ddot{e}_t \\ \ddot{e}_b \\ \ddot{e}_z \end{Bmatrix}^{\theta} = \frac{1}{\Delta t} \left(\begin{Bmatrix} \dot{e}_t \\ \dot{e}_b \\ \dot{e}_z \end{Bmatrix}^{\theta,n+1} - \begin{Bmatrix} \dot{e}_t \\ \dot{e}_b \\ \dot{e}_z \end{Bmatrix}^{\theta-\Delta\theta} \right) \quad (3.115)$$

Also similar to \mathbf{x} vector the hydrodynamic and contact pressures are assumed to be known at the previous time step and are used as an initial guess for the current time step. To start the simulation again they are set to zero. With this information available, all the forces and moments comprising (3.106) can be calculated.

The solution is achieved via three iterative loops, one for periodicity of piston secondary motion, one for the hydrodynamic and contact pressures, and one for the dynamics (Figure 3.13). Within the dynamics loop, first the axial dynamics are evaluated, y_p , v_p , a_p , φ , α_2 , $a_{cm,x}$ and $a_{cm,y}$, at the current time step. Then the oil temperature, T_{oil} , and the cylinder bore deformation, δ_c , are evaluated at the current piston position. The skirt deformation, δ_s , is also calculated with the combined effect of combustion gas pressure, piston thermal expansion, piston inertia, and hydrodynamic and contact pressures. Now from all these the oil film thickness, h , and the squeeze film velocity, \dot{h} , are calculated. This allows for the evaluation of the hydrodynamic and contact pressures, and ultimately of all the forces and moments in (3.106). Also, by evaluating the transverse accelerations via (3.115), the transverse inertias are calculated. The piston

transverse position is calculated via the Newton-Raphson method, (3.113). The procedure is repeated until the solution of \mathbf{x} is within the given tolerance usually 0.01, that is,

$$\frac{\|\mathbf{x}^{\theta,n+1} - \mathbf{x}^{\theta,n}\|}{\|\mathbf{x}^{\theta,n+1}\|} \leq 0.01 \quad (3.116)$$

Convergence is relatively fast within 2 to 5 iteration steps, except in the cases where the hydrodynamic and contact pressures are very high. This is usually around firing or for very small piston-to-cylinder liner clearances. Once the values of the transverse velocities that satisfy (3.106) have been found, the hydrodynamic and contact pressures are checked for convergence within the pressure loop. The present solutions of the hydrodynamic and contact pressures are checked with the ones from the previous pressure loop step. If they have not converged within reasonable tolerance, the pressures are adjusted via underrelaxation,

$$P_h^\theta = P_h^{\theta,k-1} + \omega_r \left(P_h^{\theta,k} - P_h^{\theta,k-1} \right) \quad (3.117)$$

$$P_c^\theta = P_c^{\theta,k-1} + \omega_r \left(P_c^{\theta,k} - P_c^{\theta,k-1} \right) \quad (3.118)$$

where k is the pressure iteration step, and $\omega_r \in [0.05, 0.5]$ is the underrelaxation factor. This factor is adjusted within the pressure loop by monitoring the pressure convergence. Once the hydrodynamic and contact pressures have converged, the simulation moves to the next time step. This is repeated for the whole cycle, $\theta \in [0, 4\pi]$.

Since the internal combustion engine is a cyclic device, the above procedure can start from any crank angle. The calculation can appropriately be started at the middle of the intake stroke, where the piston inertia is minimal and the combustion gas pressure is

relatively low. Also the initial guess for the transverse positions, velocities, and hydrodynamic and contact pressure should have no effect on the solution. However for simplicity all of them are set to zero,

$$\mathbf{x}^{\theta=0} = \mathbf{0} \quad (3.119)$$

$$P_h^{\theta=0} = P_c^{\theta=0} = 0 \quad (3.120)$$

Furthermore, the final solution of all the forces and moments experienced by the piston should be periodic. This is ensured by the periodicity loop. After the second cycle the piston secondary is checked for periodicity,

$$\mathbf{x}^{\theta} = \mathbf{x}^{\theta+4\pi} \quad (3.121)$$

Once (3.121) is satisfied within reasonable tolerance, this guarantees that all the forces and moments experienced by the piston are also periodic and the whole procedure is stopped. It has been observed that periodicity is usually achieved between 3 and 5 cycles depending on the magnitude of the hydrodynamic and contact pressures developed on the skirt and engine speed.

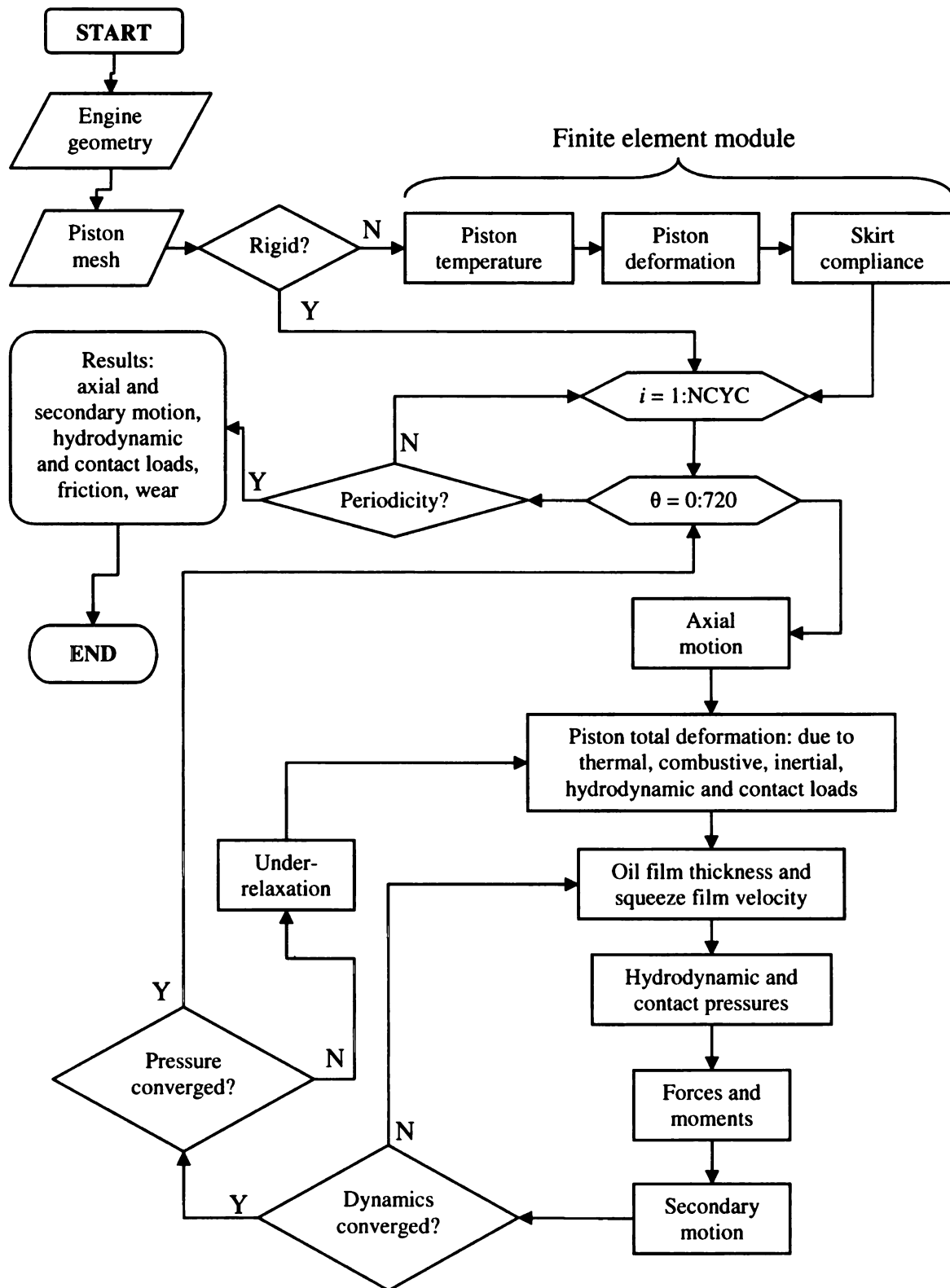


Figure 3.13: PIFEAD flow diagram

3.13 Remarks

The piston dynamics numerical model, PIFEAD, can be used to predict piston axial and secondary dynamics, hydrodynamic and contact forces, piston deformation and piston wear.

The model can also be used to investigate how piston geometry, piston stiffness, skirt profile, wrist-pin offset, lubricant viscosity, piston-to-cylinder bore clearance and cylinder bank angle affect piston dynamics and ultimately piston performance.

It can be used to assess new designs or troubleshoot existing ones. Examples of its applications are presented in Chapters 5 and 6.

CHAPTER 4. APPROXIMATION OF THE ASPERITY CONTACT PRESSURE

4.1 Introduction

The load carried by asperity contacts is a very important quantity when performing elastohydrodynamic analyses in the mixed-lubrication regime. The Greenwood-Tripp model for the contact of two nominally flat rough surfaces is traditionally used for the evaluation of these loads. In this model, it is assumed that the asperity heights follow a Gaussian distribution, thus the load carried by the asperities can be evaluated by the integration of a nonlinear function that relates the surface separation with the asperity height distribution. In order to avoid the computational burden of integrating this function numerically, several approximations have been proposed in literature.

In this chapter the quality of two of these approximations is examined: a power law approximation and a sixth order polynomial approximation proposed in research efforts for the lubrication analysis of piston rings. The lack of fit for these two approximations is identified and in turn a new exponential approximation is proposed with the coefficients derived via the method of least squares. This new approximation exhibits a better fit over the entire range of the tabulated values for the asperity height distribution integral provided by Greenwood and Tripp. The computational cost of this approximation is also found to be acceptable. It is the approximation used in PIFEAD.

4.2 Background of the Greenwood-Tripp Asperity Contact Model

Greenwood and Tripp [18] described the surfaces of sliding solids to be “as complex as the surface of the earth and, indeed, geometrically rather similar to it.” Consequently they recognised that contact cannot be described by exact mathematical equations; rather, it needs to be modelled. They extended a previous work by Greenwood and Williamson [20] to develop a model for “the contact of two nominally flat rough surfaces.” In their work they noted that the contact geometry is such, for broken-in surfaces, that elastic contact occurs. Also, they stated that the distribution of asperity heights is very close to Gaussian. This is not necessarily the case for worn surfaces, but in contact the effect is still Gaussian as the asperity heights of the parts of the surface that do not touch are not considered. With all this information available, they developed a model for the load carried by asperity interaction of two rough surfaces. They concluded that as long as the asperity height distribution is Gaussian, the mode of deformation, plastic or elastic, the asperity shape, spherical or conical, and whether the asperities are found on one or both surfaces are all unimportant.

The Greenwood-Tripp model gained vast popularity in the field of elastohydrodynamic analyses. However, it posed a computational burden, as it required the numerical integration of the Gaussian distribution. Greenwood and Tripp provided tabulated results for this integral over its effective range. This allowed for the approximation of the integral with simpler functions.

In recent years Hu et al. [23] and Arcoumanis et al. [4] archived approximations for those tabulated values while investigating the mixed lubrication of piston rings. The first proposed a power law approximation, whilst the latter proposed an approximation by

a sixth order polynomial. These approximations were used in subsequent research efforts [12, 1]. They seem to represent the model adequately, but an investigation on the quality of the approximation suggests otherwise.

4.3 The Greenwood-Tripp Model Equations

The theory and development of the Greenwood-Tripp (GT) model are extensively described in [18] and will not be repeated here. Rather, the final equations will be given. Consider two rough surfaces (Figure 4.1) separated by a gap, h . The normalised gap, H_σ , is given by,

$$H_\sigma = \frac{h}{\sigma} \quad (4.1)$$

where σ is the composite standard deviation of asperity height distribution, given by,

$$\sigma = \sqrt{\sigma_1^2 + \sigma_2^2} \quad (4.2)$$

with σ_1 and σ_2 being the standard deviations of asperity height distributions on the two surfaces.

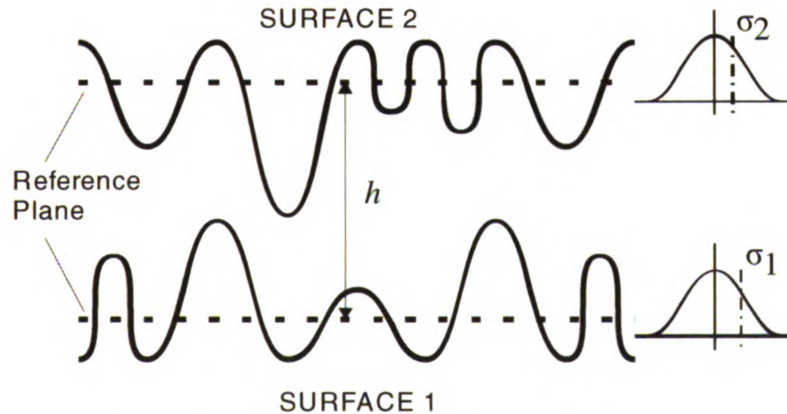


Figure 4.1: Gap between two rough surfaces

The load, P , carried by the asperities is then given by,

$$P(h) = K E' F_{5/2}(H_\sigma) \quad (4.3)$$

with,

$$K = \frac{16\sqrt{2}}{15} \pi (\eta \beta \sigma)^2 \sqrt{\frac{\sigma}{\beta}} \quad (4.4)$$

Here, η is the asperity density and β is the asperity radius of curvature on the surface of interest.

The composite modulus of elasticity, E' , is given by,

$$E' = \frac{1-\nu_1^2}{E_1} + \frac{1-\nu_2^2}{E_2} \quad (4.5)$$

with E_1 and ν_1 , being the modulus of elasticity and the Poisson ratio of the material of surface 1. Similarly, E_2 and ν_2 are for the material of surface 2.

The function $F_{5/2}(H_\sigma)$ is the integral of the Gaussian distribution of asperity heights and is given by,

$$F_{5/2}(H_\sigma) = \frac{1}{\sqrt{2\pi}} \int_{H_\sigma}^{\infty} (u - H_\sigma)^{5/2} e^{-u^2/2} du \quad (4.6)$$

It is clear that (4.6) does not have a straightforward analytical solution. It has to be either evaluated numerically, or approximated. Greenwood and Tripp [18] provided tabulated values for $F_{5/2}(H_\sigma)$ for discrete values of H_σ (Table 4.1). These values have been used to derive approximations for $F_{5/2}(H_\sigma)$.

Table 4.1: Tabulated values for (4.6)

H_σ	$F_{5/2}(H_\sigma)$
0.0	0.616 64
0.5	0.240 40
1.0	0.080 56
1.5	0.022 86
2.0	0.005 42
2.5	0.001 06
3.0	0.000 17
3.5	0.000 02
4.0	0.000 00
> 4.0	0.0

4.4 Approximations

4.4.1 Power Law

Hu et al. [23] proposed a power law approximation for $F_{5/2}(H_\sigma)$ in the form of,

$$F_{5/2}(H_\sigma) = \begin{cases} A(4.0 - H_\sigma)^Z & H_\sigma < 4.0 \\ 0 & H_\sigma \geq 4.0 \end{cases} \quad (4.7)$$

where $A = 4.4068 \times 10^{-5}$ and $Z = 6.804$. From here on the proposed approximation by Hu et al. will be referred to as HU.

4.4.2 Sixth Order Polynomial

Arcoumanis et al. [23] proposed a sixth order polynomial for the approximation of $F_{5/2}(H_\sigma)$,

$$F_{5/2}(H_{\sigma}) = \begin{cases} C_6 H_{\sigma}^6 + C_5 H_{\sigma}^5 + C_4 H_{\sigma}^4 + C_3 H_{\sigma}^3 & H_{\sigma} < 4.0 \\ + C_2 H_{\sigma}^2 + C_1 H_{\sigma} + C_0 & \\ 0 & H_{\sigma} \geq 4.0 \end{cases} \quad (4.8)$$

where $C_0 = 0.6167$, $C_1 = -1.0822$, $C_2 = 8.0203 \times 10^{-1}$, $C_3 = -3.1933 \times 10^{-1}$, $C_4 = 7.1624 \times 10^{-2}$, $C_5 = -8.5375 \times 10^{-3}$, and $C_6 = 4.2074 \times 10^{-4}$. From hereon the proposed approximation by Arcoumanis et al. will be referred to as AR.

4.4.3 Proposed Approximation

After investigating the quality of the above approximations, as discussed in the subsequent sections, an exponential approximation for $F_{5/2}(H_{\sigma})$ is proposed that provides a better universal fit to the data of Table 4.1. The approximation is of the form,

$$F_{5/2}(H_{\sigma}) = \begin{cases} \exp\left(\frac{c_1 + c_2 H_{\sigma} + c_3 H_{\sigma}^2}{1 + c_4 H_{\sigma} + c_5 H_{\sigma}^2}\right) + c_6 & H_{\sigma} < 4.0 \\ 0 & H_{\sigma} \geq 4.0 \end{cases} \quad (4.9)$$

where the coefficients, c_i , are obtained via the least squares method as,

$$\begin{aligned} c_1 &= -0.4834813 \\ c_2 &= -1.6510542 \\ c_3 &= 0.0603879 \\ c_4 &= -0.1926383 \\ c_5 &= 0.0161564 \\ c_6 &= -3.6 \times 10^{-6} \end{aligned}$$

From here on the proposed approximation will be referred to as PR approximation.

4.5 Comparison of the Approximations

4.5.1 Quality of Fit

In order to assess the quality of the fit the residuals, the standard deviation of the error, and the standard and adjusted coefficients of determination are considered.

For a set of data $\mathbf{y} \in \mathbb{R}^{n_d}$, approximated by $\hat{\mathbf{y}}$, the residual $\boldsymbol{\varepsilon}$ is given by,

$$\boldsymbol{\varepsilon} = \mathbf{y} - \hat{\mathbf{y}} \quad (4.10)$$

The standard deviation of the error, $\hat{\sigma}$, is given by,

$$\hat{\sigma} = \sqrt{\frac{\boldsymbol{\varepsilon}^T \boldsymbol{\varepsilon}}{n_d - n_b}} \quad (4.11)$$

where n_d is the number of data values and n_b is the number of regression coefficients in the approximation function.

The coefficient of determination, R^2 , is given by,

$$R^2 = 1 - \frac{\boldsymbol{\varepsilon}^T \boldsymbol{\varepsilon}}{\sum_{i=1}^{n_d} (y_i - \bar{y})^2} \quad (4.12)$$

where \bar{y} is the arithmetic mean of the data values. However, the R^2 value increases as the number of regression coefficients increases. A better estimate can be obtained via the adjusted coefficient of determination, R_a^2 , which corrects for the number of regression coefficients,

$$R_a^2 = 1 - \frac{n_d - 1}{n_d - n_b} (1 - R^2) \quad (4.13)$$

Table 4.2 shows the statistics used to assess the quality of the approximations. In general a good approximation is expected to have an R_a^2 greater than 0.9 and a relatively low $\hat{\sigma}$. Consequently Table 4.2 suggests that all three approximations are good, with the AR and PR approximations prevailing with a perfect R_a^2 . Looking at the plots for the three approximations over the entire range of H_σ (Figure 4.2), the same thing is observed. This is a good example of how the R^2 and R_a^2 can be misleading. From the graph in Figure 4.2 the HU approximation is lacking only in the range $0.0 \leq H_\sigma \leq 1.0$, whereas the other two seem to perfectly satisfy the data. However, considering segmented ranges of H_σ (Figure 4.3), the real picture is revealed. The HU approximation clearly under-predicts $F_{5/2}(H_\sigma)$ in the whole range of H_σ being highly noticeable in the range of $H_\sigma \geq 2.0$.

The AR approximation performs better in the range of $H_\sigma \leq 3.0$, however it exhibits an oscillatory behaviour in the range of $3.0 \leq H_\sigma \leq 4.0$ and even predicts a negative value around $H_\sigma \approx 4.0$. The order of magnitude of $F_{5/2}(H_\sigma)$ can be considered to be very low so the effect of these fluctuations can be negligible. However, it should be noted that the load P , (4.3), is found by multiplying $F_{5/2}(H_\sigma)$ with the composite modulus of elasticity, E' , and a constant, K . Thus, the effect on the load can be noticeable and can lead to slow or even no convergence in the iterative solution of problems involving elastohydrodynamic analyses in the mixed lubrication regime utilizing such an approximation. Furthermore, the contact pressure cannot be negative.

The newly proposed exponential approximation, PR, though, exhibits an almost perfect fit to the data over the entire range of H_σ . It satisfies all the tabulated data, and asymptotically goes to zero at $H_\sigma = 4.0$.

The residuals of the three approximations with respect to the tabulated values of Greenwood and Tripp (Table 4.1) are plotted in Figure 4.4. These again show that the PR approximation has the best fit, as the order of magnitude of its residuals is the lowest. The AR approximation has very low residuals as well. However, these residuals do not capture the oscillatory behaviour in the range of $3.0 \leq H_\sigma \leq 4.0$.

Table 4.2: Statistics for the three approximations

	HU	AR	PA
$\hat{\sigma}$	2.609×10^{-2}	1.580×10^{-4}	1.213×10^{-5}
R^2	0.986	1.000	1.000
R_a^2	0.984	1.000	1.000

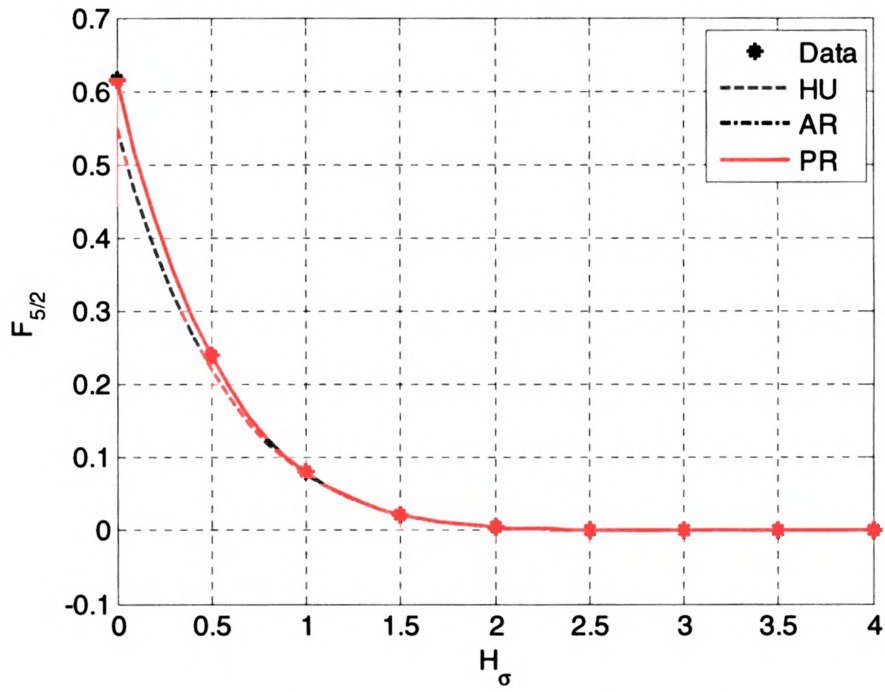


Figure 4.2: Approximations of (4.6)

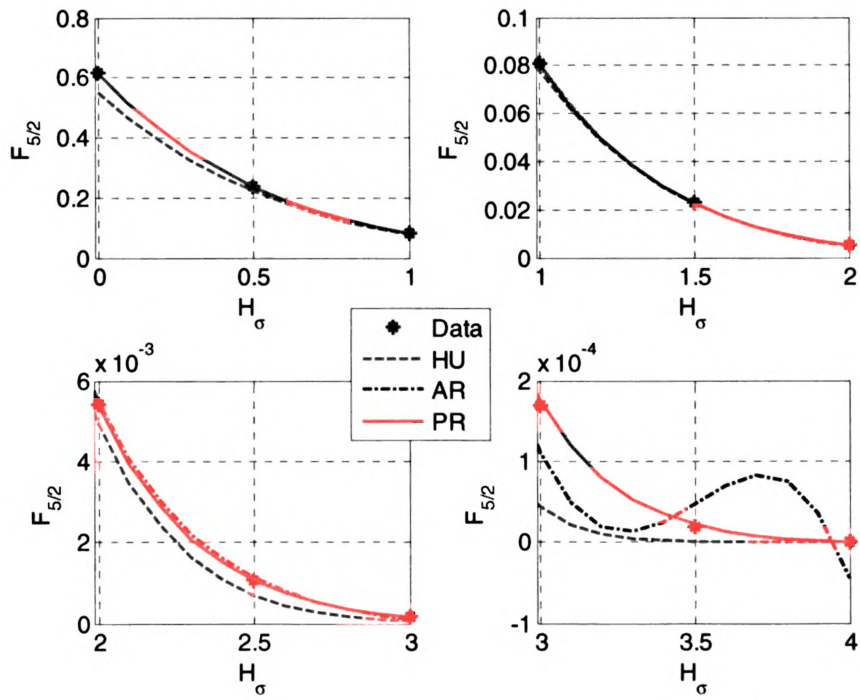


Figure 4.3: Approximations of (4.6) in segments

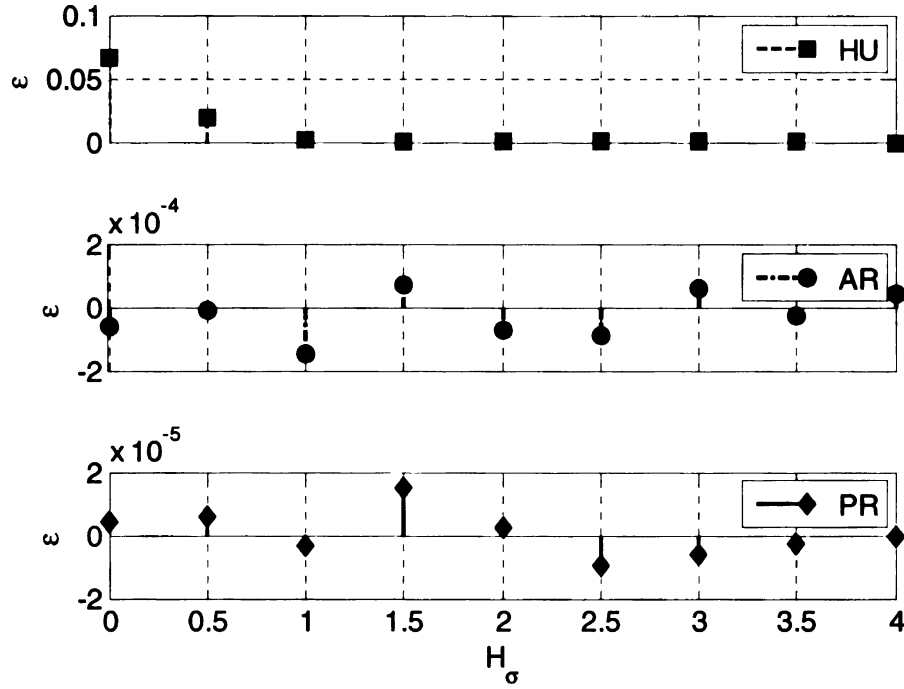


Figure 4.4: Residuals of approximations of (4.6)

4.5.2 Computation Time

When performing elastohydrodynamic analyses, the contact model needs to be evaluated several times, since the problems are nonlinear and are solved iteratively over a meshed domain. For example, in a piston dynamics analysis where the load developed at the piston skirt surface due to contact with the cylinder bore needs to be calculated, the contact model can be evaluated up to and even exceeding 100,000 times. These evaluations can lead to high computation times. Table 4.3 shows a comparison of the computation times for 10 000 evaluations of $F_{5/2}(H_\sigma)$ via the three approximations and direct numerical integration of (4.6). These evaluations were performed in MATLAB running on an Intel Core 2 Duo 1.66 GHz CPU. These results reemphasize the need of an

approximation for $F_{5/2}(H_\sigma)$. It is obvious that direct integration of (4.6) can be very expensive. The three approximations are in the same range, less than a tenth of a second per 10 000 evaluations. The new proposed approximation lies in between the ones by Hu et al. and Arcoumanis et al. In any case, considering its quality of fit described above, this becomes the approximation of choice.

Table 4.3: Computation times

	CPU time per 10 000 evaluations of $F_{5/2}(H_\sigma)$ [s]
HU	0.03125
AR	0.06250
PR	0.04688
Num. Integr.	111.96875

CHAPTER 5. PISTON DYNAMICS SIMULATIONS

5.1 New Generation Piston: A Comparison between 2-D and 3-D Numerical Models

In this section, PIFEAD is used to model a new generation piston with asymmetric thrust sides. The results predicted by the conventional 2-D piston dynamics model (motion only in the thrust plane) and the new 3-D piston dynamics model that considers translation along the wrist-pin described in Chapter 3 are compared. Here the second land interactions with the cylinder bore are also considered. It is assumed that pressures due to lubrication or scuffing have no effect on the second land deformation; however, it deforms due to combustive, inertial and thermal loads. Only the second land was chosen to be modeled as it is, traditionally, the land with the larger diameter. Thus it is expected to have the most dominant interactions with the cylinder bore in the case of insufficient heat dissipation. Of course if this happens it immediately implies that the piston design needs further development.

5.1.1 Numerical Experiments

In this section theoretical results are presented for a gasoline engine under simulated conditions. The engine geometry is based on the optical motored engine used in [49].

The piston was designed by the author based on the dimensions of the engine's original piston. The specific piston features uneven thrust side areas, 2025.03 mm² for

the major thrust side and 1775.25 mm² for the minor thrust side. Figure 5.1 shows the meshed piston geometry and Figure 5.2 shows the skirt profile of the piston.

The engine was modeled in Ricardo WAVE to obtain combustive pressure traces. Figure 5.3 shows the pressure trace at 1000 RPM, the engine speed used for the simulation results presented in this paper. The beginning of the intake stroke is at zero crank angle degrees.

The cylinder bore temperature and deformation distributions are shown in Figure 5.4 and Figure 5.5. Both of these are asymmetric. The temperature between 0 and 180 degrees is higher to simulate the effect of adjacent cylinders. The temperature drops axially along the cylinder bore. The cylinder bore deformation is higher on the major thrust side as loads are higher on that side. At the top of the cylinder the deformation is more elliptical and becomes more circular and decreases in magnitude moving down the cylinder bore.

Table 5.1 summarizes the engine and piston geometrical and material properties.

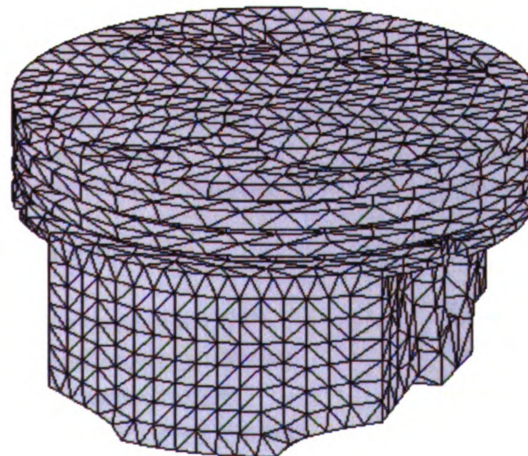


Figure 5.1: Piston mesh

Table 5.1: Engine and piston properties

Geometric properties	
Bore diameter	90.12 mm
Stroke	90.60 mm
Piston diameter	90.077 mm
Piston height	50.00 mm
Skirt length	33.02 mm
Wrist-pin offset	-0.40 mm
Wrist-pin diameter	15.00 mm
Second land diameter	90.05 mm
Second land height	3.35 mm
Cylinder bank angle	0.0 deg.
Connecting rod length	169.00 mm
Piston ovality	-6.00 μm
Major thrust side area	2025.03 mm ²
Minor thrust side area	1775.25 mm ²
Masses	
Piston mass	296.32 g
Pin mass	90.96 g
Connecting rod mass	755.14 g
Material and surface properties	
Piston modulus of elasticity	69 GPa
Cylinder modulus of elasticity	100 GPa
Piston Poisson's ratio	0.33
Cylinder Poisson's ratio	0.21
Piston roughness	0.23 μm
Cylinder roughness	0.052 μm
Skirt/Land asperity radius	1.48E+11 m ⁻²
Skirt/Land asperity density	0.39 μm
Piston/cylinder coefficient of friction	0.15
Skirt/Land hardness	115 MPa
Skirt/Land wear coefficient	2.0E-7
Oil properties	
Dynamic viscosity at 40 °C	102.40 cP
Dynamic viscosity at 100 °C	16.3 cP
Oil temperature in sump	80 °C
Oil dynamic viscosity in sump	30.1 cP

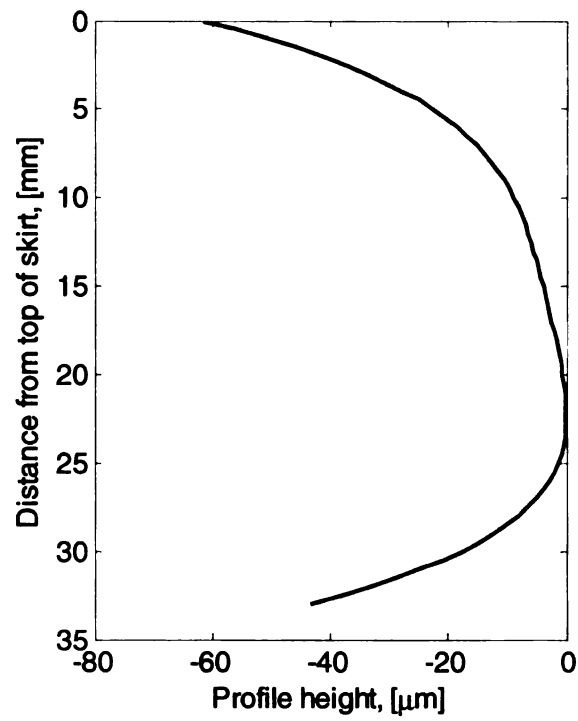


Figure 5.2: Skirt profile

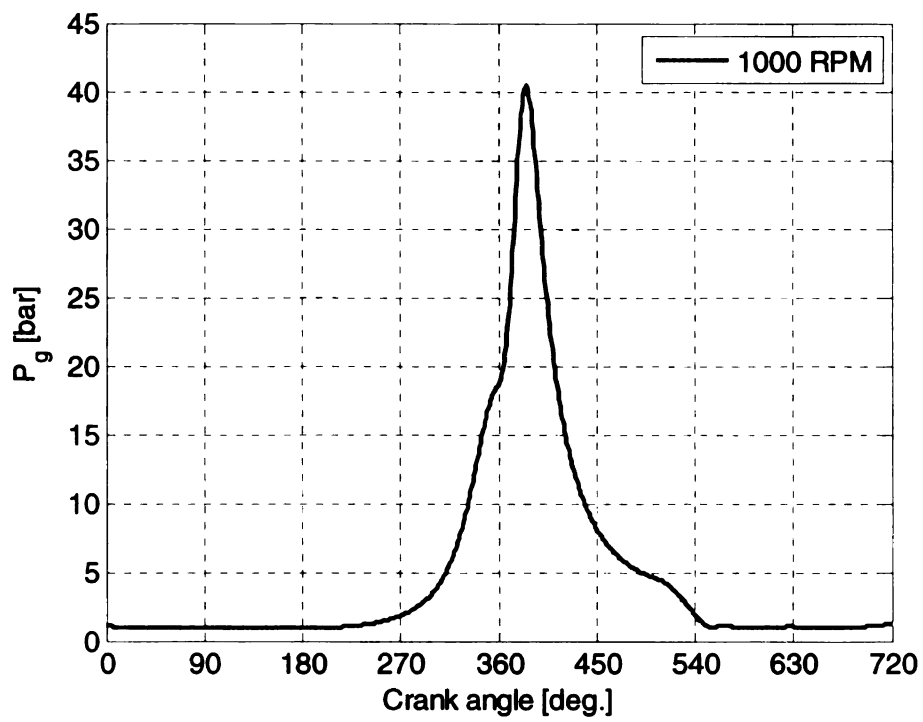


Figure 5.3: Pressure traces

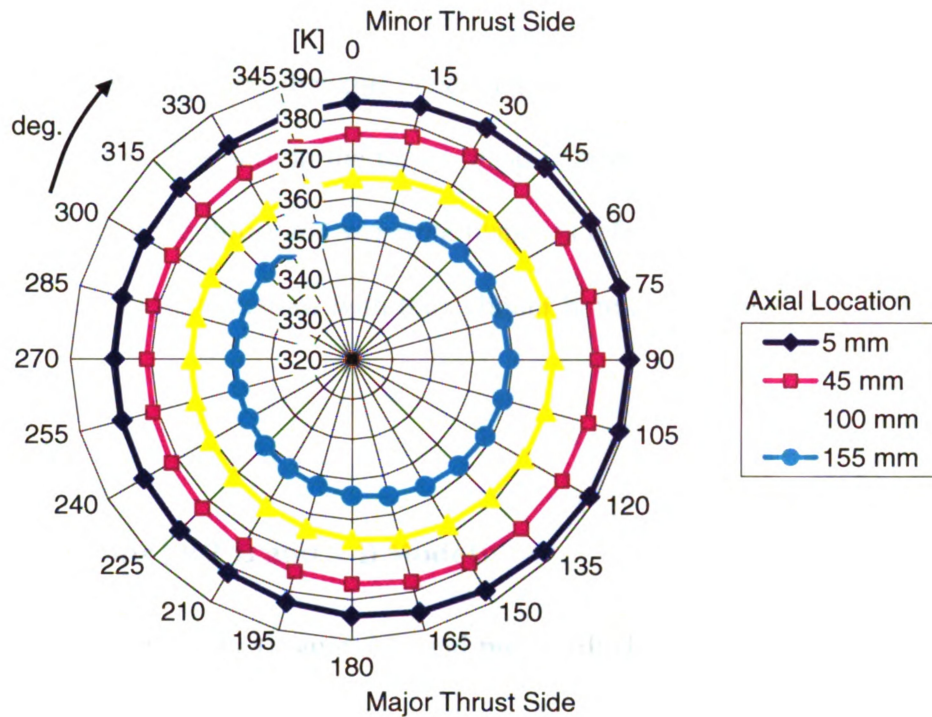


Figure 5.4: Cylinder bore temperature

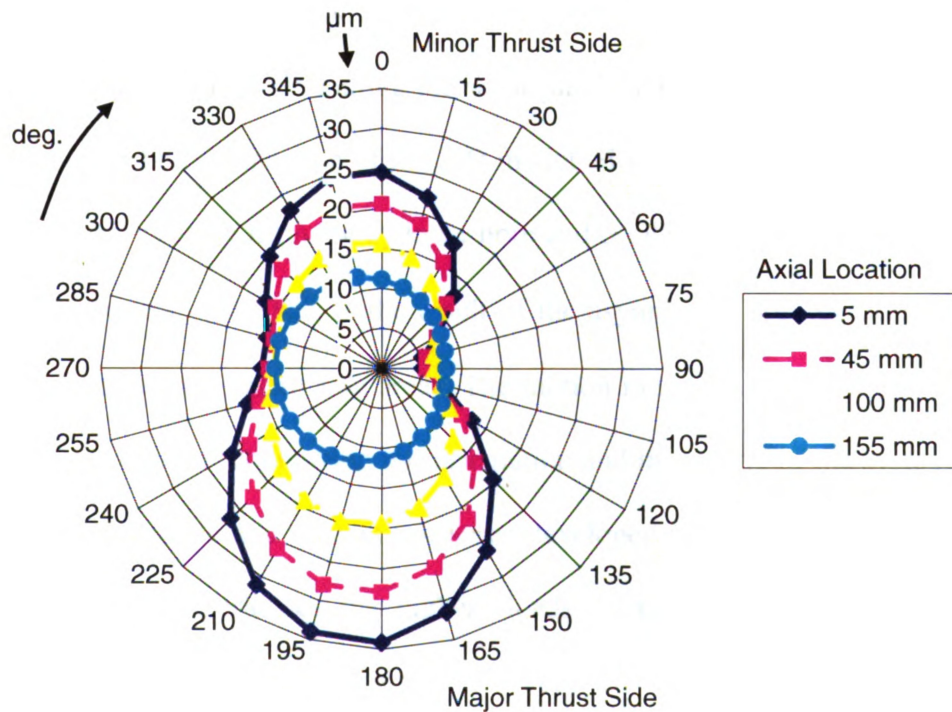


Figure 5.5: Cylinder bore deformation

In the following sections a comparison is made between simulation results obtained via different piston dynamic modeling approaches. The model that considers piston secondary motion only in the thrust plane is referred to as 2-D, and the one that considers motion in the thrust and wrist-pin planes is referred to as 3-D. The models that consider second land interactions with the cylinder bore are referred to as 2-D/Land and 3-D/Land.

5.1.2 Predictions by 2-D and 3-D Models

The pin eccentricity (Figure 5.6) and piston tilt (Figure 5.7) are not significantly different between the two models. The total side force on the piston in the X_p - Y_p plane (Figure 5.8) also shows almost no difference between the two models. This is expected, as motion and side loads in this plane are mainly dominated by the combustion gas pressure, connecting rod orientation and the inertia of the system.

Figure 5.9 shows the motion along the wrist-pin. The piston is constrained at the center of the cylinder bore in the case of the 2-D model. However, in the case of the 3-D model the piston moves away from the cylinder bore and oscillates in that position with a mean value of close to $-3\text{ }\mu\text{m}$. This is the result of the asymmetric bore deformation in conjunction with the uneven thrust side areas. The motion in this plane is not dominated by combustion gas pressure, connecting rod orientation and the inertia of the system, but rather by the hydrodynamic and contact pressures developed on the skirt. Close to and after firing the piston experiences the highest loads, consequently the highest skirt deformation, thus the motion becomes noisy as it is very sensitive to skirt pressures.

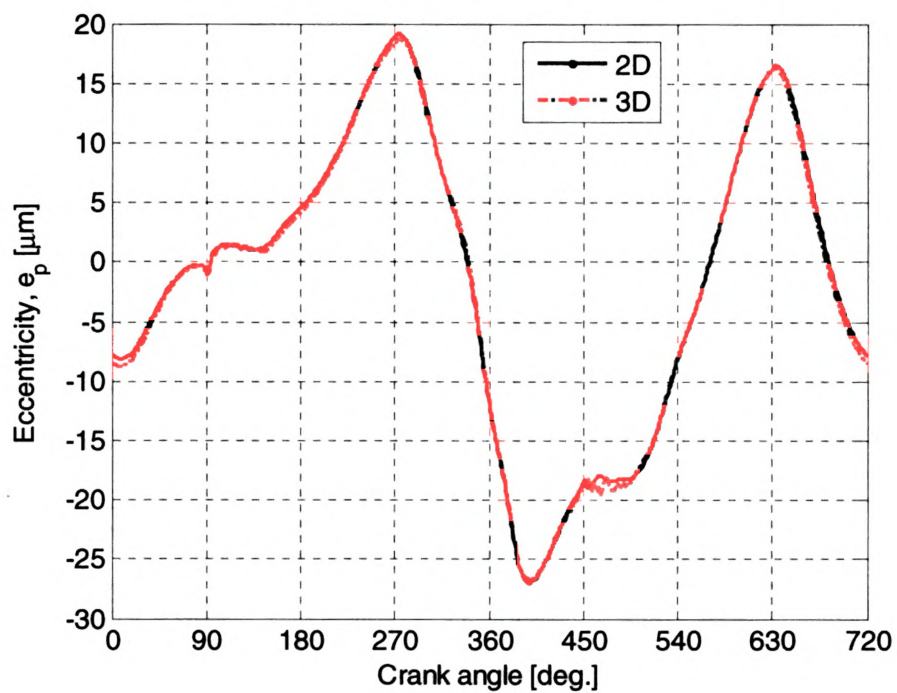


Figure 5.6: Eccentricity at wrist-pin level, X_p - Y_p plane

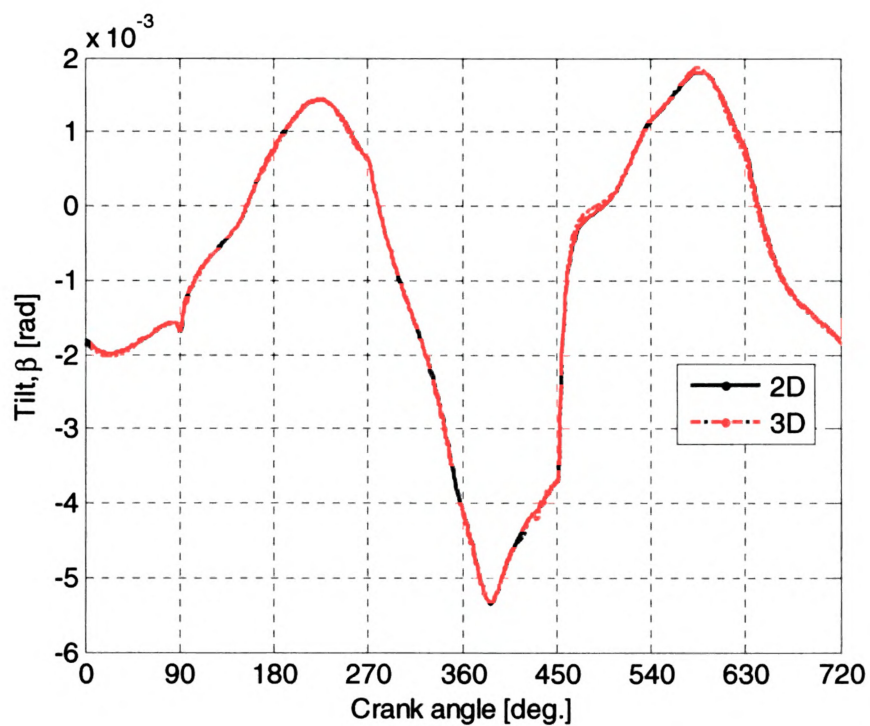


Figure 5.7: Piston tilt

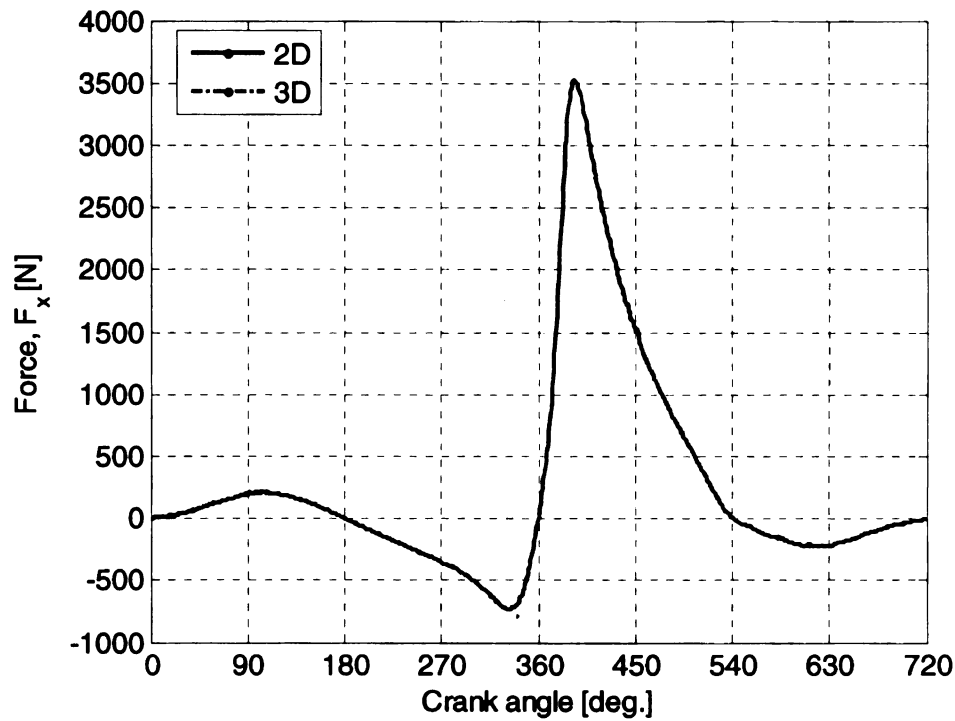


Figure 5.8: Total force in the X_p - Y_p plane

This translation along the wrist-pin leads to a difference in the prediction of skirt wear (Figure 5.10 and Figure 5.11). The 2-D model overall predicts higher wear on the skirt. Also the predicted location of wear is different. On the minor thrust side, the 2-D model predicts wear at the bottom right of the skirt only, whereas the 3-D model predicts wear at the bottom left and right of the skirt. On the major thrust side, the 2-D model predicts wear on the top left of the skirt. The 3-D model predicts this wear to be occurring about 10 degrees closer to the center of the skirt. Consequently the 3-D model becomes important when trying to predict piston wear, both in magnitude and location.

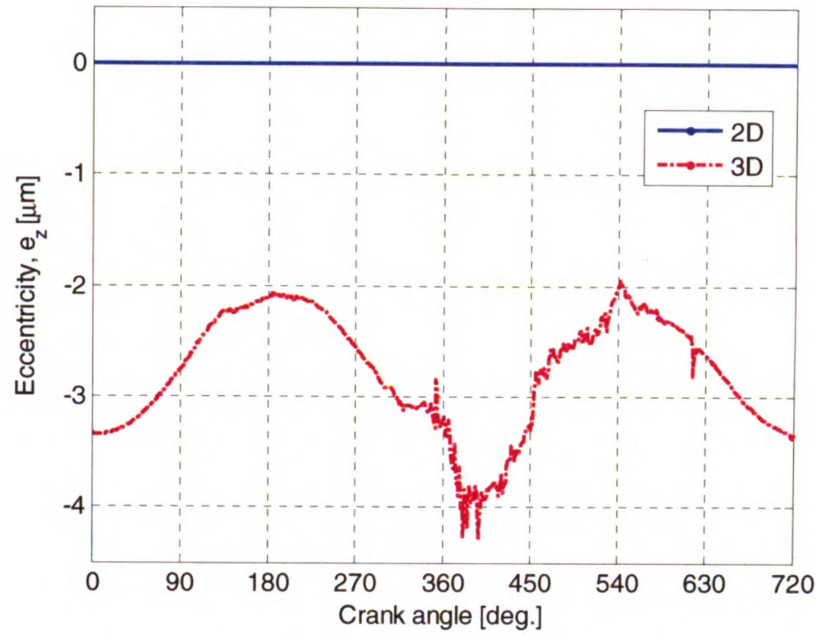


Figure 5.9: Eccentricity along the wrist-pin

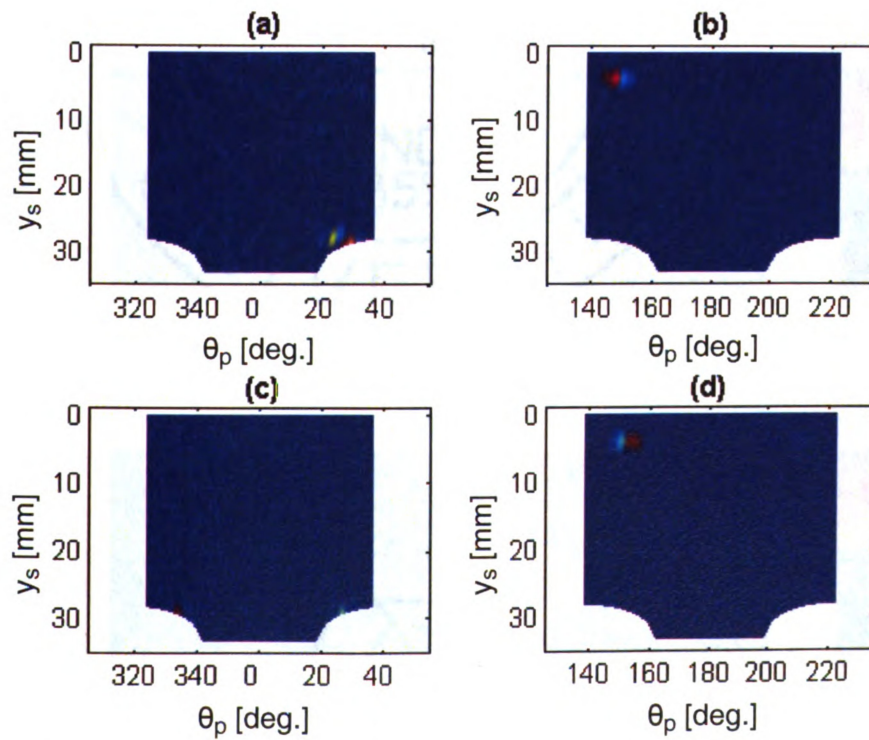


Figure 5.10: Skirt wear (a) minor thrust 2-D model, (b) major thrust 2-D model, (c) minor thrust 3-D model, (d) major thrust 3-D model

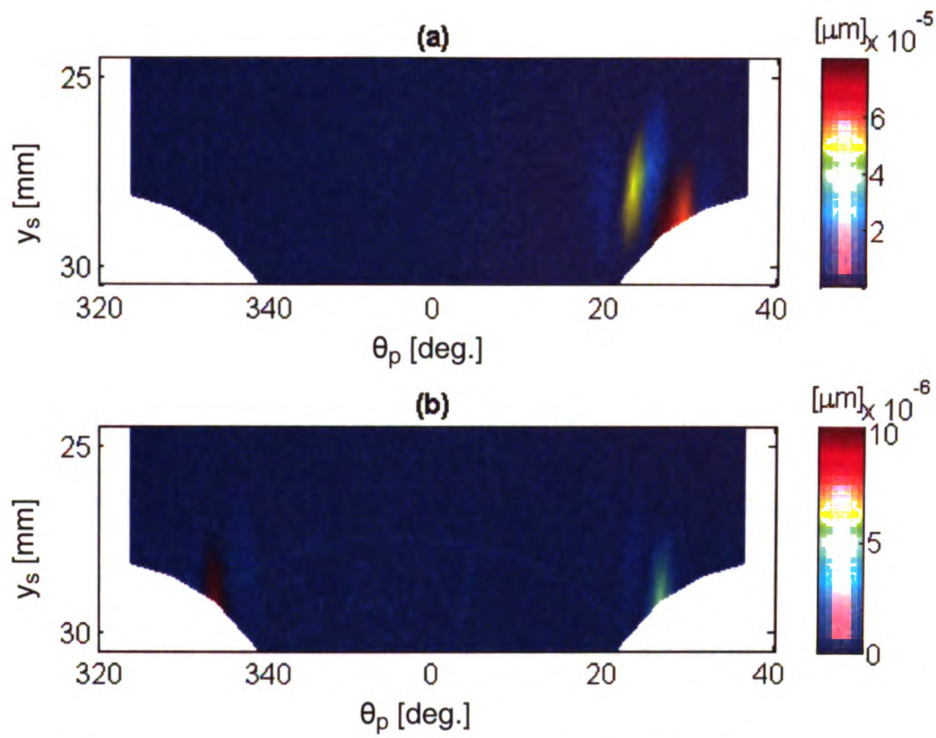


Figure 5.11: Skirt wear on minor thrust side (a) 2-D model, (b) 3-D model

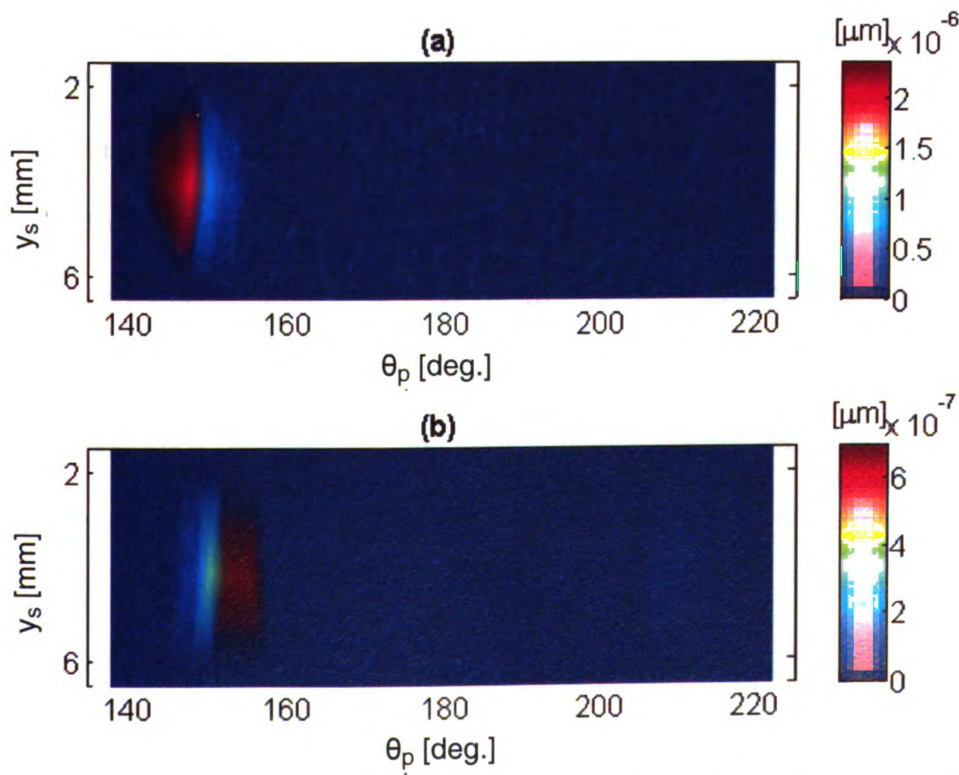


Figure 5.12: Skirt wear on major thrust side (a) 2-D model, (b) 3-D model

5.1.3 2-D/Land and 3-D/Land Models, Fully Flooded Land Lubrication

When considering the second land interactions with the cylinder bore, the piston motion changes in both X_p - Y_p and Y_p - Z_p planes (Figure 5.13 to Figure 5.14) compared to the motion predicted by the 2-D and 3-D models (Figure 5.6, Figure 5.7 and Figure 5.9). The piston tilt in this case becomes noticeably smaller and so does the eccentricity at the wrist-pin level in the X_p - Y_p plane. This is because interactions with the cylinder bore extend all the way to the second land, compared to the 2-D and 3-D models that consider interactions with the cylinder bore only at the skirt. These interactions at the second land level cause the oscillations along the wrist-pin to become smaller, with a mean value close to 3.5 μm . Also, the noise in the predicted motion disappears (compared to the one predicted by the 3-D model) since the second land deformation is assumed to be invariant to the hydrodynamic and contact pressures and the oil film between the land and the cylinder bore provides a lot of damping.

Now, considering the wear on the second land the results are very different (Figure 5.16). Both models predict about the same order of magnitude of wear. However, the 2-D/Land model predicts the wear to occur from about 0 deg. to 180 deg., whereas the 3-D/Land model predicts the wear to occur around the land's circumference. The maximum wear occurs around 90 deg., and more wear is predicted above the minor thrust side than above the major thrust side. This agrees with cylinder bore deformation (Figure 5.5).

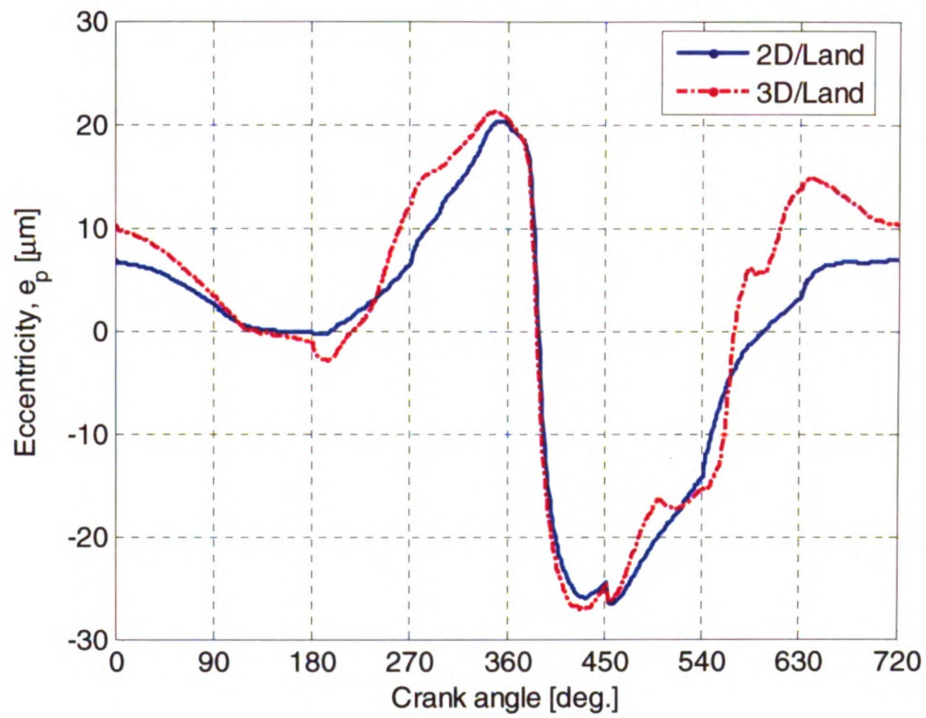


Figure 5.13: Eccentricity at wrist-pin level, X_p - Y_p plane

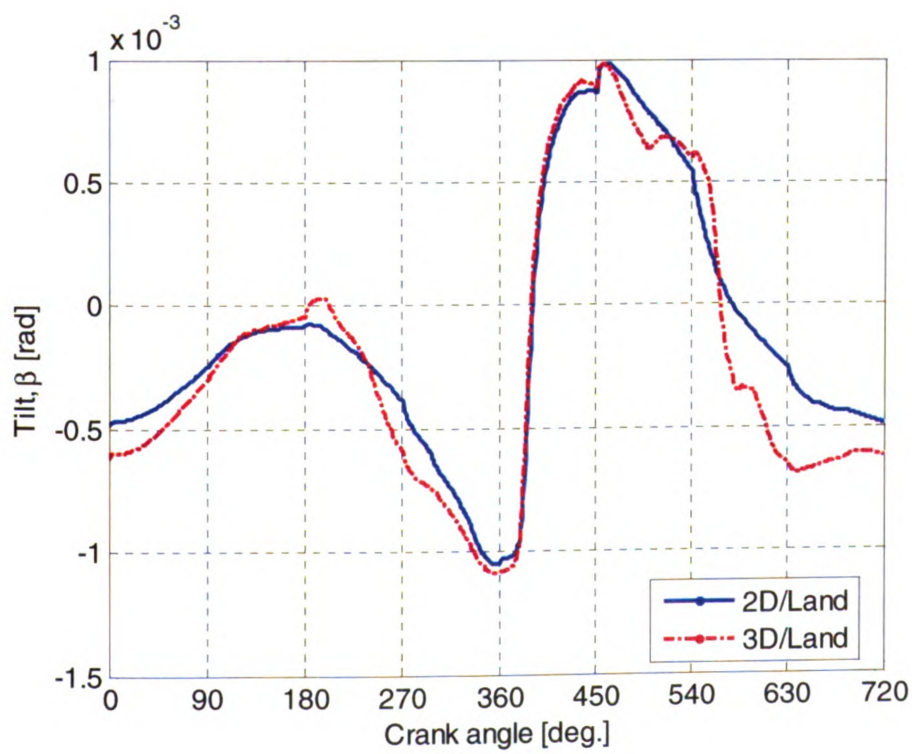


Figure 5.14: Piston tilt

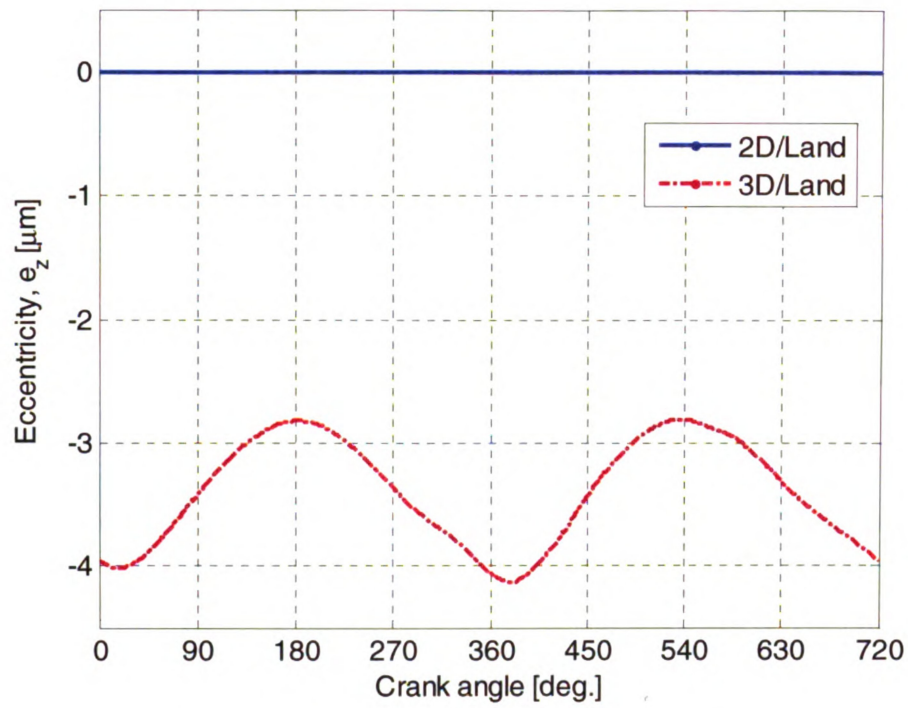


Figure 5.15: Eccentricity along the wrist-pin

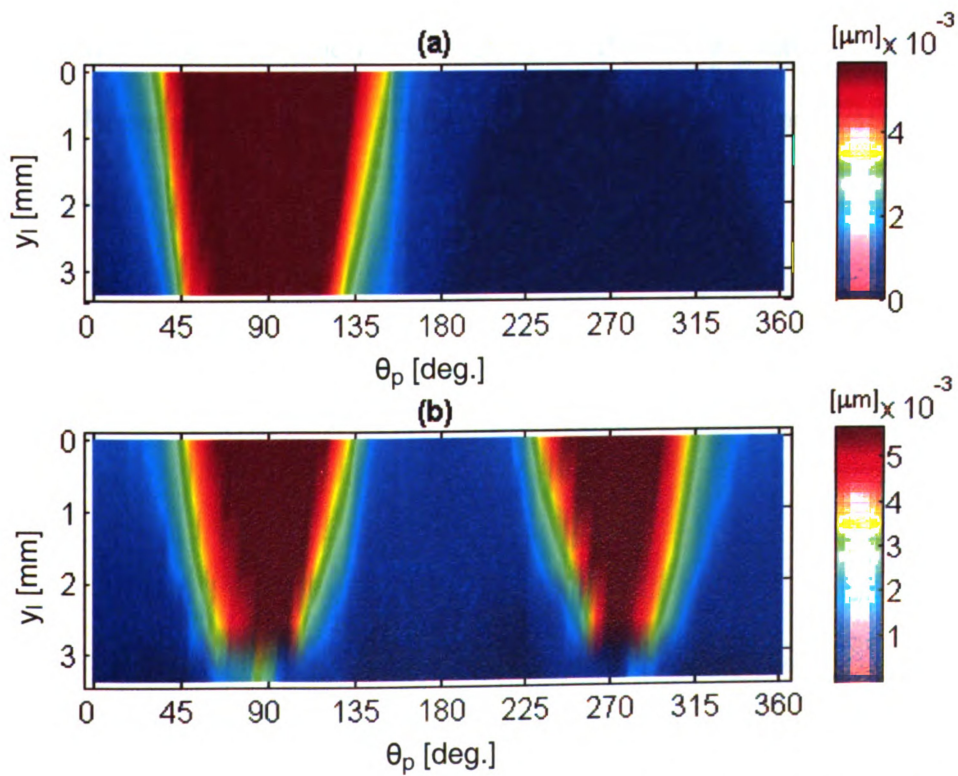


Figure 5.16: Second land wear predicted by (a) 2-D\Land and (b) 3-D\Land models

5.1.4 Dry and Fully Flooded Second Land Conditions

The assumption whether the second land lubrication conditions are either dry or fully flooded affects piston motion and as a result wear prediction.

The motion in the X_p - Y_p plane (Figure 5.17, Figure 5.18) is noticeably affected during the intake, compression and exhaust strokes. During the expansion stroke where the combustion pressure is very high, it dominates the motion; thus the effect of dry or fully flooded lubrication at the land is minimal.

The amplitudes of the motion along the wrist-pin (Figure 5.19) increase, with the piston oscillating at about $-3.6 \mu\text{m}$. In the case of dry lubrication conditions at the second land (no damping from the oil film), the motion along the wrist-pin again becomes noisy close to and after firing.

As far as the second land wear is concerned, the order of magnitude and location of the maximum is about the same for both dry and fully flooded lubrication conditions (Figure 5.20). However, under dry conditions more land wear is predicted above the major thrust side.

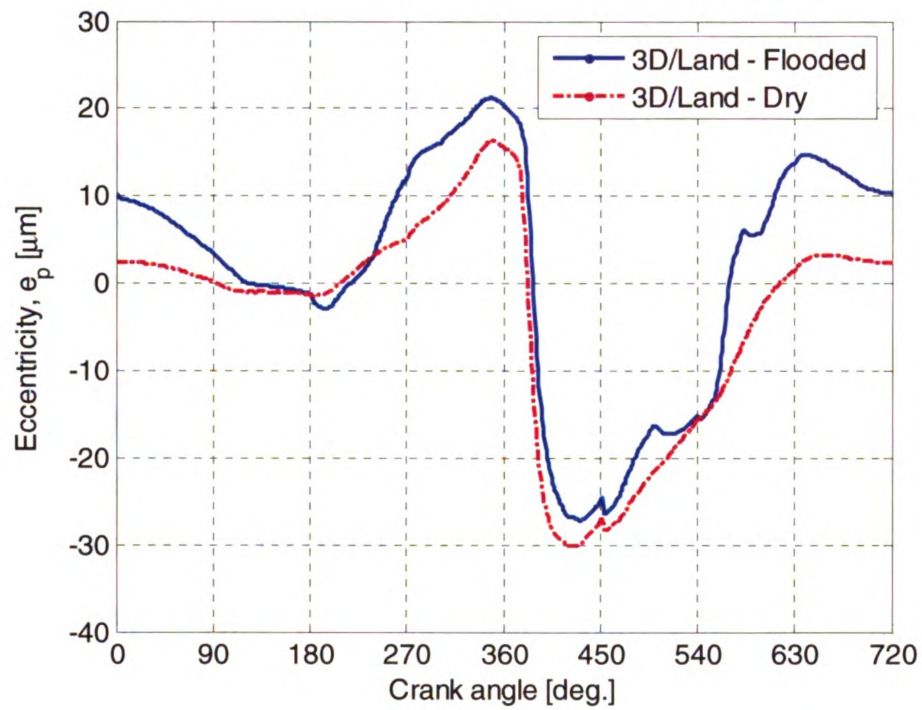


Figure 5.17: Eccentricity at wrist-pin level, X_p - Y_p plane

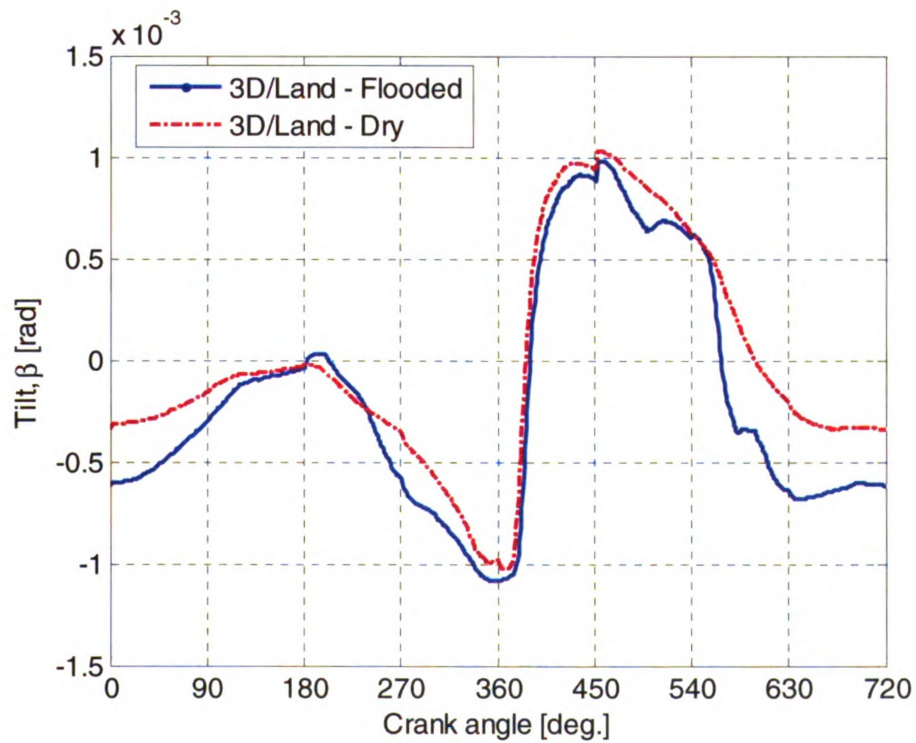


Figure 5.18: Piston tilt

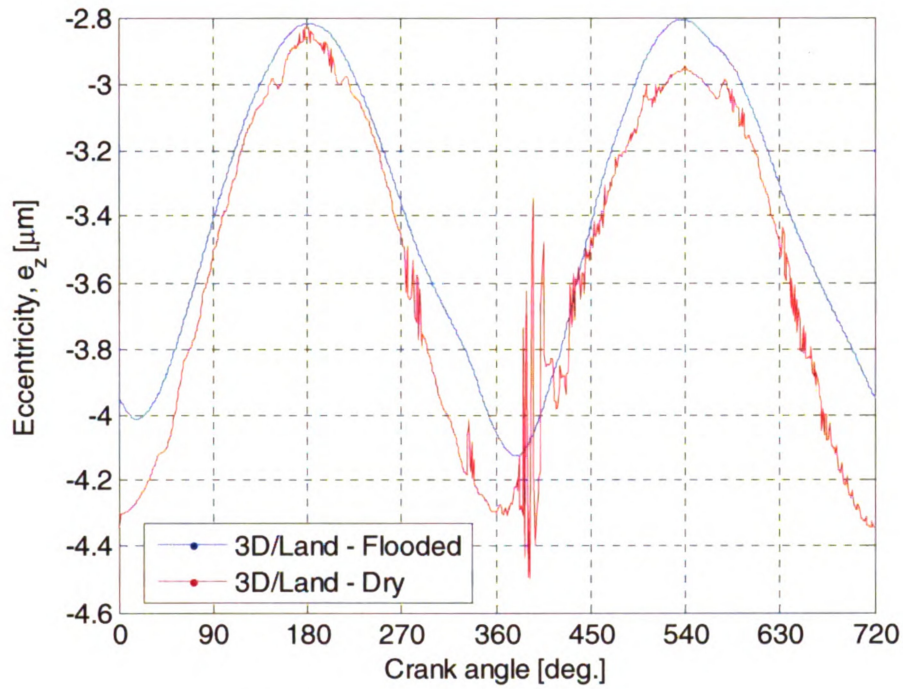


Figure 5.19: Eccentricity along the wrist-pin

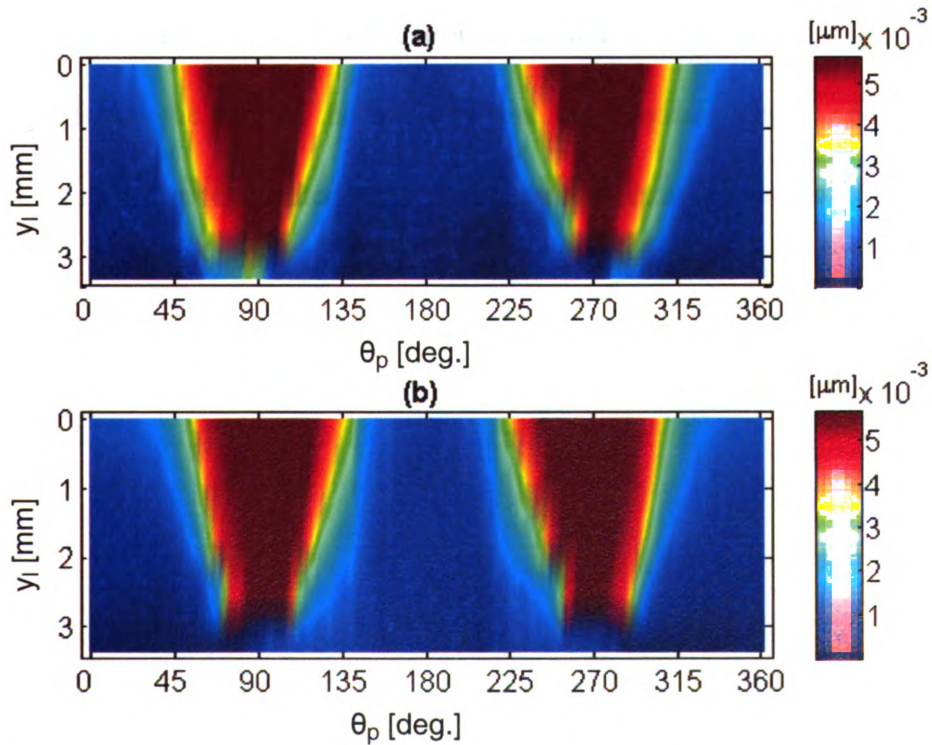


Figure 5.20: Second land wear predicted by (a) 3-D\Land – fully flooded lubrication and (b) 3-D\Land – dry lubrication models

5.1.5 Analytical Results

As a first step in validating the results obtained via the 3-D/Land model, a comparison is made between the predicted total force in the X_p - Y_p plane and its analytical evaluation from the dynamic analysis of the slider-crank mechanism. Given a piston of mass m_p , accelerating at a_p , and loaded with a combustion force F_g , the total side force on the slider can be calculated via

$$F_x = (F_g - m_p a_p) \tan(-\varphi) \quad (5.1)$$

where φ is the connecting rod orientation angle. It should be noted that this formulation does not consider the connecting rod inertia and frictional forces between the piston and the cylinder bore.

Figure 5.21 shows the hydrodynamic and contact forces as predicted by the 3-D/Land model with fully flooded lubrication conditions at the second land. F_x is the predicted total force (the sum of the hydrodynamic and contact forces) and F_x (slider-crank) is the total force as calculated by (5.1). The two are closely correlated.

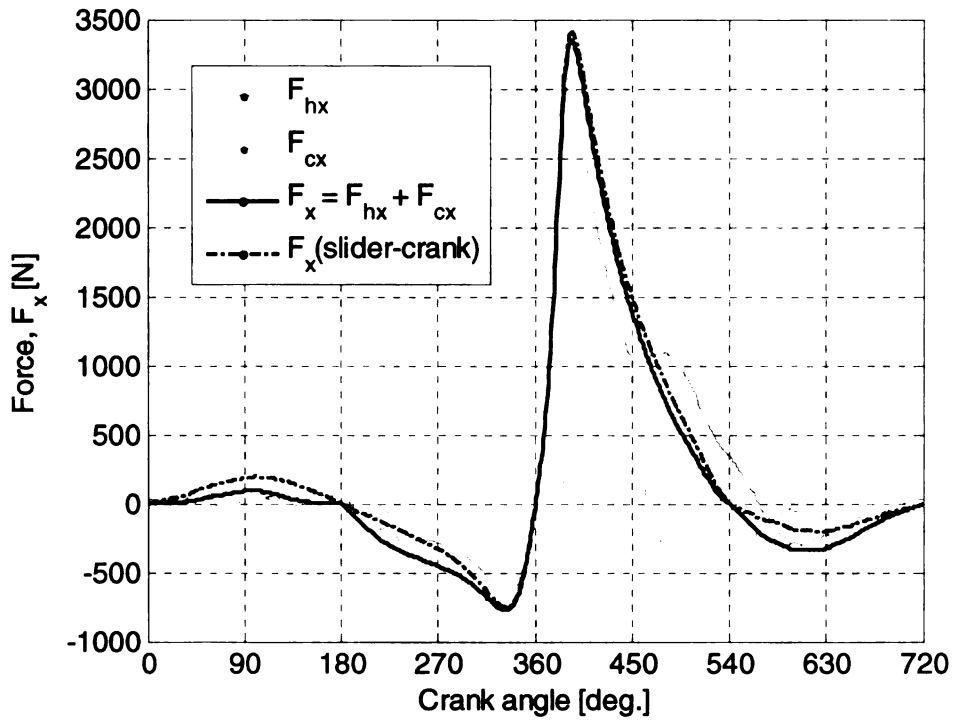


Figure 5.21: Forces in the X_p - Y_p plane

5.1.6 Remarks

It is evident from the results that the motion along the wrist-pin becomes important when considering such new generation pistons, especially with cylinder bore deformation being asymmetric. Despite the fact that piston eccentricity and piston tilt in the X_p - Y_p plane are almost invariant to the modeling approach (2-D or 3-D model), the wear prediction is greatly dependent (magnitude and location) on the computational model used.

The second land interactions with the cylinder bore have also been shown to be important in determining the magnitudes of the transverse dynamics. Also the second land modeling is crucial if one wants to predict wear on the land, a phenomenon that has

been observed to occur on pistons suffering from insufficient cooling. This problem becomes more evident with the new generation pistons that utilize very thin rings to decrease friction and inertia losses but at the same time handicap the cooling capabilities of the ring-pack.

The debate amongst engineers is what lubrication conditions to use both at the skirt and land interfaces with the cylinder bore. In this work the skirt was assumed to be fully flooded. The second land was modeled with both fully flooded and dry conditions. Both of these conditions predict similar piston dynamics during the expansion stroke only, where combustion pressure dominates. Also the piston wear predictions are different. This suggests that knowledge of oil availability at the interface is required for accurate predictions.

5.2 High-speed Piston

In this section a high-speed racing piston is considered. The present piston was failing during operation. A crack would appear at the edge of the valve pocket and would propagate towards the top ring groove. This was detrimental to the piston operation. Under some conditions piston material would break off, resulting in catastrophic engine failure. The piston did not show any scuffing marks in that area that would suggest any impacts with the cylinder liner. Table 5.2 shows the key dimensions and properties for the high-speed piston.

5.2.1 Cyclic Stress Recovery

The piston was modeled in PIFEAD and the cyclic stresses were recovered. Figure 5.22 shows the in-cylinder pressure for the two operating conditions of interest, 7500 RPM and 9000 RPM. The peak pressure at 9000 RPM is approximately 10 bar lower than at 7500 RPM. Peak pressure at 7500 RPM occurs at 369 degrees and at 9000 RPM at 373 degrees.

Figure 5.23 shows the piston axial acceleration at the two engine speeds. The acceleration at TDC at 9000 RPM is 14140 ms^{-2} higher than at 7500 RPM. This will induce a difference in peak inertial load of 6052 N, given the mass of the piston is about 428 grams.

Table 5.2: High speed piston dimensions and properties

Geometric properties	
Bore diameter	~106.25 mm
Stroke	~82.50 mm
Piston diameter	~106.06 mm
Piston height	~45.90 mm
Skirt length	~31.30 mm
Wrist-pin offset (x-coord.)	0.00 mm
Wrist-pin y-coord.	~29.90 mm
Wrist-pin diameter	~19.50 mm
Cylinder bank angle	45.0 deg.
Connecting rod length	~157.00 mm
Center of mass, x-coord.	~0.20 mm
Center of mass, y-coord.	~16.2 mm
Masses	
Piston mass	~428.0 g
Pin mass	~80.0 g
Connecting rod mass	~530.0 g
Material and surface properties	
Piston modulus of elasticity	~81 GPa
Cylinder modulus of elasticity	100 GPa
Piston Poisson's ratio	0.33
Cylinder Poisson's ratio	0.21
Piston roughness	0.23 μm
Cylinder roughness	0.052 μm
Skirt asperity density	$1.48\text{E}+11 \text{ m}^{-2}$
Skirt asperity radius	0.39 μm
Piston/cylinder coefficient of friction	0.15
Skirt hardness	162 MPa
Skirt wear coefficient	$2.0\text{E}-7$
Oil properties	
Dynamic viscosity at 40 °C	55.9 cP
Dynamic viscosity at 120 °C	5.4 cP
Oil temperature in sump	80 °C
Oil dynamic viscosity in sump	13.5 cP

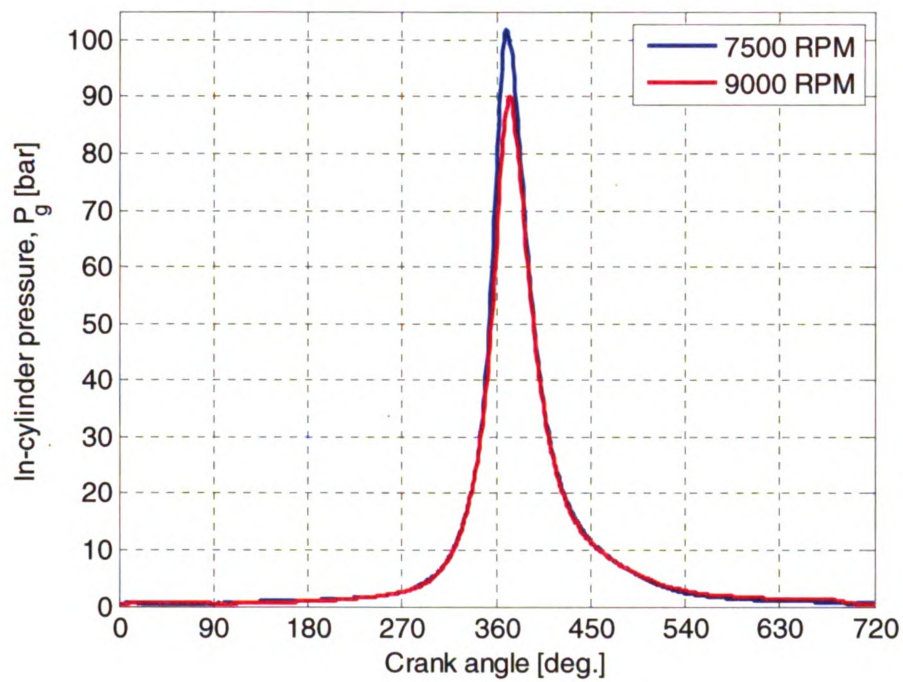


Figure 5.22: In-cylinder pressure

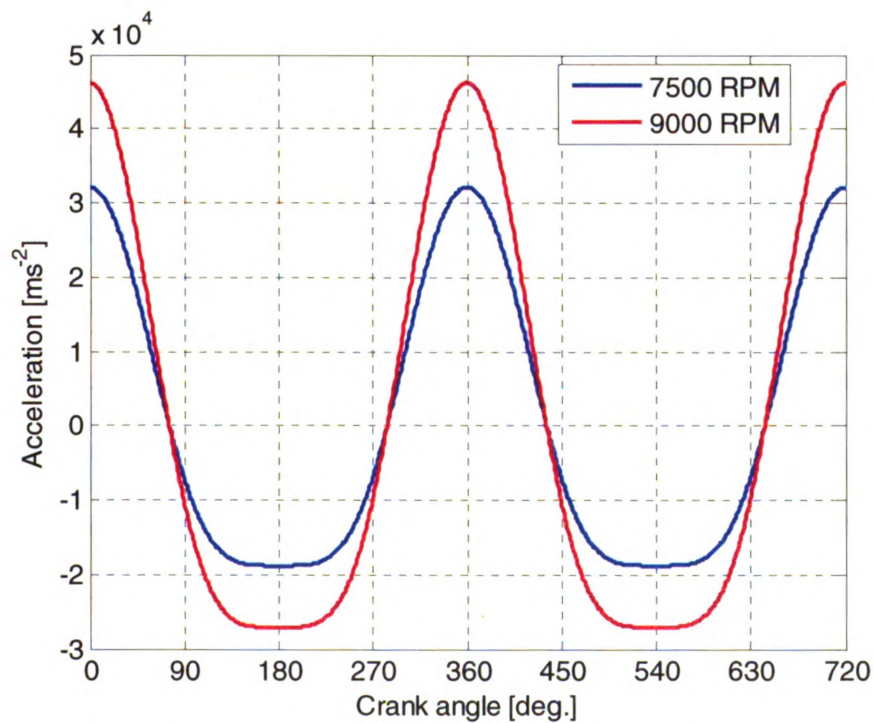


Figure 5.23: Piston axial acceleration

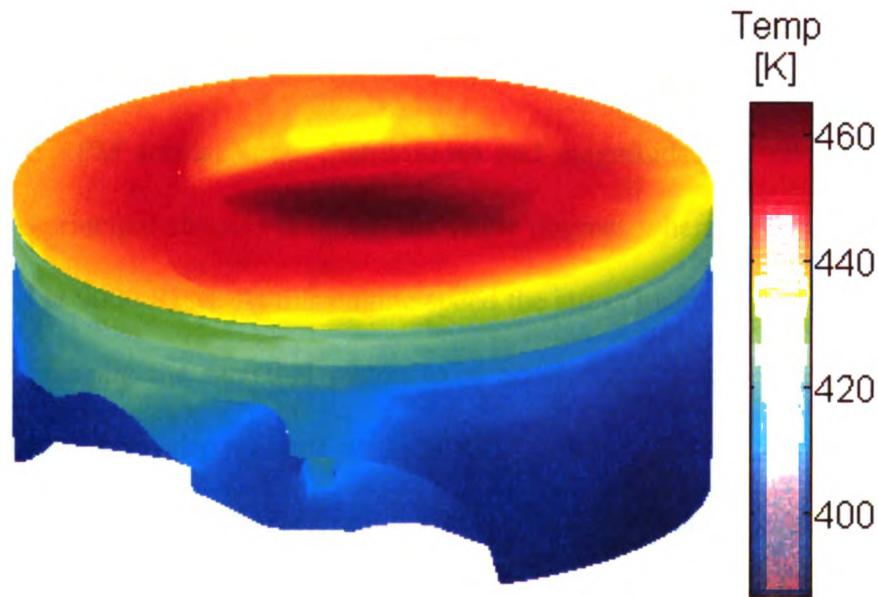


Figure 5.24: Piston temperature distribution

Figure 5.24 shows the predicted temperature distribution. It was assumed to be the same at both engine speeds. The high temperature concentration appears at the center of the crown away from the valve pocket edge where the crack would form. This suggests that high thermal loading might not be the reason for piston failure.

The stresses on the piston are recovered over the entire cycle. Here the principal stresses due to thermal, inertial and combusive loading are shown (Figure 5.25 to Figure 5.29). At the beginning of the intake stroke where inertia is high and in-cylinder pressure is low, the piston shows some stress concentration at the edge of the valve pocket (Figure 5.25). At the middle of the compression stroke where inertia is low and pressure still relatively low, the principal stresses are low (Figure 5.26) compared to the stresses at the beginning of the intake stroke. Similar stress distribution is observed at the middle of the expansion stroke (Figure 5.28). At 369 crank angle degrees where the peak in-cylinder pressure occurs at 7500 RPM and coincides with high acceleration, a high stress

concentration of about 150 MPa is observed at the valve pocket edge (Figure 5.27) for the first principal stress.

At 9000 RPM similar stress distributions and magnitudes are observed. Figure 5.29 shows the principal stresses at 373 crank angle degrees where the peak in-cylinder pressure occurs at 9000 RPM. At this engine speed the stress magnitudes are comparable to 7500 RPM, despite the fact that piston axial acceleration is much higher. This is because the peak in-cylinder pressure at 9000 RPM is lower than at 7500 RPM. Thus, when the contributions of axial acceleration and in-cylinder pressure to stress generation at each engine speed are combined, they balance.

A closer look at Figure 5.27 and Figure 5.29 shows that the distribution of high stress concentration at the valve pocket edge at 7500 RPM is slightly bigger. This suggests that in-cylinder pressure dominates stress generation rather than acceleration.

To further understand the mechanisms of failure, the 3-D von Mises yield criterion [68] is utilized. Figure 5.30 and Figure 5.31 show the von Mises yield criterion applied to nodes lying up to 14 mm below the top of the crown. All the nodal stresses lie within the 3-D cylinder satisfying the von Mises criterion.

Consequently, the above observations lead to the conclusion that crack initiation and eventually failure at the edge of the valve pocket was not due to high stress loading. Rather, it was a result of cyclic loading causing fatigue in that region and eventually crack initiation.

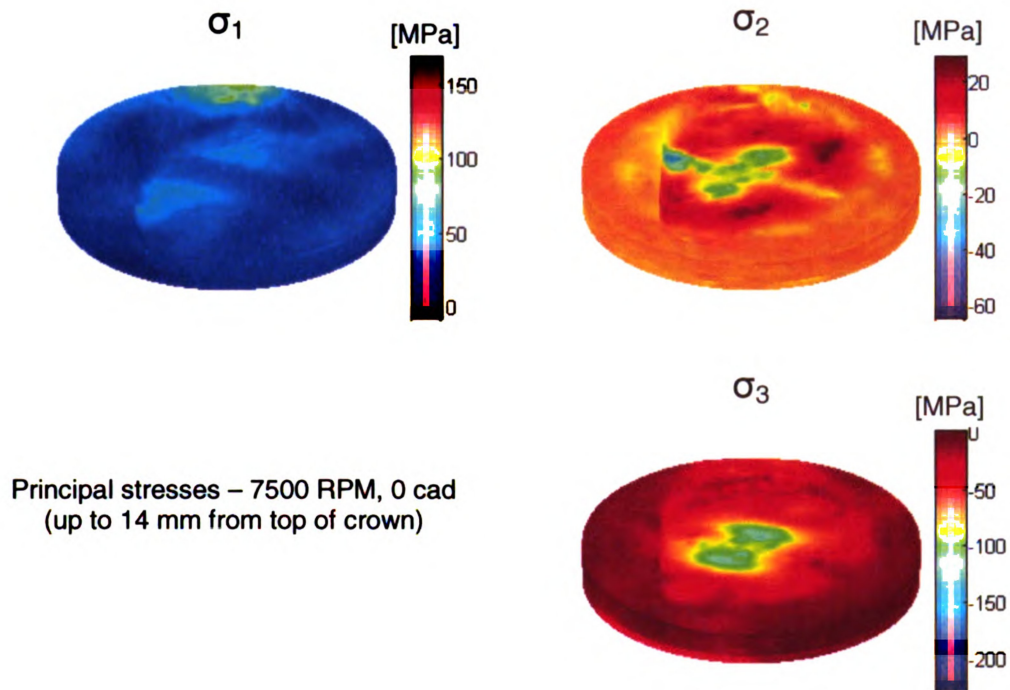


Figure 5.25: Principal stresses at 7500 RPM, 0 cad

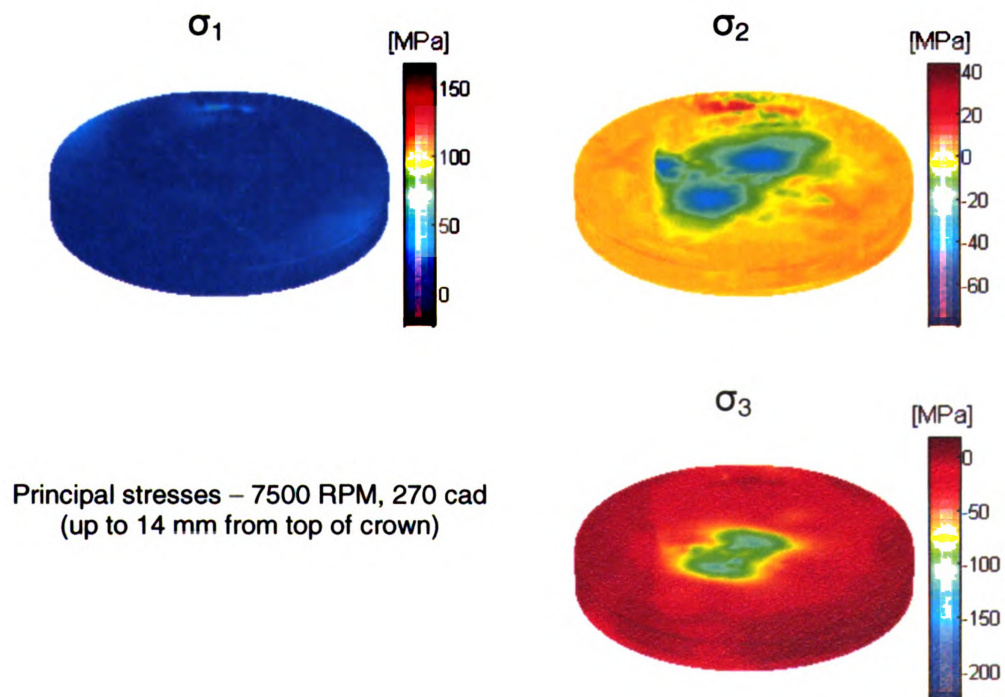


Figure 5.26: Principal stresses at 7500 RPM, 270 cad

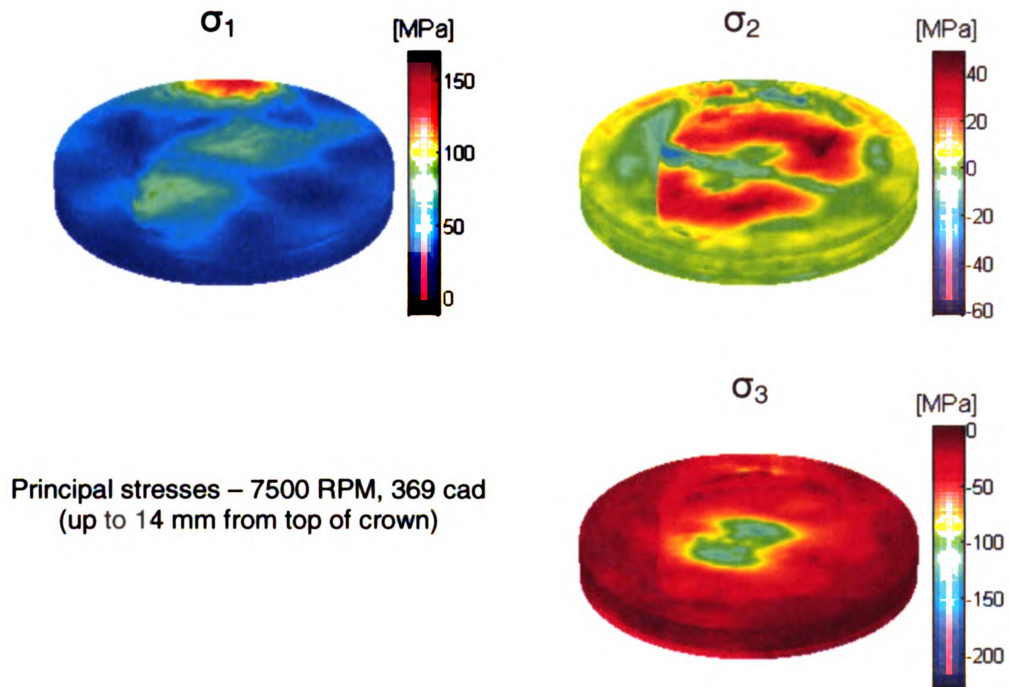


Figure 5.27: Principal stresses at 7500 RPM, 369 cad (peak in-cylinder pressure)

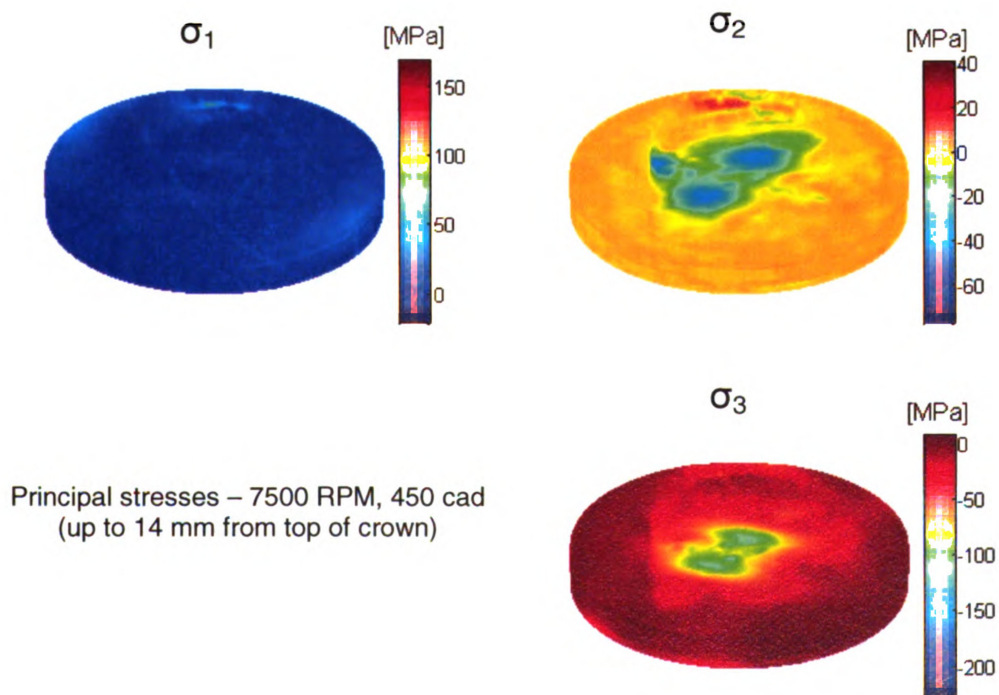


Figure 5.28: Principal stresses at 7500 RPM, 450 cad

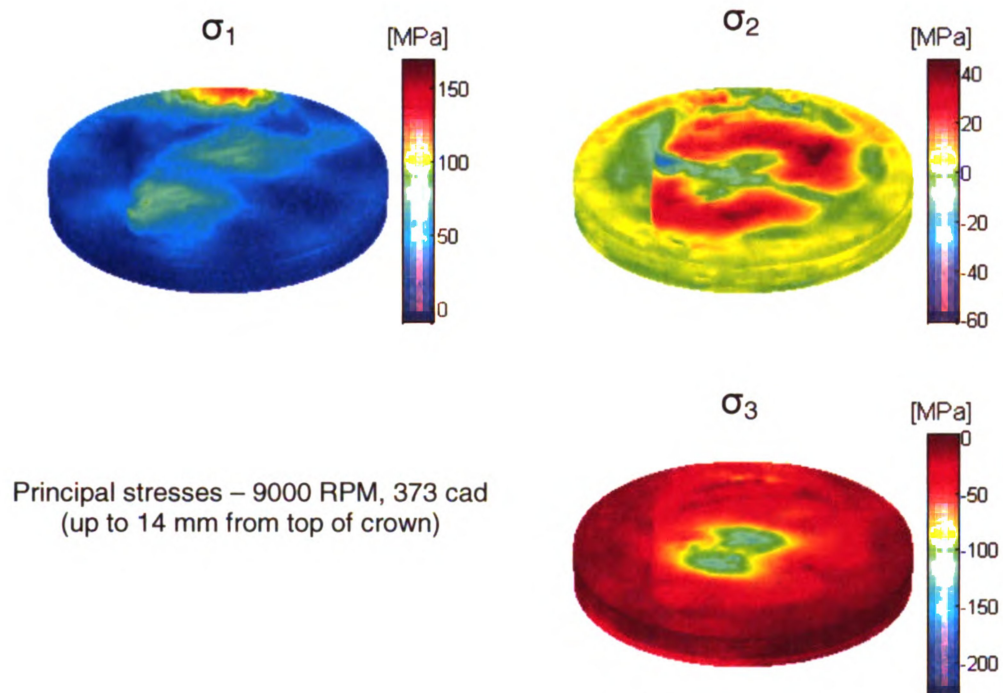


Figure 5.29: Principal stresses at 9000 RPM, 373 cad (peak in-cylinder pressure)

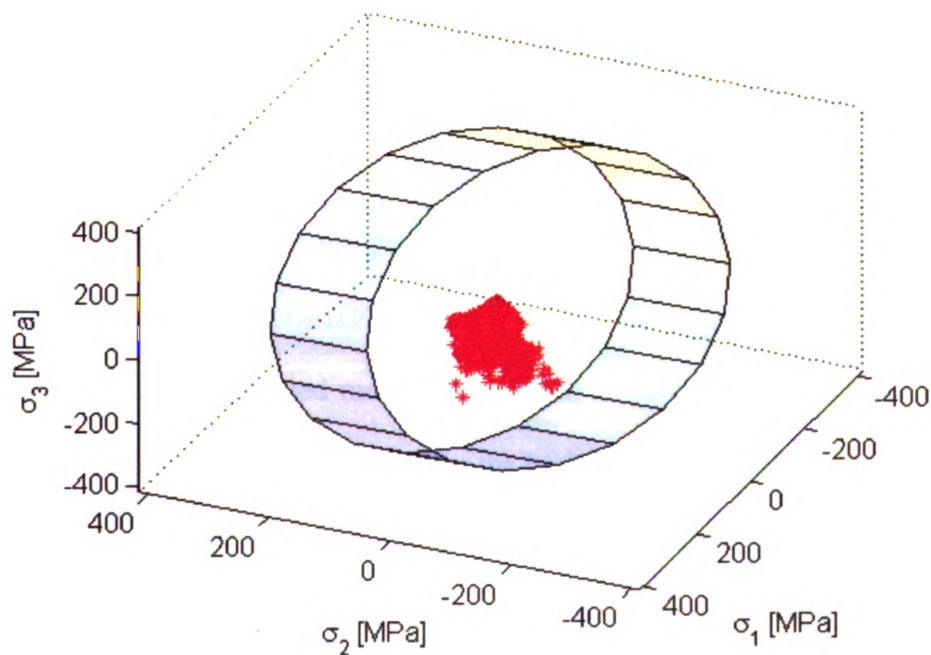


Figure 5.30: von Mises yield criterion 7500 RPM, 369 cad (peak in-cylinder pressure)

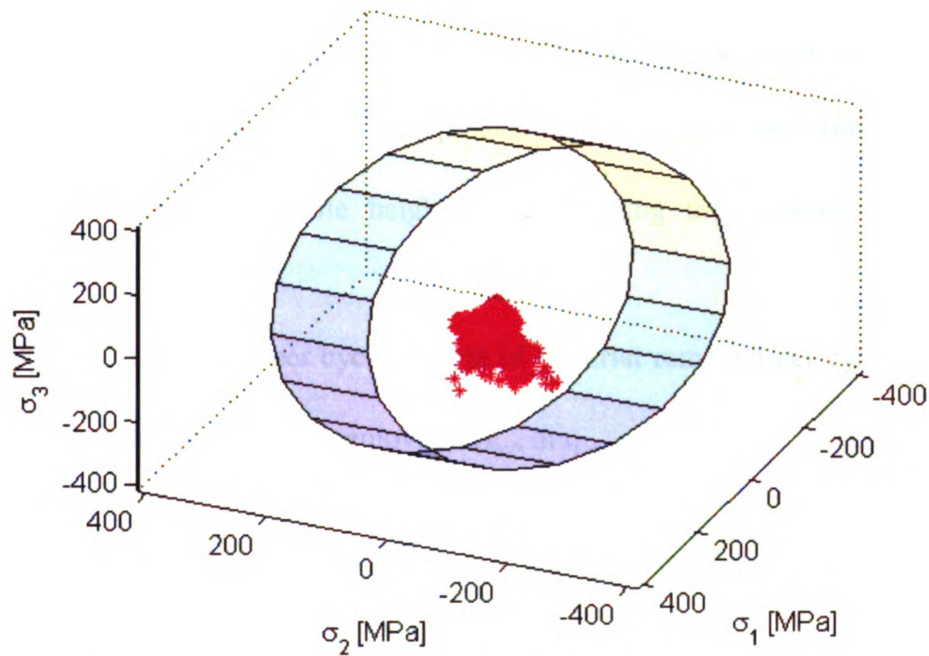


Figure 5.31: von Mises yield criterion 9000 RPM, 373 cad (peak in-cylinder pressure)

5.2.2 Progressive Wear

In this section the concept of progressive wear is introduced for piston modeling. Progressive wear concerns design engineers across many industries, as it can affect the coefficient of friction, surface roughness and oil retention capabilities of two sliding surfaces over time.

Here an initial simplified model is proposed to investigate how wear affects the frictional forces at the skirt-liner surface for the high-speed piston. It is hypothesized that wear varies linearly over time. To further simplify the model, it is assumed that the surface properties remain unchanged. Wear affects the clearance between the two sliding surfaces.

The time space T is defined to be bounded by t_o and t_f . It is divided into n intervals and the PIFEAD simulation is performed $n + 1$ times. Wear is assumed to be zero at t_o . The predicted wear is extrapolated linearly to the next time interval and subtracted from the skirt profile height, thus changing the nominal piston-to-liner clearance.

Let $h_{w,i}$ be the wear per cycle (height of material removed per cycle) at time t_i .

Then the wear (height of material removed), H_w , at t_{i+1} is

$$H_{w,i+1} = H_{w,i} + \frac{T \times N \times 30}{n} h_{w,i} \quad (5.2)$$

where T is in hours and N is the engine speed in revolutions per minute. (3.76) at t_{i+1} now becomes,

$$h = c - \left[e_{st} + (e_{sb} - e_{st}) \frac{y_s}{L} \right] \cos \theta_p - e_z \sin \theta_p + \delta_c - \delta_s - \delta_o - \delta_p + H_w \quad (5.3)$$

This model was used to examine the wear progression of the high-speed piston at 7500 RPM over an interval of two hours divided in 15-minute intervals, that is, $T = 2$ hrs and $n = 8$. The simulations were performed considering a perfectly cylindrical cylinder bore, i.e. no bore deformation.

Figure 5.32 shows the instantaneous skirt wear at the beginning of the simulation at 1 hour and 2 hours. At the beginning the wear is concentrated at the center of the skirt. As it is extrapolated and a pocket forms in that region, the wear at 1 hour appears around the center of the skirt. As time progresses, the wear appears to be random and at 2 hours it appears as spots. This is because the extrapolation does not result in a smooth surface as it is performed at each node individually. Consequently it forms peaks and valleys,

thus the spotted wear at two hours. It should also be noted that as time progresses the magnitude of instantaneous wear decreases. This is typical for engine break-in.

Figure 5.33 and Figure 5.34 show the cumulative skirt wear at 1 hour and 2 hours respectively. This wear appears to be very high and unacceptable under real operating conditions. These high magnitudes arise because of the assumptions in the progressive wear model. The wear is extrapolated linearly over the time intervals. At the initial stages when wear is high, the extrapolation magnifies it even more. This suggests that much smaller time steps are required in the progressive wear calculations to avoid this magnification. Furthermore, it is assumed that surface properties remain unchanged. In reality, as a surface wears, it polishes, thus becoming more resistant to abrasive wear. Furthermore, as the surface polishes, its oil retention properties change. All these are not accounted in the model, and so the model predicts overly high magnitudes of wear. However, it is believed that the model is a good initial tool for understanding the mechanisms of piston break-in. There is ongoing research to develop better extrapolation models for progressive wear.

As an exercise for PIFEAD, the dynamics for this piston are investigated to understand how progressive wear affects them. Figure 5.35 and Figure 5.36 show the piston secondary motion in the thrust and wrist-pin planes respectively at time zero, 1 hour and 2 hours. In the thrust plane, as the skirt wear progresses, the amplitude of the motions increases. This is the expected result as the skirt wear increases the piston to cylinder bore clearance. Considering Figure 5.36 it can be seen that at time zero the maximum amplitude of the translation along the wrist-pin is about 4 μm and occurs around firing where in-cylinder pressure peaks. On the other hand, as wear progresses

and the generation of hydrodynamic and contact forces becomes more uneven, the amplitudes of translation increase. At 2 hours even the frequency of oscillations increases. This suggests that wear progression gradually yields an unbalance of forces in the wrist-pin plane causing undesirable motion of the piston in that direction.

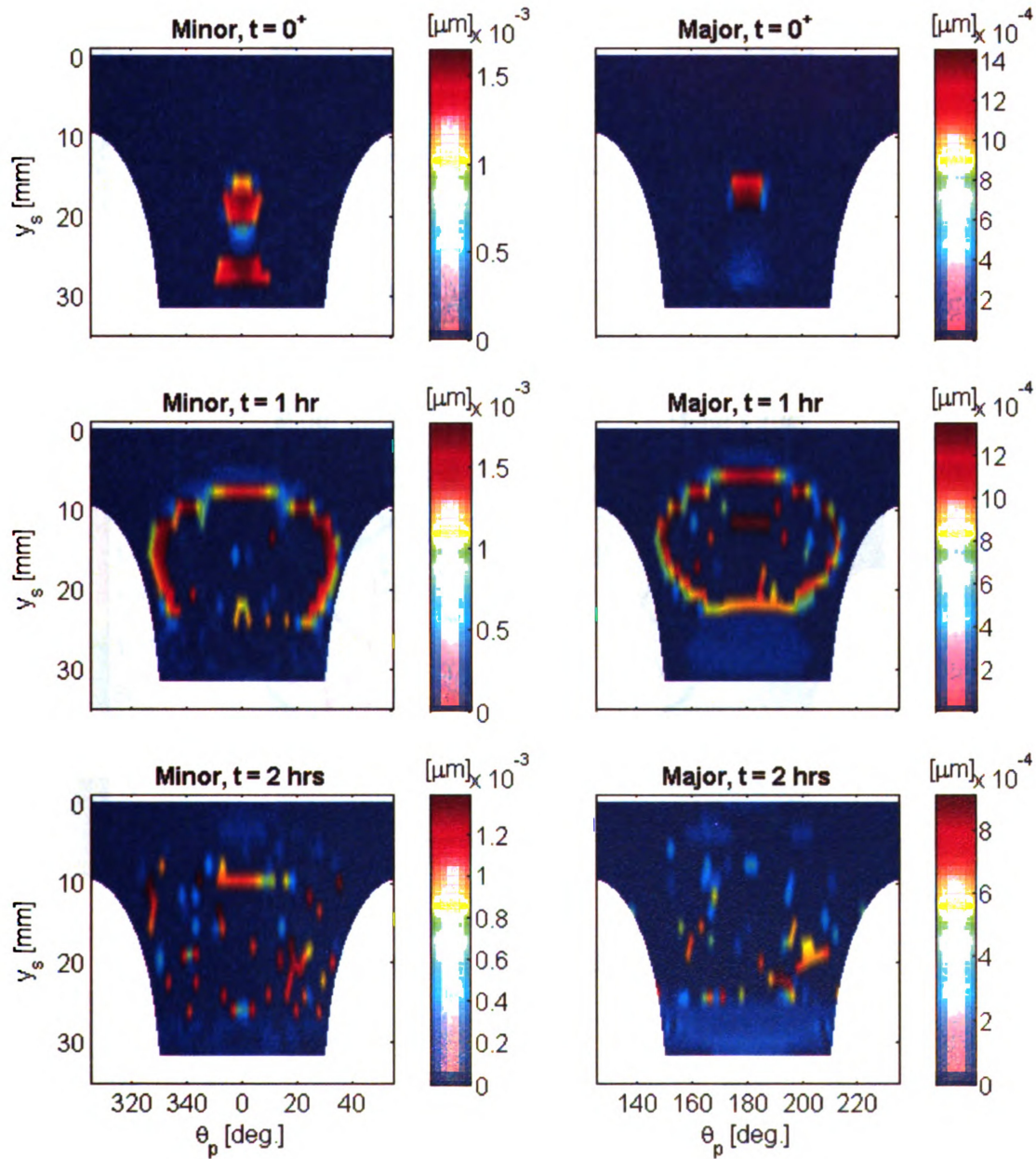


Figure 5.32: Instantaneous skirt wear

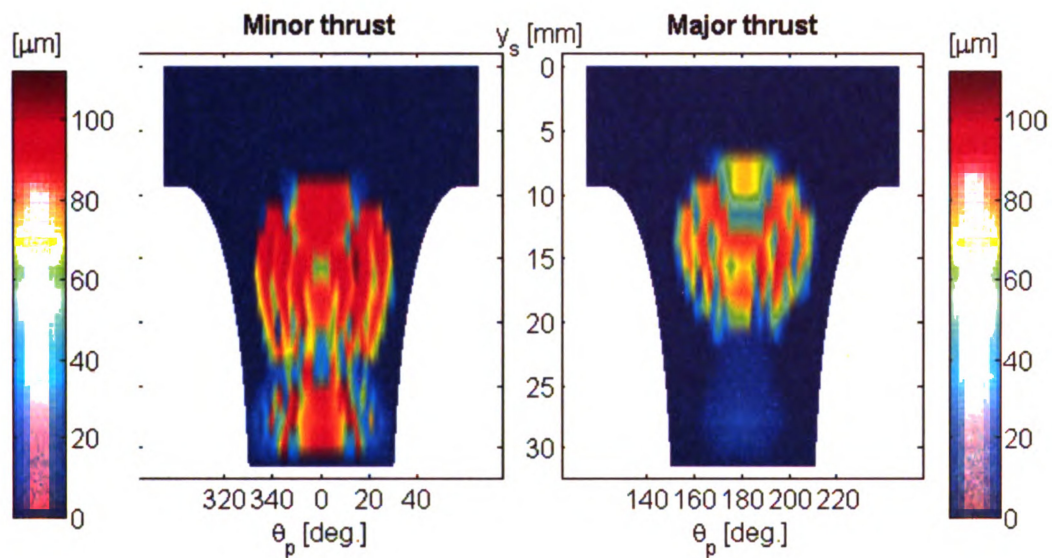


Figure 5.33: Cumulative skirt wear at 1 hour

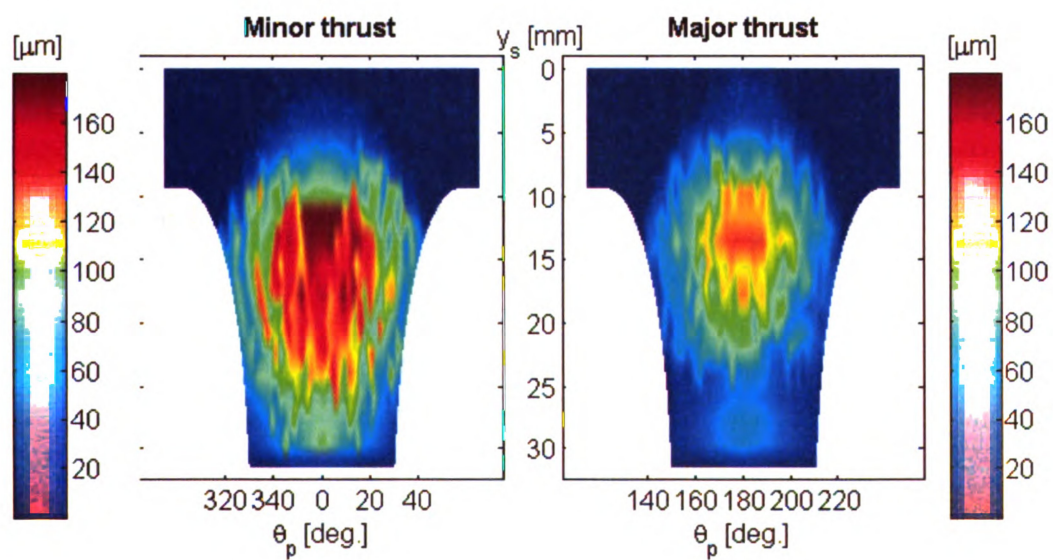
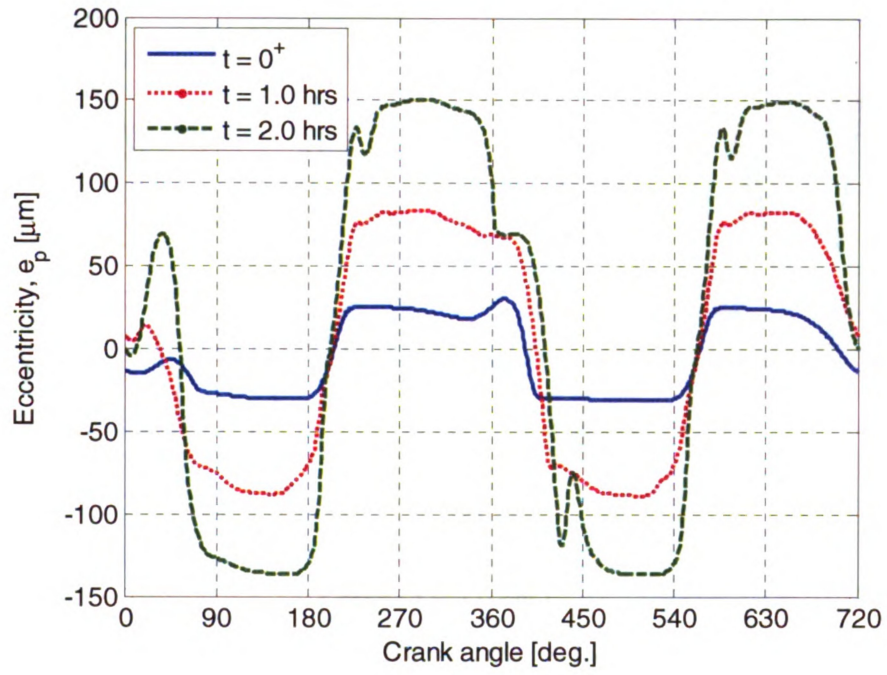
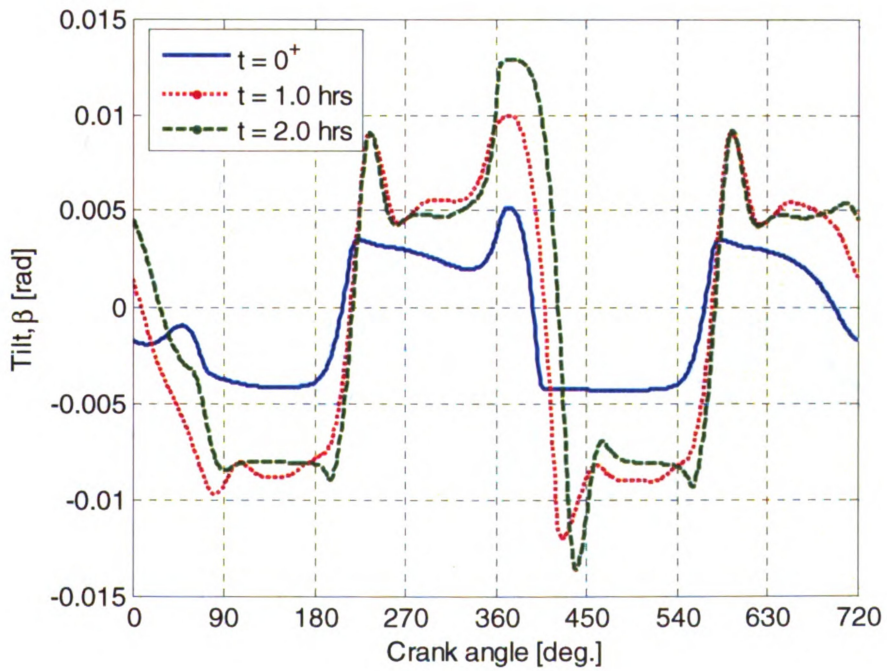


Figure 5.34: Cumulative skirt wear at 2 hours



(a)



(b)

Figure 5.35: Piston secondary motion in thrust plane
(a) eccentricity at wrist-pin level and (b) piston tilt

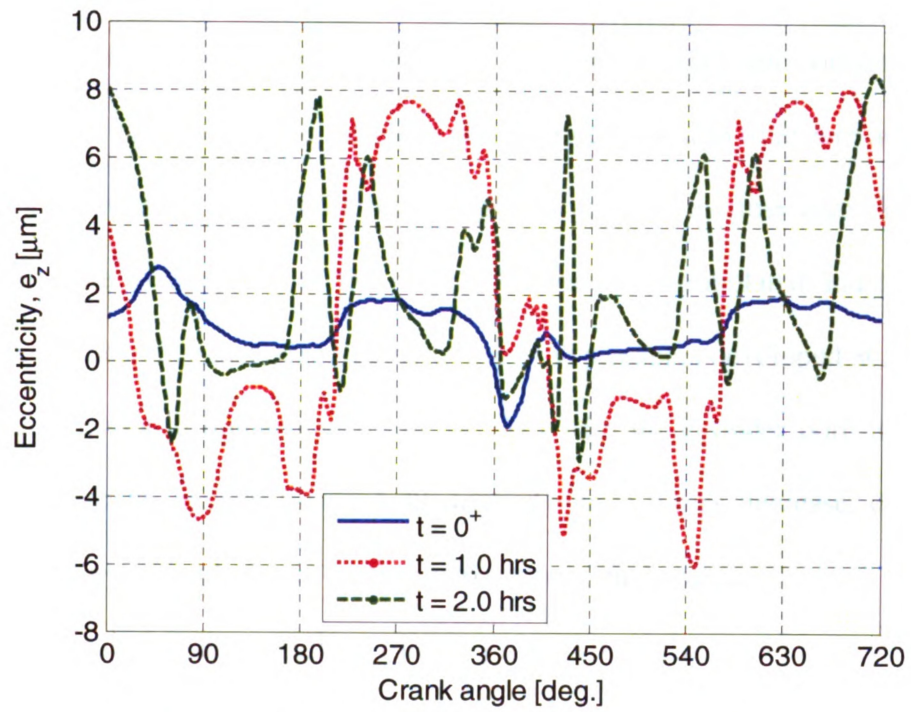


Figure 5.36: Piston translation along the wrist-pin

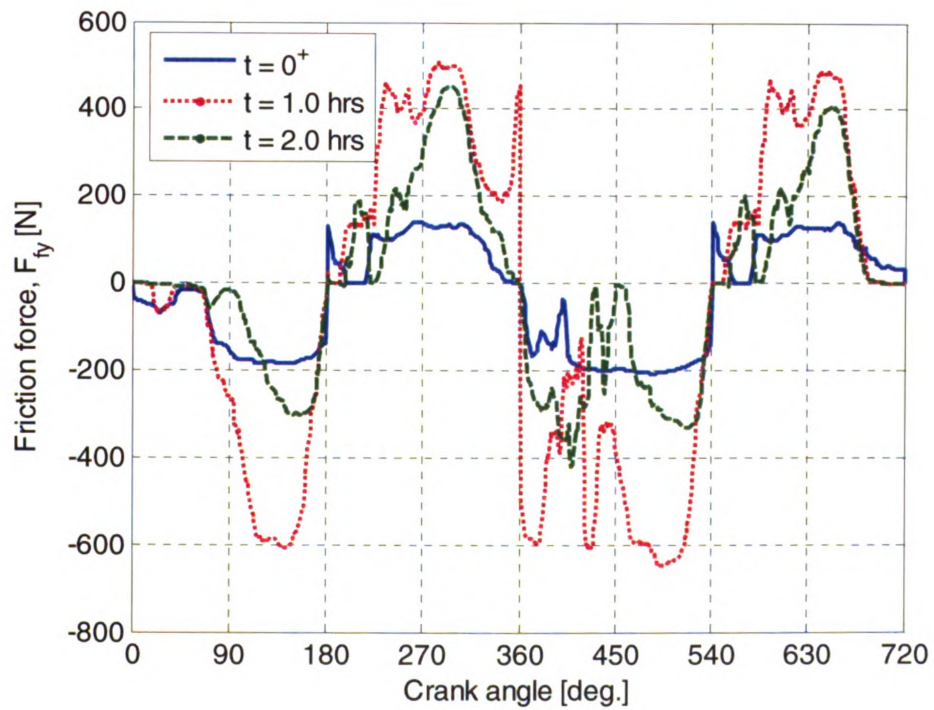
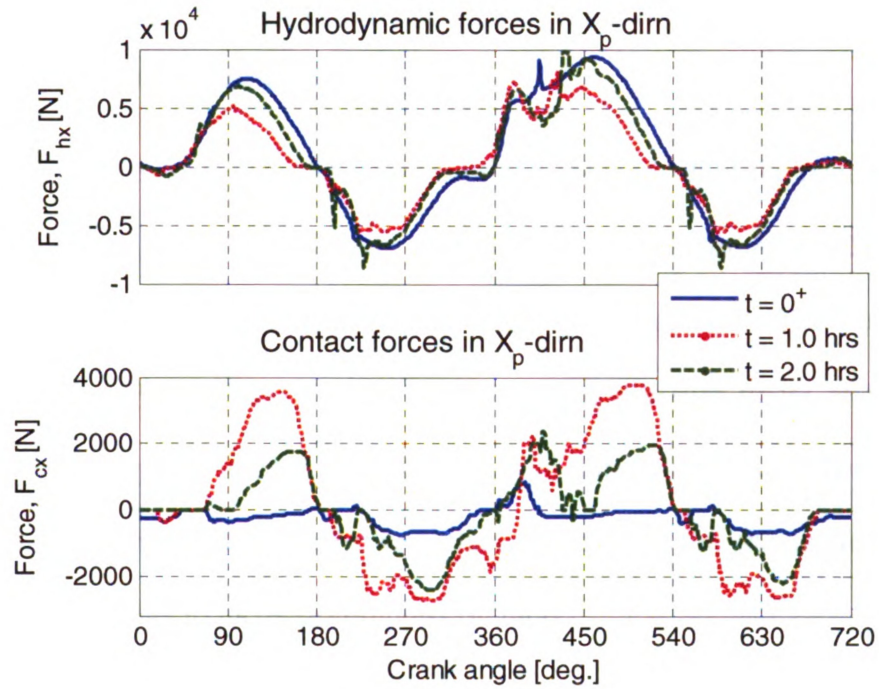


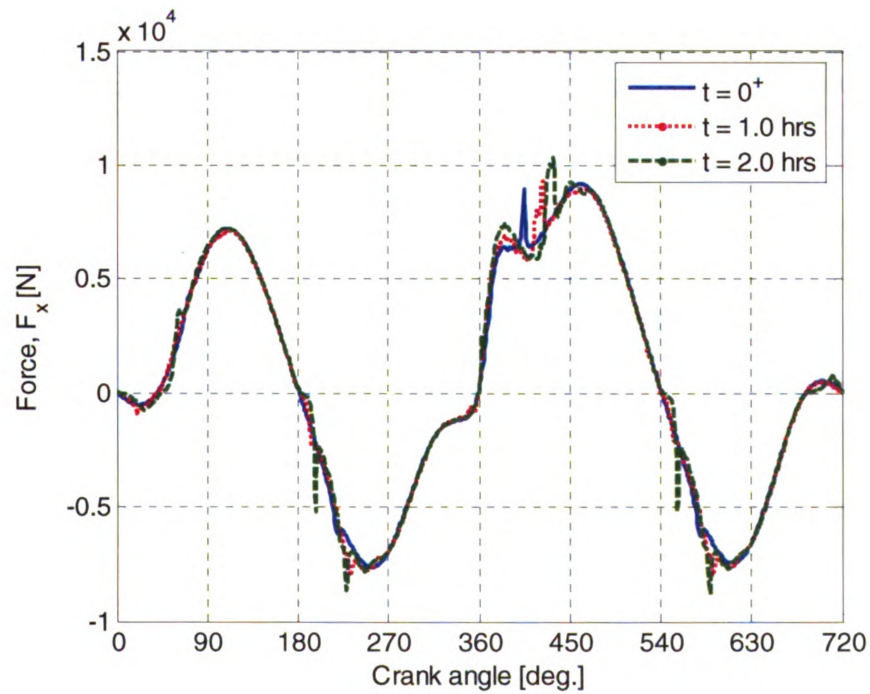
Figure 5.37: Friction force

Figure 5.37 shows the total friction force opposing the piston axial motion. One would expect this frictional force to decrease and gradually become constant from cycle to cycle. In this case the friction increases at 1 hour compared to time zero and then starts decreasing again at 2 hours, still being higher compared to time zero. This is again attributed to the assumptions in the model. As wear is extrapolated and the piston-to-cylinder bore clearance increases, the hydrodynamic pressures developed at the skirt drop (3.69). This results in higher contact of the skirt with the cylinder bore to support the piston. This can be seen in Figure 5.38: hydrodynamic forces decrease, contact forces increase, but the total side forces on the piston remain unchanged.

The results obtained from this initial progressive wear model are not quantitative rather they are qualitative. The predicted results satisfy the equations governing the system. The progressive wear model is a good initial tool to investigate piston break-in. It requires more research effort in order to improve the wear extrapolation model while incorporating the effects of wear on surface properties.



(a)



(b)

Figure 5.38: Piston side forces in thrust plane (a) hydrodynamic and contact and (b) total force

5.3 Assessing the Piston Performance of a Development Engine Relative to a Production Engine

This section deals with the assessment and comparison of the piston performance of a development engine relative to a production engine. Both are 2.0L 4-cylinder engines. They will be discussed in more detail in Chapter 7. The simulations are performed using PIFEAD at 3000 RPM WOT. The pressure traces at this operating condition are shown in Figure 7.14. The key piston dimensions and properties are shown in Table 5.3. The main difference between the two pistons is that the one for Engine 2 has a dome-shaped crown to increase compression ratio.

Figure 5.39 shows the cylinder bore deformation at two axial locations (0 mm and 50 mm from the top of the cylinder) for the two engines. It should be noted here, that the deformation for Engine 2 is eccentric relative to the cylinder center axis. It is biased towards the positive direction in the wrist-pin plane.

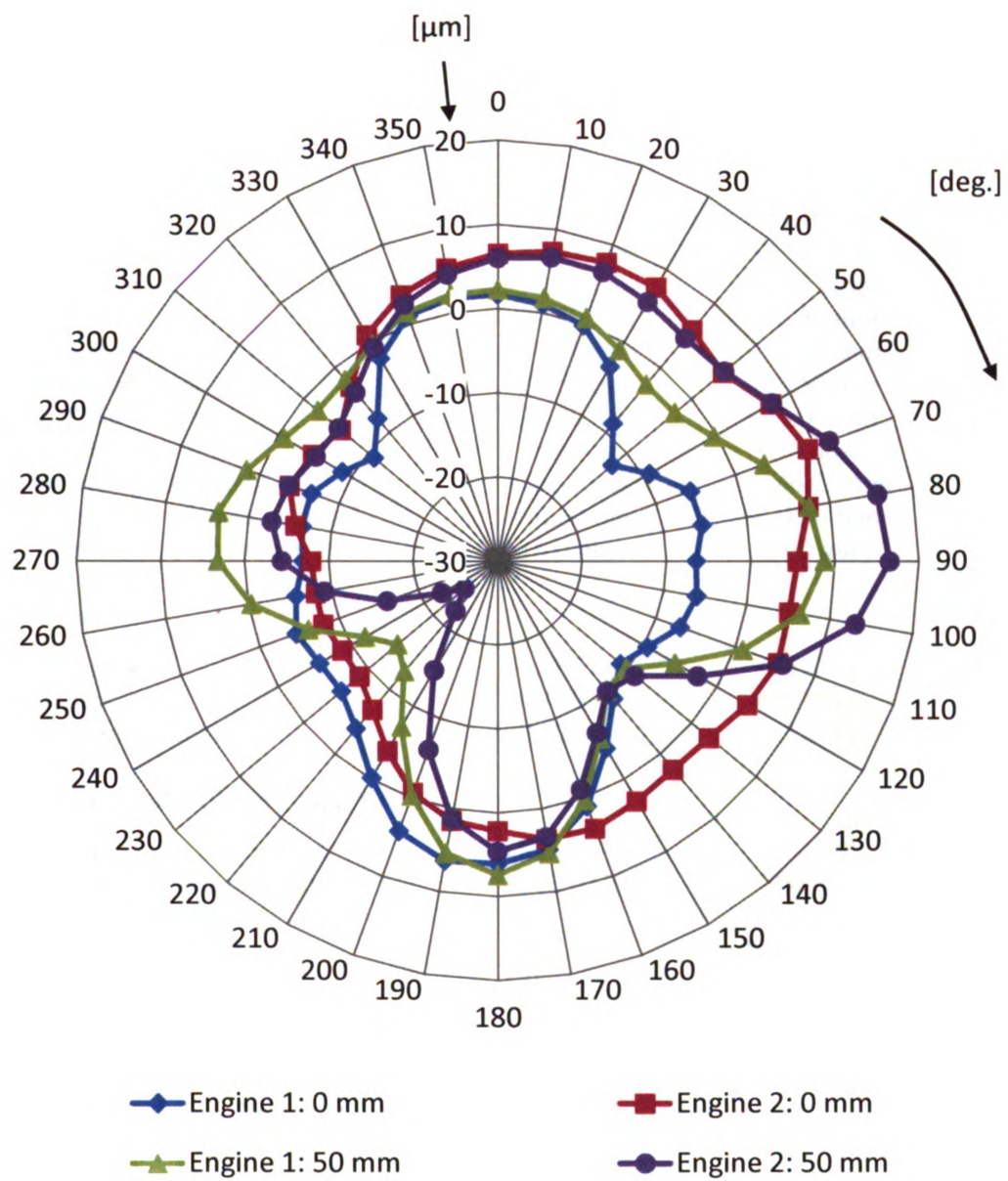


Figure 5.39: Cylinder bore deformation for the two engines

Table 5.3: Piston dimensions and properties

	Engine 1	Engine 2
Geometric properties		
Bore diameter	~87.50 mm	~87.52 mm
Stroke	~83.10 mm	~83.10 mm
Piston diameter	~87.47 mm	~87.49 mm
Piston height	~50.80 mm	~50.57 mm
Skirt length	~34.40 mm	~31.66 mm
Wrist-pin offset (x-coord.)	~ -0.80 mm	~ -0.60 mm
Wrist-pin y-coord.	~28.50 mm	~28.50 mm
Wrist-pin diameter	~22.00 mm	~21.00 mm
Cylinder bank angle	0.0 deg.	0.0 deg.
Connecting rod length	~146.25 mm	~146.25 mm
Piston center of mass, x-coord.	~ -0.30 mm	~ -0.50 mm
Piston center of mass, y-coord.	~16.0 mm	~13.0 mm
Masses		
Piston mass	~0.300 kg	~0.320 kg
Pin mass	~0.170 kg	~0.170 kg
Connecting rod mass	~0.520 kg	~0.520 kg
Material and surface properties		
Piston modulus of elasticity	~82.0 GPa	~82.0 GPa
Cylinder modulus of elasticity	~200.0 GPa	~200.0 GPa
Piston Poisson's ratio	0.33	0.33
Cylinder Poisson's ratio	0.30	0.30
Piston roughness	1.0 μm	1.0 μm
Cylinder roughness	1.0 μm	1.0 μm
Skirt asperity density	3.1E+9 m ⁻²	3.1E+9 m ⁻²
Skirt asperity radius	275.0 μm	275.0 μm
Piston/cylinder coefficient of friction	0.15	0.15
Oil properties		
Dynamic viscosity at 40 °C	41.56 cP	41.56 cP
Dynamic viscosity at 100 °C	6.07 cP	6.07 cP
Oil reference temperature	25 °C	25 °C
Oil dynamic viscosity at ref. temp.	89.66 cP	89.66 cP

The piston translation along the wrist-pin is shown in Figure 5.40. The two pistons have similar motion. However, the piston of Engine 1 oscillates about the cylinder bore center axis, whereas the piston of Engine 2 oscillates at about 8 μm from the cylinder bore axis. This is because of the eccentric cylinder bore deformation of Engine 2 shown in Figure 5.39. This again proves the necessity of piston dynamics numerical models that consider translation along the wrist-pin.

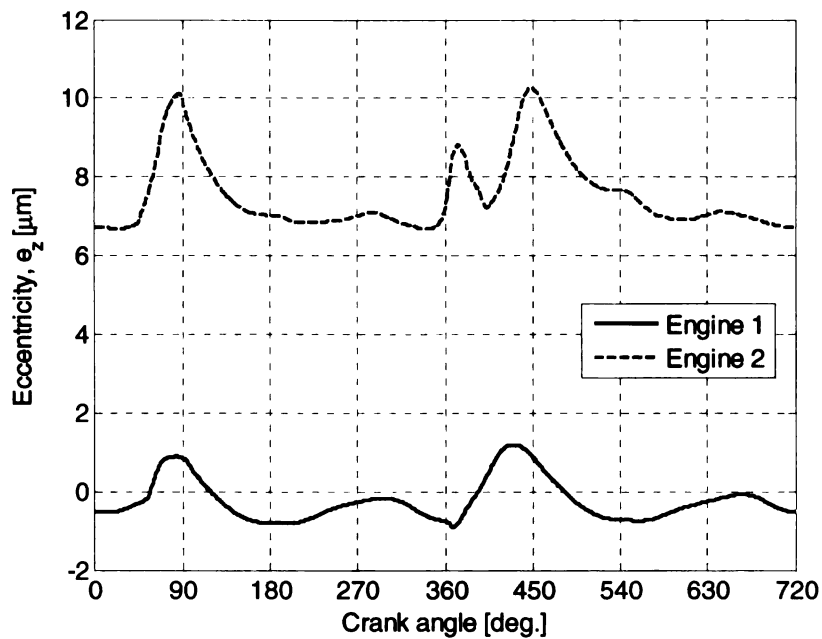
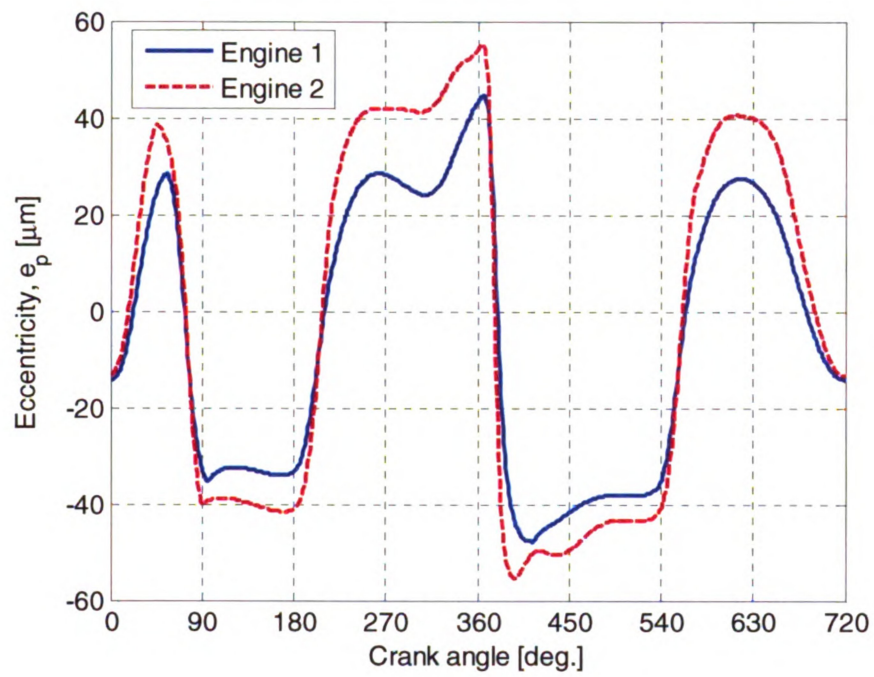
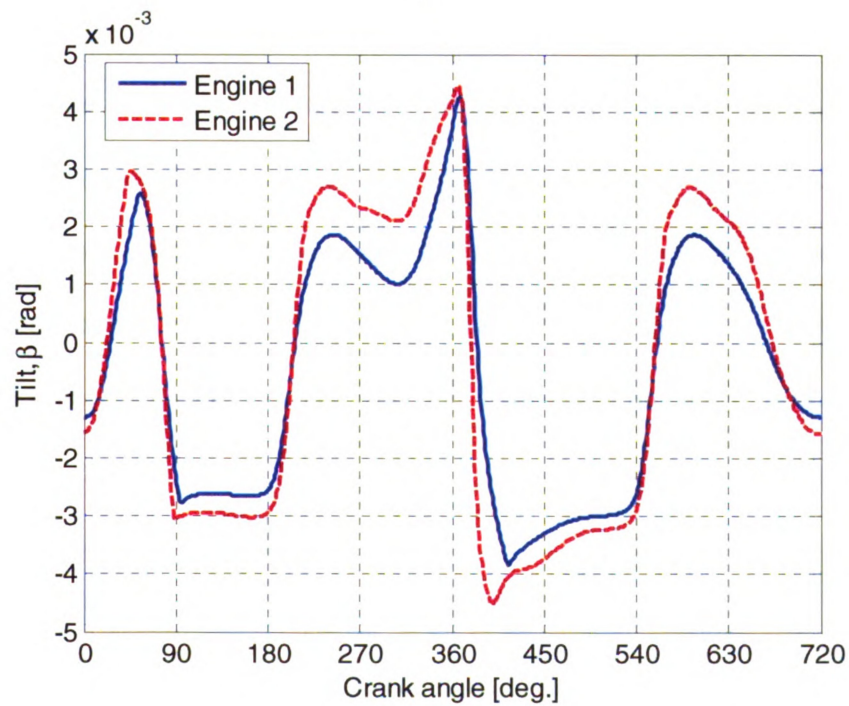


Figure 5.40: Piston translation along the wrist-pin

The piston secondary motion in the thrust plane is shown in Figure 5.41. The higher in-cylinder pressure for Engine 2 forces the piston to move closer to the cylinder liner. The two pistons have approximately the same skirt surface area. Thus the hydrodynamic forces developed are not sufficient to support the piston, and it contacts the cylinder bore for the extra support (Figure 5.43 a). This results in an increase in friction for Engine 2 during the compression stroke (Figure 5.42).



(a)



(b)

Figure 5.41: Piston secondary motion in thrust plane
(a) eccentricity at wrist-pin level and (b) piston tilt

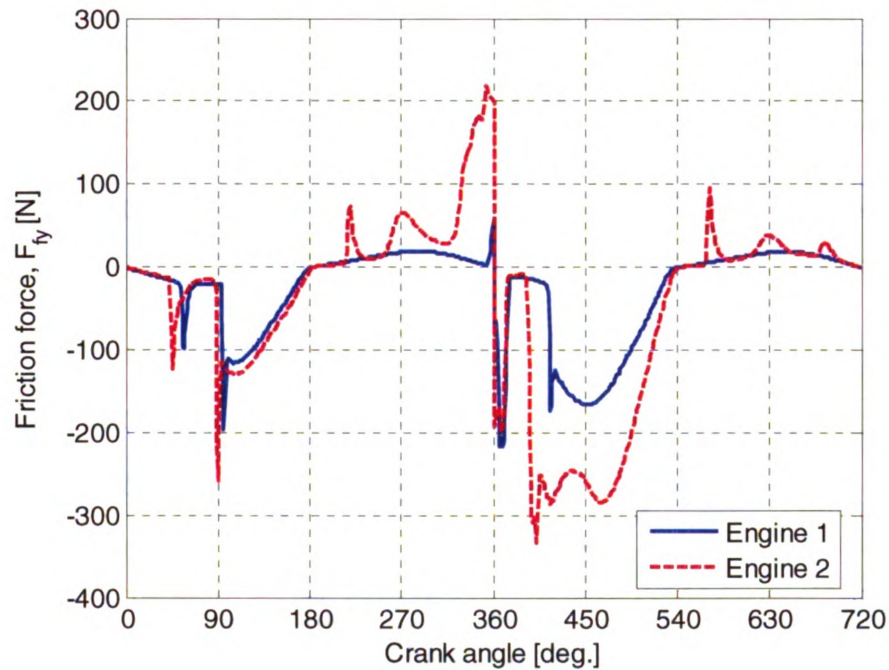
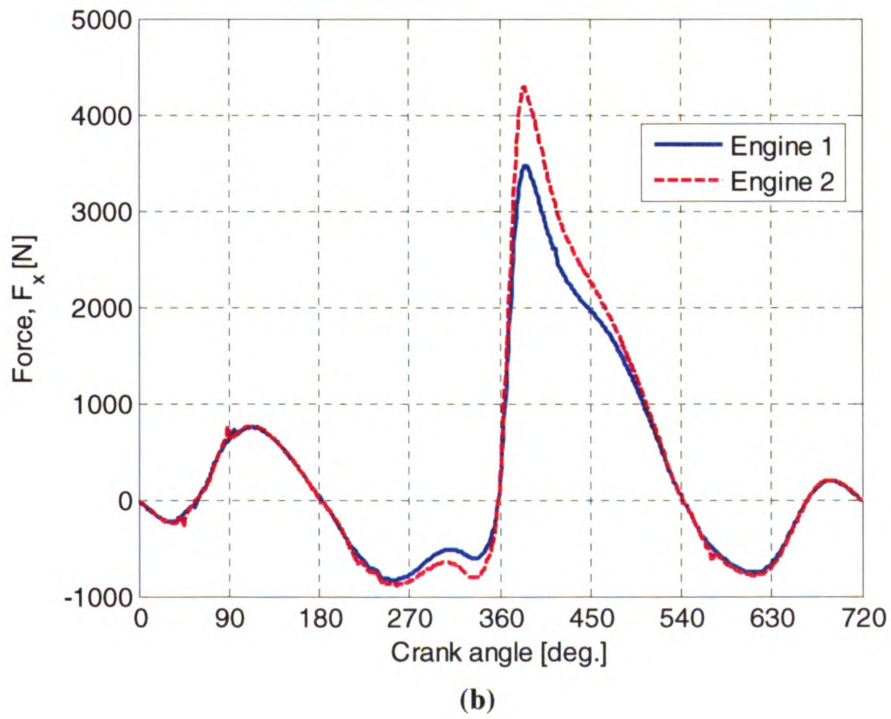
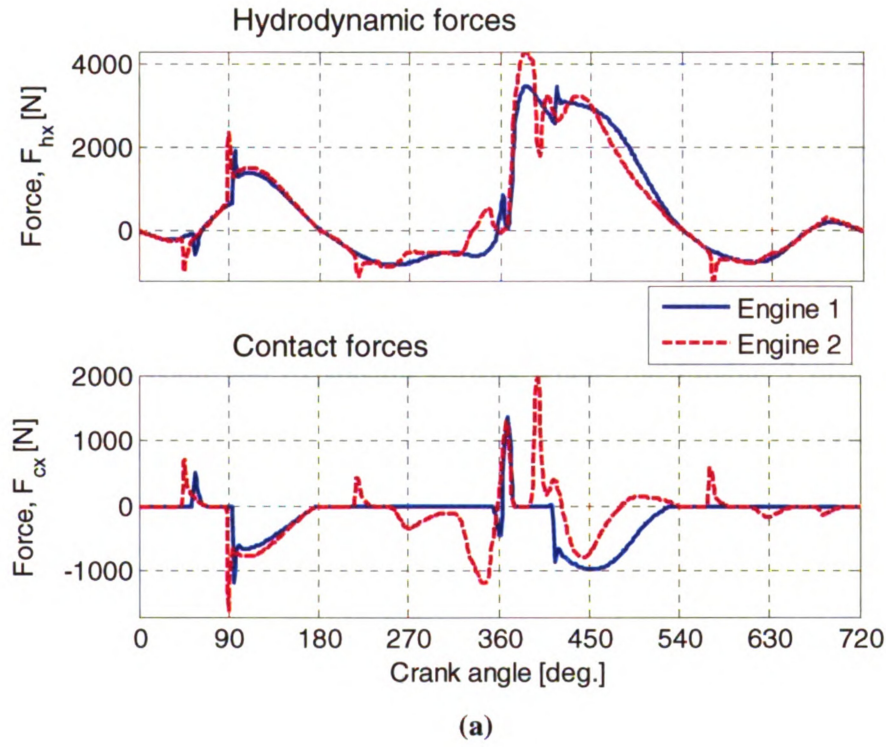


Figure 5.42: Friction force

During the expansion stroke, the two pistons are closer to the major thrust side and also tilted towards it. This creates a wedge effect and thus high hydrodynamic forces pushing the pistons away from the major thrust side. The Engine 1 piston experiences higher hydrodynamic forces. Thus it is pushed more heavily on the minor thrust side, resulting in higher contact. Despite this, the hydrodynamic shear dominates and the Engine 2 piston experiences higher friction during the expansion stroke (Figure 5.42).



**Figure 5.43: Piston side forces in thrust plane
(a) hydrodynamic and contact and (b) total force**

Figure 5.43b shows the total forces for the two engines. During intake and exhaust strokes, where the in-cylinder pressures are low, the two pistons experience similar loads in the thrust plane. The difference in side loads appears after the middle of the expansion stroke and lasts for most of the expansion stroke.

Overall the two pistons are similar in performance. The difference is only noticed during the compression and expansion strokes where the Engine 2 piston experiences higher frictional loads. With everything being equal, this is the expected result as the in-cylinder pressure of Engine 2 is higher. This implies that piston design should be improved in order to maintain the same performance as Engine 1. This can be achieved by designing a lighter piston to make up for the frictional losses.

5.4 Wear Prediction for a Heavy-duty Diesel Engine Piston

In this section a heavy duty-diesel engine piston is modeled in an attempt to predict the mechanisms causing wear. The specific piston was showing wear on the inboard side of the engine block (Figure 5.44). This could be either the major or minor thrust side depending where the piston is mounted, on the left or right bank. It is hypothesized that gravity might play a role in this phenomenon, as the masses of the piston, wrist-pin and connecting rod are significantly high. Wear would tend to occur at cold conditions when the engine was idling at no load.

Table 5.4 shows the key piston dimensions and properties used in the model. Figure 5.45 shows the in-cylinder pressure trace at 750 RPM, no-load condition. Figure 5.46 shows the cylinder bore deformation used for the simulations.

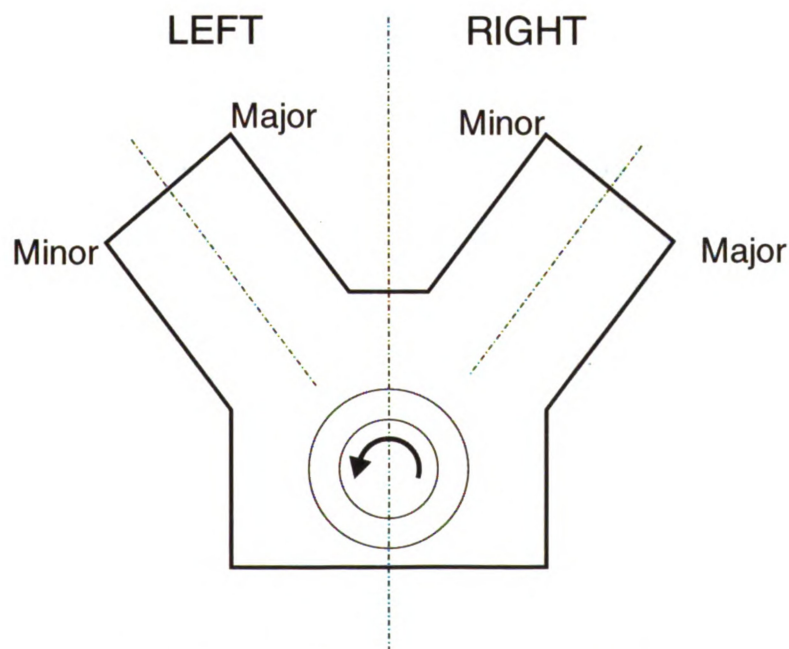


Figure 5.44: Engine block configuration

Table 5.4: Heavy-duty diesel piston dimensions and properties

Geometric properties

Bore diameter	~158.70 mm
Stroke	~190.00 mm
Piston diameter	~158.60 mm
Piston height	~161.00 mm
Skirt length	~118.50 mm
Wrist-pin offset (x-coord.)	0.00 mm
Wrist-pin y-coord.	~112.10 mm
Wrist-pin diameter	~65.00 mm
Cylinder bank angle	30.0 deg.
Connecting rod length	~320.00 mm
Piston center of mass, x-coord.	~0.00 mm
Piston center of mass, y-coord.	~60.50 mm

Masses

Piston mass	~6.900 kg
Pin mass	~2.450 kg
Connecting rod mass	~10.130 kg

Material and surface properties

Piston modulus of elasticity	~159 GPa
Cylinder modulus of elasticity	101 GPa
Piston Poisson's ratio	0.29
Cylinder Poisson's ratio	0.25
Piston roughness	4.0 μm
Cylinder roughness	3.0 μm
Skirt asperity density	1.32E+8 m^{-2}
Skirt asperity radius	35.0 μm
Piston/cylinder coefficient of friction	0.15
Skirt hardness	1689 MPa
Skirt wear coefficient	7.17E-8

Oil properties

Dynamic viscosity at 40 °C	91.98 cP
Dynamic viscosity at 100 °C	13.14 cP
Oil reference temperature	150 °C
Oil dynamic viscosity at ref. temp.	4.15 cP

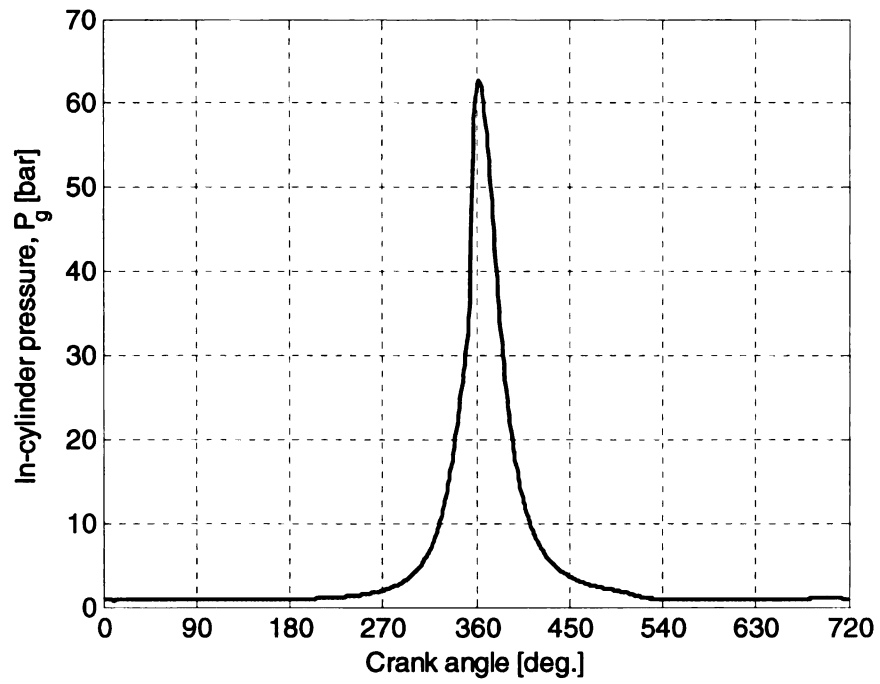
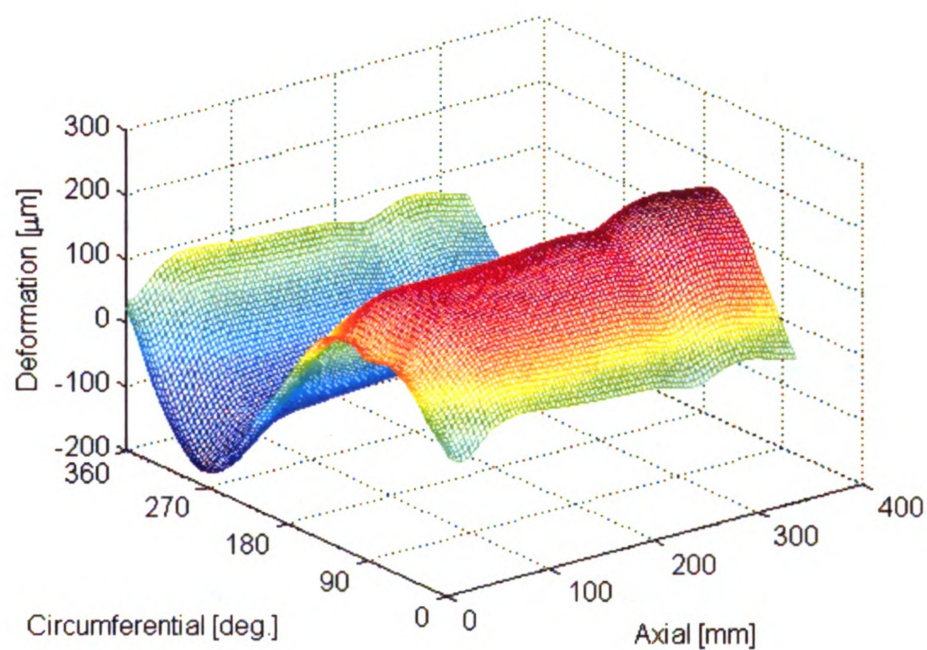
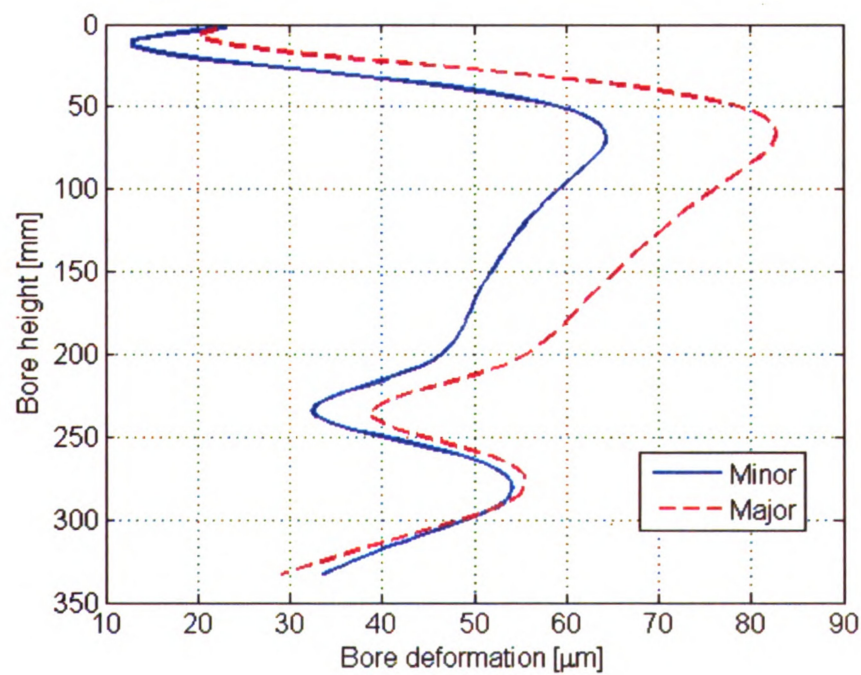


Figure 5.45: In-cylinder pressure at idle (750 RPM) no-load conditions



(a)



(b)

Figure 5.46: Cylinder bore deformation (a) three-dimensional and (b) along cylinder bore length at minor and major thrust sides

5.4.1 Skirt Compliance

The skirt compliance for this piston is calculated as described in Section 3.2.1, (3.9) and (3.11). The diagonal terms of the skirt compliance \mathbf{C} are plotted in Figure 5.47. The skirt for the specific piston is flexible in the middle and more rigid around the edges. The skirt tail is very flexible. At around 100 mm there is a low flexibility region extending across the skirt. This is induced by a reinforcement behind the skirt and this could be a potential reason for wear appearing in that region.

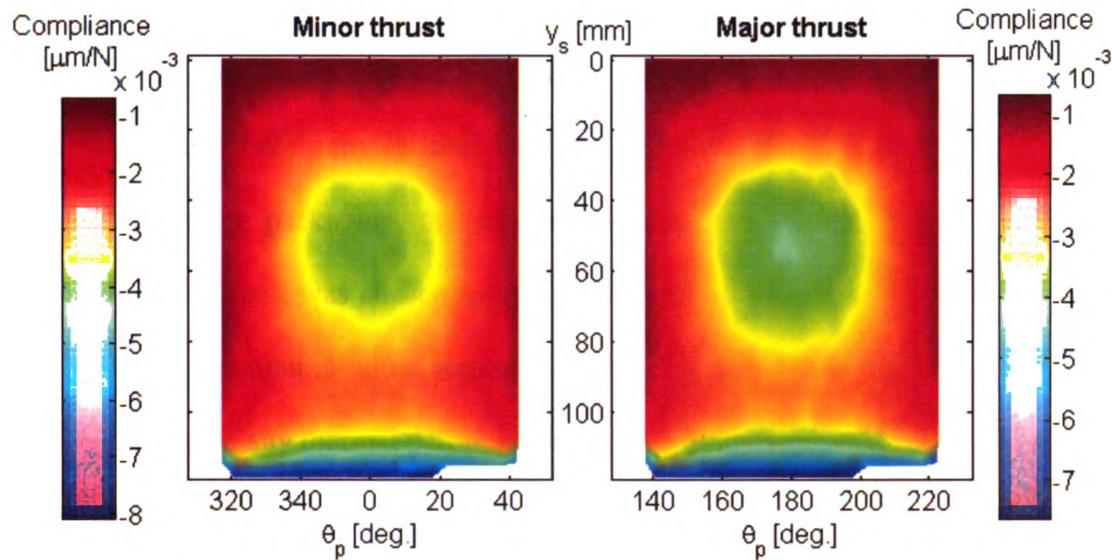


Figure 5.47: Skirt compliance of the heavy duty diesel piston

5.4.2 Investigations on Skirt Wear

In order to investigate the mechanisms that cause skirt wear, different cases were examined. Table 5.5 lists these cases.

Table 5.5: Simulation cases

Description	
Case 1	Bore diameter = 158.70 mm, Bore temperature const = 373 K
Case 2	Bore diameter = 158.65 mm, Bore temperature const = 373 K
Case 3	Bore diameter = 158.65 mm, Bore temperature as Figure 5.48
Case 4	Bore diameter = 158.65 mm, Bore temperature as Figure 5.49

These cases were chosen in order to investigate how the magnitude of bore deformation and bore temperature, in conjunction with gravity, affects skirt wear. Because of engine packaging, the inboard side is likely to get hotter faster than the outboard side. Thus it was chosen to be hotter (Figure 5.49) in Case 4. The simulations were performed assuming initial stages of engine start. Thus the piston was assumed not to have undergone any thermal deformation.

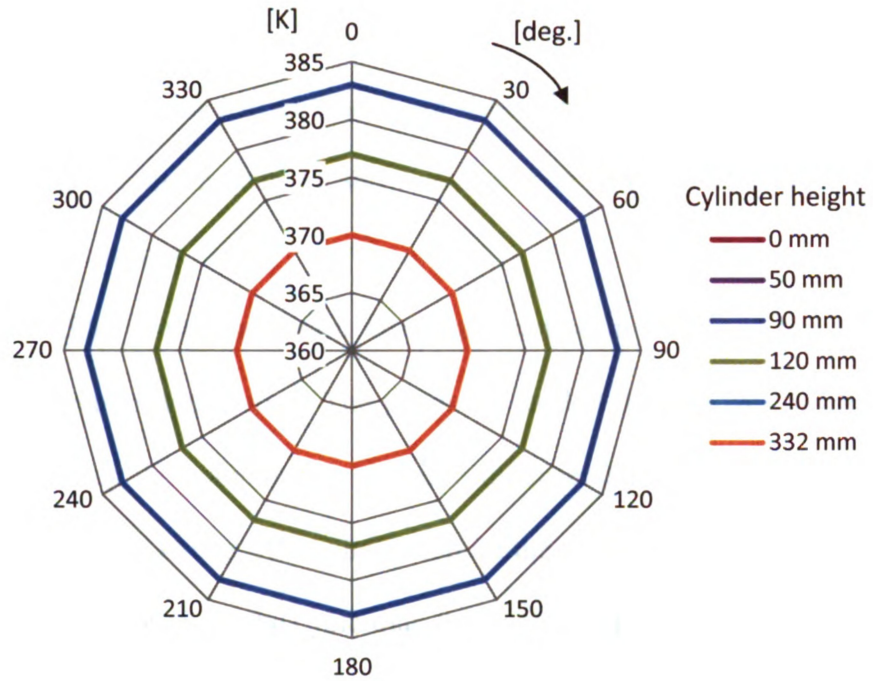


Figure 5.48: Symmetric temperature distribution decreasing along cylinder bore length

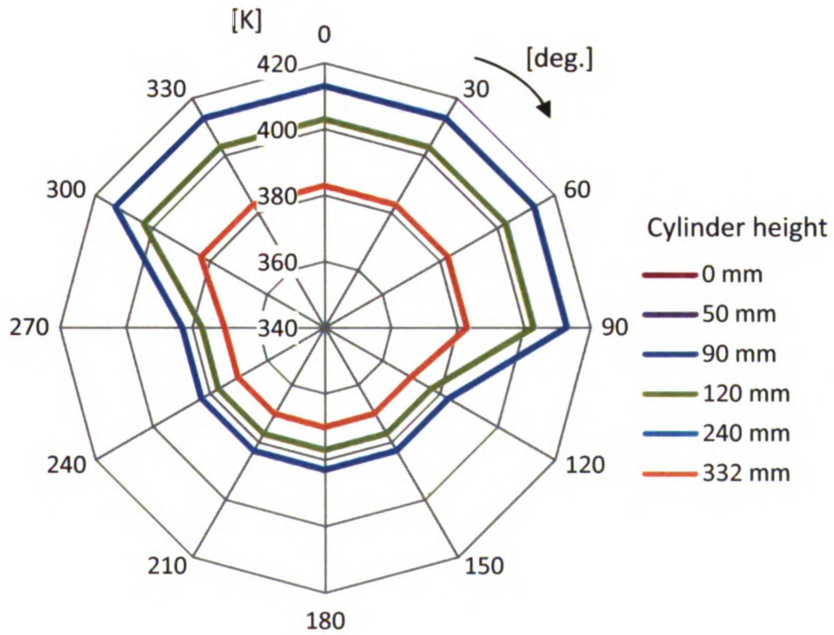


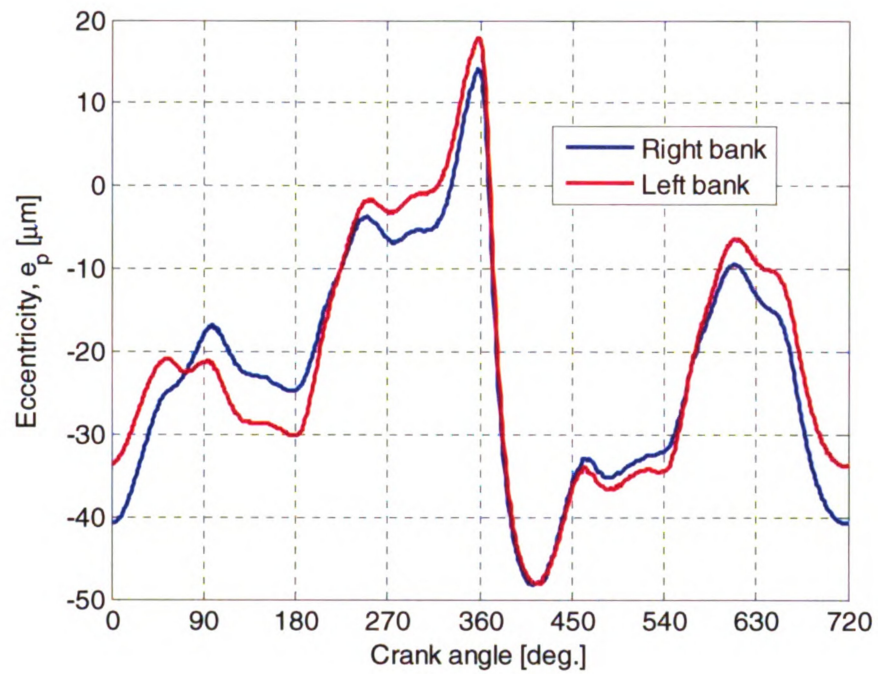
Figure 5.49: Asymmetric temperature distribution, hotter imposed on the inboard side of either bank

5.4.2.1 Case 1

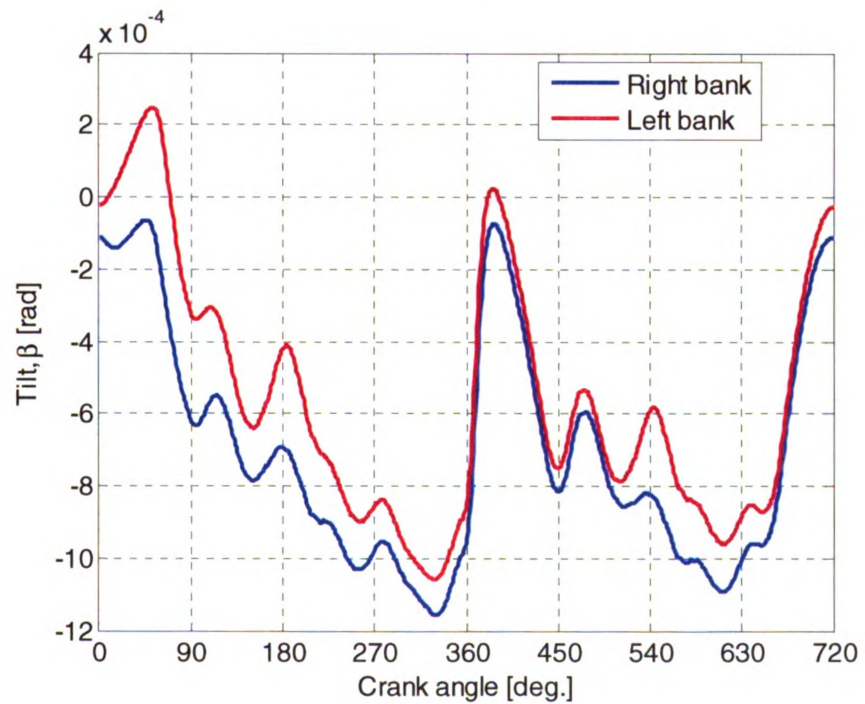
The results obtained from Case 1 are shown in Figure 5.50 to Figure 5.52. Under these conditions the piston does not show any wear on either bank. It is purely supported by hydrodynamic forces.

Figure 5.50 shows the piston secondary motion in the thrust plane. It is evident that gravity affects piston motion. The piston on the left bank moves much closer to the minor thrust during the compression stroke. Similar tendency is seen during the exhaust and part of the intake stroke. Also, the piston on the right bank is tilted more toward the major thrust side throughout the cycle than the piston on the left bank. This suggests that in the event of contact gravity, will tend to promote wear on the inboard side.

Figure 5.51 shows the piston translation along the wrist-pin. The piston oscillates at about 148 μm from the cylinder bore center axis. This is because the cylinder bore deformation used is eccentric along the wrist-pin plane. This is once again a proof that 3-D piston dynamics numerical models are necessary.



(a)



(b)

Figure 5.50: Piston secondary motion in thrust plane
(a) eccentricity at wrist-pin level and (b) piston tilt, Case 1

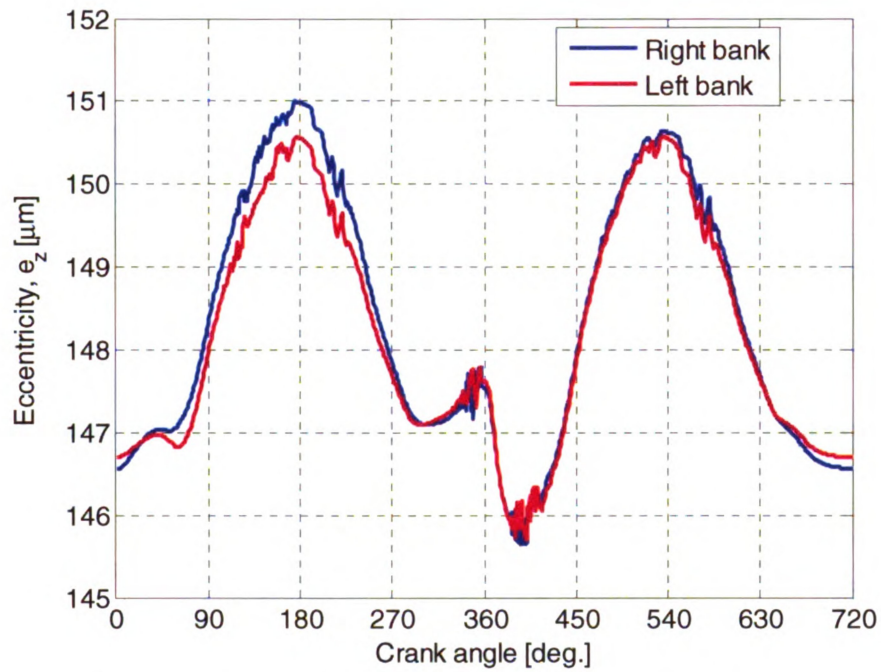


Figure 5.51: Piston translation along the wrist-pin, Case 1

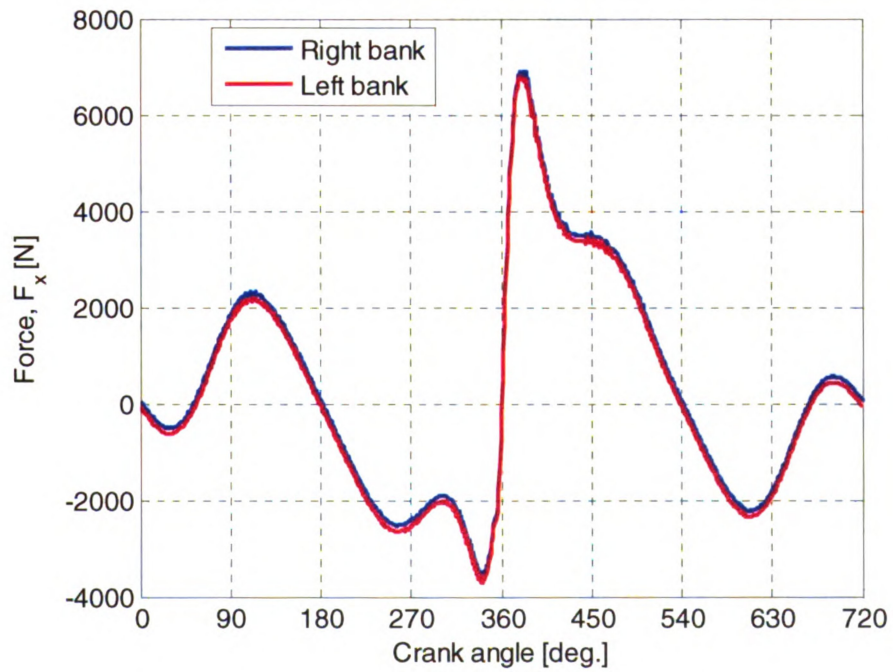


Figure 5.52: Piston total side force, Case 1

Figure 5.52 shows the total piston side forces, which in this case are purely hydrodynamic. The peak side force occurs at 380 cad on the major thrust side. Figure 5.53 shows an analysis of the side loads on the piston. Here the mass of the connecting rod is ignored. At a V-angle of 30 degrees the weight component for the piston is 44 N and for the wrist-pin is 12 N. At this crank angle and operating condition, the piston assembly requires approximately 6845 N to be supported. As a result the major thrust side of the piston on the right bank experiences higher loading than that of the piston on the left bank in order to counterbalance gravity.

Figure 5.54 shows the actual piston from the second cylinder on the left bank of the engine run at no load. In this case the piston shows no wear marks. The marks on the major thrust side are caused by the scouring effect of the oil when it is pressurized to support the piston. This is consistent with the predictions of Case 1, no wear marks from contact, and high hydrodynamic pressures on the major thrust side.

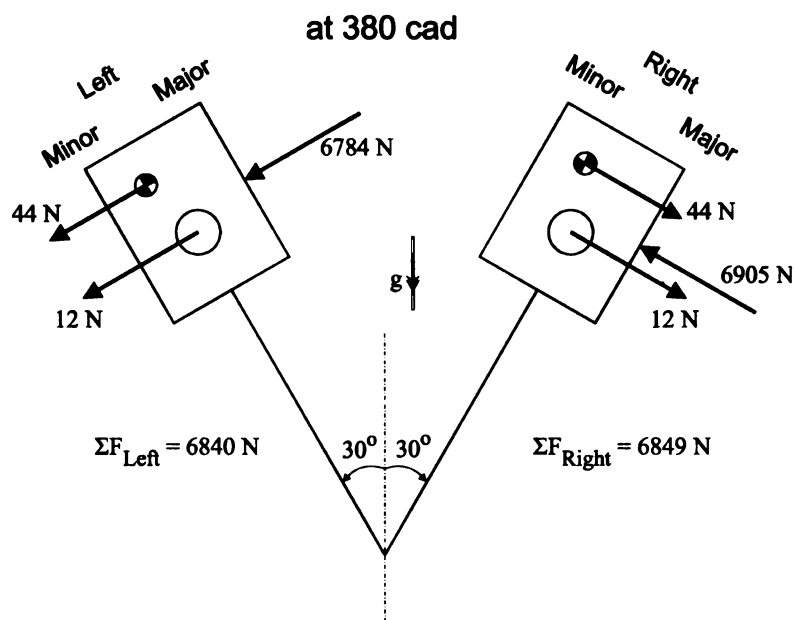
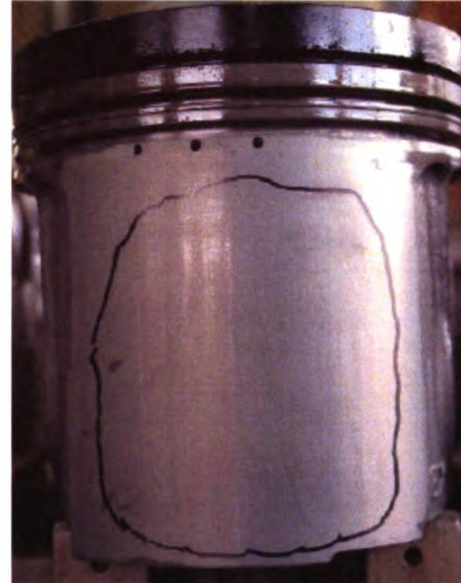


Figure 5.53: Side force analysis at 380 crank angle degrees



(a)

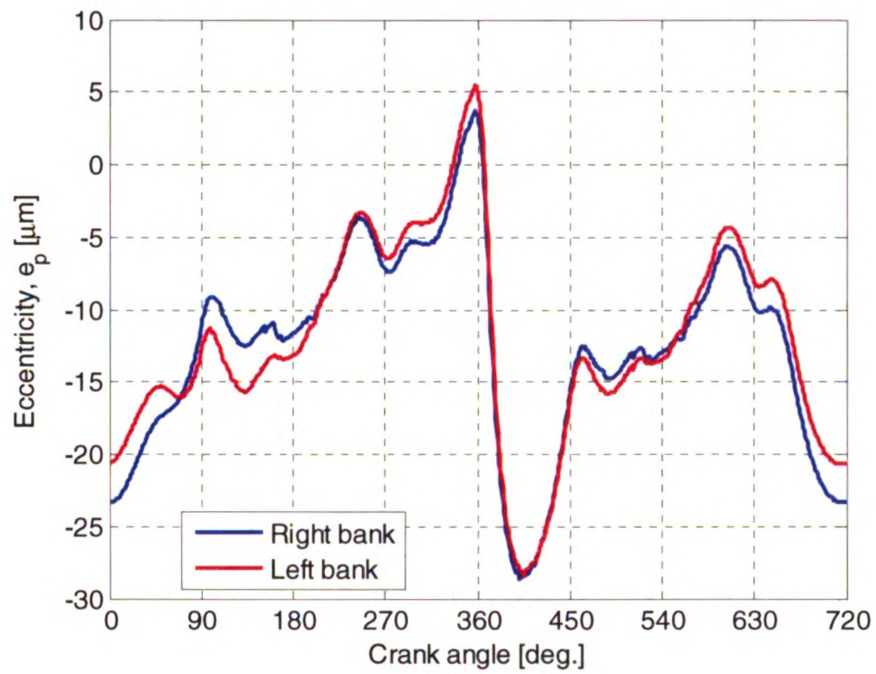


(b)

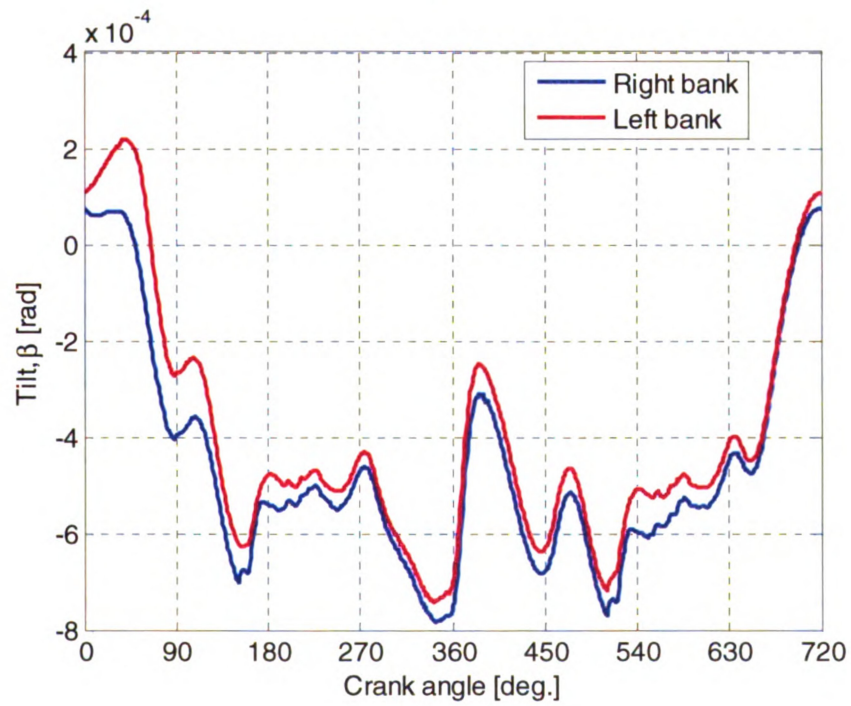
**Figure 5.54: Typical loading on left bank with the engine run at no load
(a) minor thrust side and (b) major thrust side**

5.4.2.2 Case 2

For the second case the cylinder bore nominal diameter was reduced by 50 μm . This was done to investigate how fluctuations in bore diameter which occur during operation affect piston skirt wear. This decrease in bore diameter reduces the amplitudes of piston secondary motion in the thrust plane (Figure 5.55) compared to Case 1 (Figure 5.50). The general trends of the motion are equivalent.



(a)



(b)

Figure 5.55: Piston secondary motion in thrust plane
(a) eccentricity at wrist-pin level and (b) piston tilt, Case 2

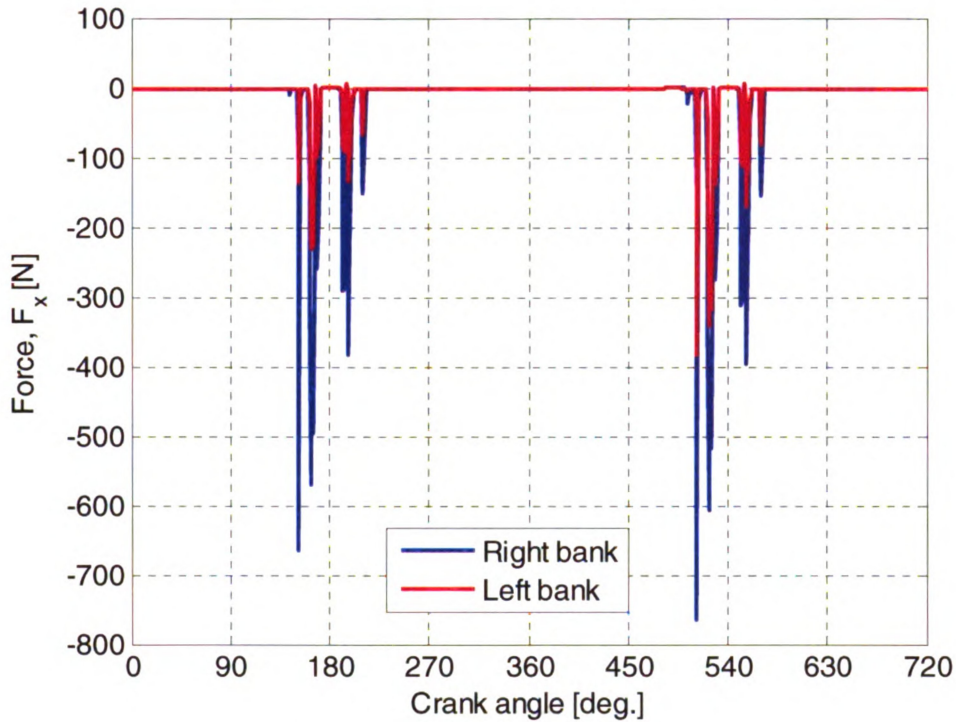


Figure 5.56: Skirt contact forces, Case 2

In this case there is also some skirt contact (Figure 5.56). The contact appears right before and after the BDC, and it is significantly higher on the minor thrust independent of the cylinder bank. A closer look at the wear distribution (Figure 5.57 and Figure 5.58) shows some wear on the major thrust side as well. On the left bank, where the major thrust side is on the inboard side, the wear magnitude is higher compared to the right bank. Similarly, the wear magnitude and distribution is higher on the minor thrust side of the right bank, which is on the inboard side. This is consistent with the hypothesis that gravity makes the inboard side more vulnerable to wear.

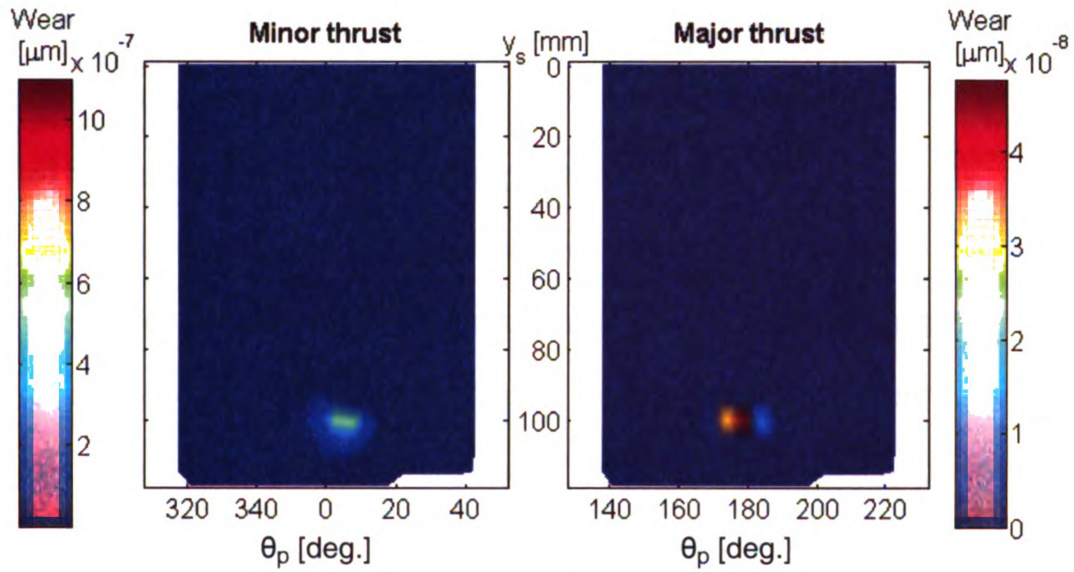


Figure 5.57: Skirt wear, left bank, Case 2

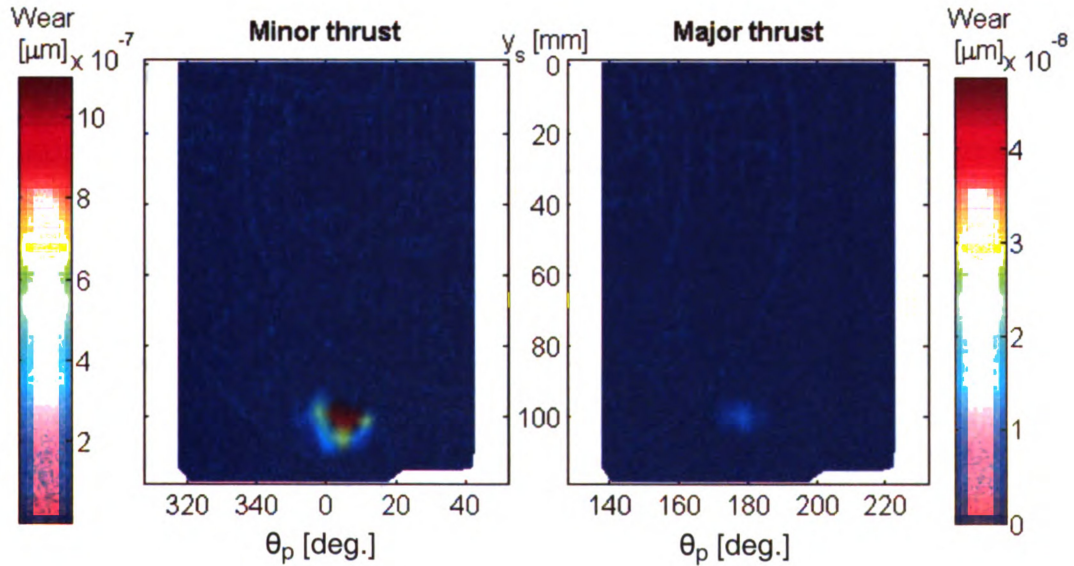


Figure 5.58: Skirt wear, right bank, Case 2

5.4.2.3 Case 3

For Case 3 the cylinder bore temperature profile was changed. The temperature was assumed to be constant circumferentially and decrease along the cylinder bore

length, (Figure 5.48) with the highest at 383 K and the lowest at 370 K. The piston secondary motion (Figure 5.60 compared to Figure 5.55) does not seem to be greatly affected by this temperature gradient along the bore length.

The skirt contact (Figure 5.59) with the cylinder bore appears at the same stage of the cycle before and after BDC. The peak contact force magnitudes, though, are lower here (compared to Case 2 Figure 5.56). This is because the oil temperature at the bottom of the cylinder is 3 K lower for this case than Case 2. Since the oil is more viscous, it can support higher loads. The skirt wear distribution (Figure 5.61 and Figure 5.62) is also very similar to the one predicted in Case 2.

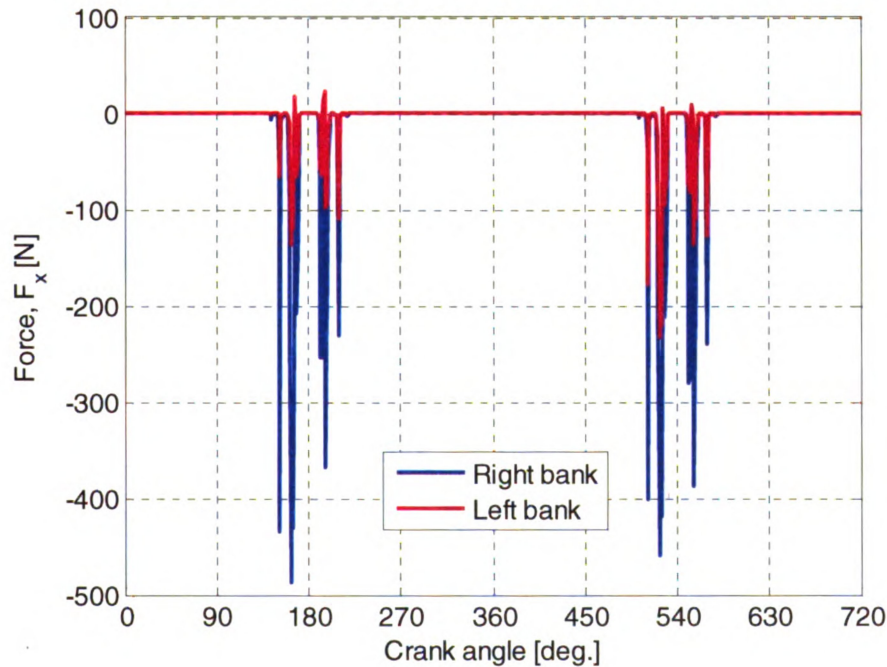
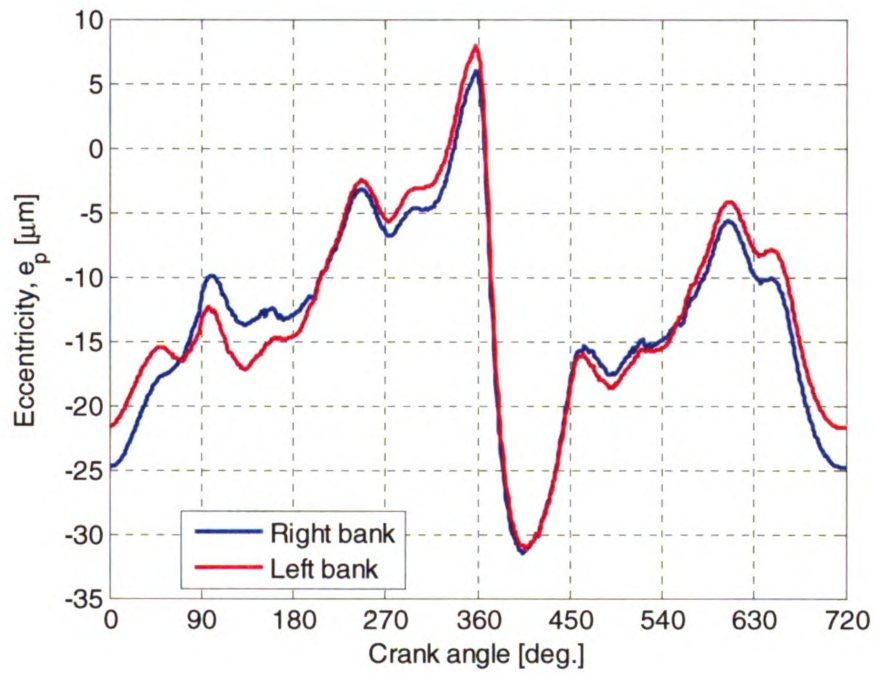
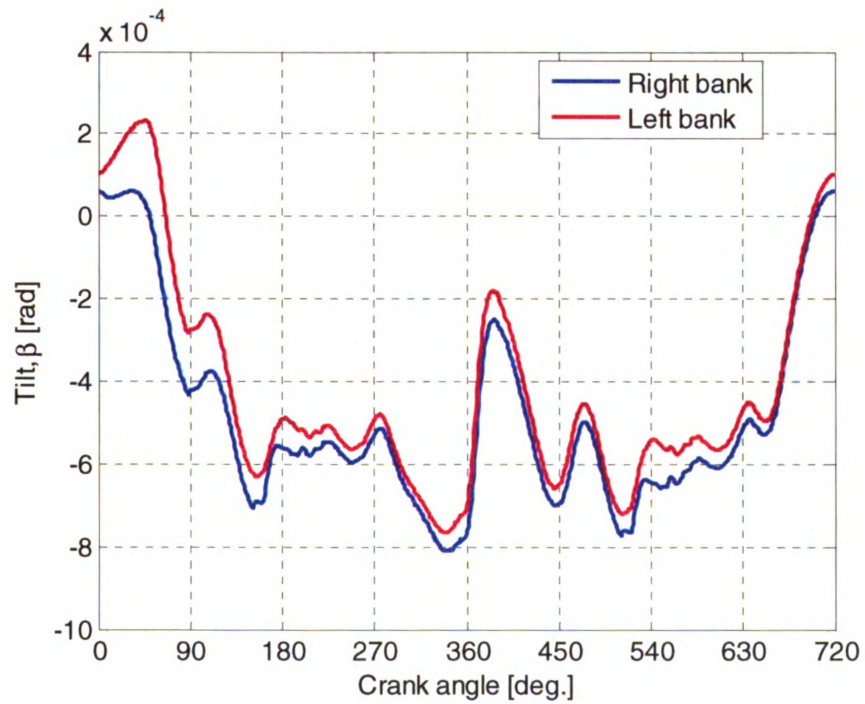


Figure 5.59: Skirt contact forces, Case 3



(a)



(b)

**Figure 5.60: Piston secondary motion in thrust plane
(a) eccentricity at wrist-pin level and (b) piston tilt, Case 3**

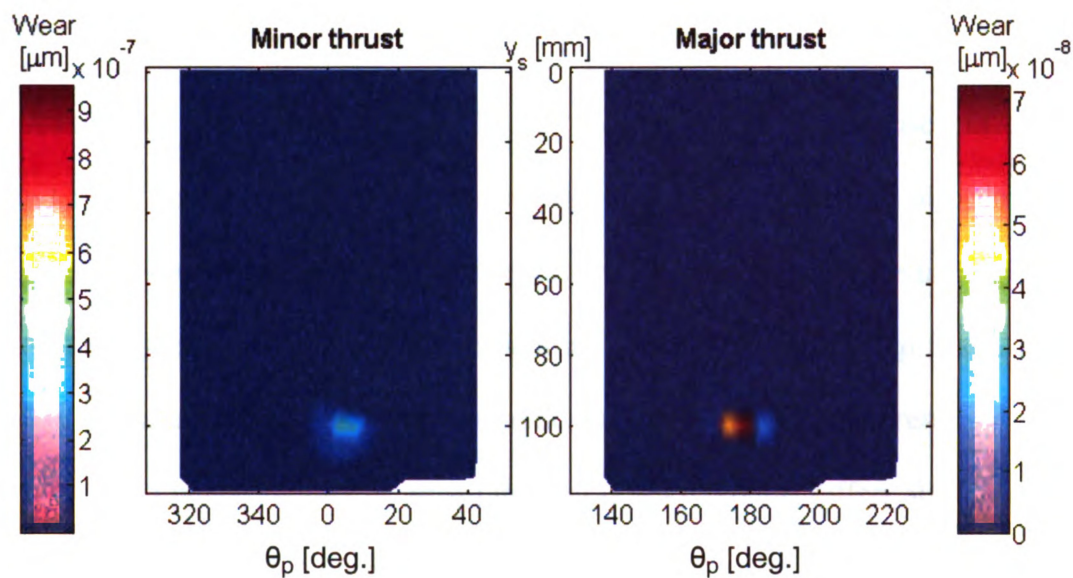


Figure 5.61: Skirt wear, left bank, Case 3

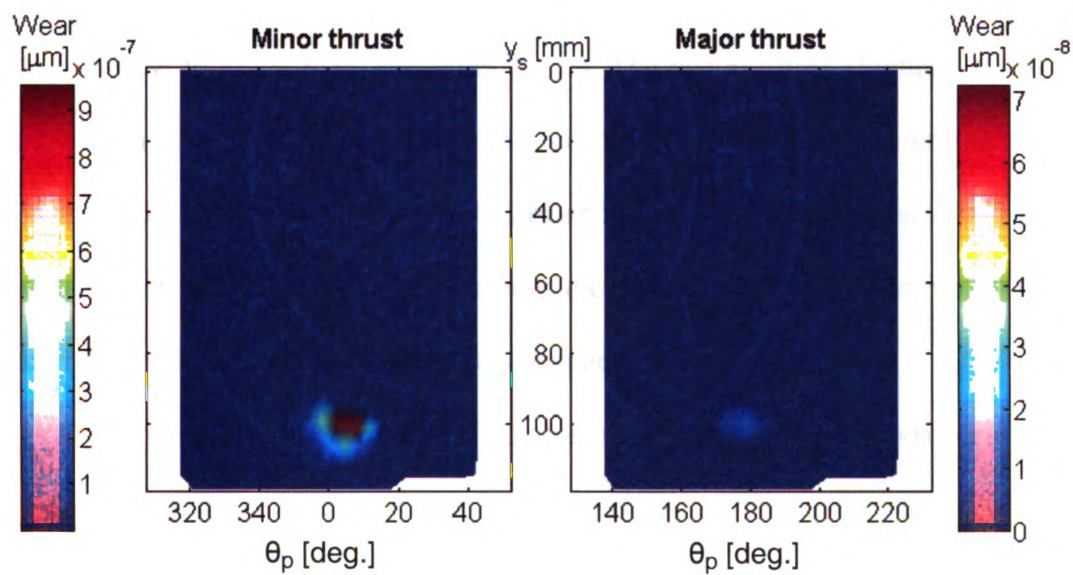


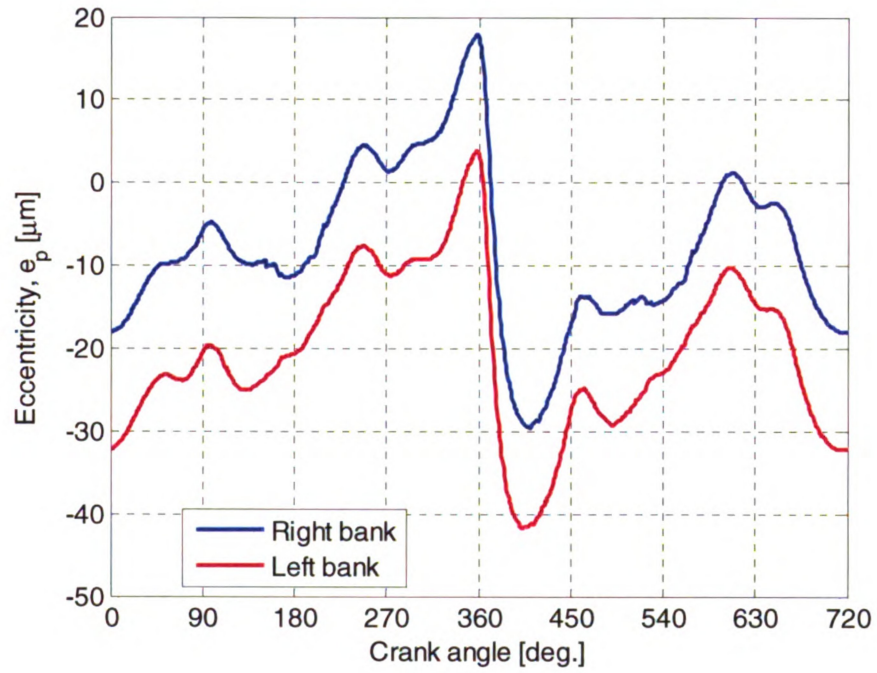
Figure 5.62: Skirt wear, right bank, Case 3

5.4.2.4 Case 4

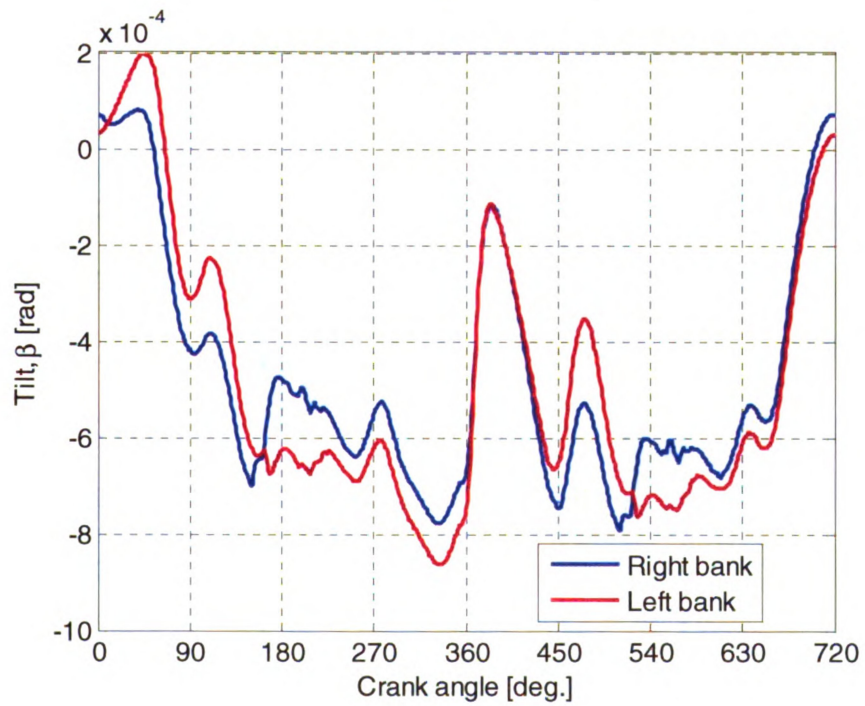
For Case 4 a temperature profile for the cylinder bore was used in order to account for a hotter inboard side (Figure 5.49). The temperature was also decreasing along the cylinder bore length. This profile was chosen because of engine packaging. The inboard sides are not exposed to the ambient air so are likely to heat up faster than the outboard side after engine start. This assumption yields some interesting results.

The piston eccentricity at wrist-pin level (Figure 5.63 a) differs significantly for the two pistons. The piston on the left bank is very closer to the major thrust side, which is the inboard side. The piston on the right bank is closer to the minor thrust side, which again is the inboard side. This is due to the lower viscosity of the oil on the hotter side which gives rise to lower hydrodynamics forces. The piston tilting (Figure 5.63 b) does not show such noticeable differences as the eccentricity. During the compression stroke, the tilting for the piston on the right bank is biased toward the minor thrust side compared to the piston on the left bank. This was not the case in Case 3. Again, the higher oil temperature on the inboard side causes this change.

The hotter inboard side also affects piston motion along the wrist-pin (Figure 5.64). In Case 1 it was observed that the pistons on the two banks had very similar motions in this direction. However, the difference in piston eccentricity (Figure 5.63 a) forces the pistons to seek and find a new equilibrium in the wrist-pin plane.



(a)



(b)

Figure 5.63: Piston secondary motion in thrust plane
(a) eccentricity at wrist-pin level and (b) piston tilt, Case 4

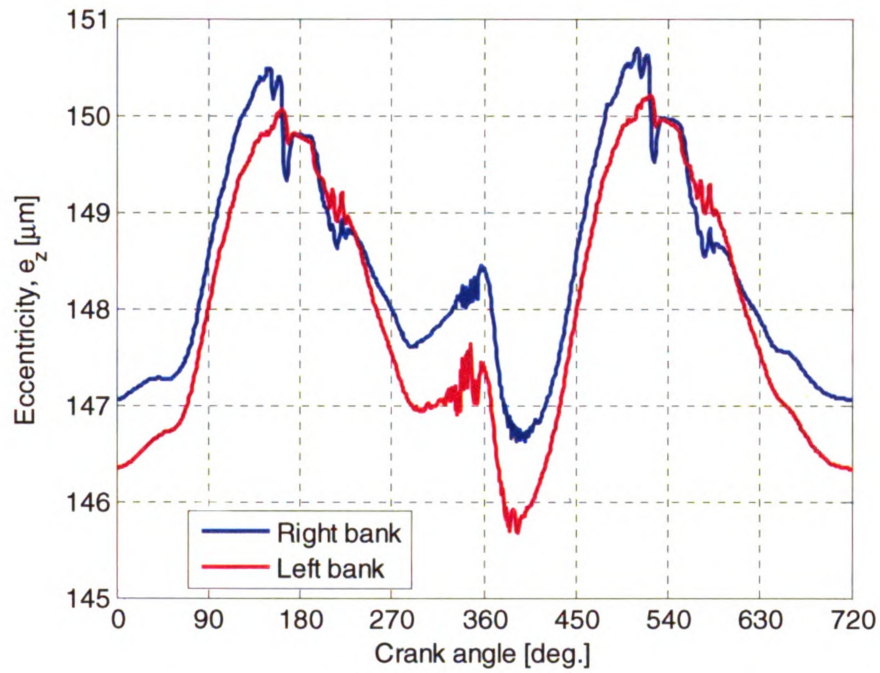


Figure 5.64: Piston translation along the wrist-pin, Case 4

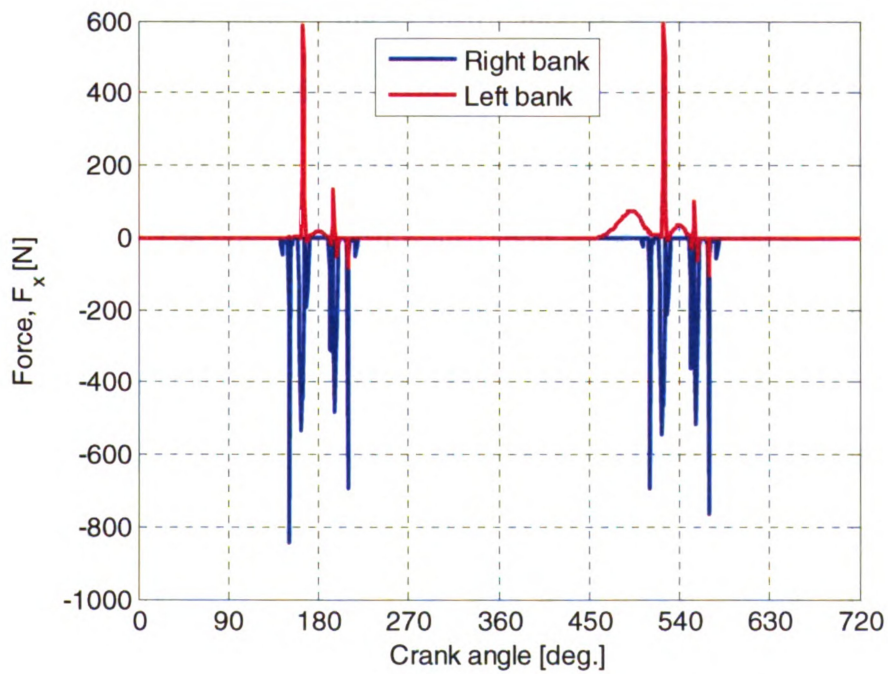


Figure 5.65: Skirt contact forces, Case 4

Furthermore this case shows significant contact force magnitude on both thrust sides, on the major for the piston on the left bank and on the minor for the piston on the right bank. Both of these are the inboard sides.

The predicted skirt wear is shown in Figure 5.66 and Figure 5.68 for left and right banks respectively. Figure 5.67 and Figure 5.69 show a typical piston loading pattern on the piston that has just initiated scuff when run at no load on the left and right banks respectively. For both cases the predicted results show consistency with the ones obtained from testing.

For the piston on the left bank (Figure 5.66) wear is predicted towards the top of the major thrust side as well as towards the bottom. This is consistent with the skirt flexibility shown in Figure 5.47; the skirt is more flexible around its center, thus it would be less likely to wear there. Similar loading is seen from tests (Figure 5.67). The piston from the test, however, shows a higher distribution of wear on the major thrust side. It should be noted that the predicted results were obtained on certain assumptions. The actual cylinder bore deformation and temperature profiles at this operating condition were not available. The predicted results also show some minute wear on the minor thrust side, whereas the one from tests shows no wear on this side. This predicted wear is so small ($\sim 1.0\text{E-}7 \mu\text{m}$) that it is assumed negligible.

For the piston on the right bank (Figure 5.68), wear is predicted on the minor thrust side towards the bottom of the skirt with some very low magnitude wear on the major thrust side. A similar pattern is seen on the minor thrust side of the test piston (Figure 5.69); however, again it shows no wear signs in the outboard major thrust side.

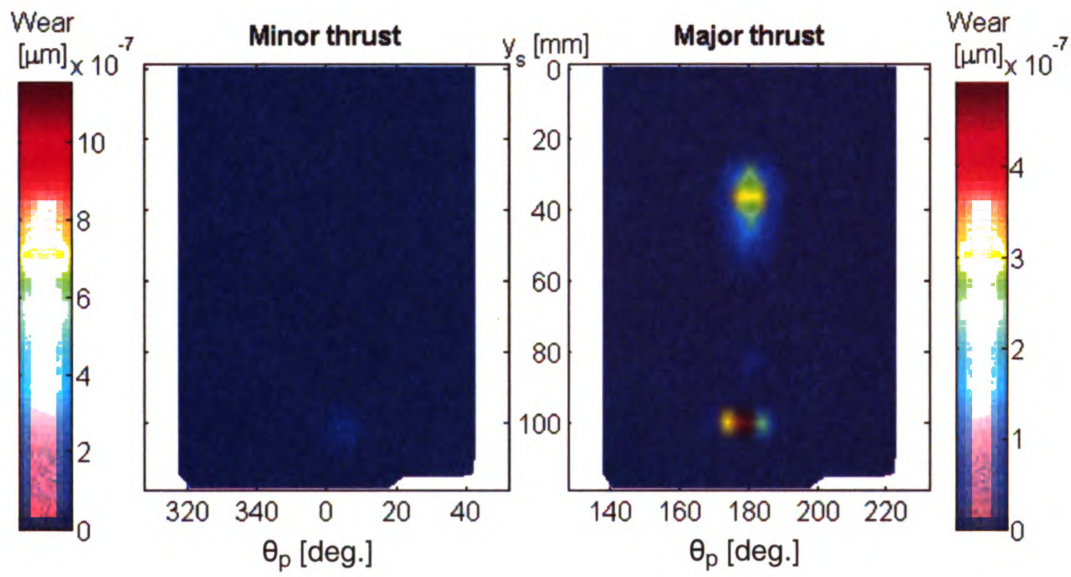
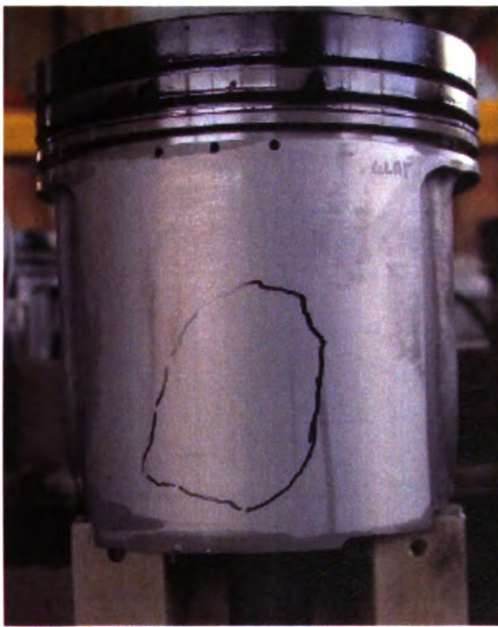
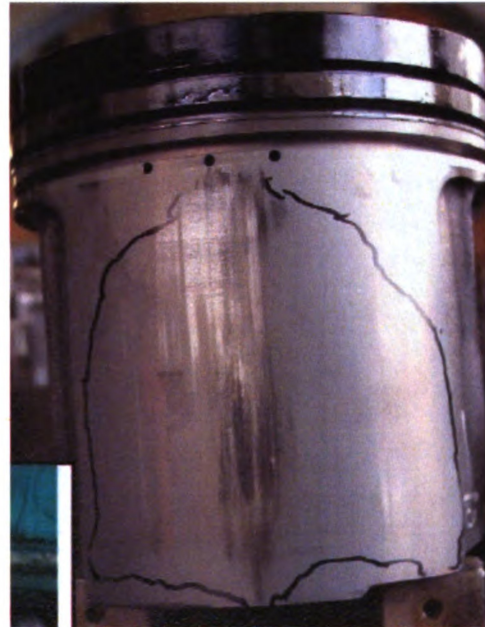


Figure 5.66: Skirt wear, left bank Case 4



(a)



(b)

Figure 5.67: Piston wear on left bank (a) minor thrust side and (b) major thrust side

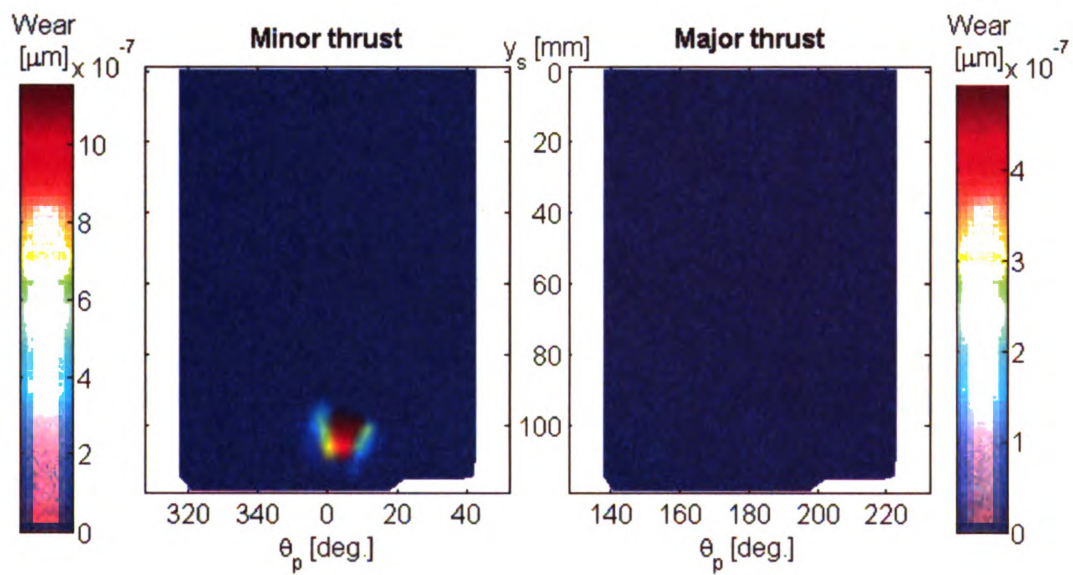


Figure 5.68: Skirt wear, right bank, Case 4

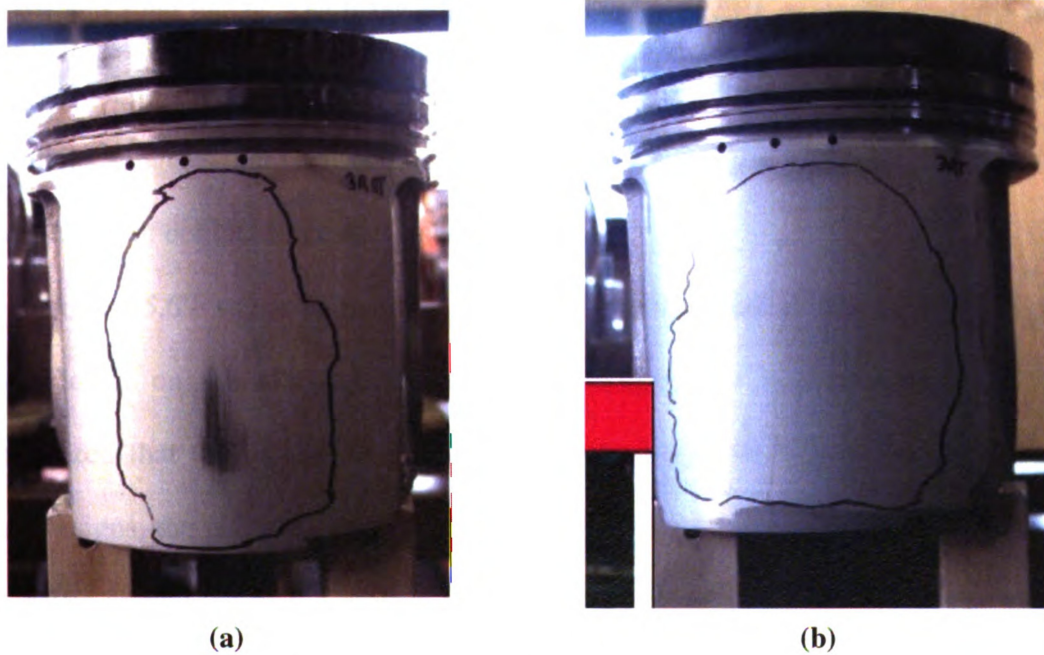
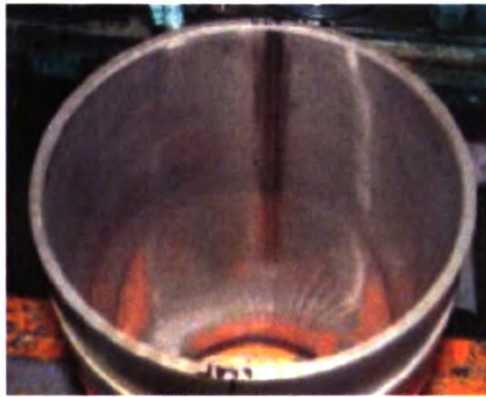
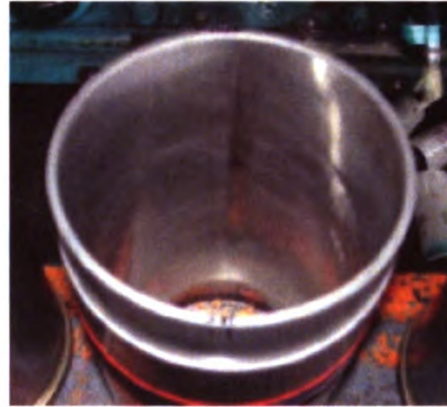


Figure 5.69: Piston wear on right bank (a) minor thrust side and (b) major thrust side



(a)



(b)

Figure 5.70: Wear marks on cylinder liner (a) left bank bottom of major thrust side, (b) right bank bottom of minor thrust side

Figure 5.70 shows the wear marks from the cylinder liner of the test engine from both left and right banks. The wear marks appear at the bottom of the liner on the major thrust side on the left bank and on the minor thrust side on the right bank. The location of these marks suggests that wear occurs when the piston is at BDC which is consistent with the prediction of contact forces at Cases 2, 3, and 4.

Figure 5.69 suggests that the numerical model predicts the location of wear slightly lower on the skirt from where it is observed in tests (Figure 5.70). It is hypothesized that this is due to one of the known limitations of the model. In some engine designs, the piston skirt drops below the cylinder bore at BDC (Figure 5.71). For the specific engine the piston drop is about 20 mm which is consistent with the location where wear is observed. Once the skirt drops below the cylinder liner, there is no generation of hydrodynamic or contact pressures. The pressures, though, developed in the region surrounded by the cylinder liner can lead to moments which favor tilting about the wrist-pin and thus making the inboard side more vulnerable to wear.

In the present numerical model, the piston drop is ignored. It is assumed that the skirt is always surrounded by the cylinder bore. Hence, when the piston is at BDC, hydrodynamic and contact force are generated until the very bottom of the skirt. Hence it is believed that this limitation causes the predicted wear to appear lower on the skirt than the observed wear from engine tests.

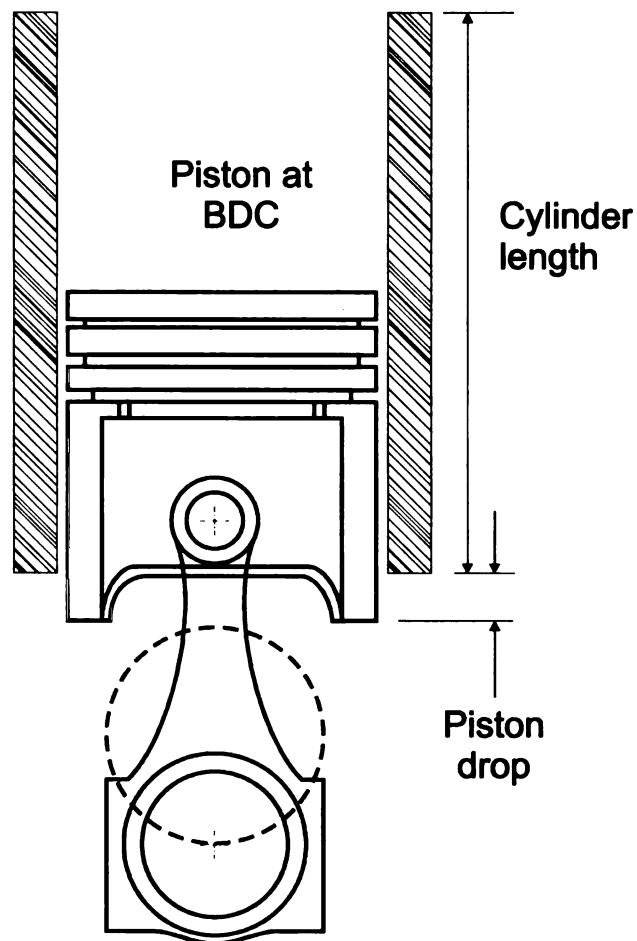


Figure 5.71: Piston drop

5.4.3 Remarks

These numerical experiments and the observations from tests lead to some conclusions. Gravity can make the inboard side of V-engines more vulnerable to wear no matter if that side is the major or minor thrust side. This is magnified in heavy-duty diesel engines where the mass of the piston assembly is significantly high compared to light-duty engines. Also these heavy-duty engines are usually operated at low speeds, 750-1500 RPM, which makes piston inertia less dominant over gravity compared to light-duty engines which operate at higher speeds.

Cylinder bore deformation can promote skirt wear. A 50 μm change in the nominal cylinder bore diameter which effectively changed the cylinder bore deformation profile resulted in skirt wear.

The oil temperature distribution can greatly affect the prediction of wear. It has been observed that a careful selection of the cylinder bore temperature distribution profile can yield results which are comparable to ones observed in tests.

The piston drop, despite the fact that it has been ignored so far in the model, appears to be a crucial factor in the correct prediction of skirt wear.

All these suggest that in order to make definitive conclusions for the root causes of skirt wear in this engine, accurate representations are required for the cylinder bore temperature and deformation distributions at these operating conditions. Furthermore, the numerical model needs to be improved to account for piston drop.

CHAPTER 6. AN OPTIMIZATION ALGORITHM FOR PISTON SKIRT PROFILES

6.1 Introduction

Internal combustion engine design is driven by several goals, most notably improving efficiency and increasing user comfort. Achieving these goals is greatly affected by piston design. An important aspect of piston design, affecting both efficiency and comfort, is the design of the piston skirt profile. The piston skirt is the part of the piston below the oil-ring groove; it acts as a bearing surface supporting the reciprocating piston within the cylinder bore. A well designed, barrel-shaped skirt profile can help reduce piston slap (noise) and skirt friction, both important factors contributing to engine efficiency and user comfort. The skirt achieves this by aiding in the build-up of hydrodynamic pressures, facilitating support of the piston within the center of the cylinder, and avoiding slapping on the cylinder bore walls. The design of the skirt profile is critical. Too high a profile can lead to severe contact between the skirt and the cylinder bore, which will result in the loss of power. The optimal shape profile balances piston slap and skirt friction and can improve engine efficiency and user comfort significantly. In this chapter the optimization of the skirt profile of a piston of a 3.0 liter engine mounted on a single cylinder research engine is discussed. The optimization is performed using an adaptive response surface method, tailored specifically to piston skirt design.

The relation between skirt profile and piston performance involves complex, non-linear behavior. Supporting the analysis of this behavior, a number of piston performance

simulation software implementations are in use in industry as well as in engine research, e.g. [6, 16, 57, 81, 82, 29, 74, and 53]. These models consider the effects of the skirt profile but treat profile height as prescribed input, usually provided as 2-D coordinates along the skirt length. The models are quite effective in analyzing piston performance, but they are complex, computationally intensive, and available to practicing engineers primarily as black-box software packages. Thus formal optimization of piston skirt profiles is difficult to perform.

Since piston performance simulations are carried out using black-box software packages, optimization of skirt profiles needs to be performed on surrogate models. The interested reader is referred to [64] and [72] for a thorough review of surrogate modeling techniques. In this work the pseudo-adaptive response surface method (pARSM) is introduced, tailored specifically to solve the piston skirt profile optimization problem. The method is a variation of the *adaptive* response surface method (ARSM) presented in [71] and [70]. The modifications introduced here are designed to address issues that arise specifically in piston skirt design and to simplify the procedure while retaining much of its basic structure, balancing ease of use with efficiency and mathematical rigor.

6.2 Overview of Piston Modeling and Performance

The assessment of piston lateral dynamics, which define piston slap and skirt friction, requires the solution of a highly nonlinear problem. The interested reader is referred to Chapter 3 for a detailed analysis of the piston dynamics problem. Here the most relevant results used in the evaluation of the performance of a piston skirt design are included.

The piston position within the cylinder directly affects the oil film thickness (Figure 6.1). For small tilt angles β the oil film thickness h is given by,

$$h = h_o - \delta \quad (6.1)$$

In (6.1) h_o is the oil film thickness due to the elastohydrodynamic effects. It is a function of several variables, including the cylinder diameter (d_{cyl}), the piston skirt nominal diameter (d_n), the eccentricity at the wrist pin level (e_p), the piston tilt (β) and the elastic deformations of the skirt and cylinder bore (δ_s and δ_b), i.e.,

$$h_o \equiv h_o(d_{cyl}, d_n, e_p, \beta, \delta_s, \delta_b) \quad (6.2)$$

The variable δ in (1) represents the height of the skirt profile. This is the design variable in the optimization problem considered in this work.

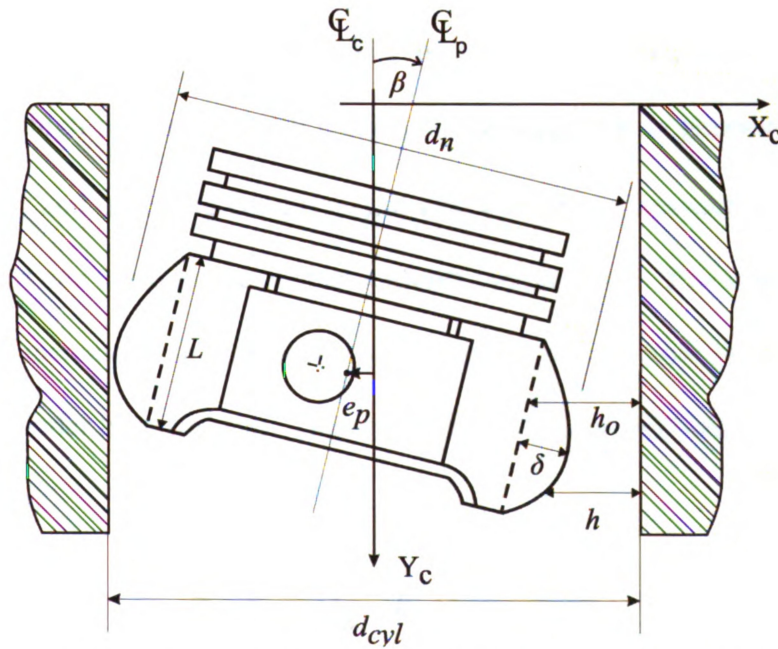


Figure 6.1: Representation of skirt profile and oil film thickness

All parameters appearing in (6.1) and (6.2) affect the piston transverse acceleration \ddot{e}_p and the piston angular acceleration $\ddot{\beta}$. High magnitudes of the transverse and angular accelerations suggest higher impacts of the piston on the cylinder wall. This leads to energy losses in the form of noise and increased discomfort for the vehicle occupants. Consequently, in standard practice the root mean square (RMS) values of accelerations are used to measure the performance of the piston skirt as it relates to piston slap. Here the function A_{RMS} in (6.3) will be used as the objective function in the design problem.

$$A_{RMS} = \left[\frac{1}{720} \int_0^{720} \left[\ddot{e}_p(h(\delta), \theta) L^{-1} \right]^2 + \left[\ddot{\beta}(h(\delta), \theta) \right]^2 d\theta \right]^{1/2} \quad (6.3)$$

In (6.3) L is the skirt length, used to normalize the transverse acceleration. The integral is evaluated over a full four-stroke cycle, which is 720 crank angle degrees.

The net friction work on the skirt is an additional measure of piston skirt performance. A high profile typically leads to a low A_{RMS} but in general (depending on engine geometry and operating conditions), it also leads to an increase in the net friction work on the skirt due to excessive contact with the cylinder bore. This is undesirable, as it can result in an increase in the net power loss of the engine, as well as increased wear of the skirt and cylinder bore surfaces. Thus a constraint will be imposed on the net friction work on the skirt,

$$W_{fr} = \frac{s}{720} \int_0^{720} F_f(h(\delta), \theta) d\theta \quad (6.4)$$

Here s is the total distance traveled by the piston over a cycle and F_f is the total friction force on the skirt. Using piston transverse and angular accelerations and friction work on the skirt to assess piston performance is standard practice.

The engine configuration used for this work is the spark-ignition engine used in [48] and [49]. Some of the main engine and piston data are shown in Table 6.1. A cylinder bore deformation is considered in the simulations as described in [48]. Analysis is performed using PIFEAD (Chapter 3) as the modeling software.

A PIFEAD simulation can be performed considering a rigid, a semi-elastic or an elastic piston. A rigid piston simulation assumes that the piston experiences no deformations. In the case of a semi-elastic piston simulation the piston experiences deformations due to thermal, inertial and combustive pressure loads; however, its deformation is invariant to the hydrodynamic and contact loads developed at the skirt surface. An elastic piston simulation considers the piston deformations due to the skirt loads. Such a model is computationally very expensive compared to the other two, as the problem becomes highly nonlinear. Fortunately, results obtained by semi-elastic and elastic simulation are comparable, and therefore in the following sections the semi-elastic piston model is used.

Table 6.1: Engine and piston data

Piston skirt nominal diameter, d_n	= 90.0 mm
Piston pin offset	= -0.4 mm
Cylinder bore diameter, d_{cyl}	= 90.03 mm
Stroke	= 90.6 mm
Connecting rod length	= 169.0 mm
Coefficient of friction (piston-cylinder bore)	= 0.15
Engine speed	= 3000 RPM

6.3 Optimization Problem

6.3.1 Design Variables In Piston Skirt Design

To represent the geometry of the skirt profile a quartic polynomial interpolation is used. A schematic of the skirt profile is shown in Figure 6.2. The design variables are the skirt profile parameters a_0 , a_1 , a_2 , a_3 and a_4 , defined as follows:

a_0 is the profile height at the top of the skirt

a_1 is the profile height at the bottom of the skirt

a_2 is the location along the skirt length where the skirt profile height is at maximum

a_3 is the skirt profile maximum height, and

a_4 is the first derivative of the profile at the top of the skirt.

The piston nominal diameter d_n is measured at the widest point on the skirt, that is, at a_2 where the skirt profile height is maximum. The skirt profile local coordinate system (x_s - y_s) on a final production piston is referenced on the piston nominal diameter, thus on a reference skirt profile $a_3 = 0$. During the optimization process a_3 can vary and if the optimal value deviates from zero, this would result in a change of the piston's nominal diameter. The parameters a_0 , a_1 and a_3 can take both negative and positive values; a_2 and a_4 can take only positive values. Using these variables the skirt profile can be readily described by a quartic polynomial of the form

$$\delta(y_s) = C_0 + C_1 y_s + C_2 y_s^2 + C_3 y_s^3 + C_4 y_s^4 \quad (6.5)$$

In (6.5) y_s is the skirt coordinate along its length, and C_0 to C_4 are coefficients that can be derived as explicit functions of the five design variables and the skirt length. Their definition is included in Appendix A.

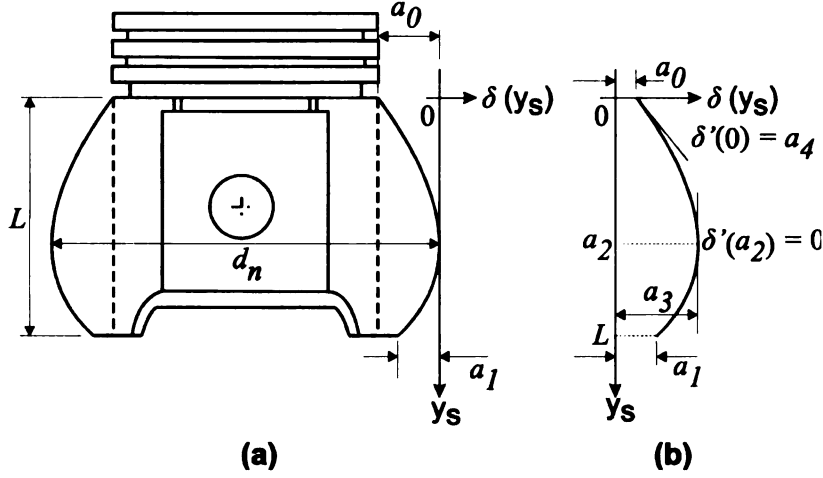


Figure 6.2: Skirt profile described by a quartic polynomial (a) skirt profile coordinate system referenced to the piston nominal diameter, (b) design variables

6.4 Geometric Constraints

A constraint has to be imposed on $\delta(y_s)$ in (6.5) to ensure that the profile is always barrel-shaped. One way to achieve this is by imposing a constraint on the first derivative of $\delta(y_s)$. For instance, a constraint that requires that the discriminant of the first derivative of $\delta(y_s)$ be negative guarantees that the profile $\delta(y_s)$ has only one stationary point [45]. The discriminant of a general cubic polynomial of the form, $f(x) = c_3x^3 + c_2x^2 + c_1x + c_0$ is

$$D_3(f) = c_1^2 c_2^2 - 4c_0 c_2^3 - 4c_1^3 c_3 + 18c_0 c_1 c_2 c_3 - 27c_0^2 c_3^2 \quad (6.6)$$

and the first derivative of $\delta(y_s)$ is given by

$$\delta'(y_s) = C_1 + 2C_2 y_s + 3C_3 y_s^2 + 4C_4 y_s^3 \quad (6.7)$$

Combining (6.6) and (6.7) results in the desired constraint.

6.4.1 Problem Formulation

The performance of the piston is measured by the functions A_{RMS} and W_{fr} , defined in (6.3) and (6.4). In the present formulation the RMS acceleration is used as the objective function, while a bound on the maximum allowable friction work is imposed as a performance constraint. Formally, the optimization problem is:

Optimization Problem

Find $\mathbf{a} = \{a_0, a_1, a_2, a_3, a_4\}^T \in \mathbb{R}^5$ that

$$\text{Minimize } A_{RMS} = \left[\frac{1}{720} \int_0^{720} \left[\ddot{e}_p(h(\delta), \theta) L^{-1} \right]^2 + \left[\ddot{\beta}(h(\delta), \theta) \right]^2 d\theta \right]^{\frac{1}{2}}$$

(6.8)

Subject to $g_1(\mathbf{a}) = W_{fr} - W_{\max} \leq 0$

$$g_2(\mathbf{a}) = D_3(\delta'(y_s)) + \varepsilon \leq 0$$

$$\mathbf{a}_{\min} \leq \mathbf{a} \leq \mathbf{a}_{\max}$$

The complexity of the simulation models required to evaluate A_{RMS} and W_{fr} prevents the solution of the optimization problem, (6.8), directly. Instead, its solution is sought through the use of a surrogate optimization problem where the piston performance measures $A_{RMS}(\mathbf{a})$ and $W_{fr}(\mathbf{a})$ are replaced by surrogate functions $\hat{A}_{RMS}(\mathbf{a})$ and $\hat{W}_{fr}(\mathbf{a})$. The surrogate optimization problem is:

Surrogate Optimization Problem

$$\begin{aligned}
 &\text{Find} \quad \mathbf{a} = \{a_0, a_1, a_2, a_3, a_4\}^T \in \mathbb{R}^5 \\
 &\text{Minimize} \quad \hat{A}_{RMS}(\mathbf{a}) \\
 &\text{Subject to} \quad \hat{g}_1 = \hat{W}_{fr}(\mathbf{a}) - W_{\max} \leq 0 \\
 &\quad \quad \quad g_2(\mathbf{a}) = D_3(\delta'(y_s)) + \varepsilon \leq 0 \\
 &\quad \quad \quad \mathbf{a}_{\min} \leq \mathbf{a} \leq \mathbf{a}_{\max}
 \end{aligned} \tag{6.9}$$

In (6.8) and (6.9), \mathbf{a}_{\min} and \mathbf{a}_{\max} represent lower and upper bounds on the design variables. These bounds are selected based on the nominal piston to cylinder bore clearance and on the operating conditions. W_{\max} is the maximum allowable net friction work done on the skirt. In the absence of severe contact between the skirt surface and the cylinder bore, hydrodynamic shear dominates friction. Thus, friction work varies linearly with engine speed, and therefore W_{\max} is selected based on the operating condition. Typically, the bound W_{\max} is set to a lower value for lower engine speeds because at these speeds hydrodynamic shear is low. Higher friction values are allowed at higher

speeds because hydrodynamic shear is higher and thus W_{max} is increased at these speeds. Constraint g_2 guarantees that feasible skirt profiles have only one stationary point (ϵ is a small positive number, e.g., 0.005). Functions $\hat{A}_{RMS}(\mathbf{a})$ and $\hat{W}_{fr}(\mathbf{a})$ are the surrogate functions, respectively, for the acceleration and the friction work, constructed as described in the following section.

6.4.2 Skirt Profiles Described by Other Equations

6.4.2.1 Non-Uniform Rational Basis Splines

The skirt profile can alternatively be defined by Non Uniform Rational Basis Splines (NURBS). The NURBS are well known for their ability to represent freeform surfaces mathematically. They are widely used in computer graphics and computer-aided design (CAD). A NURBS curve, $Q(x)$ is defined by its order, k , its control points, B_i , its weights, w_i , and a knot vector, \mathbf{t} .

$$Q(x) = \frac{\sum_i w_i B_i N_{i,k}(x)}{\sum_i w_i N_{i,k}(x)} \quad (10)$$

where $N_{i,k}$ is the i^{th} basis function of order k , given by

$$N_{i,1}(x) = \begin{cases} 1 & \text{if } t_i \leq x \leq t_{i+1} \\ 0 & \text{otherwise} \end{cases} \quad (11)$$

$$N_{i,k}(x) = \frac{(x - t_i) N_{i,k-1}(x)}{t_{i+k-1} - t_i} + \frac{(t_{i+k} - x) N_{i+1,k-1}(x)}{t_{i+k} - t_{i+1}}$$

For a thorough discussion on NURBS the reader is directed to [56].

Conic sections can be described by quadratic NURBS curves, and the knot vector for a curve with three control points is given as,

$$\mathbf{t} = \{0, 0, 0, 1, 1, 1\} \quad (12)$$

A conic section is used to describe the NURBS skirt profile shown in Figure 6.3(a). The control points appear as 3-D coordinates; however the third coordinate corresponds to the weight, $B_i(y_s, \delta(y_s), w_i)$. The two control points at the edges have a weight of 1. As before, a_0 is the profile height at the top of the skirt, a_1 is the profile height at the bottom of the skirt, and a_2 is the location along the skirt length where the skirt profile height is at maximum. In this case a_3 is the position of the third control point along $\delta(y_s)$, and a_4 is the weight of the third control point. No further constraints are required in this case, and by varying these five variables the shape of the profile changes, always being barrel-shaped. The disadvantage of this profile is that with three control points it is very difficult to obtain an adequate curvature.

The curvature of a NURBS profile with four control points as shown in Figure 6.3(b) can be much easier controlled. However, the design variables increase to eight, as the extra control point introduces another three and in turn the cost of optimization.

The advantage of this type of profile is that NURBS would not require a geometric constraint and any random combination of design variables would yield a barrel-shaped profile, as long as their upper and lower bounds are selected carefully.

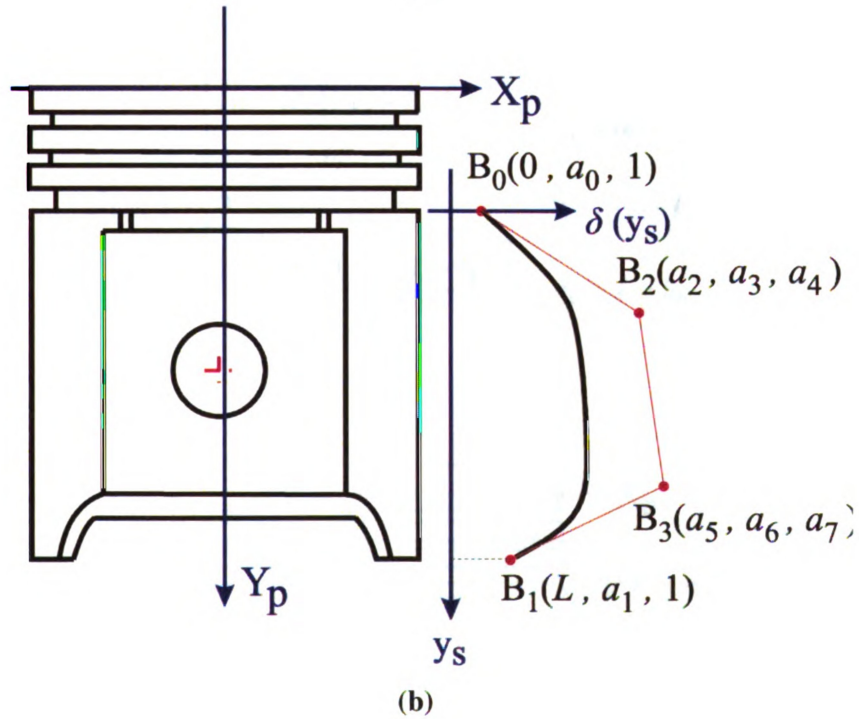
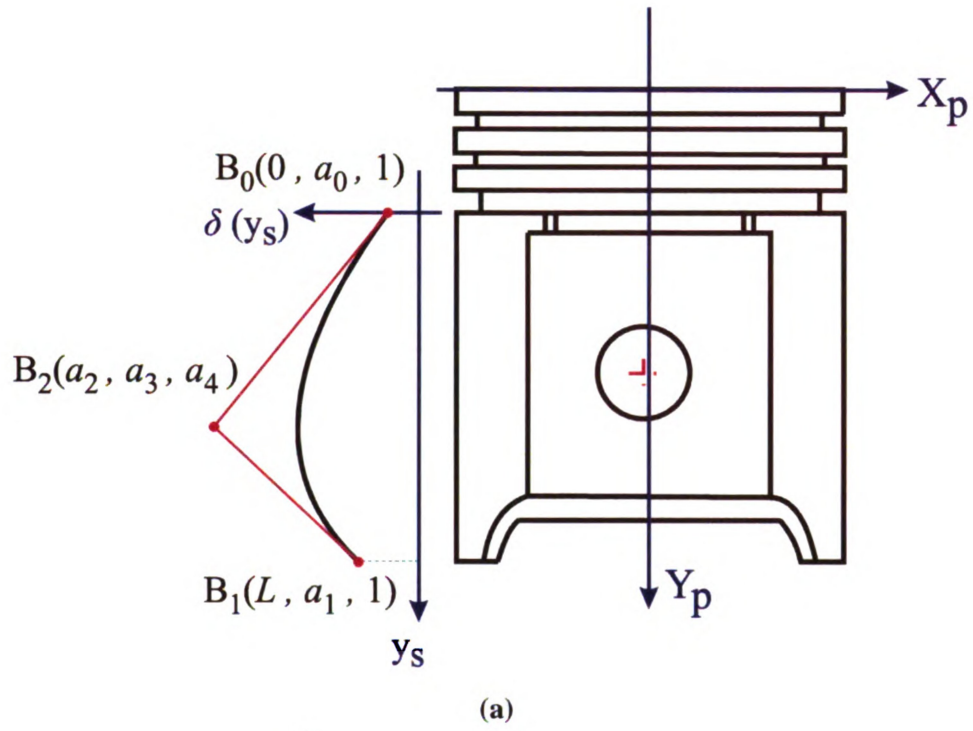


Figure 6.3: Skirt profile described by NURBS with (a) three and (b) four control points

6.4.2.2 Barrel Equation

The barrel equation is also widely used to describe skirt profiles. Starting from the generalized equation (6.13) of a barrel formed by parabolic segments symmetrical about the midplane, (6.14) can be derived describing the skirt profile shown in Figure 6.4. Such a profile again has only five design variables: the piston nominal diameter R_n , the radii at the top and bottom of the skirt, r_t and r_b , and the effective heights of the top and bottom parts of the barrel shape, h_t and h_b . As with the NURBS profile, a careful selection of the limits of the design variables eliminates the need of any geometric constraints.

$$f(y_s) = R_n + a \left(y_s - \frac{1}{2}L \right)^2 \quad (6.13)$$

$$\delta(y_s) = \begin{cases} \frac{(r_t - R_n)(y_s - h_t)^2}{h_t^2} & y_s < h_t \\ 0 & h_t \leq y_s \leq L - h_b \\ \frac{(r_b - R_n)(y_s - L + h_b)^2}{h_b^2} & y_s > L - h_b \end{cases} \quad (6.14)$$

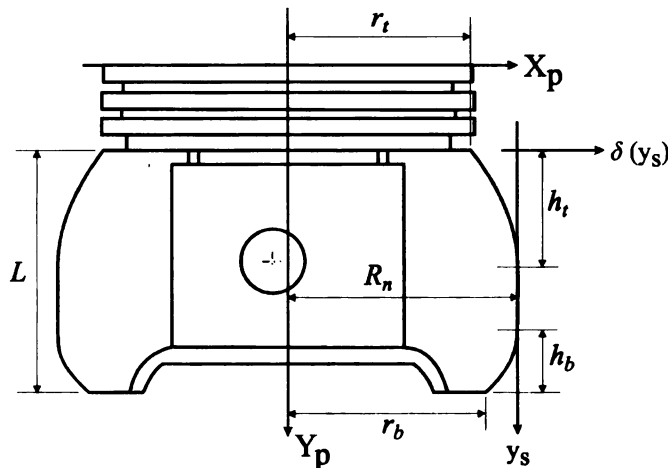


Figure 6.4: Skirt profile described by the barrel equation

6.5 The Surrogate Model

Surrogate models for \hat{A}_{RMS} and \hat{W}_{fr} are built by fitting a polynomial response surface to data values obtained from computer simulations performed on a small set of design sampling points. The set of all such design points is sometimes referred to as the design library. Quadratic and cubic polynomial response surfaces are explored here, in order to assess their adequacy in the context of the piston skirt profile optimization problem. The general form of the polynomial response surface approximation \hat{y} (either \hat{A}_{RMS} or \hat{W}_{fr}) in n design variables is given by

$$\hat{y} = \alpha_0 + \sum_{i=1}^n \alpha_i x_i + \sum_{i=1}^n \alpha_{ii} x_i^2 + \sum_{i=1}^n \sum_{\substack{j=1 \\ i < j}}^n \alpha_{ij} x_i x_j + \sum_{i=1}^n \sum_{\substack{j=1 \\ i \neq j}}^n \gamma_{ij} x_i^2 x_j + \sum_{i=1}^n \gamma_{ii} x_i^3 \quad (6.15)$$

This represents a cubic polynomial response surface approximation where α 's and γ 's are the regression coefficients and x 's are the design variables. A quadratic response surface approximation can be readily obtained by setting all γ 's to zero. The above equation can be written in matrix form as

$$\boldsymbol{\varepsilon} = \mathbf{y} - \mathbf{X}\mathbf{b} \quad (6.16)$$

In (6.16) $\boldsymbol{\varepsilon}$ is the vector of the residual error, \mathbf{y} is the vector of data values and \mathbf{b} is the vector of the regression coefficients. For n_d data points and n_b regression coefficients, matrix $\mathbf{X} \in \mathbb{R}^{n_d \times n_b}$ is given by

$$\mathbf{X} = \begin{bmatrix} \xi_1(\mathbf{x}_1) & \xi_2(\mathbf{x}_1) & \cdots & \xi_{n_b}(\mathbf{x}_1) \\ \xi_1(\mathbf{x}_2) & \xi_2(\mathbf{x}_2) & \cdots & \xi_{n_b}(\mathbf{x}_2) \\ \vdots & \vdots & \ddots & \vdots \\ \xi_1(\mathbf{x}_{n_d}) & \xi_2(\mathbf{x}_{n_d}) & \cdots & \xi_{n_b}(\mathbf{x}_{n_d}) \end{bmatrix} \quad (6.17)$$

where ξ_j is a monomial appearing in the polynomial equations for the i^{th} design, $\mathbf{x}_i \in \mathbb{R}^n$. The regression coefficient vector \mathbf{b} in (6.16) is obtained via least-squares minimization of the error $\boldsymbol{\epsilon}$. The quality of the surrogate model is evaluated using standard performance measures: the coefficient of determination R^2 ; the adjusted coefficient of determination R_a^2 ; the standard deviation of the error or data noise $\hat{\sigma}$; the normalized residual r and the estimated standard error, ϵ_{es} . These are standard quantities and their definition is included in Appendix A for completeness.

6.5.1 Adjustment of Regression Coefficients by IRLS

In this methodology the quality of a response surface is improved using an iteratively reweighed least-squares (IRLS) method [5]. Papila and Haftka [52] used IRLS to identify outliers in the design library and repair them. They report that an adjusted coefficient of determination R_a^2 value of 0.9 and above is required for an adequate fit. Here IRLS is used to obtain new regression coefficients for the response surface when the standard least-squares method yields an R_a^2 of less than 0.9. The response surface is approximated first via least-squares, (6.17), and the R_a^2 value is calculated. If the R_a^2 value is below 0.9, the IRLS method is used to adjust the vector of the regression coefficients iteratively. The residual at each iteration step, $\boldsymbol{\epsilon}^{(\kappa)}$, is given by

$$\boldsymbol{\epsilon}^{(\kappa)} = \mathbf{y} - \mathbf{X}\mathbf{b}^{(\kappa)} \quad (6.18)$$

Regression coefficients $\mathbf{b}^{(\kappa)}$ are obtained via

$$\mathbf{W}^{(\kappa)} \mathbf{X} \mathbf{b}^{(\kappa+1)} = \mathbf{W}^{(\kappa)} \mathbf{X} \mathbf{b}^{(\kappa)} + \mathbf{W}^{(\kappa)} \boldsymbol{\varepsilon}^{(\kappa)} \quad (6.19)$$

where the weighting matrix $\mathbf{W}^{(\kappa)}$ is diagonal with elements $w_i^{(\kappa)}$, assigned and adjusted at each iteration κ according to Beaton and Tukey [5],

$$w_i^{(\kappa)} = \begin{cases} \left[1 - \left(\frac{|\varepsilon_i^{(\kappa)} / \hat{\sigma}|}{B} \right)^2 \right]^2 & \text{if } |\varepsilon_i^{(\kappa)} / \hat{\sigma}| \leq B \\ 0 & \text{otherwise} \end{cases} \quad (6.20)$$

B is a tuning constant, usually $1 < B < 3$, here set to 1.9, as used in [52]. If all the weights w_i are set to one, IRLS reduces to the standard least-squares. Iterations stop when $\|\mathbf{b}^{(\kappa+1)} - \mathbf{b}^{(\kappa)}\|$ is less than a prescribed tolerance. While there is no rigorous proof of convergence of this strategy, the method is very robust and has never failed to converge in the present optimization problem.

6.5.2 Generation of the Initial Set of Design Points

The evaluation of piston performance functions A_{RMS} and W_{fr} requires the use of complex, computationally expensive black-box analysis tools. Typically such tools fail if the piston skirt shape is not barrel-shaped, i.e., they fail for any design that does not satisfy constraint g_2 in (6.8) or (6.9). Therefore the initial set of designs must be g_2 -feasible and thus a standard Latin Hypercube Design (LHD) will not be sufficient to generate it. Instead a space-filling strategy is used, modified to account for constraint g_2 on the geometry of the skirt. Two alternatives are investigated:

(i) A max-min strategy. This strategy seeks points that maximize the function

$$d_{\min}(\mathbf{x}_1, \dots, \mathbf{x}_{n_d}) = \min_{i < j \leq n_d} d_{ij} = \|\mathbf{x}_i - \mathbf{x}_j\|$$

and satisfy constraint g_2 . As function d_{\min} is highly non-convex, direct maximization of d_{\min} is very difficult and computationally intensive even for a small number of points n_d . Instead, the heuristic strategy of Stinstra et al. [65] is used. In this strategy, after simple scaling is used to normalize the range $I_a = [a_{\min}, a_{\max}]$ of each variable, an initial set of n_d , g_2 -feasible designs \mathbf{x}_i is generated (e.g., by generating a larger number of LHD points and rejecting those that violate g_2). The position of each point \mathbf{x}_i is adjusted by solving the following problem for $i = 1, \dots, n_d$

Problem S_i : For fixed $\mathbf{x}_1, \dots, \mathbf{x}_{i-1}, \mathbf{x}_{i+1}, \dots, \mathbf{x}_{n_d}$ find \mathbf{x}_i that

$$\begin{aligned} &\text{maximizes} && d_{\min}^{(i)} \\ &\text{subject to} && d_{\min}^{(i)} \leq \|\mathbf{x}_i - \mathbf{x}_j\|, \quad j = 1, \dots, i-1, i+1, \dots, n_d \\ &&& g_2(\mathbf{x}_i) \leq 0 \\ &&& \mathbf{0} \leq \mathbf{x}_i \leq \mathbf{1} \end{aligned}$$

Problems S_i are solved using a simulated annealing algorithm. The sequence of problems S_i is repeated until no significant changes in the design points are detected. Note that the solution of this problem depends implicitly on the range I_a , as a_{\min} and a_{\max} are used in the normalization of the design variables.

(ii) A LHD Strategy with Filtering. This is a trivial implementation of a LHD strategy that generates $n > n_d$ (unconstrained) designs and rejects those that violate constraint g_2 . If n is sufficiently large, it is always possible to find the n_d g_2 -feasible designs within the initial set. If more than n_d g_2 -feasible designs are found, points with smaller values of the distance function $d_{ij} = \|\mathbf{x}_i - \mathbf{x}_j\|$, $j > i$ are rejected. This simple idea degrades the quality of LHD as a space-filling design, but, from experience, without ill consequences.

In this application, when the resulting set of initial designs is used as a starting design library for surrogate-based optimization, both strategies yield solutions of similar performance. When only a small number of sampling points is used (n_d small), the max-min strategy tends to fill the boundaries of the design space first, while the simpler LHD strategy produces more uniform spatial distributions.

6.5.3 Adding a Point to an Existing Set

On occasion it may be necessary to add a new point to an existing set of n_d-1 designs. In the case of strategy (i) above, this is achieved using a modified max-min augmentation strategy, simply by solving Problem S_{n_d} above to find \mathbf{x}_{n_d} . Alternatively, an augmented LHD strategy with filtering, (consistent with (ii) in Section 6.5.2) may be used. In pARSM, addition of new points is necessary only as prescribed in Section 6.6 (item vi).

6.6 The Pseudo-Adaptive Response Surface Method

This section outlines the pseudo-adaptive response surface method (pARSM), developed to solve the piston skirt profile optimization problem. The method is a variation of the adaptive response surface method (ARSM) method presented in [70]. Both ARSM and pARSM are iterative heuristics.

ARSM progressively reduces the size of the design domain by finding new bounds at each iteration. This reduction is accomplished through separate optimization problems that require the solution of $2n$ additional nonlinear optimization problems at each step, where n is the number of design variables. ARSM also implements a search algorithm to place the new LHD-generated points in the underrepresented regions of the reduced design space.

pARSM is designed to address the specific features of the piston skirt design optimization problem (6.8). In pARSM the design space is not reduced but only adjusted. This eliminates the need for intermediate optimization problems and simplifies the algorithm. The adjustment in the design space takes place through:

- The addition to the design library of solutions of the surrogate optimization problem (6.9) that improve upon the current design library.
- Adjustments to the allowable range of the design variables $I_a = [a_{\min}, a_{\max}]$
- Corrections to the relative importance of the data points within the surrogate approximation using IRLS .

At each pARSM iteration, one point in the design library is replaced and the surrogate model is updated. A descent (merit) function Ψ is used to check the quality of candidates to enter/leave the library,

$$\Psi(\mathbf{a}) = A_{RMS}(\mathbf{a}) + \eta \left[\max(g_1(\mathbf{a}), 0) \right] \quad (6.21)$$

where η is a scaling factor. It is selected based on the performance values of a reference design, described later. Constraint g_2 does not appear in Ψ since all candidates satisfy g_2 .

This is an outline of the pARSM iterative procedure:

- i. To start the algorithm, an initial range $I_a = [a_{\min}, a_{\max}]$ is prescribed and the initial design library is built using one of the strategies described in Section 4.2. The performance of each member of the library is evaluated by invoking the piston analysis model (a total of n_d function evaluations).
- ii. Let $D = \{\mathbf{a}_1, \dots, \mathbf{a}_{n_d}\}$ be the current design library and let Ψ_i represent the “merit” of the i -th data point in the library, i.e., $\Psi_i \equiv \Psi(\mathbf{a}_i)$. Each iteration of the pARSM algorithm starts with the construction of the current surrogate model using D , as described in Section 6.5. The quality of the approximation is monitored and adjustments to the model are made using IRLS (Section 6.5.1) if necessary. This identifies designs with large residual errors and assigns them low weights. As a result, designs with large residual errors will have less impact on the solution of the surrogate optimization problem (6.9), performed in the following step.
- iii. The surrogate optimization problem, (6.9), is solved using the current surrogate model. An off-the-shelf gradient-based algorithm (from MATLAB’s optimization toolbox) is used for this purpose. The bounds

for the optimal design variables are defined by the range I_a . Let \mathbf{a}^* be the solution. \mathbf{a}^* is a *candidate* design that may replace an element of the design library D . The performance of \mathbf{a}^* is evaluated by invoking the piston analysis model.

- iv. The element in D with highest value of Ψ is removed from the design library D .
- v. If $\Psi(\mathbf{a}^*) \leq \Psi_i$ for all $\mathbf{a}_i \in D$ (\mathbf{a}^* is “better” than any point in D), \mathbf{a}^* is accepted and added to D . The design variable range I_a is tightened to match the maximum and minimum values of entries a_j in elements in D . Otherwise,
- vi. If $\Psi(\mathbf{a}^*) > \Psi_i$ for some $\mathbf{a}_i \in D$ (\mathbf{a}^* is “worse” than some point in D), \mathbf{a}^* is discarded. The design variable range I_a is tightened to match the maximum and minimum values of entries a_j in elements remaining in D . The augmentation strategy described in Section 6.5.3 is used to generate a new point $\hat{\mathbf{a}}$. The performance of $\hat{\mathbf{a}}$ is evaluated by invoking the piston analysis model and $\hat{\mathbf{a}}$ is added to D if $\Psi(\hat{\mathbf{a}}) \leq \Psi_i$ for all $\mathbf{a}_i \in D$. If an $\hat{\mathbf{a}}$ that is “better” than any point in D is not found within five new point generations, the process is stopped.

The process is repeated from (ii) for a prescribed number of iterations or function evaluations or until no improvement in the merit function is observed.

6.7 Selecting the Interpolation Model in Piston Skirt Design

Second and third order polynomials are evaluated to assess which surrogate model order is adequate for the piston skirt profile optimization problem. In each case,

$$n_d = n_b + \text{round}(n_b/2)$$

data points are generated (recall that n_b is the number of regression coefficients). This number of data points was chosen to avoid surrogate models close to saturation (saturation occurs when the number of data points equals the number of regression coefficients, twenty-one for the second order polynomial or forty-six for the third order polynomial). Sampling points are generated using the LHD strategy with filtering described in Section 6.5.2. The data were obtained using a semi-elastic piston model with an engine speed of 3000 RPM.

Table 6.2 shows the statistics for the two polynomial orders for both the objective function and the normalized constraint on the friction work. It is observed that

(i) The second order polynomial seems to approximate the objective (acceleration) function better, as it has slightly higher standard and adjusted coefficients of determination (R^2 and R_a^2), a lower standard deviation ($\hat{\sigma}$), and a lower maximum estimated standard error ($\max \varepsilon_{es}$). However, it has a slightly larger range for the normalized residual ($r_{\max} - r_{\min}$) than the third order polynomial.

(ii) The approximation of the constraint on the friction work, as measured by the coefficients of determination (R^2 and R_a^2), is of better quality than that of the objective function. In this case the third order polynomial outperforms the second order polynomial

in all the performance measures except for the range of the normalized residual (r_{\max} - r_{\min}).

For the present set of data points both polynomial fits return an R_a^2 value well above 0.9. In pARSM, in cases where R_a^2 is below the desirable target of 0.9, the response surface will be refitted using the IRLS algorithm. Typically, once the pARSM iteration starts and the worst data points are discarded, the least squares method is sufficient in approximating the performance functions. It has been observed that using either a rigid or a semi-elastic piston model at lower engine speeds, the R_a^2 value may drop below 0.9 when approximating the friction constraint.

Table 6.2: Surrogate model statistics

	2 nd order RS	3 rd order RS
n_b	21	46
n_d	32	69
Objective function		
R^2	0.985	0.983
R_a^2	0.957	0.950
$\hat{\sigma}$	26.529	26.995
r_{\min}	-1.861	-1.610
r_{\max}	1.049	1.007
$\max \varepsilon_{es}$	24.105	26.302
Normalized constraint, g_1		
R^2	0.996	0.997
R_a^2	0.990	0.991
$\hat{\sigma}$	0.018	0.016
r_{\min}	-1.038	-1.475
r_{\max}	1.397	1.488
$\max \varepsilon_{es}$	0.017	0.016

In terms of computation time, the second order polynomial clearly outperforms the third order model. For the cases studied here, 1.8 hours of computations (in an Intel Core 2 Quad 2.66 GHz processor personal computer) and 57 function evaluations were needed to perform one optimization using the second order polynomial model, while 3.2 hours and 100 function evaluations were required by the third order polynomial model.

In summary, in simulations using a semi-elastic piston model, the third order polynomial surrogate model is more computationally demanding and does not provide substantially superior approximations of the relevant performance functions when compared to a second order model. In rigid piston, lower engine speed simulations (not reported here) the third order model was found to be slightly better but the difference is not significant to justify the additional complexity. Furthermore, numerical experiments have shown that the third order model may lead to a design space of more complex topography and this occasionally results in convergence failures in the gradient-based algorithm used to solve the surrogate optimization problem. For these reasons, the third order model should be used with caution.

6.8 Skirt Profile Optimization

This section presents the skirt profile optimization results for a piston from a 3.0L production engine mounted on a single cylinder research engine, as predicted by pARSM. Starting from a reference profile, the goal is to find an improved skirt profile that will reduce piston slap and keep the net friction work done on the skirt below a prescribed level. The acceleration function A_{RMS} is used as the indicator of piston slap.

The results presented here are for the engine operating at 3000 RPM (medium speed), where it spends most of its time. The peak in-cylinder pressure at 3000 RPM is 47.05 bar (medium load). For this operating condition the net indicated work is 636.7 J/cycle per cylinder. It is estimated that about 1% of this work is lost at the skirt, which amounts to about 6.4 J/cycle of friction work.

In order to reduce computational effort, the piston is assumed to be semi-elastic, that is, it can deform due to thermal, inertial and combustive pressure loads, but its deformation is invariant to the hydrodynamic and contact loads developed at the skirt-cylinder bore interface (a PIFEAD elastic piston model simulation for this piston and operating conditions requires about 25 times more computer time than a simulation that uses a semi-elastic model).

The results are compared with the performance of the piston with the reference skirt profile

$$\mathbf{a}_{ref} = \{-110.5 \quad -42.6 \quad 20.43 \quad 0.0 \quad 0.0133\}^T$$

This profile is similar to the design used in a 6-cylinder engine in a popular passenger automobile in production until very recently. For this profile, at 3000 RPM,

$$A_{RMS}^0 = 966.02 \text{ s}^{-2} \text{ and } W_{fr}^0 = 6.55 \text{ J/cycle.}$$

In the optimization the maximum allowable net friction work done on the skirt, W_{max} , is set to 6.5 J/cycle, seeking to reduce the acceleration performance of the reference design without significantly increasing the friction. The lower and upper bounds on the design variables are set to

$$\mathbf{a}_{min} = \{-125 \quad -60 \quad 17 \quad -10 \quad 0.01\}^T$$

$$\mathbf{a}_{\max} = \{-95 \quad -30 \quad 22 \quad 10 \quad 0.035\}^T$$

These bounds are chosen having knowledge of the magnitudes of cylinder bore and skirt deformations and also that the piston will have to operate over a range of engine speeds. Typically a higher profile is required at lower engine speeds. Variables a_0 , a_1 , and a_3 are in micrometers, a_2 in millimeters and a_4 is non-dimensional.

The results are summarized in Table 6.3. Optimization was performed using a set of 32 initial data points and a second order polynomial surrogate model, referred to as SPO32. A solution was also obtained with 69 initial data points and a third order polynomial surrogate model approximation, referred to as SPO69. The results show how significant reductions in piston slap and friction work result from the optimization of the skirt profile. The objective function was reduced to about 70% of the reference skirt profile value, while the friction work was kept within desired limits, regardless of the order of the surrogate model approximation used. Both approximation strategies produce similar results, with differences of only 1.3% in A_{RMS} . In both cases the friction constraint was active at the optimum. It is noted, however, that in numerical experiments using a rigid piston model, engine speed at 1000 RPM and $W_{\max} = 6.5$ J/cycle, the friction constraint is often inactive.

The optimal profiles are displayed in Figure 6.5. Compared to the reference profile, they are higher at the top and bottom of the skirt but lower at mid-skirt. This results in a decrease of the piston's nominal diameter and a looser fit of the cold piston within the cylinder bore. At the operating temperature however, the reduction in skirt profile height balances the skirt thermal expansion and deformations due to combustive and inertial loads, to yield an enhanced performance. Also, the more plateau-like skirt

profiles allow for the build-up of higher hydrodynamic pressures, which limit lateral accelerations.

The design variables a_0 and a_1 approach the upper bound in the optimal solutions. This suggests that the profile could become even higher at the top and bottom of the skirt if the bounds were relaxed, perhaps improving performance. However, since the profiles were optimized only for a specific engine operating condition (3000 RPM), it is important to retain the bounds to exclude designs that may be poor performers over a range of operating conditions.

Figure 6.6 and Figure 6.7 show the acceleration and friction work results graphically for the reference and the SPO32 optimized profiles. The improvement in performance achieved with the optimal skirt profile is identified in the optimized design by the smoother acceleration traces over the cycle and lower amplitudes. The optimized profile results in a decrease of about 4 N in the peak friction value.

Figure 6.8 shows the iteration history of (true) acceleration (A_{RMS}) and friction (W_{fr}) values at each pARSM iteration for case SPO32. Note that the first optimal design (obtained from the first solution of the surrogate problem (6.9) and the initial set of 32 design points) is infeasible ($W_{fr} = 6.872$ J/cycle). After 22 iterations, convergence to a design with a minimum $A_{RMS} = 671.6$ s⁻² and feasible (but active) friction constraint ($W_{fr} = 6.499$ J/cycle) is achieved. Figure 6.8 also shows that reducing acceleration and friction are competing objectives in this problem.

Figure 6.9 shows the iteration history of the merit function (Ψ^*) of the best design in the library after each pARSM iteration. Flat portions of the curve represent time spent

by the algorithm improving the quality of the approximation. Overall, steady improvement is observed until pARSM converges to the final design.

Table 6.3: Summary of results

REFERENCE DESIGN		SPO32 – Optimal profile 2 nd order surrogate $n_d = 32$		SPO69 – Optimal profile 3 rd order surrogate $n_d = 69$	
A_{RMS} / A^0_{RMS}	W^0_{fr} / W_{max}	A^*_{RMS} / A^0_{RMS}	W^*_{fr} / W_{max}	A^*_{RMS} / A^0_{RMS}	W^*_{fr} / W_{max}
1.0	1.008	0.695	0.9998	0.713	0.9955
		Total function evaluations: 57		Total function evaluations: 100	
-110.50, -42.60, 20.43, 0.0, 0.0133		-97.19, -31.48, 17.20, -8.69, 0.0153		-95.13, -35.58, 21.99, -9.99, 0.0153	

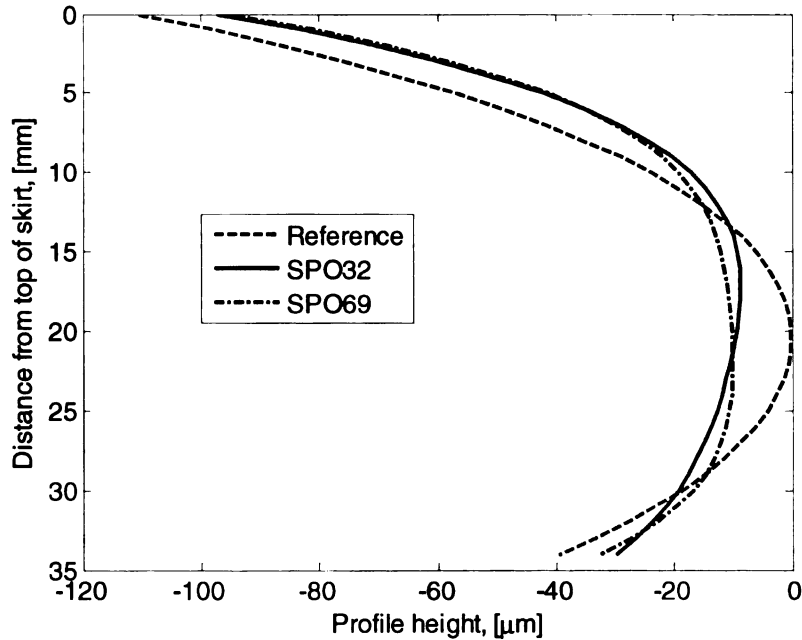
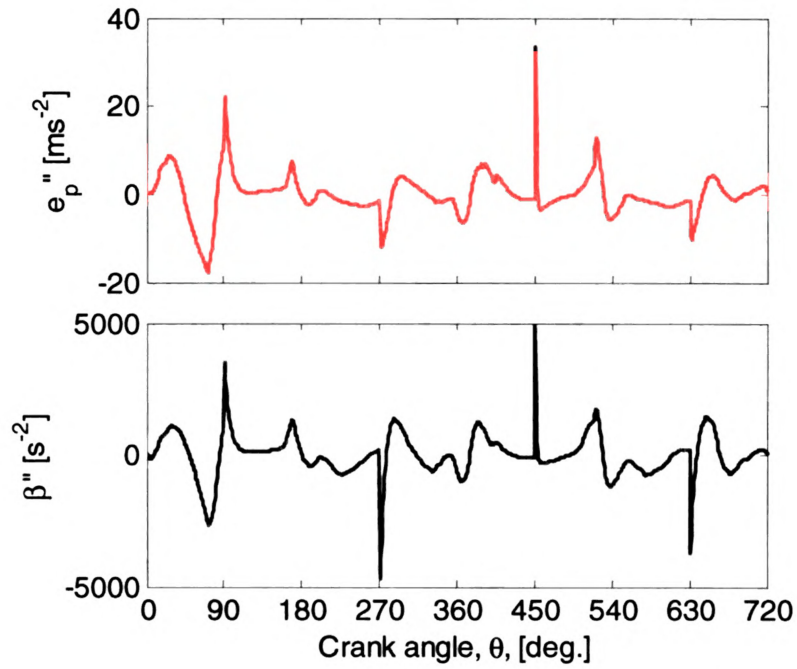
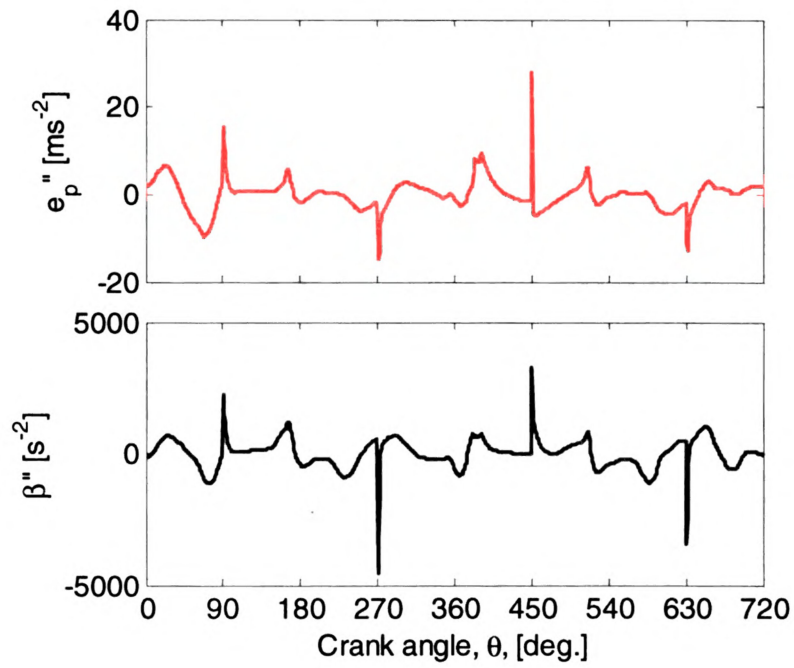


Figure 6.5: Skirt profiles, reference (SPI) and optimized (SPO32 and SPO69)



(a)



(b)

Figure 6.6: Transverse and angular accelerations in the reference (a) and optimized SPO32 (b) profile

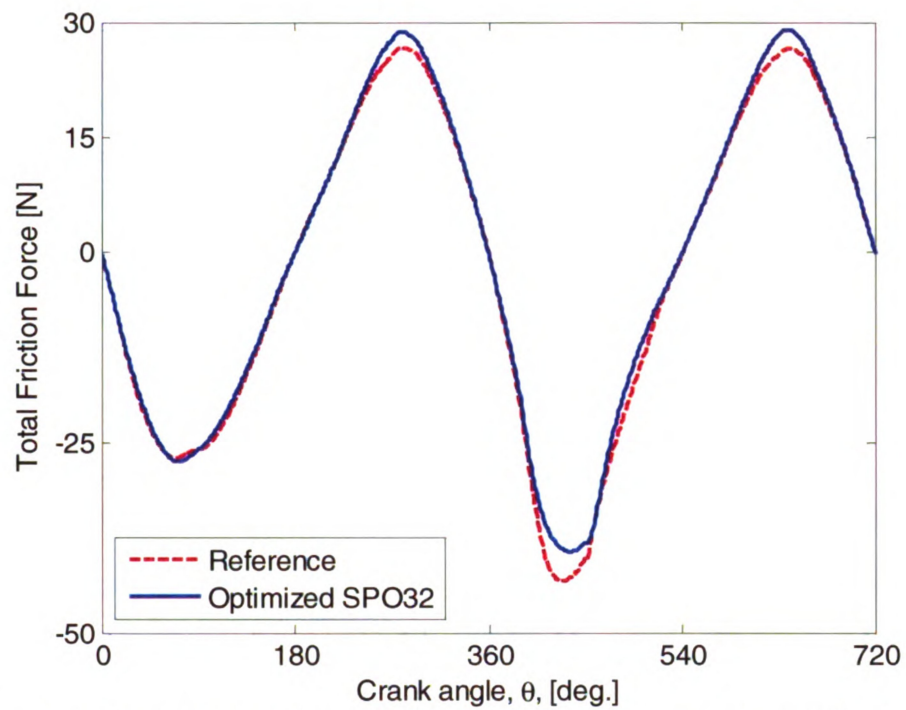


Figure 6.7: Total friction forces in the reference and optimized SPO32 profiles

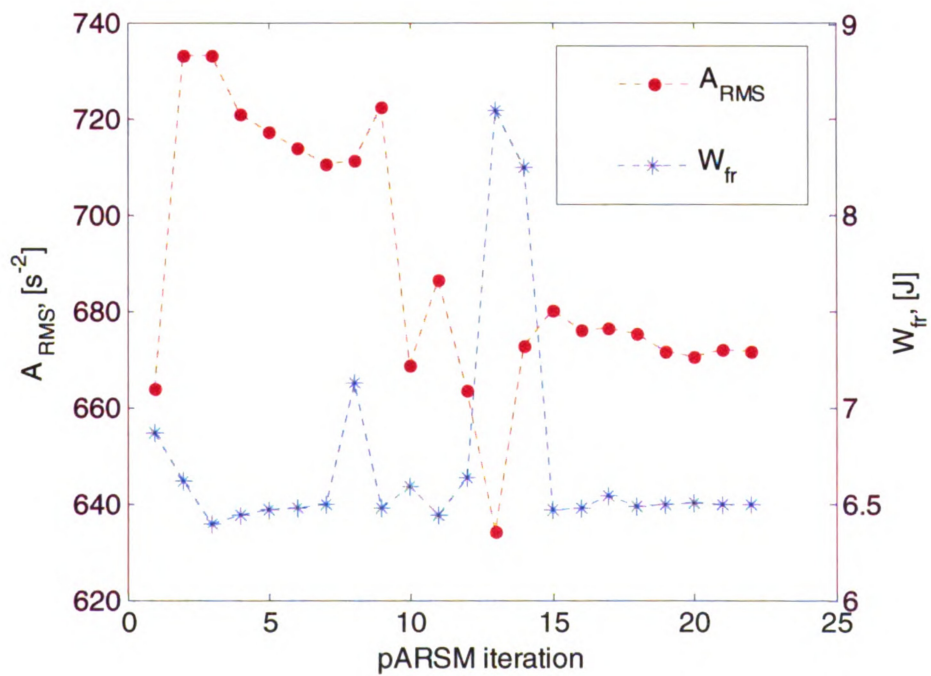


Figure 6.8: pARSM iteration history for the SPO32 profile

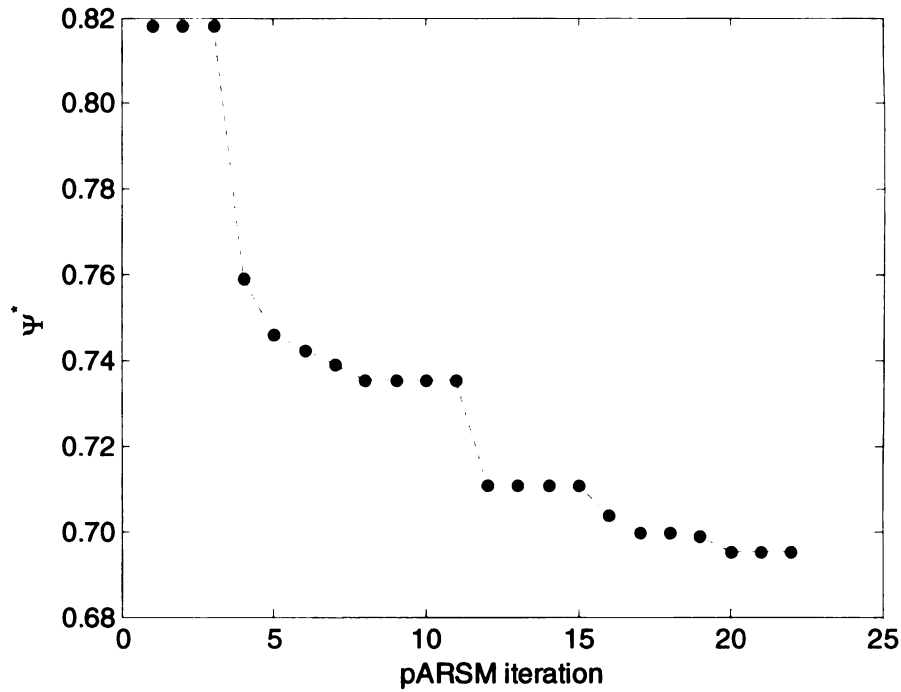


Figure 6.9: Best merit function in design library at each pARSM iteration for the SPO32 profile

6.8.1 Robustness of pARSM

In order to test how sensitive pARSM-produced designs are to the initial set of design points, ten experiments were performed where in each case iterations were started from a different set of 32 design points. Points were generated randomly using the LHD strategy with filtering. The results from these optimizations are reported in Table 6.4 and in Figure 6.10. The piston skirt profiles (Figure 6.10) and their performance is very similar across all ten runs. The normalized objective function values (A^*_{RMS}/A^0_{RMS}) are within a maximum deviation of 0.013 from the mean value of 0.680, and in all cases the friction constraint is active.

The data reported in Table 6.4 is now used to look into more details of the performance of the pARSM while solving this piston design problem. One measure of the success of a pARSM optimization run may be expressed by comparing the performance of the final design with the performance of the best *feasible* design in the initial set of 32 points, i.e., the quantity

$$e = \frac{\min_{i \in D^0} A_{RMS}(\mathbf{a}_i) - A_{RMS}(\mathbf{a}^*)}{A_{RMS}^0} \quad (6.22)$$

In (6.22) D^0 is used to denote the initial set of 32 points, *excluding* infeasible designs. From the results in Table 6.4 we note that improvement is achieved in all runs, ranging from a small improvement of about 9% in run 5 to a maximum improvement of about 25% in run 9.

Additional insight into the performance of pARSM can be gained from the ratios $\Psi^*/\Psi^{*,1}$. Here Ψ^* is the final value of the merit function while $\Psi^{*,1}$ is the best value of Ψ in the design library after solving only the *first* surrogate model problem (6.9). Improvement is achieved in all cases: on average, Ψ is reduced to about 36% of its first optimal value, $\Psi^{*,1}$. The ratio $\Psi^*/\Psi^{*,1}$ could also be interpreted as a measure of how ‘close’ the initial surrogate optimization solution is to the final answer in function space. It is noted that there appears to be little correlation between this ‘distance’ and the number of function evaluations required to bridge it. For instance, 14 function evaluations were needed to reduce $\Psi^{*,1}$ to 5% of its value in run 9, while after 49 evaluations Ψ^* is still 35% of $\Psi^{*,1}$ in run 10.

Table 6.4: Summary of optimization results at 3000 RPM

Run	A^*_{RMS} / A^0_{RMS}	W^*_{fr} / W_{max}	e	$\Psi^* / \Psi^{*,1}$	Evaluations after the first 32
1	0.676	1.000	16.36 %	0.058	20
2	0.679	0.999	21.10 %	0.946	11
3	0.672	1.000	11.39 %	0.983	11
4	0.671	1.000	12.51 %	0.189	11
5	0.704	1.000	9.07 %	0.274	40
6	0.689	0.993	12.60 %	0.054	14
7	0.684	0.995	20.45 %	0.380	47
8	0.667	1.000	12.12 %	0.046	25
9	0.665	0.999	25.50 %	0.050	14
10	0.696	1.000	16.82 %	0.646	49

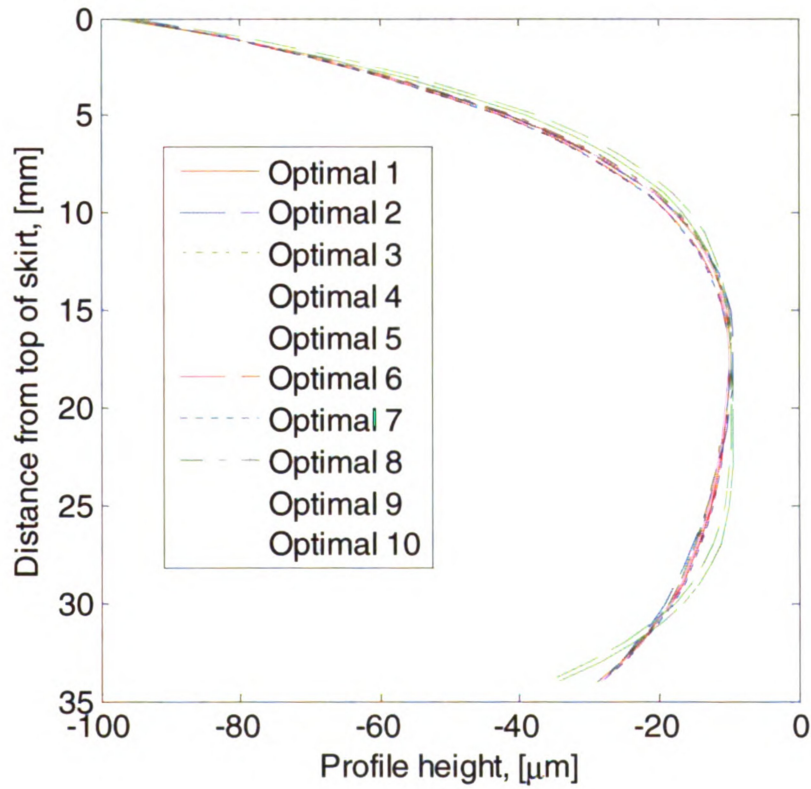


Figure 6.10: Skirt profiles

6.8.2 Effects of IRLS

It was observed in numerical experiments with the reference piston that IRLS does not engage in problems where conditions are set at medium to high engine speeds. This is because at these speeds there is sufficient build-up of hydrodynamic pressures at the skirt surface to support the piston within the center of the cylinder bore, and this avoids contact. However, at lower engine speeds some skirt profiles produce excessive contact. When this occurs there is a sharp change in the friction function and this results in large errors in the surrogate model. Usually, a small number of the initial designs will be such skirt profiles. When building the surrogate model, these designs return large residual errors and cause IRLS to engage and assign to them low weights. Such designs would never be desirable because of their high friction work values. They are infeasible and far away from the constraint boundary.

In order to investigate the effect of IRLS at low engine speeds, ten skirt profile optimizations at 1000 RPM were performed, representative of idle conditions. Under such conditions noise induced by environmental factors (wind, road surface) are minimal and thus engine noise becomes more noticeable. At 1000 RPM, the reference profile yielded performance values $A_{RMS}^0 = 173.09 \text{ s}^{-2}$ and $W_{fr}^0 = 2.37 \text{ J/cycle}$. Taking into account these values, the bound W_{max} was set to 4.0 J/cycle, significantly higher than the reference value of the friction work, seeking a significant reduction in A_{RMS} and thus in engine noise. In all runs, the friction constraint was inactive.

The optimizations were run by building surrogate models using both IRLS and a standard least squares method (LS). The initial 32 designs were the same in both cases. A summary of the results is shown in Table 6.5. In the table, N_i denotes the number of

pARSM iterations when IRLS was engaged and N_f denotes the number of function evaluations after the initial 32. IRLS engaged sometimes at every pARSM iteration, sometimes only during the first few pARSM iterations. Using IRLS often reduced the number of function evaluations, sometimes significantly, without much degradation of design performance (in run 5 IRLS required ten additional function evaluations, but it reached a design with about 18% lower objective function value, suggesting that perhaps in this run pARSM with the LS algorithm stopped too soon).

In summary, IRLS was not needed at moderate or high speeds, and at low engine speeds it led to a slightly lower number of function evaluations. Convergence was to solutions that are not significantly different from those obtained from the standard least squares method. The optimal profiles obtained from run 3 are shown in Figure 6.11, showing that in this run the two solutions are very similar, even though the LS method returns a better objective function. Finally, it is emphasized that while the behavior reported was typical of the piston design optimization problem, the observations do not allow for any claims to be made regarding the performance of the IRLS algorithm in a different context.

Table 6.5: Summary of optimization results at 1000 RPM

Run	IRLS			LS	
	N_i	N_f	A_{RMS}^* / A_{RMS}^0	N_f	A_{RMS}^* / A_{RMS}^0
1	6	11	0.540	12	0.540
2	11	45	0.528	56	0.547
3	18	19	0.581	34	0.532
4	7	7	0.538	40	0.522
5	7	21	0.539	11	0.655
6	11	11	0.530	11	0.530
7	10	10	0.525	55	0.527
8	6	6	0.602	10	0.608
9	12	35	0.528	32	0.545
10	16	16	0.546	34	0.544

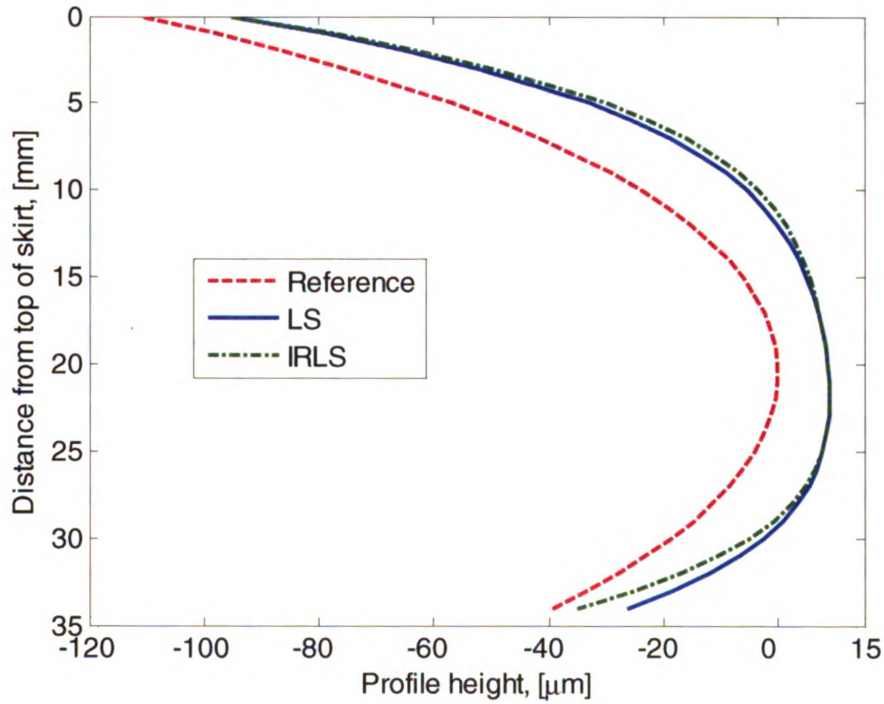


Figure 6.11: Skirt profiles obtained from optimization 3 at 1000 RPM

6.8.3 Optimal Profiles at Different Operating Conditions

In this section a skirt profile optimization is performed at an engine speed of 5000 RPM (high speed) and the optimal profile is compared to the solutions found at 1000 RPM and 3000 RPM.

At 5000 RPM the reference profile yielded $A_{RMS}^0 = 2859.48 \text{ s}^{-2}$ and $W_{fr}^0 = 10.84 \text{ J/cycle}$. Here W_{max} is set to 12.5 J/cycle, considering the already high acceleration and friction values of the reference design and the time spent at this operating condition. This is expected to lead to a significant reduction in the A_{RMS} value, and accordingly, to a reduction in the engine induced noise.

The performance values of the optimal profile are shown in Table 6. The friction work constraint is active, even though the bound W_{max} was set higher than the friction work value for the reference design. This implies that a further reduction in the A_{RMS} value can be achieved by relaxing the friction constraint.

Figure 6.12 shows the optimal profiles obtained at the three different operating conditions. These profiles show the importance of selecting the bounds (a_{min} and a_{max}) in order to have a high performance profile over a range of speeds. At lower speeds a relatively higher profile is required, whereas at higher speeds the competition between the objective function (A_{RMS}) and the constraint (W_{fr}) determine the height of the profile.

A production piston, however, can have only one profile. This gives rise to the necessity of optimizing the skirt profile over a range of operating conditions. Such an optimization is beyond the scope of this work, but in future work it could be included by modifying pARSM to handle multiple objectives, as there would be one A_{RMS} and one

W_{fr} value for each engine speed of interest. A less complex approach would be to apply weights for each operating condition based on its duration to allow for a single objective function.

Table 6.6: Summary of results at 5000 RPM

REFERENCE DESIGN		5000 RPM – Optimal profile	
A_{RMS} / A_{RMS}^0	W_{fr}^0 / W_{max}	A_{RMS}^* / A_{RMS}^0	W_{fr}^* / W_{max}
1.0	0.867	0.563	1.000
		Total function evaluations: 46	
-110.50, -42.60, 20.43, 0.0, 0.0133		-95.22, -30.16, 17.40, -5.21, 0.0183	

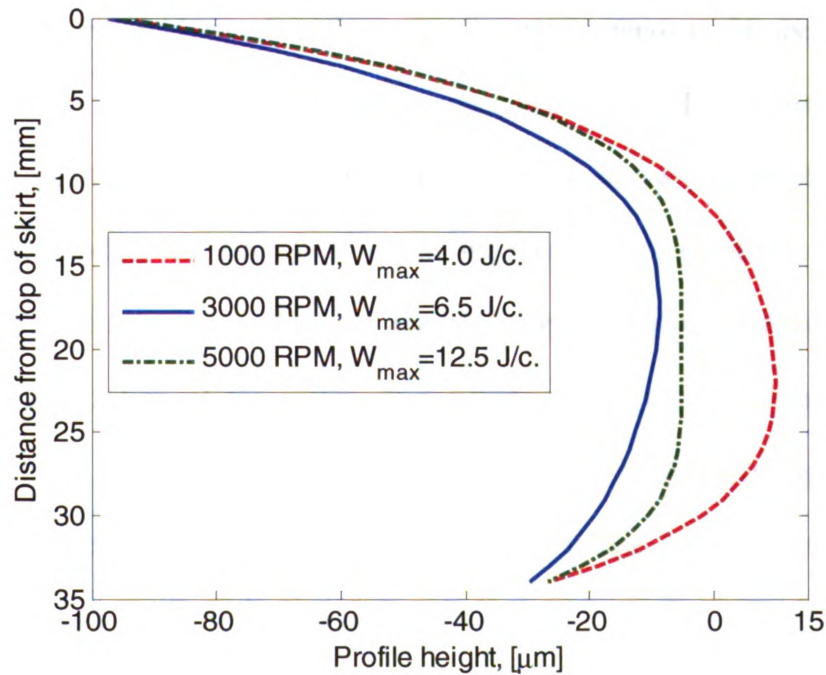


Figure 6.12: Optimal skirt profiles at different engine speeds

6.9 Final Remarks

The tailor-made pseudo-adaptive response surface method (pARSM) methodology performs very well in addressing specific features of the optimization of the piston skirt design problem, balancing ease of use with efficiency and mathematical rigor. This has been verified through a number of real-life examples, one of which is presented in this chapter. pARSM can be used either in the optimization of existing piston skirt profiles given new operating conditions, or as an aid in the design of new pistons.

The geometric constraint on the skirt profile makes it difficult to use standard space-filling techniques to populate the design space along with black-box simulation software. To alleviate this problem, two space-filling strategies were explored, a modified max-min formulation and a much simpler LHD approach followed by filtering. Both strategies yield comparable results. The max-min strategy tends to fill the boundaries of the design domain first and then the interior space, whereas LHD fills the space evenly. This suggests that the max-min strategy be used only when the number of data points is sufficiently large, e.g., when the ratio of the number of data points to the number of dimensions is greater than ten. Otherwise, the LHD seems more appropriate.

The optimization of the piston skirt profile was explored using two different response surfaces based on second and third order polynomial approximations. Numerical results consistently show that the third order polynomial response surface does not improve enough upon the second order to justify its increased computational cost. A third order polynomial approximation required almost twice as many function evaluations and occasionally led to convergence problems in the solution of the surrogate optimization problem. This could be a very significant difference where an elastic piston

is considered, as a single such analysis may require anywhere from one hour to twenty hours of computation time, depending on operating conditions, mesh size and computer used. Furthermore, to take full advantage of a third order polynomial approximation would require using a robust global optimization algorithm to solve the surrogate problem, which would increase the complexity and cost of the procedure significantly.

The methodology discussed only optimizes the skirt profile for a specific operating condition. Yet in a production engine a piston must perform over a range of operating conditions. This suggests exploring a multi-objective optimization version of the problem, attempting to optimize the skirt profile shape for several operating conditions, perhaps using different weight factors for different conditions. Weights could be assigned, for instance, based on the expected time spent at each condition. However, the problem is not quite the same as a typical multi-objective optimization problem because the feasible set changes with each operating condition (the friction bounds are typically different for different engine speeds).

CHAPTER 7. RING-PACK PRESSURES AND BLOW-BY

7.1 Introduction

In this chapter the commercial software package CASE is used to model the ring pack of three different engines and the predicted ring-pack pressures and blow-by are compared to measured ones. The limitations of the conventional 2-D modeling approach of the ring-pack are identified and lead to the new modeling recommendations presented in the next chapter.

7.2 The Leakage Coefficient

The physics of ring-pack motion and gas flow are very complex, thus requiring the introduction of coefficients to model certain processes. One such coefficient in CASE is the leakage coefficient, $\lambda_{p,i}$. This coefficient defines a leakage channel height when the ring is seated either at the top or bottom of the groove (Figure 7.1). This coefficient is required to account for leakage passages that can appear at operating conditions. The groove and ring deform thermally which causes waviness on the two surfaces, thus prohibiting perfect sealing. Also leakage flow can exist through the micro-channels in between the surface asperities.

The leakage channel height is given as a function of the channel height when the ring is seated at the bottom of the groove and the leakage coefficient,

$$h_{p,i} = \lambda_{p,i} h_i \quad (7.1)$$

where $i = 1, 2, \dots$ no. of rings, and

$$p = \begin{cases} t & \text{top of groove} \\ b & \text{bottom of groove} \end{cases} \quad (7.2)$$

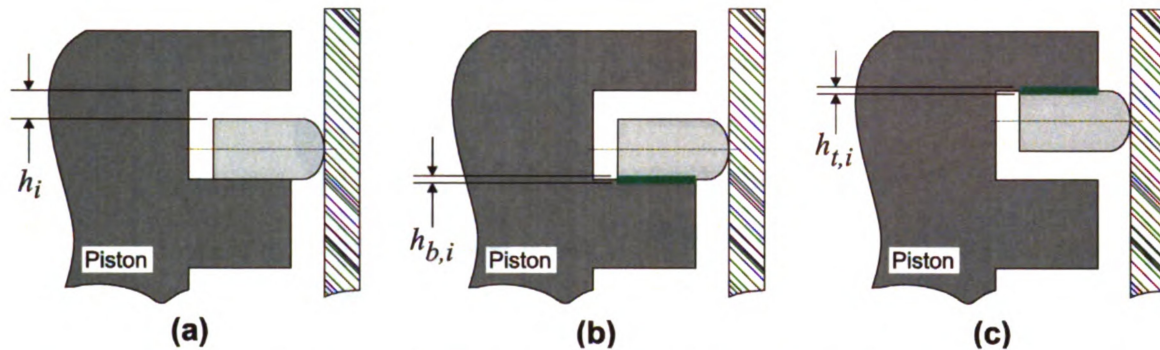


Figure 7.1: Ring leakage: (a) channel height and (b) leakage height when ring is seated at the bottom of the groove and (c) leakage height when ring is seated at the top of the groove

In the next sections it is shown that correct selection of these leakage coefficients can result in excellent correlation of data from numerical experiments with actual measurements.

7.3 Ring-pack Pressures

A gasoline single-cylinder research engine with an instrumented piston was used to obtain the measured ring-pack pressures¹. The engine was motored at 1500 RPM with a 2 psi boost to bring the in-cylinder pressure closer to low load operating conditions (Figure 7.3). The ring-pack of the engine is a three-ring one and was modeled in CASE to predict interring gas pressures. The ring-pack consisted of a rectangular top compression

¹ The experimental data for the ring-pack pressures were provided by Mid-Michigan Research, LLC.

ring, a Napier second compression ring and a three-piece oil ring. Figure 7.2 shows the pressures measured.

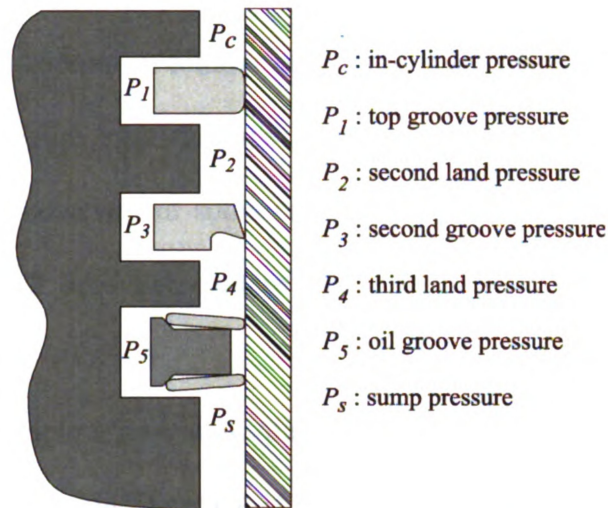


Figure 7.2: Ring-pack pressures

Table 7.1 shows the channel heights for the three rings when they are seated at the bottom of the groove. Table 7.2 shows the set of leakage coefficients used for two different simulations. The two sets are referred to as Leakage 1 and Leakage 2. In Figure 7.3 the in-cylinder gas pressure is shown at 1500 RPM with a 2 psi boost. The measured and simulation results from the two set of leakage coefficients are compared in Figure 7.4 to Figure 7.8.

In Figure 7.4 the top groove pressure is shown. It is very close to the in-cylinder pressure. Both leakage coefficient sets predict this pressure very close to the measured one. This is because the top ring spends most of the time in the high in-cylinder pressure range sitting at the bottom of the groove (Figure 7.9), thus the flow in the groove has no restriction. The differences start appearing in the second land pressure (Figure 7.5). The first set of leakage coefficients, Leakage 1, which was tuned by the trial and error

method, has very good correlation with the measured second land pressure. The second set does not predict peak pressure or trends in pressure fluctuations correctly. For example, at around 180 crank angle degrees there is a rise in second land pressure, but Leakage 2 set fails to capture it. Similar observations are made moving down the ring-pack (Figure 7.6 to Figure 7.8). Leakage 1 set enables the prediction of the trends in pressure fluctuations; however, in some cases it fails to correctly predict the pressure magnitudes. Leakage 2 does not capture trends in pressure fluctuations or pressure magnitudes correctly.

Figure 7.9 to Figure 7.11 show the ring location relative to the bottom of the groove. All three rings begin the cycle at the top of the groove. At the middle of the intake stroke, as the piston starts to decelerate, inertia pushes the rings at the bottom of the groove. The top ring remains seated until the middle of the expansion stroke, as in-cylinder pressure which acts directly on it dominates inertia. After 450 crank angle degrees, one would expect it to return to the bottom of the groove as the piston slows down. However, it remains at the top of the groove. This is because the pressure in the second land is sufficiently high to dominate the top ring's inertia. This high second land pressure keeps the second ring seated until after the middle of the expansion stroke.

The second ring exhibits flutter (instability) soon after the middle of the compression stroke. This is because of competition between second land pressure and second ring inertia. The pressure in the second land is not sufficiently high to dominate inertia thus the ring lifts as the piston decelerates. During the process of the ring lifting, gas flows past the ring into the third land, dropping the pressure in the second land. This reduces the resistance to flow from the top groove to the second land, thus second land

pressure rises and pushes the ring down. This motion creates a passage from the high-pressure second land to the lower-pressure third land. Consequently pressure in the second land drops, third land pressure increases, and in combination with inertia the ring flutters. The process continues until the in-cylinder pressure becomes high enough and the land pressures are high enough to dominate inertia. The Leakage 2 set predicts an extended flutter range of 48 crank angle degrees compared to the Leakage 1 set which predicts a range of 41 crank angle degrees. This is because the leakage coefficients for the second set are lower, and thus it takes longer for the in-cylinder pressure to dominate. The prediction of flutter is consistent with the pressure measurements of the second land (Figure 7.5), second groove (Figure 7.6) and third land (Figure 7.7). These three measurements show pressure fluctuations around 330 crank angle degrees which suggest second ring flutter in that region.

The oil ring (Figure 7.11) exhibits similar motion to the second ring. However, the third land pressure is not sufficiently high to compete with inertia after the middle of the compression stroke. Thus the third ring lifts and remains at the top of the groove rather than fluttering. It is pushed back down around 360 crank angle degrees where the in-cylinder pressure and hence the third land pressure get sufficiently high.

From these simulations and measurements it can be seen that correct tuning of the leakage coefficients is essential to predict ring-pack pressures correctly. The calculated pressure results suggest that further tuning of Leakage 1 set would yield a better prediction of the pressure in the lower ring-pack region. The prediction of ring location within the groove does not seem to be greatly affected by the leakage coefficient. This is because in the low-pressure parts of the cycle (intake and exhaust strokes) the ring

motion is dominated by inertia. This conclusion is not definitive. Perhaps a leakage coefficient set that would yield closer correlation of pressure magnitudes at the lower regions of the ring-pack would also result in more vivid differences in ring motion compared to the Leakage 2 set.

Table 7.1: Channel height

	Height [mm]
h_1	0.030
h_2	0.057
h_3	0.020

Table 7.2: Leakage coefficients

	$\lambda_{t,1}$	$\lambda_{b,1}$	$\lambda_{t,2}$	$\lambda_{b,2}$	$\lambda_{t,3}$	$\lambda_{b,3}$
Leakage 1	0.07	0.07	0.20	0.20	0.15	0.15
Leakage 2	0.01	0.01	0.10	0.10	0.10	0.10

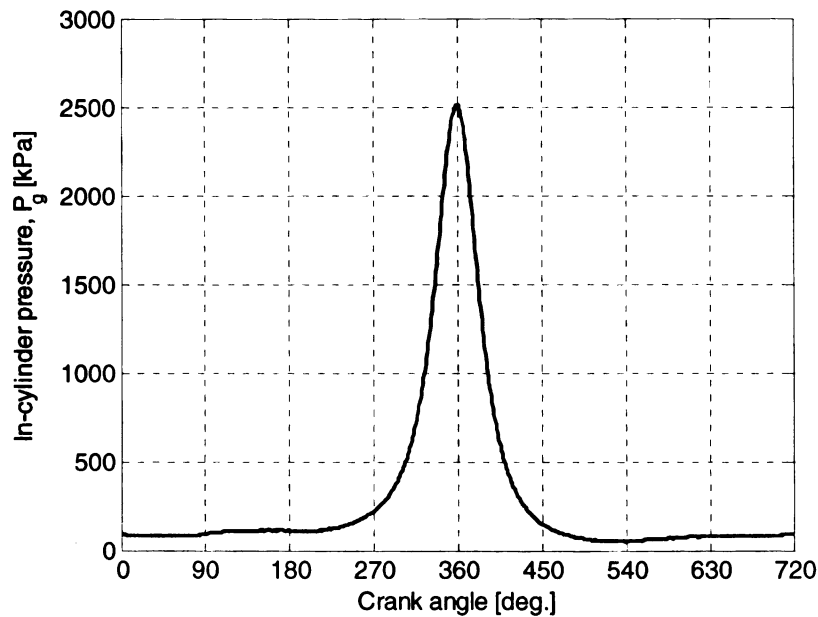


Figure 7.3: In-cylinder pressure at 1500 RPM 2 psi boost

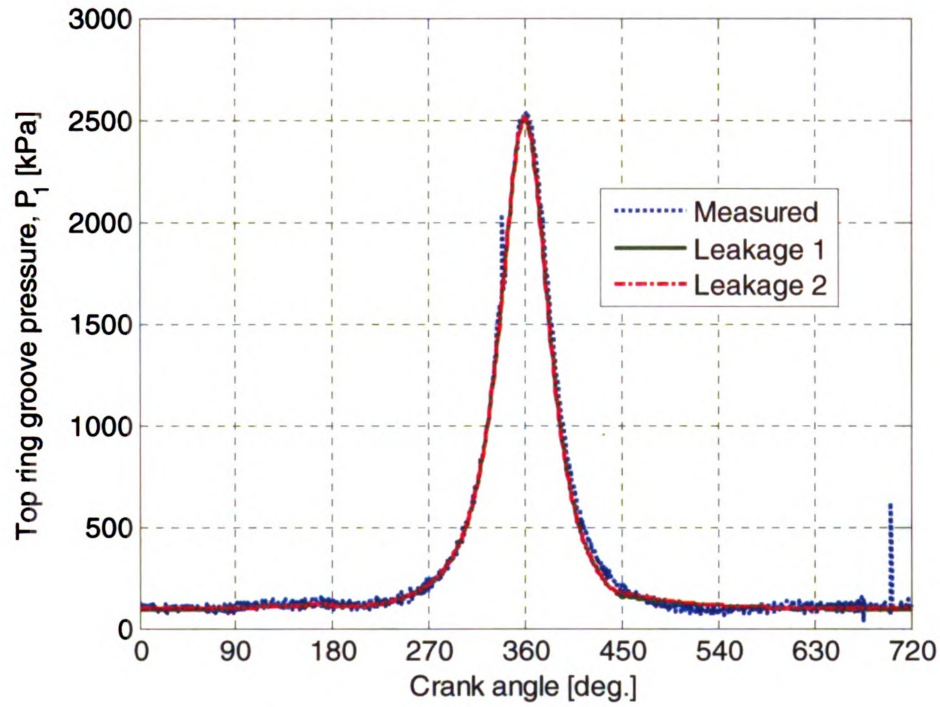


Figure 7.4: Top ring groove pressure

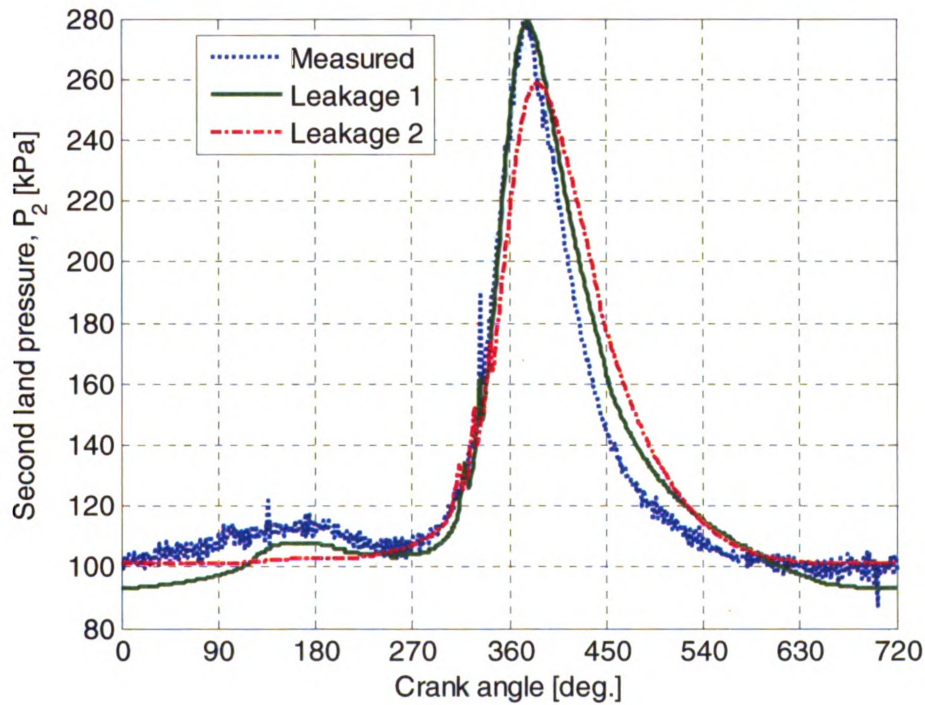


Figure 7.5: Second land pressure

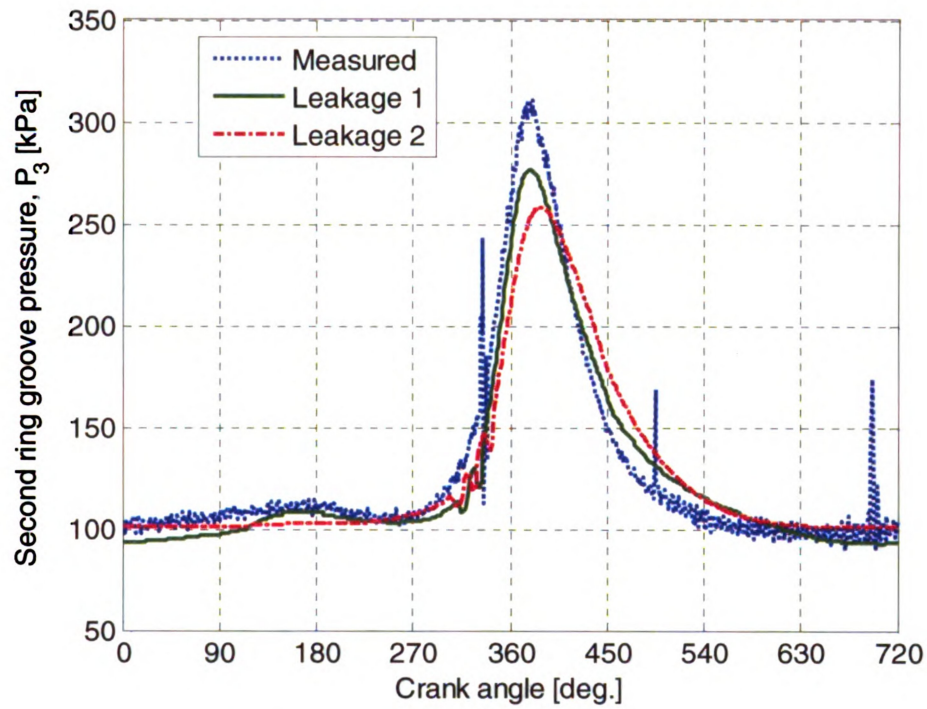


Figure 7.6: Second ring groove pressure

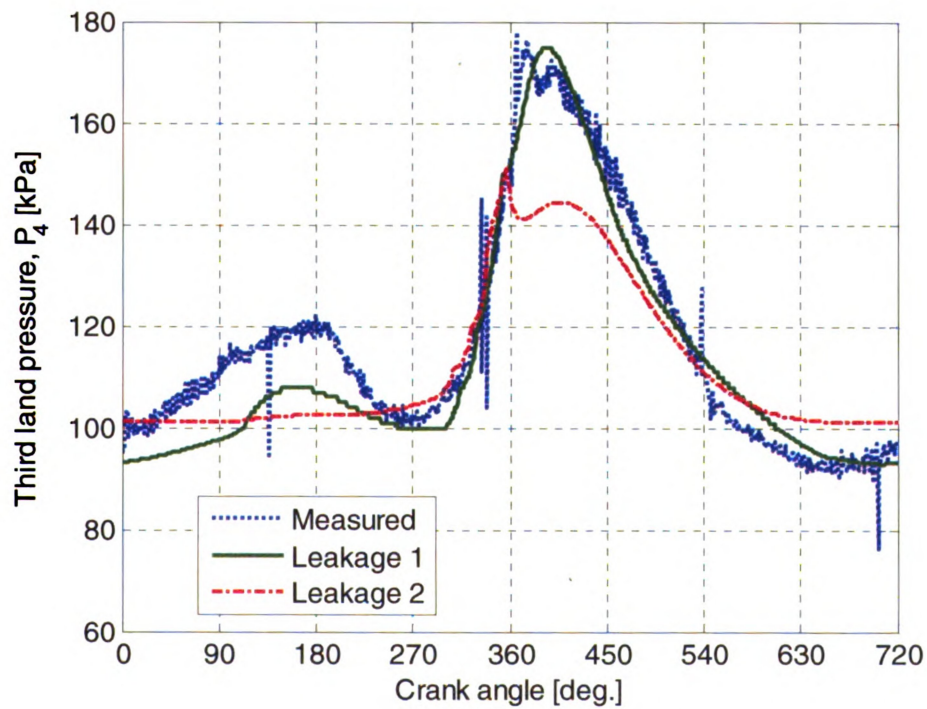


Figure 7.7: Third land pressure

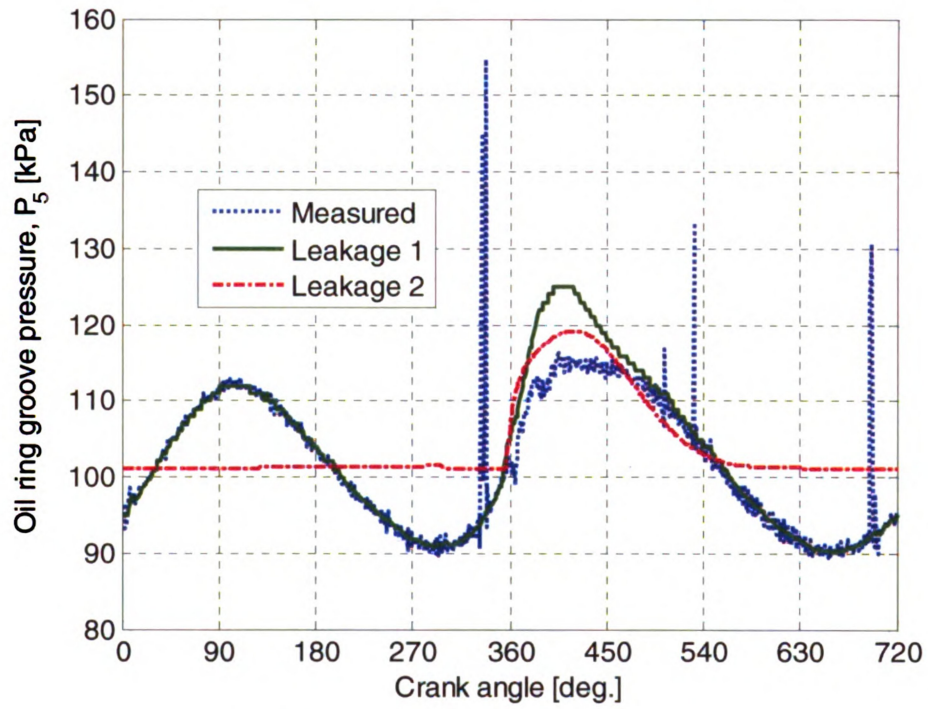


Figure 7.8: Oil ring groove pressure

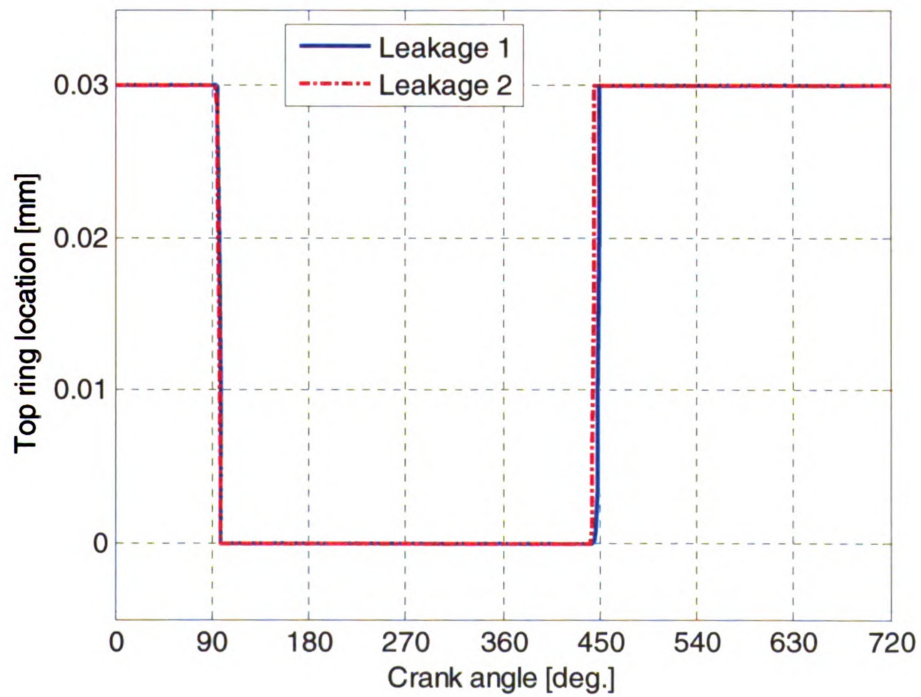


Figure 7.9: Top ring location relative to bottom of groove

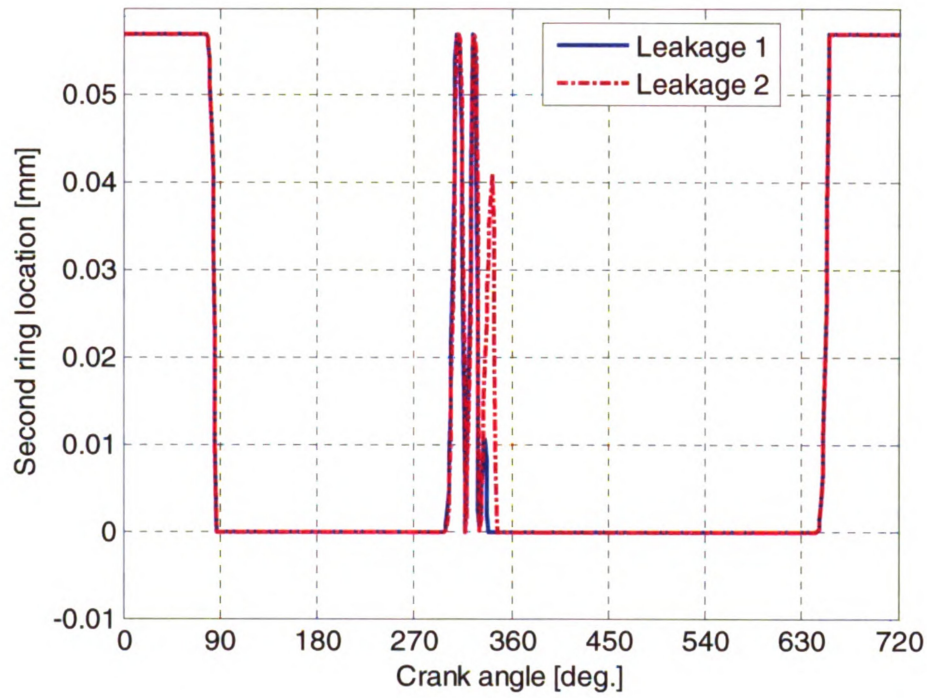


Figure 7.10: Second ring location relative to bottom of groove

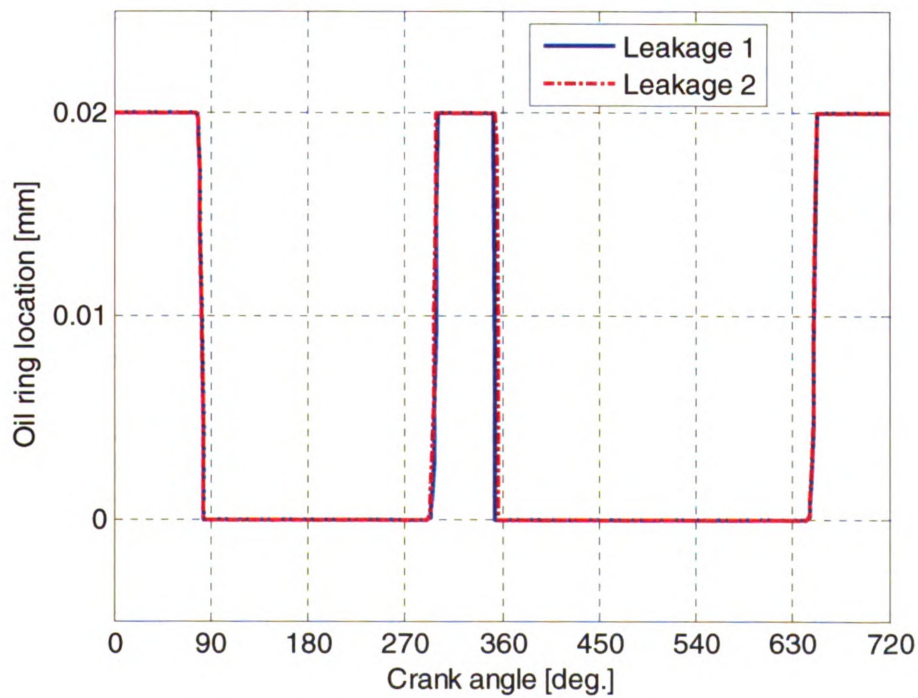


Figure 7.11: Oil ring location relative to bottom of groove

7.4 Ring-pack Blow-by

Blow-by is defined as the flow of combustion gases from the combustion chamber to the crankcase through the ring-pack. Blow-by affects emissions, oil degradation rate, and useful work of the engine. Figure 7.12 shows the main blow-by mechanisms. Blow-by occurs at the instances when the ring floats in the groove. The ring floats when it moves from one groove side to the other. If this happens during the compression or expansion strokes when in-cylinder pressure is high it can lead to increased blow-by.

Another mechanism is ring collapse. This will occur at low engine loads high engine speeds. In this case the inertia forces will dominate the pressure forces above the ring, and the ring remains seated at the top of the groove. At these conditions a point can exist that the pressure above the ring is high enough compared to the pressure in the groove (behind the ring). This will cause ring collapse; that is, the ring will move radially away from the cylinder bore, creating a passage for gas flow. The interested reader is referred to [14] where a more in-depth description of ring collapse can be found, as well as a relation for the pressures surrounding the ring that will dictate ring collapse.

The third blow-by mechanism is gas flow past the ring end gap. When the ring is fitted to the cylinder bore the two ends do not seal completely. This allows for the creation of a flow passage which is purely dependent on end gap clearance. The end gap clearance is usually utilized to regulate interring gas pressures.

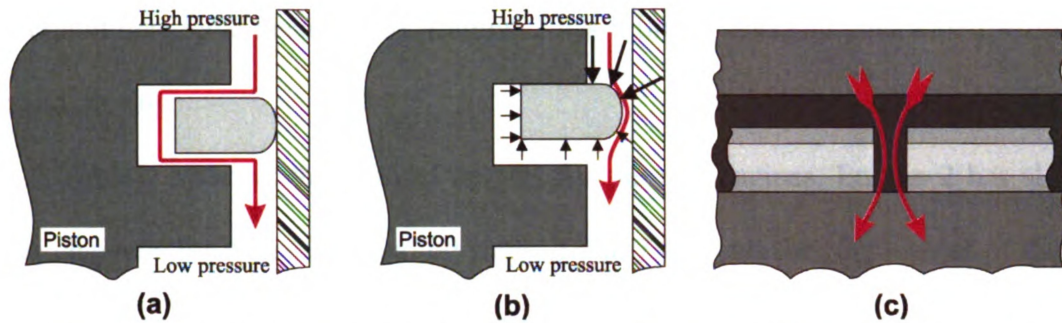


Figure 7.12: Blow-by mechanisms, (a) ring floating, (b) ring collapse and (c) through end gap

In this section the blow-by of two gasoline engines is investigated. These are 2.0L 4-cylinder engines. Engine 1 is a production engine, whereas Engine 2 is in the development stage. The objective is to assess the performance of its ring-pack relative to the production Engine 1 ring-pack. Blow-by and in-cylinder pressure measurements are available only for Engine 1. The in-cylinder pressure measurements are available only at full load (WOT) conditions. In order to calculate the global blow-by map the WOT in-cylinder pressures were scaled down to correspond to different loading conditions. Figure 7.13 shows the in-cylinder pressure traces at 3000 RPM. From here on they are referred to as:

- WOT wide open throttle (full load)
- 75P three quarters of full load
- 50P half of full load
- 25P one quarter of full load (low load)

It is estimated that the in-cylinder pressures of Engine 2 will be approximately 15 bar higher at peak pressure than Engine 1, thus the Engine 1 pressures are scaled to correspond to Engine 2 pressures. Figure 7.14 shows the in-cylinder pressures at 3000 RPM WOT. The peak measured Engine 1 in-cylinder pressure is 64 bar and the scaled Engine 2 peak pressure is at 79 bar. Similarly all the other pressures, at all speeds and

load conditions, have been scaled. Engine 2 has a bigger end gap clearance for the top ring and oil ring.

Table 7.3 shows the channel heights for the two engines. Engine 2 has slightly higher channels for the second and oil rings. Table 7.4 shows the ring masses of the two engines. Engine 2 has a slightly lighter top ring but heavier second ring. The total mass of the ring-pack, though, is the same for both engines. Table 7.5 shows the ring end gap clearances for the two engines.

Another factor that is considered in the comparison is the cylinder bore deformation. As explained in Chapter 8, bore deformation affects ring-bore conformability and ultimately blow-by and ring cooling. Hence the simulations are performed for all cylinders of Engine 1 and only cylinder 1 of Engine 2.

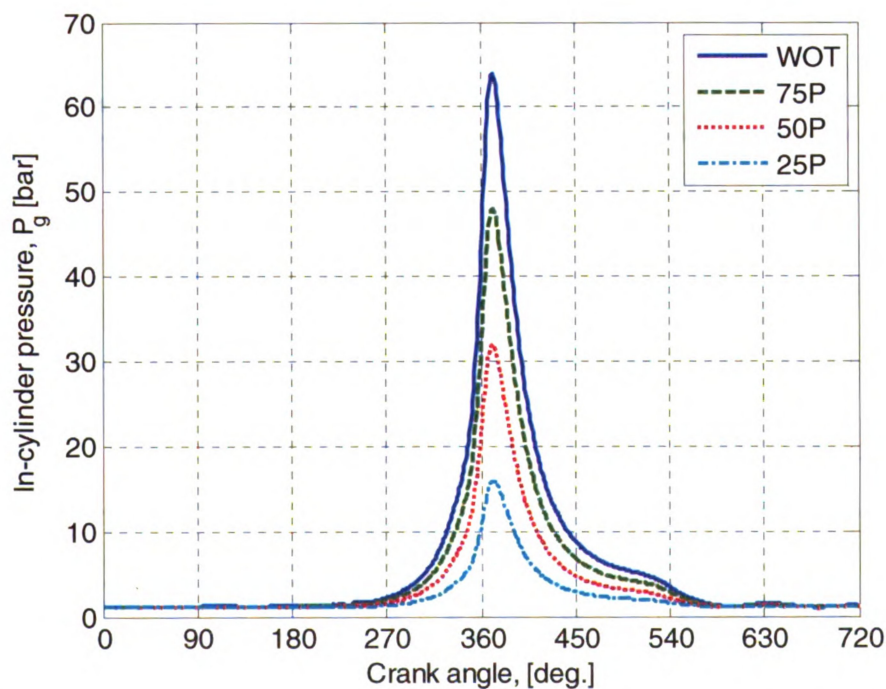


Figure 7.13: In-cylinder pressure traces for Engine 1 engine at 3000 RPM

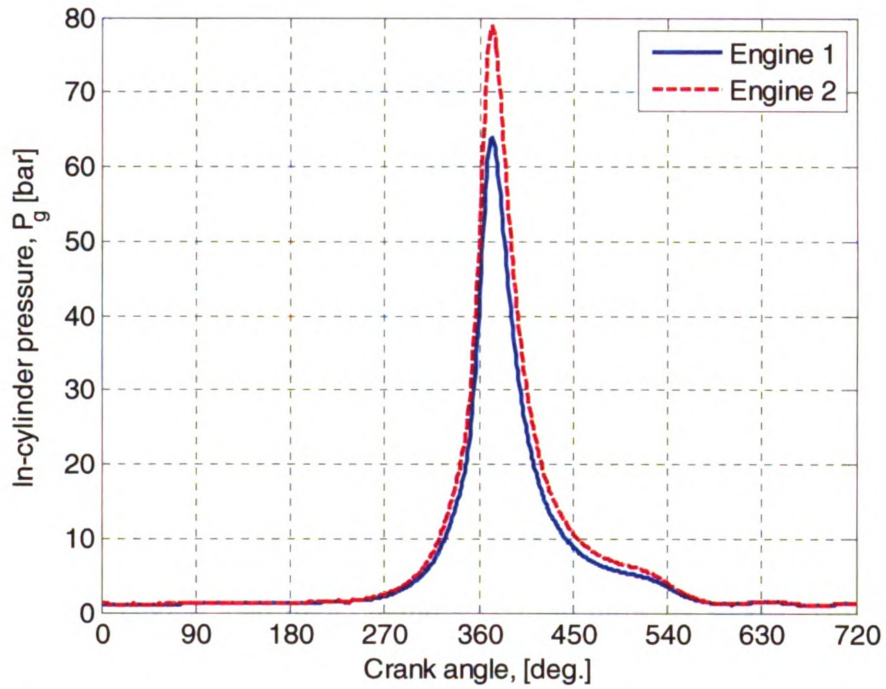


Figure 7.14: In-cylinder pressure traces for Engine 1 and Engine 2 engines at 3000 RPM WOT

Table 7.3: Ring-pack channel heights for the two engines

	Engine 1	Engine 2
h_1 [mm]	0.060	0.060
h_2 [mm]	0.050	0.060
h_3 [mm]	0.105	0.106

Table 7.4: Ring masses

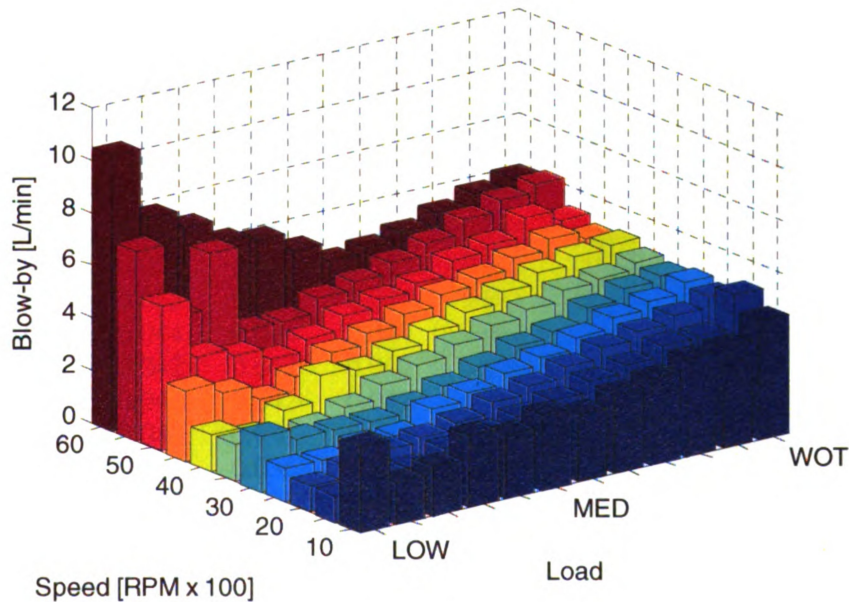
	Engine 1	Engine 2
Top ring [g]	7.0	6.75
Second ring [g]	6.9	7.15
Oil ring [g]	5.9	5.9

Table 7.5: End gap clearances

	Engine 1	Engine 2
Top ring [mm]	0.210	0.250
Second ring [mm]	0.550	0.550
Oil ring [mm]	0.275	0.330

7.4.1 Tuning the CASE Model for Blow-by

A typical blow-by map for an engine is shown in Figure 7.15, and this one corresponds to Engine 1. The blow-by increases with engine load and engine speed. However, at low engine load high engine speed the blow-by spikes. This is caused by either ring floating (ring moves towards the top of the groove toward the end of the compression stroke) or ring collapse.

**Figure 7.15: Measured blow-by (average per cylinder)**

Following the methodology described in Section 7.3, the leakage coefficients for the model of Engine 1 here are tuned at the full load (WOT) condition to correlate the predicted blow-by with the measured one. Table 7.6 shows the sets of tuned leakage coefficients at the different engine speeds. The comparison of the predicted blow-by with the measured one is shown in Figure 7.16. It can be seen that the leakage coefficients can be adjusted such that the predicted blow-by correlates well with the measured one. The problem is that each engine speed requires a different set of leakage coefficients except at mid-range, 3000 and 3500 RPM. This will make the setup of blow-by map simulations very tedious. Also it suggests that the different load conditions would require different sets of leakage coefficients. This would deviate computational tools such as CASE from their essence, accessible fast predictive tools. It is desirable to have only one set of coefficients which will correctly predict blow-by over the entire range of engine loads and engine speeds.

Table 7.6: Leakage coefficients and blow-by per cylinder at WOT

Engine speed [RPM]	$\lambda_{t,1}$	$\lambda_{b,1}$	$\lambda_{t,2}$	$\lambda_{b,2}$	$\lambda_{t,3}$	$\lambda_{b,3}$	Calculated ² [L/min]	Measured ³ [L/min]
1000	0.055	0.055	0.055	0.055	0.055	0.055	4.46	4.53
1500	0.052	0.052	0.052	0.052	0.052	0.052	5.07	5.10
2000	0.045	0.045	0.045	0.045	0.045	0.045	4.60	4.67
2500	0.044	0.044	0.044	0.044	0.044	0.044	4.88	4.82
3000	0.042	0.042	0.042	0.042	0.042	0.042	4.78	4.67
3500	0.042	0.042	0.042	0.042	0.042	0.042	4.84	4.82
4000	0.041	0.041	0.041	0.041	0.041	0.041	5.24	4.10
4500	0.036	0.036	0.036	0.036	0.036	0.036	4.90	4.96
5000	0.038	0.038	0.038	0.038	0.038	0.038	5.36	5.24
5500	0.040	0.040	0.040	0.040	0.040	0.040	6.27	6.23
6000	0.039	0.039	0.039	0.039	0.039	0.039	6.15	6.09

² Average per cylinder.

³ Average per cylinder.

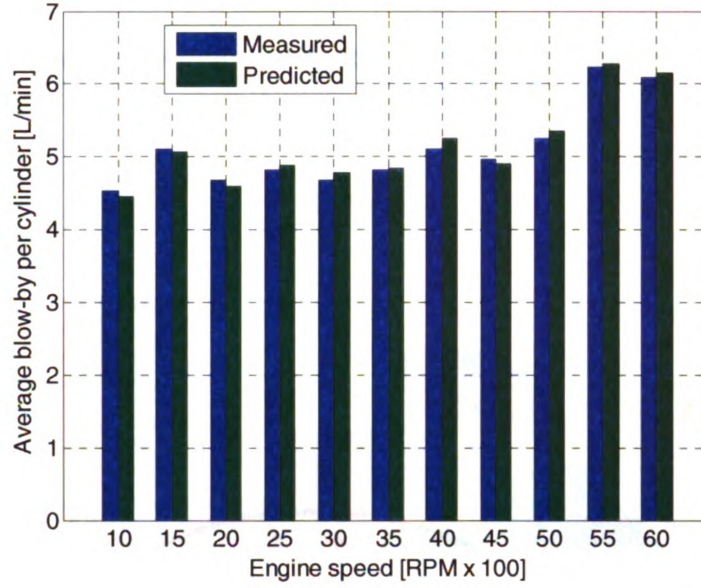


Figure 7.16: Predicted and measured blow-by at WOT

In order to make the blow-by comparison between the different cylinders of Engine 1 and between Engine 1 and Engine 2, three sets of leakage coefficients are selected from Table 7.6, at low, mid and high engine speeds.

- Leakage 1 : $\lambda_{t,i} = \lambda_{b,i} = 0.055$ (1000 RPM in Table 7.6)
- Leakage 2 : $\lambda_{t,i} = \lambda_{b,i} = 0.042$ (3000 RPM in Table 7.6)
- Leakage 3 : $\lambda_{t,i} = \lambda_{b,i} = 0.039$ (6000 RPM in Table 7.6)

Figure 7.17 shows the predicted blow-by for the four cylinders of Engine 1 using the Leakage 2 set. It is evident that for this engine configuration, cylinder bore deformation has negligible effect on the blow-by. This suggests good ring conformability in all four cylinders. The predicted blow-by does not match the measured in terms of magnitude; however, the trends are similar. Blow-by increases with engine load and engine speed. Only at 6500 RPM low engine load a spike is predicted in blow-by, whereas the measured blow-by shows spikes over a wider range of engine loads and at

lower speeds. It should be noted, though, that the in-cylinder pressures for the lower load conditions in the simulations were scaled down from the full load in-cylinder pressures.

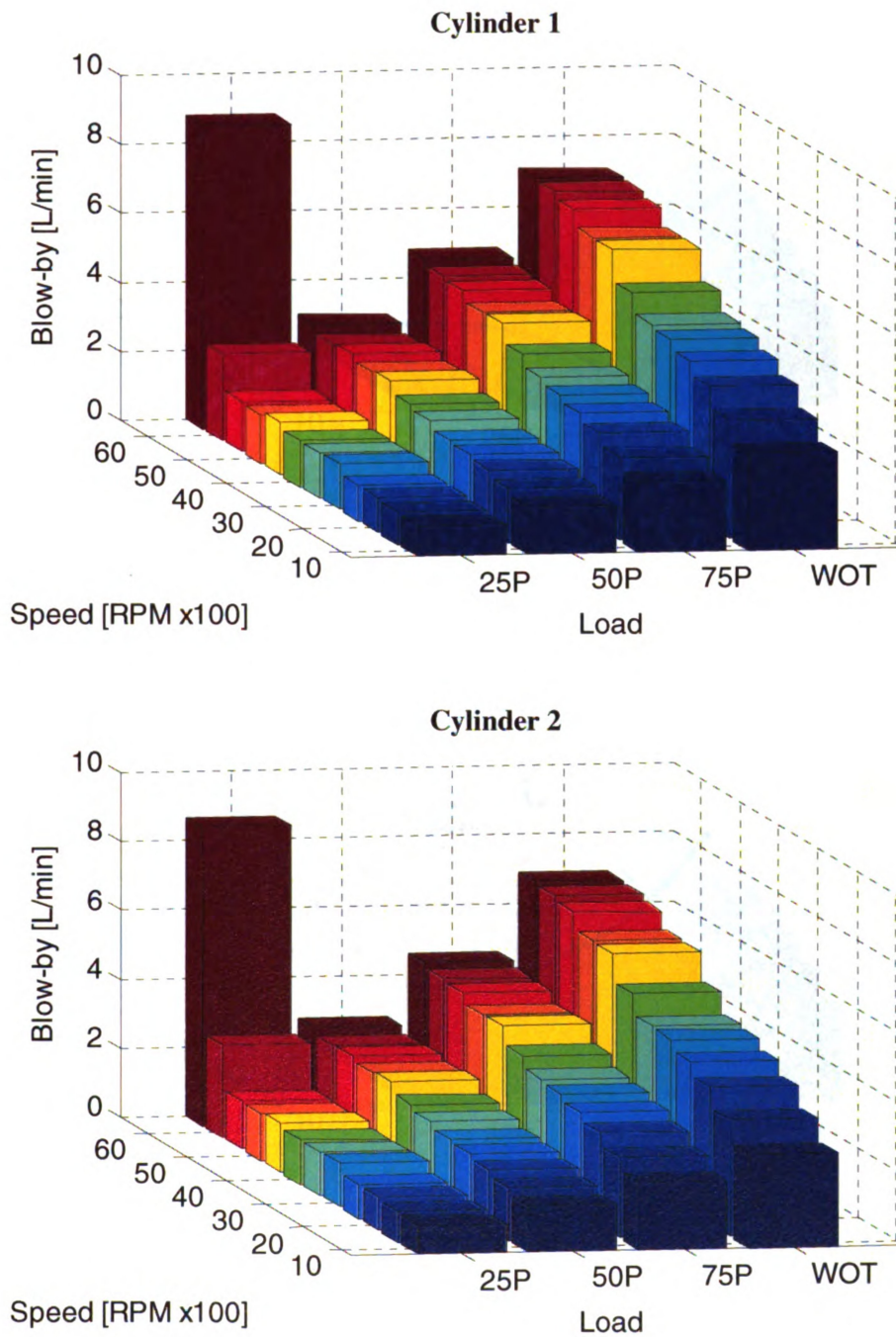


Figure 7.17: Predicted blow-by for the four cylinders of Engine 1 using Leakage 2

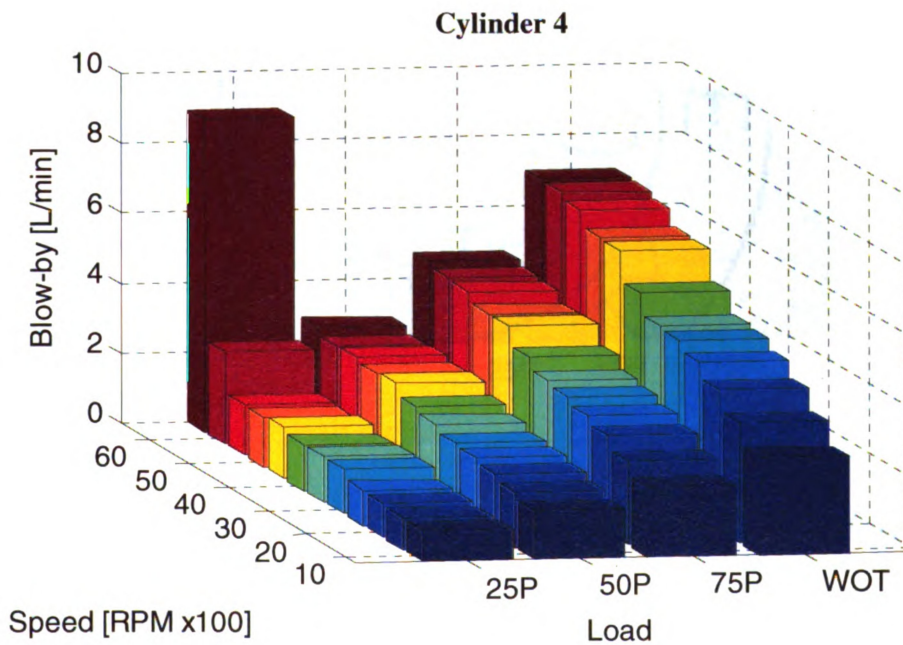
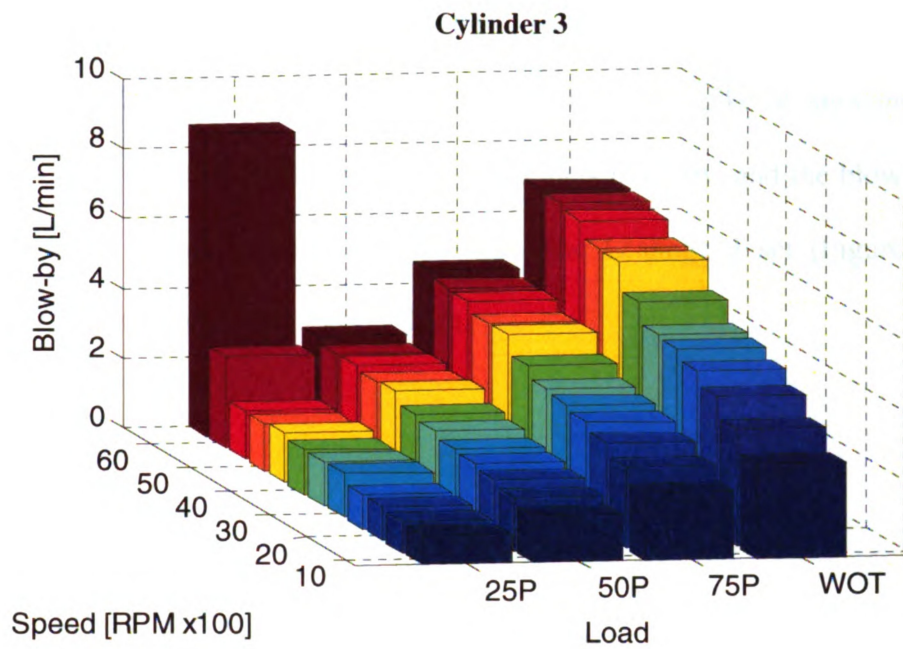


Figure 7.18: Predicted blow-by for the four cylinders of Engine 1 using Leakage 2

Using different leakage coefficients for cylinder 1, differences in predicted blow-by maps are seen. In the case of the Leakage 1 set (Figure 7.19), blow-by at WOT is high. It peaks at 12.2 L/min which even exceeds the blow-by spike at high-speed, low-load condition. This leakage coefficient set over-predicts blow-by, and the blow-by map does not follow the trends of the measured one. The Leakage 3 set (Figure 7.20) yields comparable results with the Leakage 2 set.

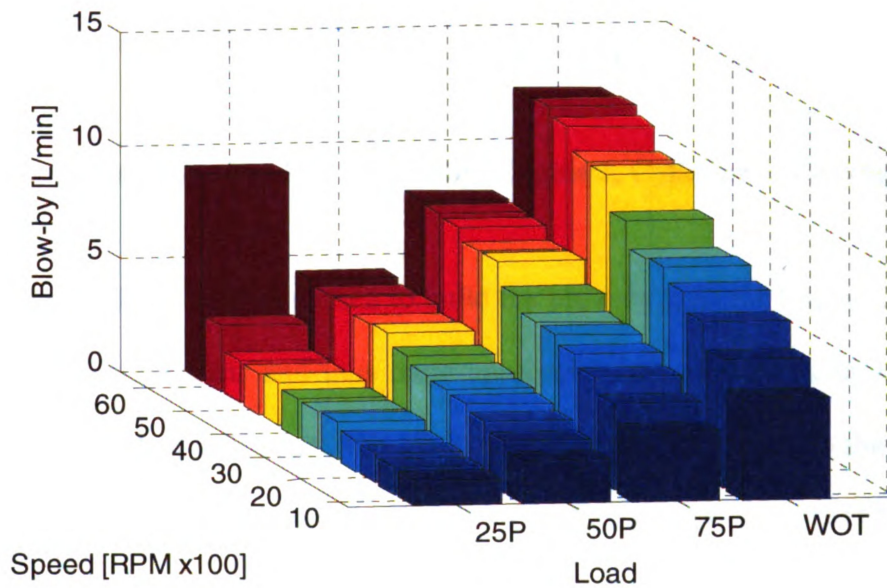


Figure 7.19: Predicted blow-by, Engine 1, Cylinder 1, Leakage 1

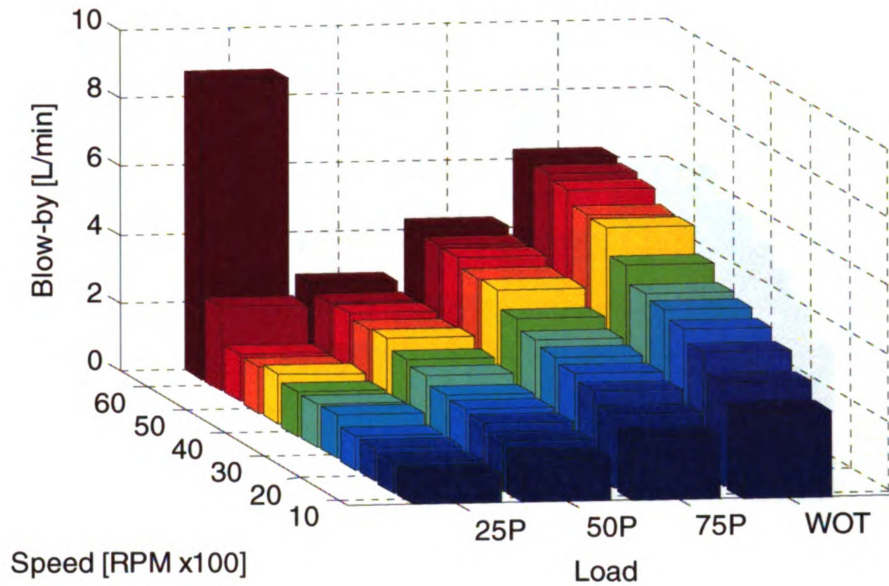


Figure 7.20: Predicted blow-by, Engine 1, Cylinder 1, Leakage 3

The Leakage 2 set is chosen to build the blow-by map for Engine 2 as it is tuned for the mid-range speeds and thus more appropriate than the Leakage 3 set, which is tuned for the high-speed range. The Leakage 1 set is clearly not desirable, as it fails to capture the trends in the blow-by map. Figure 7.21 shows the predicted blow-by map of cylinder 1 of Engine 2. For this configuration the blow-by has a perfectly linear relationship with engine speed and loads. Blow-by spikes are not predicted at the high-speed, low-load condition.

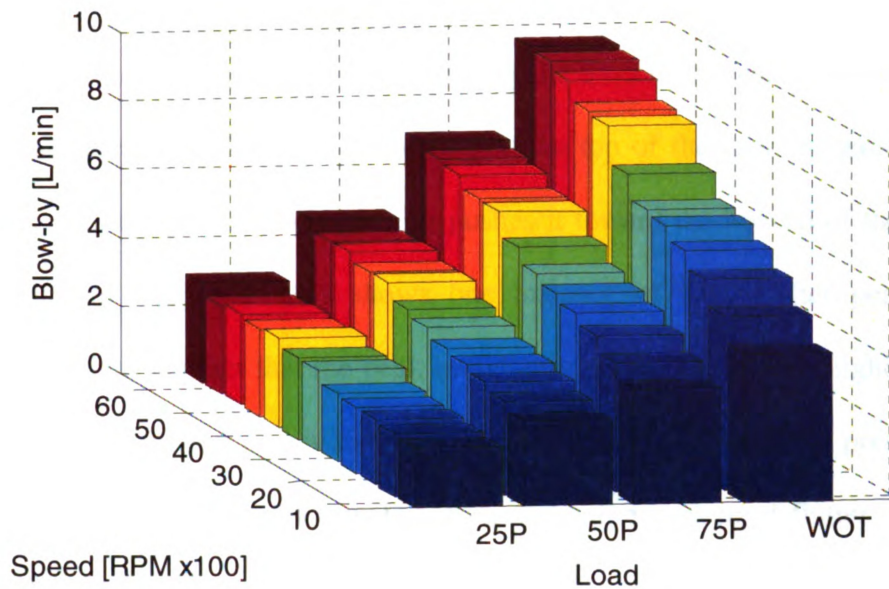


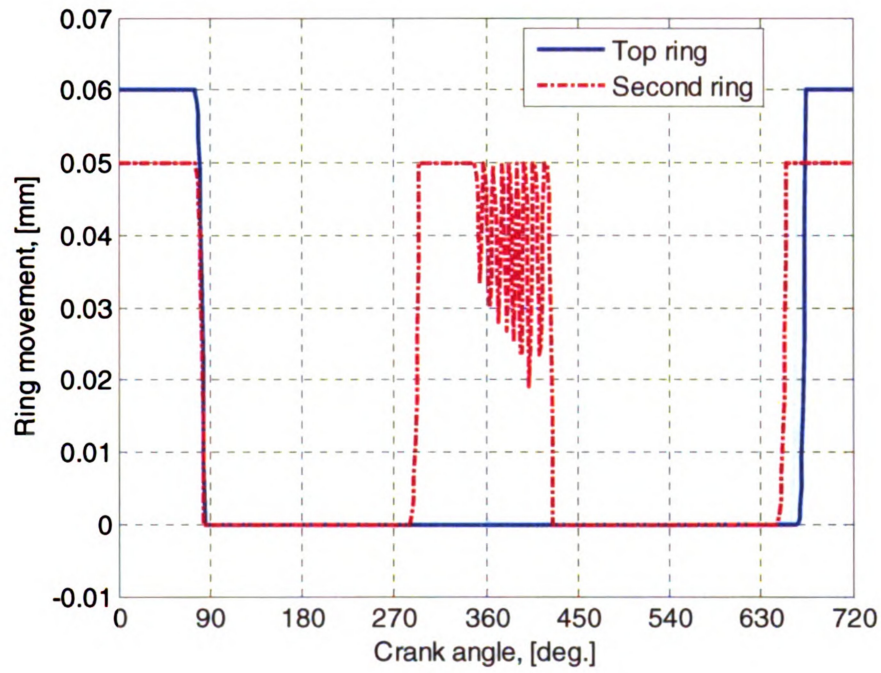
Figure 7.21: Predicted blow-by, Engine 2, Cylinder 1, Leakage 2

The CASE model does not predict ring collapse at any operating condition for either engine. In order to understand the mechanism of blow-by for these engines, the axial ring location relative to the bottom of the groove is examined.

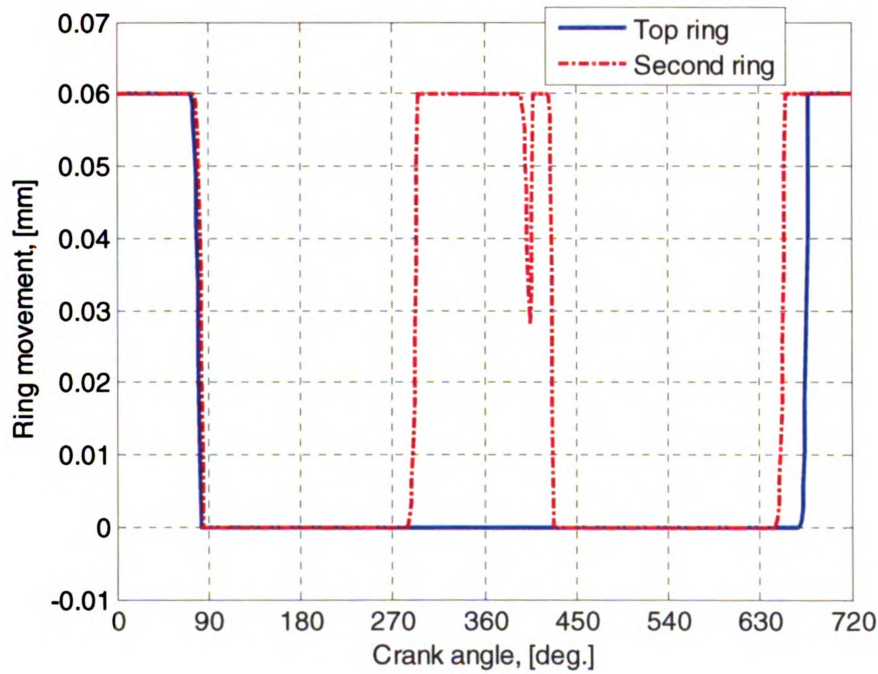
Figure 7.22 and Figure 7.23 show the predicted ring location of the top two rings for cylinder 1 of the two engines at 6500 RPM and WOT and low load, respectively. At WOT the ring-packs exhibit similar behavior. The top ring is seated at the bottom of the groove for most of the cycle, except at the beginning of the intake and end of the exhaust strokes. The second ring follows the same motion but also lifts after the middle of the compression stroke and remains towards the top of the groove until close to the middle of the expansion stroke. The noticeable difference is the duration of second ring flutter for Engine 1. The second ring of Engine 1 is lighter than that of Engine 2, and thus inertia is

lower. This phenomenon suggests that the second land pressure becomes sufficiently high and overcomes inertia, thus pushing the ring downward. The second ring floats and creates a passage for extra gas flow, increasing the third land pressure while relieving the second land pressure. This pushes the ring to the top of the groove again. The process continues until the net force on the ring pushes it toward the bottom of the groove. The second ring of Engine 2 only shows one instance of flutter after peak in-cylinder pressure. Despite the fact that the peak in-cylinder pressure is 15 bar higher and the end gap clearance of the top ring is bigger than Engine 1, the second land pressure does not become sufficiently high to dominate inertia and cause prolonged flutter. This indicates that the ring-pack of Engine 2 is better designed.

At the low load condition (Figure 7.23), the motions observed at the beginning of the intake stroke and end of the exhaust stroke are similar to those at the high load condition (Figure 7.22). The noticeable differences are the reduction of second ring flutter and lift of the top ring for Engine 1 and the absence of second ring flutter for Engine 2. The top ring of Engine 1 is heavier than that of Engine 2. In conjunction with its lower in-cylinder pressure, ring inertia dominates toward the end of the compression stroke, thus lifting the top ring. When the in-cylinder pressure peaks at around TDC, it becomes sufficiently high to push the top ring back to the bottom of the groove. This motion (floating) of the top ring handicaps its sealing capabilities, thus resulting in the spike in the blow-by observed at this condition (Figure 7.17). The pressure buildup in the second land does not become sufficiently high to cause prolonged ring flutter as observed at WOT.

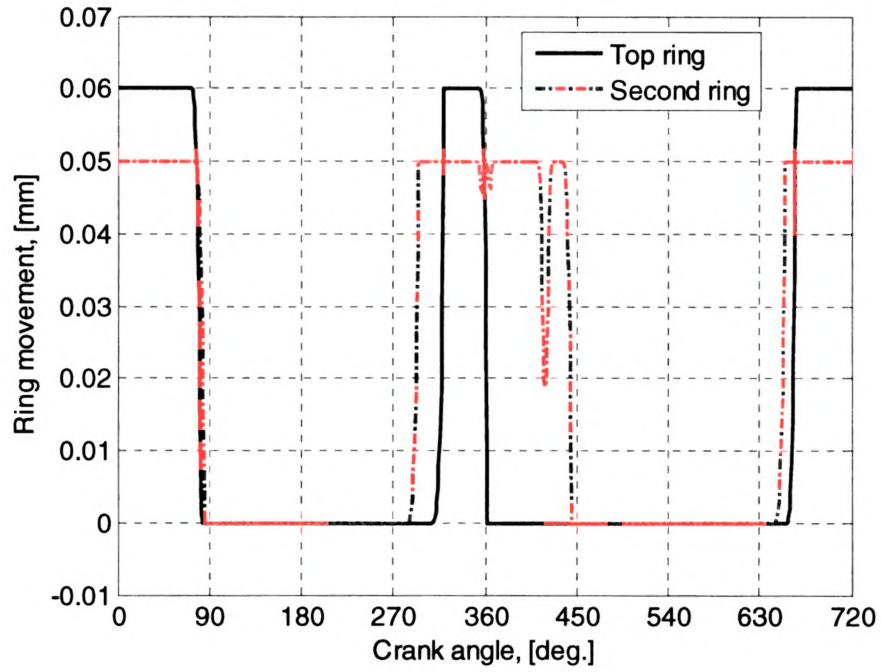


(a)

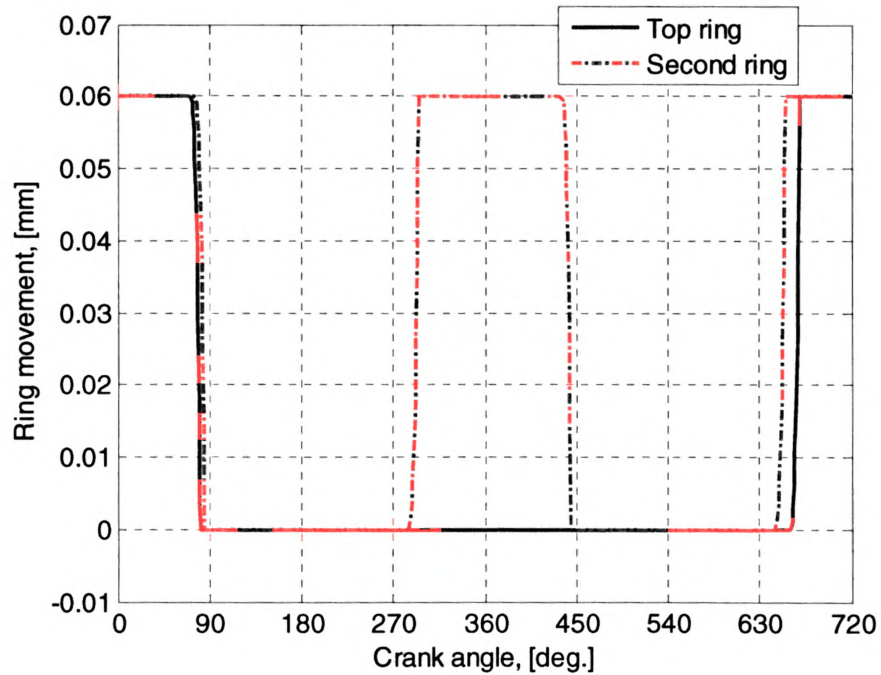


(b)

Figure 7.22: Predicted ring location, Cylinder 1, Leakage 2, Load WOT, 6500 RPM
(a) Engine 1 and (b) Engine 2



(a)



(b)

**Figure 7.23: Predicted ring location, Cylinder 1, Leakage 2, Load 25P, 6500 RPM
(a) Engine 1 and (b) Engine 2**

Engine 2 exhibits no top ring movement during the compression stroke. This is achieved by the higher in-cylinder pressure and also the lower inertia of the top ring. These effects keep it seated at the bottom of the groove and hence there is no spike in the predicted blow-by for this engine (Figure 7.21). Also the second ring flutter is completely eliminated.

In conclusion, given the available data, the ring-pack of Engine 2 is designed better than that of Engine 1. The second ring instability is limited at high-speed, high-load conditions, and it is absent at high-speed, low-load conditions. Also, the blow-by is better controlled in this engine. These results, however, cannot be considered conclusive as they were predicted by tuning the leakage coefficients at one operating condition and then using the set to build the blow-by maps. Perhaps this implies the need for an improved model for ring dynamics. The foundation for such an improved model is introduced in the next chapter.

CHAPTER 8. AN INTRODUCTION TO 3-D NUMERICAL MODELING OF PISTON RING DYNAMICS

8.1 Background

Conventional numerical models for the prediction of ring dynamics perform the calculations in a two-dimensional domain under the assumption that variations in gas flow and ring motion at different axial locations along the circumference are negligible. Figure 8.1 shows an axial cross-section of a ring-pack where the calculations are performed to predict the groove pressures P_1 , P_3 and P_5 , the land pressures P_2 and P_4 and the motion of the three rings given the boundary conditions P_c and P_s .

The calculations in this two-dimensional domain proved to be adequate for ring-pack designs of the last several decades. However, all the efforts to increase engine efficiency and control emissions in recent years result in much tighter clearances. These, in conjunction with piston secondary motion and the use of smaller asymmetric rings, necessitate the introduction of improved numerical models.

Figure 8.2 shows typical variations in groove and land volumes at the end of the compression stroke and beginning of the expansion stroke. At the end of the compression stroke, the ring piston is sliding on the minor thrust side, thus the volumes in this cross-section are smaller than the ones on the major thrust side cross-section. Similarly, at the beginning of the compression stroke, the piston moves to the major thrust side, thus making the volumes on the minor thrust side bigger. This dynamic change of volumes continues throughout the cycle. These changes in volume from side to side affect the

interring gas pressures and ultimately ring motion, ring twist, friction, blow-by and emissions.

Considering the secondary motion of the piston described in Chapter 3, the land and groove volumes at any circumferential location are dictated by it,

$$V = f(\text{ring and groove geometry}, e_p \cos \theta, e_z \cos \theta, \beta) \quad (8.1)$$

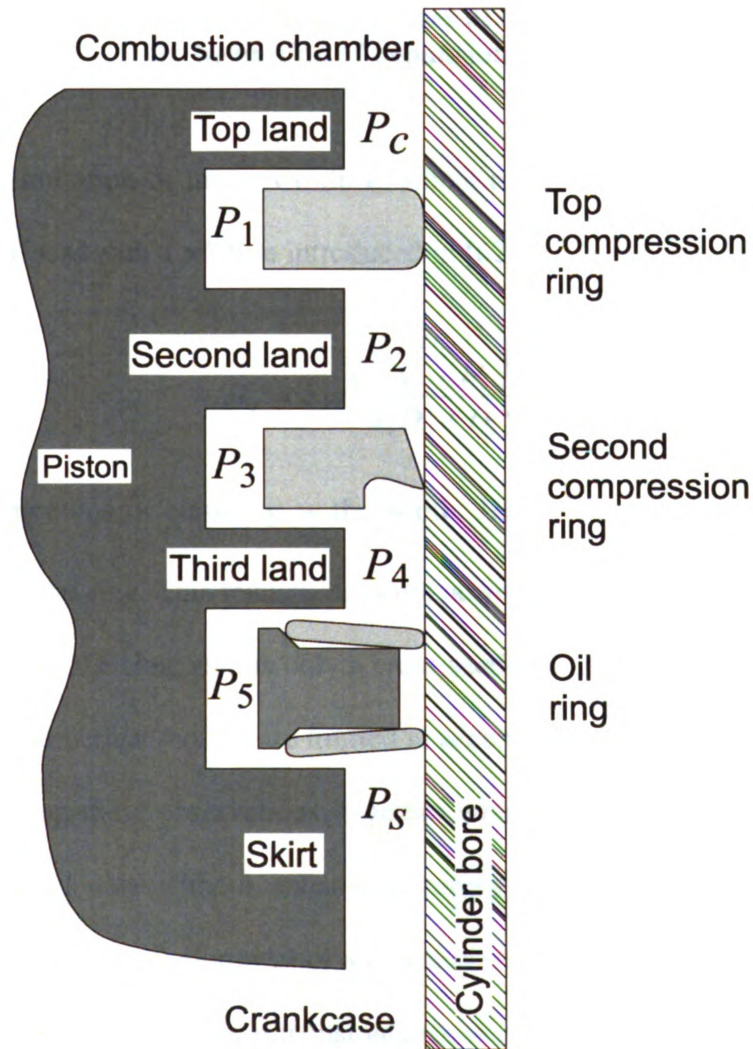
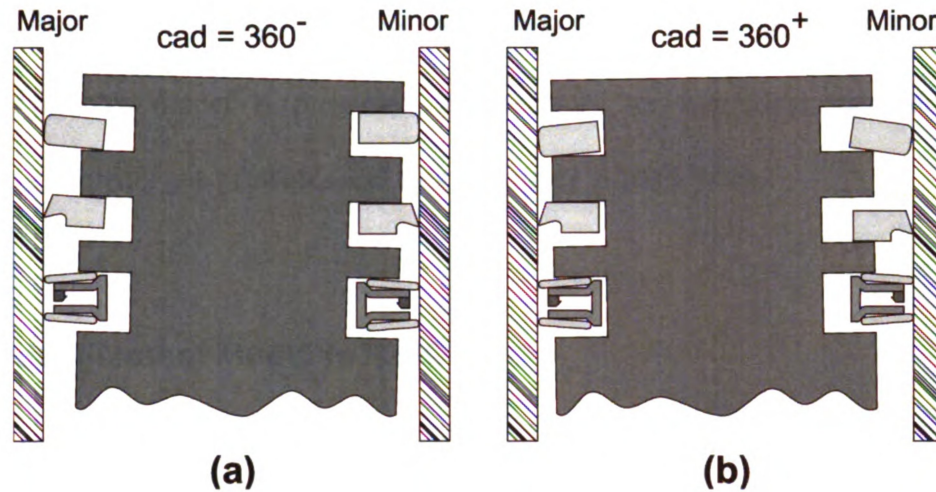


Figure 8.1: Axial cross-section of ring-pack



**Figure 8.2: Typical groove and land volumes at (a) end of compression stroke
(b) beginning of expansion stroke**

Another limitation of these two-dimensional models is the approximation of the **ring** torsional stiffness with a relation introduced in [62],

$$T_r = E w^3 \frac{\ln\left(\frac{D_o}{D_i}\right)}{3(D_o + D_i)} \quad (8.2)$$

where E is the modulus of elasticity, w the width, D_o the outside diameter, and D_i the **inside** diameter of the ring. This relation does not account for the stiffness variation along **the circumference** of the ring, as it is only a cross-sectional property. Hence conventional **two-dimensional** numerical models are limited in accurately predicting ring twist.

After making these observations, together with the fact that modeling results do **not match** measured data without exhaustive tuning (see Chapter 7), it was deemed **appropriate** to initiate the development of a new numerical model that will account for all **the dynamic** variations in the three-dimensional space.

In this chapter the finite element model which will act as the foundation of the 3-D ring dynamics model is presented. Furthermore the numerical methodology for calculating interring gas pressures and ring dynamics is introduced.

8.2 Finite Element Model in RING

RING is a commercial numerical model for ring dynamics. It is part of the CASE suite [6]. The finite element in RING, which is used for the ring-bore conformability analysis, uses planar frame elements (Figure 8.3). Such elements have three degrees of freedom (DOF) at each node, two translational and one rotational. Although such elements are adequate for predicting ring-bore conformability, they cannot be used to predict ring twist along the ring circumference for rings with asymmetric cross sections. Furthermore, the loads on the ring are implemented as point forces in the radial direction at each node, and moments are ignored. However, a distributive pressure load along the ring circumference will result in point forces and bending moments.

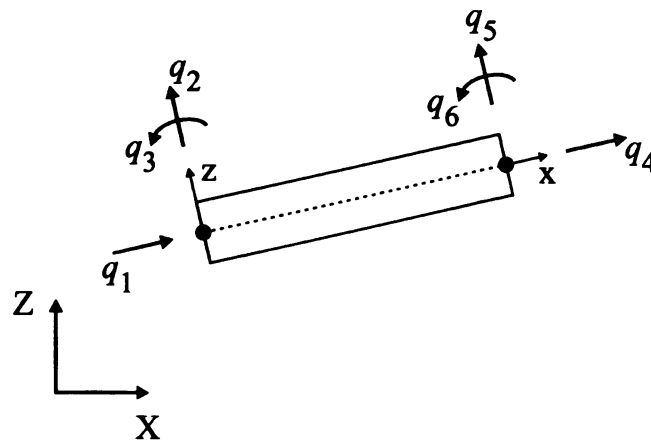


Figure 8.3: Planar frame element

8.3 Finite Element Model for a 3-D Ring

The finite element model for a 3-D ring introduced here uses space frame elements (Figure 8.4). Such an element possesses twelve DOF, six at each node. For node 1:

q_1 : translation along the local x-axis

q_2 : translation along the local y-axis

q_3 : translation along the local z-axis

q_4 : rotation about the local x-axis

q_5 : rotation about the local y-axis

q_6 : rotation about the local z-axis

Respectively q_7 to q_{12} correspond to node 2. This element is suitable for **predicting** ring twist along the ring circumference and coupling the ring dynamics. The **theory** behind this element will not be discussed in detail. The interested reader is directed **to** [59] or any other finite element book for an in-depth discussion of the theory. The **basics** only are given here.

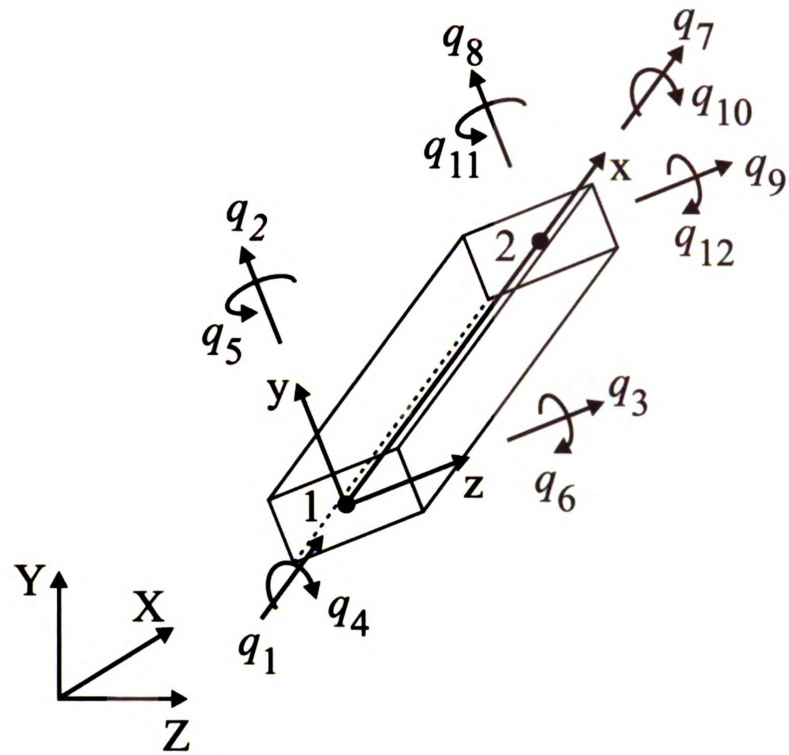


Figure 8.4: Space frame element

The local stiffness matrix of the element is given by,

$$\mathbf{K}_L = \begin{bmatrix} \mathbf{K}_{11} & \mathbf{K}_{21}^T \\ \mathbf{K}_{21} & \mathbf{K}_{22} \end{bmatrix} \quad (8.3)$$

with,

$$\mathbf{K}_{11} = \begin{bmatrix} \frac{EA}{l} & 0 & 0 & 0 & 0 & 0 \\ 0 & \frac{12EI_{zz}}{l^3} & 0 & 0 & 0 & \frac{6EI_{zz}}{l^2} \\ 0 & 0 & \frac{12EI_{yy}}{l^3} & 0 & -\frac{6EI_{yy}}{l^2} & 0 \\ 0 & 0 & 0 & \frac{GJ}{l} & 0 & 0 \\ 0 & 0 & -\frac{6EI_{yy}}{l^2} & 0 & \frac{4EI_{yy}}{l} & 0 \\ 0 & \frac{6EI_{zz}}{l^2} & 0 & 0 & 0 & \frac{4EI_{zz}}{l} \end{bmatrix} \quad (8.4)$$

$$\mathbf{K}_{21} = \begin{bmatrix} -\frac{EA}{l} & 0 & 0 & 0 & 0 & 0 \\ 0 & -\frac{12EI_{zz}}{l^3} & 0 & 0 & 0 & \frac{6EI_{zz}}{l^2} \\ 0 & 0 & \frac{12EI_{yy}}{l^3} & 0 & -\frac{6EI_{yy}}{l^2} & 0 \\ 0 & 0 & 0 & -\frac{GJ}{l} & 0 & 0 \\ 0 & 0 & -\frac{6EI_{yy}}{l^2} & 0 & \frac{2EI_{yy}}{l} & 0 \\ 0 & \frac{6EI_{zz}}{l^2} & 0 & 0 & 0 & \frac{2EI_{zz}}{l} \end{bmatrix} \quad (8.5)$$

$$\mathbf{K}_{22} = \begin{bmatrix} \frac{EA}{l} & 0 & 0 & 0 & 0 & 0 \\ 0 & \frac{12EI_{zz}}{l^3} & 0 & 0 & 0 & -\frac{6EI_{zz}}{l^2} \\ 0 & 0 & \frac{12EI_{yy}}{l^3} & 0 & \frac{6EI_{yy}}{l^2} & 0 \\ 0 & 0 & 0 & \frac{GJ}{l} & 0 & 0 \\ 0 & 0 & \frac{6EI_{yy}}{l^2} & 0 & \frac{4EI_{yy}}{l} & 0 \\ 0 & -\frac{6EI_{zz}}{l^2} & 0 & 0 & 0 & \frac{4EI_{zz}}{l} \end{bmatrix} \quad (8.6)$$

and the local nodal displacement and load vectors are given by (8.7) and (8.8) respectively,

$$\mathbf{q}_L = \{q_1 \ q_2 \ q_3 \ q_4 \ q_5 \ q_6 \ q_7 \ q_8 \ q_9 \ q_{10} \ q_{11} \ q_{12}\}^T \quad (8.7)$$

$$\mathbf{f}_L = \{f_1 \ f_2 \ f_3 \ f_4 \ f_5 \ f_6 \ f_7 \ f_8 \ f_9 \ f_{10} \ f_{11} \ f_{12}\}^T \quad (8.8)$$

These are in the element local coordinate system x-y-z. Before assembly they **need** to be transformed to the global coordinate system X-Y-Z. This is achieved by the **trans**formation matrix, \mathbf{T} , so that

$$\mathbf{q}_L = \mathbf{T}\mathbf{q} \quad (8.9)$$

where \mathbf{T} is given by assembling diagonally the transformation matrix \mathbf{T}_s ,

$$\mathbf{T} = \begin{bmatrix} \mathbf{T}_s & \mathbf{0} & \mathbf{0} & \mathbf{0} \\ \mathbf{0} & \mathbf{T}_s & \mathbf{0} & \mathbf{0} \\ \mathbf{0} & \mathbf{0} & \mathbf{T}_s & \mathbf{0} \\ \mathbf{0} & \mathbf{0} & \mathbf{0} & \mathbf{T}_s \end{bmatrix} \quad (8.10)$$

In turn \mathbf{T}_s is derived in two stages. In stage one the direction cosines for the local axis relative to the global axis are derived assuming the local z-axis is parallel to the X-Z plane, yielding the transformation matrix \mathbf{T}_a . In the second stage the transformation matrix \mathbf{T}_b is derived which accounts for the rotation of the member's principal axis (Figure 8.5).

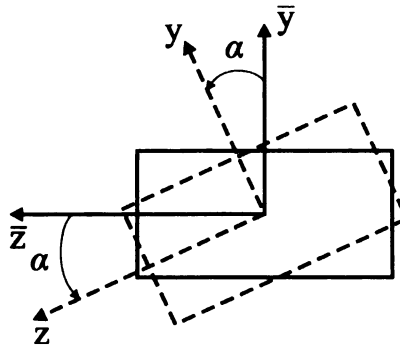


Figure 8.5: Principal axis (y-z) rotation, viewed from the positive x-direction

The two transformation matrices are given by,

$$\mathbf{T}_a = \begin{bmatrix} l_{ox} & m_{ox} & n_{ox} \\ -(l_{ox}m_{ox})/d & (l_{ox}^2 + n_{ox}^2)/d & -(m_{ox}n_{ox})/d \\ -n_{ox}/d & 0 & -l_{ox}/d \end{bmatrix} \quad (8.11)$$

and,

$$\mathbf{T}_b = \begin{bmatrix} 1 & 0 & 0 \\ 0 & \cos \alpha & \sin \alpha \\ 0 & -\sin \alpha & \cos \alpha \end{bmatrix} \quad (8.12)$$

where,

$$l_{ox} = \frac{X_2 - X_1}{l} \quad (8.13)$$

$$m_{ox} = \frac{Y_2 - Y_1}{l} \quad (8.14)$$

$$n_{ox} = \frac{Z_2 - Z_1}{l} \quad (8.15)$$

with l being the element length and $d = \sqrt{l_{ox}^2 + n_{ox}^2}$. The transformation matrix \mathbf{T}_s is then obtained by,

$$\mathbf{T}_s = \mathbf{T}_b \mathbf{T}_a \quad (8.16)$$

In the case where the element is vertical, that is the x-axis is parallel to the Y-axis, the transformation matrix \mathbf{T}_b , is of different form than what is given in (8.12). This is not applicable to the present model and thus it is not given.

The relation between local and global nodal displacements is given by,

$$\mathbf{q}_L = \mathbf{T} \mathbf{q} \quad (8.17)$$

resulting to the global system of equations,

$$\mathbf{K} \mathbf{q} = \mathbf{f} \quad (8.18)$$

with,

$$\mathbf{K} = \mathbf{T}^T \mathbf{K}_L \mathbf{T} \quad (8.19)$$

The order of the system is six times the number of nodes.

The load vector, \mathbf{f} , due to a distributive force is calculated using the equations for a beam element (Figure 8.6). A beam element is subjected to transverse loads and bending moments, and the nodal displacements are transverse in the plane of loading and rotational about the plane of loading.

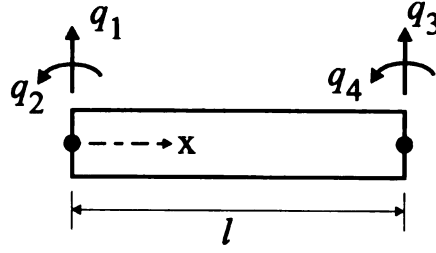


Figure 8.6: Beam element

The load vector for a beam element, \mathbf{f}_b , subjected to a distributive load p_0 , is given by,

$$\mathbf{f}_b = \int_0^l \mathbf{N}^T p_0 dx \quad (8.20)$$

where, \mathbf{N} is the matrix of shape functions,

$$\mathbf{N} = [N_1 \quad N_2 \quad N_3 \quad N_4] \quad (8.21)$$

with,

$$\begin{aligned} N_1 &= (2x^3 - 3lx^2 + l^3)/l^3 \\ N_2 &= (x^3 - 2lx^2 + l^2x)/l^2 \\ N_3 &= (3lx^2 - 2x^3)/l^3 \\ N_4 &= (x^3 - lx^2)/l^2 \end{aligned} \quad (8.22)$$

Evaluating (8.20) yields,

$$\mathbf{f}_b = \frac{1}{12} p_0 l \{6 \quad l \quad 6 \quad -l\}^T \quad (8.23)$$

where entries 1 and 3 are transverse loads and entries 2 and 4 are bending moments.

Now referring to Figure 8.4, in the case of a space frame element, a distributive force loading in the x-z plane will yield a load vector as,

$$\mathbf{f}_L = \frac{1}{12} p_0 l \{0 \ 0 \ 6 \ 0 \ l \ 0 \ 0 \ 0 \ 6 \ 0 \ -l \ 0\}^T \quad (8.24)$$

and a distributive force loading in the x-y plane will yield a load vector as,

$$\mathbf{f}_L = \frac{1}{12} p_0 l \{0 \ 6 \ 0 \ 0 \ 0 \ l \ 0 \ 6 \ 0 \ 0 \ 0 \ -l\}^T \quad (8.25)$$

The global load vector is then obtained by the relation,

$$\mathbf{f} = \mathbf{T}^T \mathbf{f}_L \quad (8.26)$$

8.4 Ring Discretization and Coordinate Transformation

A schematic of the ring in its global coordinate system is shown in Figure 8.7. Here, D is the compressed diameter of the ring when fitted to the bore, e_c is the end gap clearance and w is the ring width. The nodes are placed along the ring at a radius R given by,

$$R = D - \frac{w}{2} \quad (8.27)$$

The ring is discretized with n nodes, where n has to be odd and in the range of 91 to 181, that is,

$$n = 2z + 1 ; z \in [45, 90] \quad (8.28)$$

The angular location of each node is given by θ .

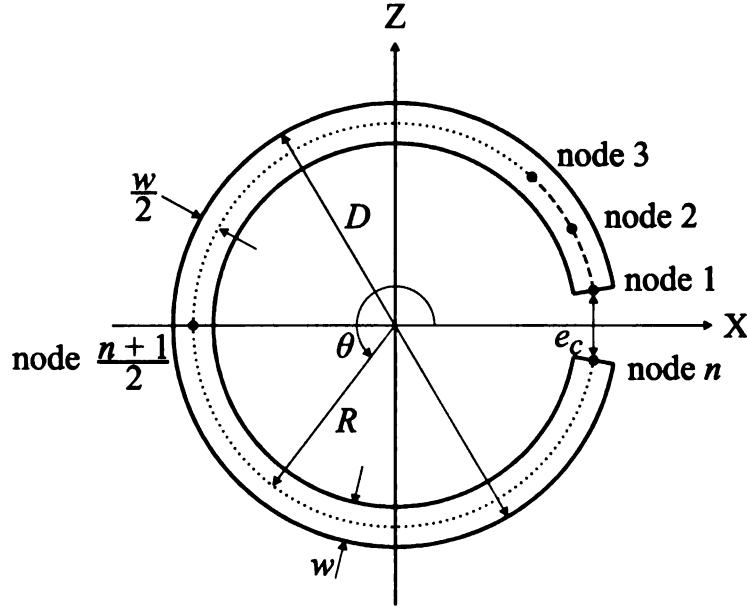


Figure 8.7: Ring in its global coordinate system (viewed from the negative Y-direction)

In calculating the ring-bore conformability the radial displacements at each node need to be known. The ring twist is given by the rotation about the tangential axis of each node. This is achieved by a coordinate transformation from the global coordinate system to a local radial-tangential coordinate system (r-t) shown in Figure 8.8. The figure is viewed from the negative Y-direction, and it does not show displacements in that direction. The transformation is given by,

$$\begin{Bmatrix} r \\ t \\ Y \\ \beta \end{Bmatrix} = \begin{bmatrix} \cos \theta & \sin \theta & 0 & 0 & 0 \\ -\sin \theta & \cos \theta & 0 & 0 & 0 \\ 0 & 0 & 1 & 0 & 0 \\ 0 & 0 & 0 & -\sin \theta & \cos \theta \end{bmatrix} \begin{Bmatrix} q_1 \\ q_3 \\ q_2 \\ q_4 \\ q_6 \end{Bmatrix} \quad (8.29)$$

where r is the radial displacement and β is the ring twist.

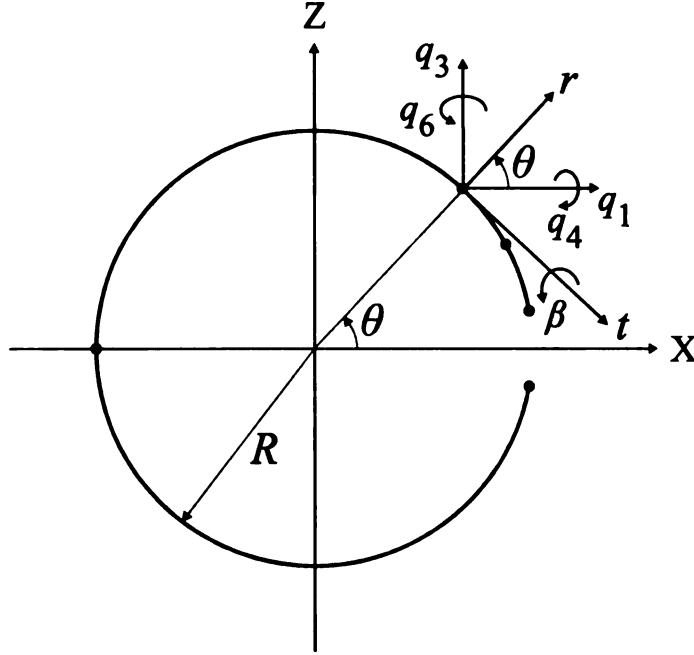


Figure 8.8: Radial-tangential coordinate system

Conforming the ring to the bore will affect the end gap clearance. The change in end gap clearance (Figure 8.9) is calculated by evaluating the length of vector $\bar{\mathbf{C}}$ in (8.30). If the end gap clearance is zero a warning issued. Also to ensure that the gap is not negative, that is, there is no overlap of the first and last element, a unit vector, (8.31), in the direction of vector $\bar{\mathbf{C}}$ is calculated. As long as $n_Z > 0$ there is no overlap.

$$\bar{\mathbf{C}} = -\bar{\mathbf{B}} + \bar{\mathbf{A}} \quad (8.30)$$

$$\frac{\bar{\mathbf{C}}}{|\bar{\mathbf{C}}|} = n_X \hat{\mathbf{i}} + n_Y \hat{\mathbf{j}} + n_Z \hat{\mathbf{k}} \quad (8.31)$$

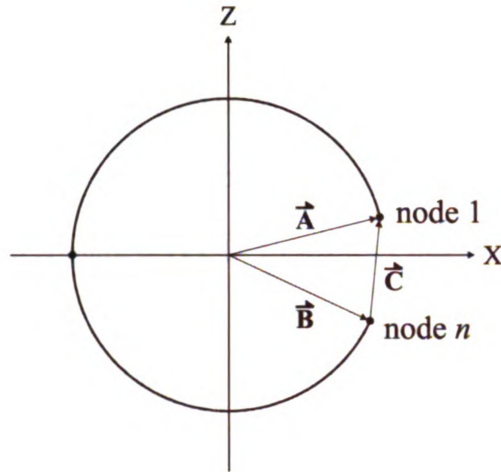


Figure 8.9: Ring end gap

In the case where the ring is not conforming to the bore this will create additional passages for gas flow. The area created due to this non-conformability is approximated by triangles and trapezoids. For example, for the schematic shown in Figure 8.10 the gas flow area, A_{flow} , would be approximated as,

$$A_{flow} = \frac{1}{2}l c_3 + l \frac{c_3 + c_4}{2} + \frac{1}{2}l c_4 \quad (8.32)$$

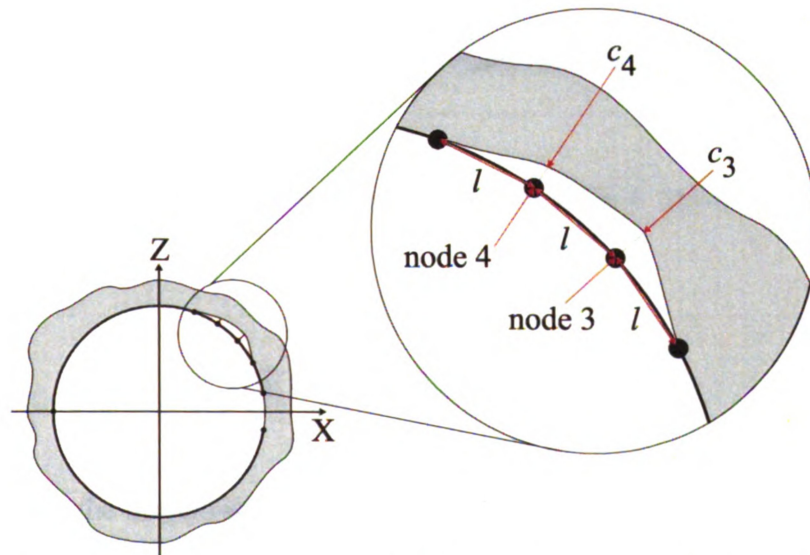


Figure 8.10: Flow area created due to non-conforming nodes

8.5 Bore Deformation

The bore deformation can be input as data from measurements or finite element analysis of the cylinder block. It should be input in two dimensions, the circumferential location and axial location (Figure 8.11). Deformations that will enlarge the nominal bore diameter are positive.

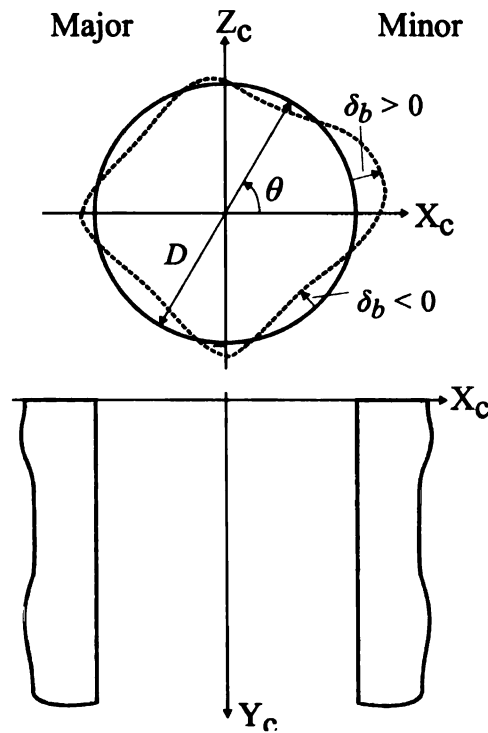


Figure 8.11: Bore deformation

Alternatively the bore deformation can be simulated using a 4th order cosine function of the form,

$$\delta_b = \sum_{i=2}^4 \lambda_i \cos[i(\theta + \phi_i)] \quad (8.33)$$

where the λ_i 's are the amplitudes and ϕ_i 's are the phases. The zeroth and first orders are omitted as they represent magnification and translation respectively.

8.6 Gap Location

The gap location of the ring can be varied to investigate effects on conformability and ultimately dynamics and blow-by. The gap location is described by an angle ϕ , measured counter-clockwise from the minor thrust side (Figure 8.12).

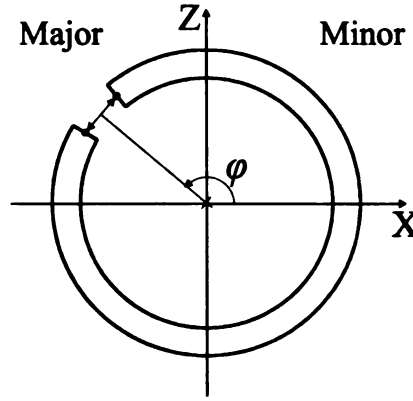


Figure 8.12: Gap location

8.7 Ring-bore Conformability - Methodology

Given the complex topology of the bore deformation, the ring conformability cannot be achieved by the standard minimization of the potential energy of the system (8.34).

$$\Pi = \frac{1}{2} \mathbf{q}^T \mathbf{K} \mathbf{q} - \mathbf{q}^T \mathbf{f} \quad (8.34)$$

While the ring is fitted into the distorted bore and exposed to the gas pressure loads, some nodes will be displaced inwards and other outwards. The conformability is achieved iteratively using a fix-and-release (of constraints) strategy.

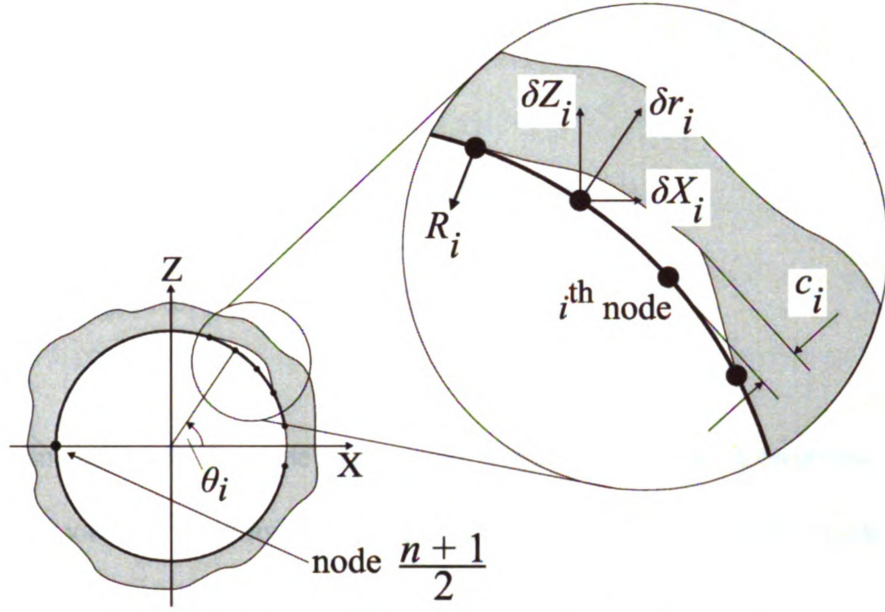


Figure 8.13: Nodal clearances and displacements

The nodal displacements of the ring exposed to the solid cylinder bore have to obey a non-penetration condition. Referring to Figure 8.13, this non-penetration condition at the i^{th} node can be in the form of a constraint expressed as,

$$g_i = \delta r_i - c_i = \delta X_i \cos \theta_i + \delta Z_i \sin \theta_i - c_i \leq 0 \quad (8.35)$$

It should be noted that when the above constraint is satisfied the reaction force, R_i , is zero. If the constraint is active then the reaction force is less than zero.

$$\begin{aligned} g_i &< 0; R_i = 0 \\ g_i &= 0; R_i < 0 \end{aligned} \quad (8.36)$$

Also it should be noted that,

$$g_i = \delta r_i - c_i = -\delta X_i - c_i \leq 0; \quad \text{for } i = \frac{n+1}{2} \quad (8.37)$$

The ring-bore conformability problem can then be expressed as,

$$\begin{aligned}
 &\text{Find:} && \mathbf{q} \\
 &\text{that minimizes:} && \Pi = \frac{1}{2} \mathbf{q}^T \mathbf{K} \mathbf{q} - \mathbf{q}^T \mathbf{f} \\
 &\text{subject to:} && g_i \leq 0
 \end{aligned}$$

Minimization of the potential energy requires that the derivatives of Π with respect to q_i vanish, yielding (8.18). For the system to be solved some boundary conditions (constraints) have to be applied to prevent rigid body motion. Due to the symmetry of the ring all 6 DOF of node $(n+1)/2$ are constrained in order to jump start the iterative process. The first DOF of node $(n+1)/2$, in X-direction, can be released during the iterative fix-and-release strategy, while the other five are constrained throughout.

In solving the ring-bore conformability problem there are two cases to consider:

- i. The constraint g_i is satisfied and is inactive, that is $g_i < 0$. In such a case the solution of the problem follows directly from (8.18) and implementation of the above described boundary conditions at node $(n+1)/2$.
- ii. The constraint g_i is active, that is $g_i = 0$. In such a case the contact constraint has to be incorporated into the potential energy to solve the ring-bore conformability problem. This is achieved using the penalty method [36, 77].

The penalty method is a well-known method, and it is used widely in the solution of contact problems via finite element methods. An alternative approach would be the Lagrange multiplier method, however, this method would increase the order of the system and thus computation time. The penalty method, for each active constraint, adds a penalty to the potential energy. For the present problem, (8.35) can be written in matrix form as

$$\mathbf{g} = \mathbf{A}\mathbf{q} - \mathbf{c} = \mathbf{0} \quad (8.38)$$

The potential energy is then modified to account for the penalties,

$$\Pi_g = \frac{1}{2} \mathbf{q}^T \mathbf{K} \mathbf{q} - \mathbf{q}^T \mathbf{f} + \frac{1}{2} \mathbf{g}^T \lambda \mathbf{g} \quad (8.39)$$

where λ is the penalty number. The choice of λ is dependent on the problem. The recommended range found in literature is,

$$\lambda = \lambda_r \max [\text{diag}(\mathbf{K})] ; \lambda_r \in [10^4, 10^6] \quad (8.40)$$

If $\lambda = 0$ then (8.39) reduces to (8.34). When λ is large the penalty of violating the constraints is large; thus in minimizing the potential energy, the constraints are closely satisfied. Again minimization of the potential energy requires that the derivatives of Π_g with respect to q_i vanish, yielding

$$[\mathbf{K} + \mathbf{A}^T \lambda \mathbf{A}] = \mathbf{f} + \mathbf{A}^T \lambda \mathbf{c} \quad (8.41)$$

8.7.1 The Fix-and-release Strategy

In the process of solving the ring-bore conformability problem, that is fitting the ring to the distorted bore, a fix-and-release strategy is employed. The steps are outlined below.

- i. Build the global stiffness matrix.
- ii. Build the global load vector due to ring tension and gas pressure behind the ring.
- iii. Calculate bore deformation at ring level.
- iv. Fix all the DOF of node $(n+1)/2$, except the first one, in the X-direction.
- v. Check bore deformation at each node. If deformation is less than or equal to zero, (8.35) is active, thus build (8.38).
- vi. Solve (8.41).
- vii. Calculate radial displacements and reaction forces at each node.
- viii. Check for each node: (a) if the radial reaction is greater than zero release the node, (b) if the radial displacement is greater than the bore deformation fix the node, that is, (8.35) is active. If (a) or (b) is true go back to step vi. Otherwise return the ring-bore conformability.

8.8 Choosing the Penalty Number

In Section 8.7 it was indicated that the penalty number, λ , is problem-dependent and it ideally lies within a range (8.40). In order to decide on the choice for λ , the finite element solution for two cases is compared. In each case three different λ 's ($\lambda = 10^4$, $\lambda =$

10^5 , and $\lambda = 10^6$) lying within the range are tested. The ring is discretized with 91 nodes.

The ring properties are given in Table 8.1.

Table 8.1: Ring properties

Ring diameter, D [mm]	87.5
Ring width, w [mm]	2.8
Cross-sectional area, A [mm ²]	3.27
Second moment of inertia I_{yy} [mm ⁴]	2.03
Second moment of inertia, I_{zz} [mm ⁴]	0.38
Polar moment of inertia, J [mm ⁴]	2.4
Principal axis angle, α [deg.]	0
Modulus of elasticity, E [N mm ⁻²]	196.1e+3
Poisson's ration, ν	0.3
Distributive force, p_0 [N mm ⁻¹]	0.5

In the first case, the radial displacements are calculated at each node due to the distributive load, p_0 . All the DOF's of the centre node, node 46, are fixed. Two non-penetration conditions (8.35) are imposed on nodes 20 and 60 with $c_{20} = 1$ mm and $c_{60} = -1$ mm. The radial displacements are shown in Figure 8.14. It is clear that each λ returns equivalent results.

In the second case the ring is fitted to a distorted bore. The bore deformation and the radial displacements of the fitted ring for different λ 's are shown in Figure 8.15. Again each λ returns equivalent results.

Consequently in the context of the ring-bore conformability the penalty number is chosen at the middle of the recommended range,

$$\lambda = 10^5 \quad (8.42)$$

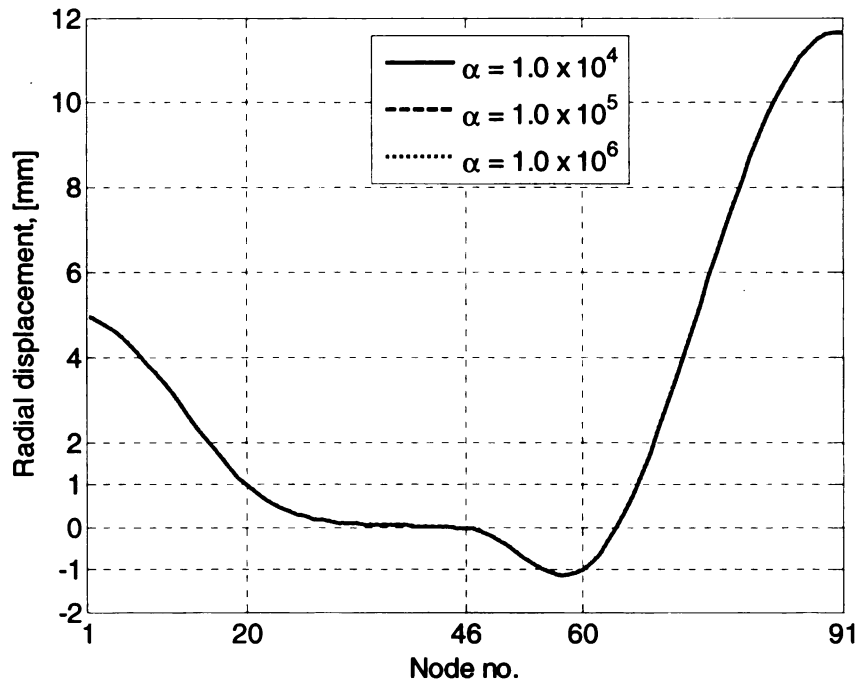


Figure 8.14: Radial displacements prediction due to a distributive load with different penalty numbers

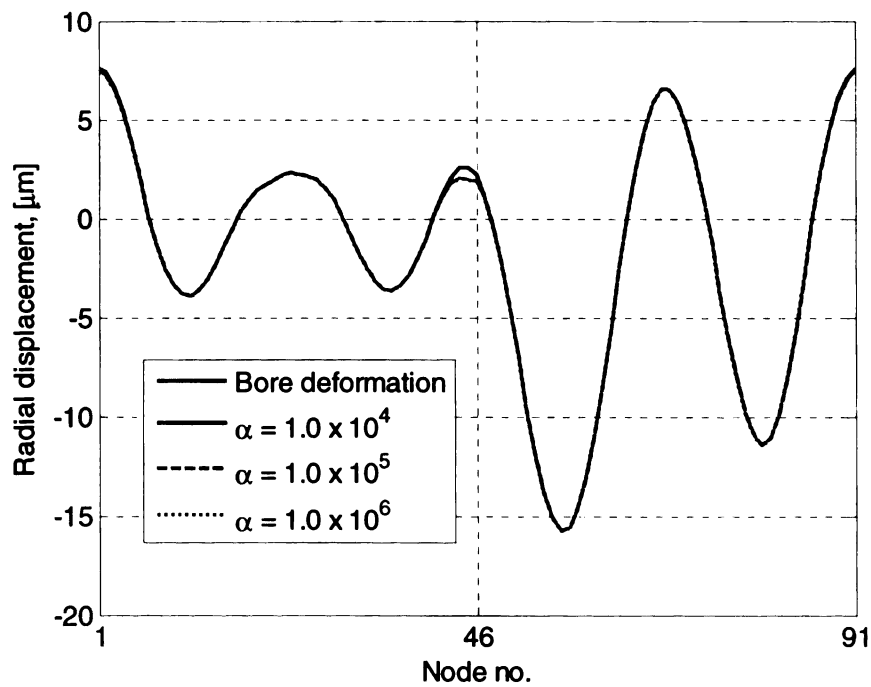


Figure 8.15: Ring fitted to distorted bore with different penalty numbers

8.9 Validating the Ring Finite Element Model

In order to check the adequacy of the ring finite element model and to ensure that it is free of any programming errors, a comparison is made with the analytical solution of a half ring.

Given a semi-circular ring (Figure 8.16) of radius R and constant cross-sectional properties, subjected to a uniform distributive load p_0 , and constrained at one end, the radial and tangential displacements are given by [43],

$$\delta_r = \frac{p_0 R^4}{EI_{yy}} \left(1 - \cos \theta + \frac{\theta}{2} \sin \theta \right) + \frac{p_0 R^2}{EA} \left(1 - \cos \theta + \frac{\theta}{2} \sin \theta \right) + \frac{6 p_0 R^2}{5GA} \left(\frac{\theta}{2} \sin \theta \right) \quad (8.43)$$

$$\delta_t = \frac{p_0 R^4}{EI_{yy}} \left(\theta - \frac{\theta}{2} \cos \theta - \frac{1}{2} \sin \theta \right) - \frac{p_0 R^2}{EA} \left(\frac{\theta}{2} \cos \theta + \frac{3}{2} \sin \theta \right) + \frac{6 p_0 R^2}{5GA} \left(\frac{1}{2} \sin \theta - \frac{\theta}{2} \cos \theta \right) \quad (8.44)$$

The transformation between the radial-tangential coordinate system and the global X-Z coordinate system can be made using the equations in (8.29).

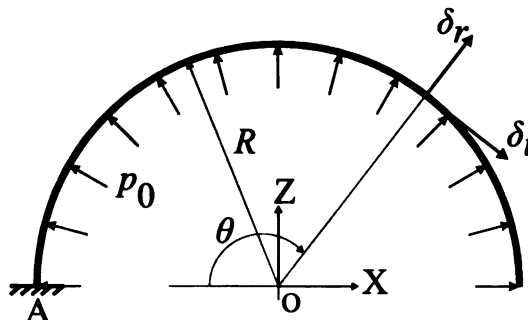


Figure 8.16: Half ring subjected to uniform distributive load

The ring properties shown in Table 8.1 were used in the comparison between the analytical and finite element model results. The semi-circular ring is discretized with 46 nodes. The deformed shape of the ring is shown in Figure 8.17. It can be seen that the analytical and finite element model results are equivalent.

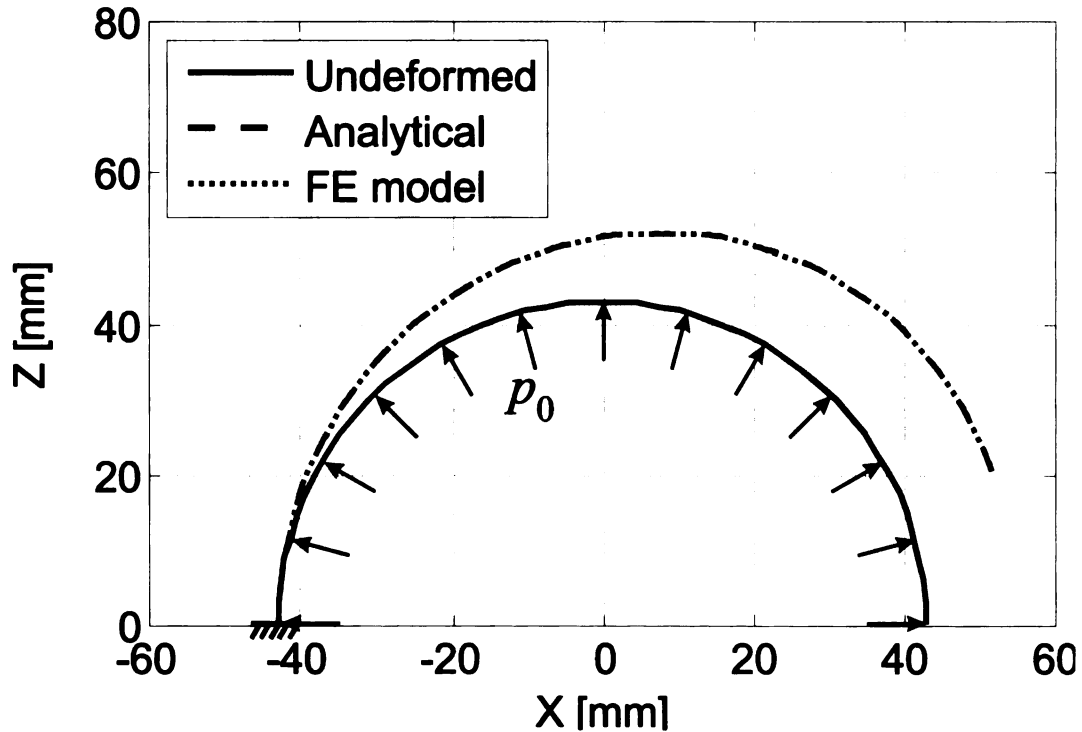


Figure 8.17: Comparing analytical with finite element model results

8.10 Choosing the Number of Nodes

In order to assess the accuracy achieved by increasing the number of nodes and ultimately selecting an adequate number of nodes, several test runs were performed. The number of nodes discretizing the ring was varied while the ring was fitted to the distorted bore shown in Figure 8.15. The ring properties are as of the top compression ring in

Table 8.3 with no pressure loading behind the ring. The results are shown in Table 8.2 and Figure 8.18. The case of 91 nodes is selected as the base, and the rest are normalized with respect to this. At 91 nodes the gas flow area is $1.2437\text{e-}02 \text{ mm}^2$ and the end gap clearance is 0.15035 mm.

It is observed that beyond 91 nodes the results are comparable, especially for the end gap clearance. Clearly the maximum number of nodes is the optimal, as the approximation errors of the gas flow area in (8.32) are minimized. However, the number of iterations needed to fit the ring in the distorted bore appears to be linearly related with the number of nodes. In this specific case, as the number of nodes doubles the number of iteration doubles. Similar trends have been observed when fitting the ring to bore deformations of different topologies. It should be noted that at each iteration the system of equations from the finite element model has to be solved.

Let the system be of order $m = 6n$, where n is the number of nodes. The solution of such system using Gauss elimination is of order $m^3/3$. The cost of fitting the ring to the distorted bore as a function of the number of nodes then is,

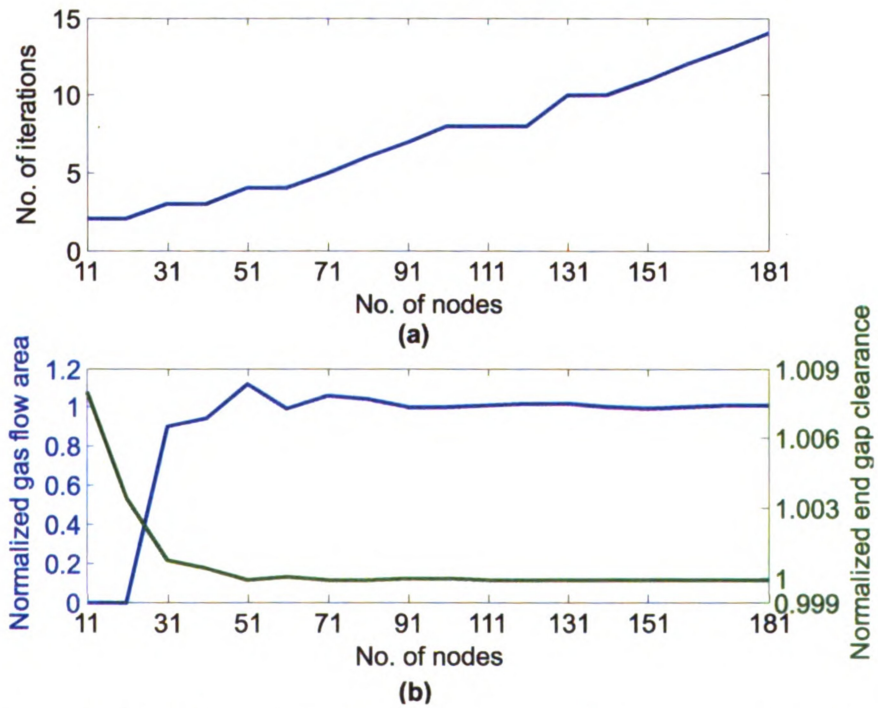
$$\text{cost}(n) = k(n) \frac{216n^3}{3} \quad (8.45)$$

where $k(n)$ is the number of iterations. Thus doubling the number of nodes will make the simulation much more expensive as (8.45) suggests that $\text{cost} \sim n^4$.

Consequently 91 nodes is the recommended number and that is what will be used from here on.

Table 8.2: Effect of number of nodes

Number of nodes	Number of iterations	Normalized gas flow area	Normalized end gap clearance
11	2	0.0000	1.0080
21	2	0.0000	1.0035
31	3	0.9004	1.0008
41	3	0.9415	1.0004
51	4	1.1197	0.9999
61	4	0.9984	1.0001
71	5	1.0612	0.9999
81	6	1.0473	0.9999
91	7	1.0000	1.0000
101	8	1.0019	1.0000
111	8	1.0144	1.0000
121	8	1.0234	0.9999
131	10	1.0211	0.9999
141	10	1.0045	1.0000
151	11	0.9976	1.0000
161	12	1.0042	0.9999
171	13	1.0130	0.9999
181	14	1.0109	0.9999

**Figure 8.18: Effect of number of nodes on (a) number of iterations
(b) on the normalized gas flow area and end gap clearance**

8.11 Sample Numerical Results

In this section some sample results are presented, demonstrating the capabilities of the ring-bore conformability model.

The ring properties are shown in Table 8.3. It is assumed the ring groove pressure (pressure behind the ring) is known *a priori* (Figure 8.19). Finally, the rings are fitted to a distorted bore as shown in Figure 8.20.

The results are shown in Figure 8.21 through Figure 8.24 for the top ring, Figure 8.25 through Figure 8.29 for the second ring, and Figure 8.30 through Figure 8.33 for the oil ring segment.

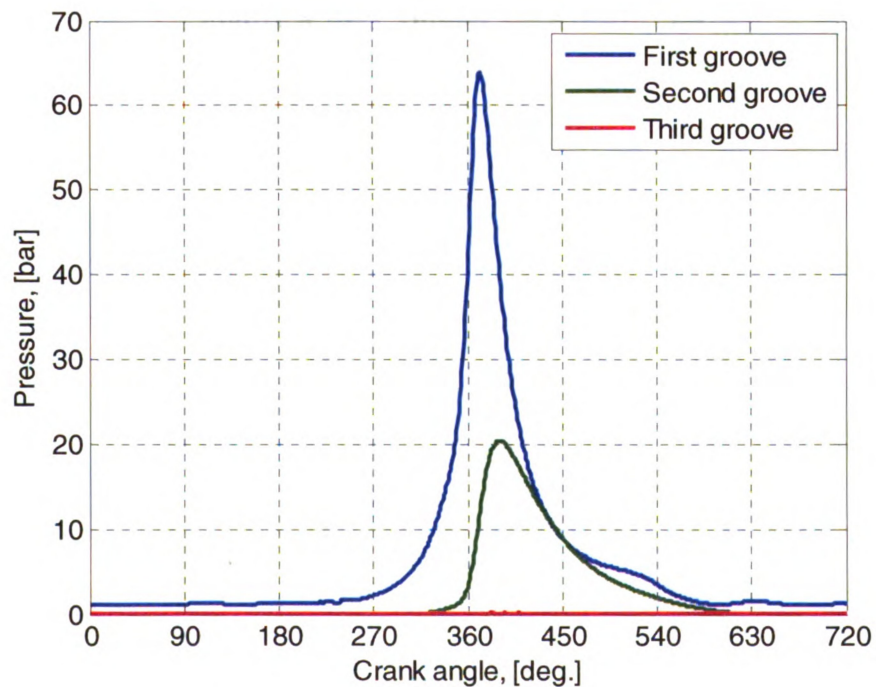
The top ring, as it is exposed to higher pressure load behind it, conforms to the bore better than the second ring. The oil ring segment has the best conformability to the bore despite the very low pressure behind it. This is due to the high diametral force needed to bring it to a diameter of 87.5 mm from the free shape in conjunction with the low second moment of inertia.

The top ring and oil ring segment exhibit no twist, as the principal axis of their cross sections align with the global coordinate system. The second ring, though, exhibits twist as the principal axes are at an angle of 2.71 degrees. The twist is greatly affected by the groove pressure. It can be seen in Figure 8.26 that the maximum twist occurs close to 360 crank angle degrees where the groove pressure is the highest. The ring twist varies significantly along the circumference.

Finally, the flow area and end gap clearance are dependent on the location of the ring and the applicable bore distortion.

Table 8.3: Ring-pack properties

	Top ring	Second ring	Oil ring segment
Ring diameter, D [mm]	87.5	87.5	87.5
Ring width, w [mm]	2.8	3.3	2.3
Cross-sectional area, A [mm ²]	3.27	3.73	0.86
Second moment of inertia I_{yy} [mm ⁴]	2.03	3.18	0.26
Second moment of inertia, I_{zz} [mm ⁴]	0.38	0.42	0.01
Polar moment of inertia, J [mm ⁴]	2.4	3.6	0.28
Principal axis angle, α [deg.]	0	2.71	0
Modulus of elasticity, E [N mm ⁻²]	196.1e+3	108.0e+3	196.1e+3
Poisson's ration, ν	0.3	0.3	0.3
Diametral force, [N]	15.5	14.9	67.0

**Figure 8.19: Ring groove pressure**

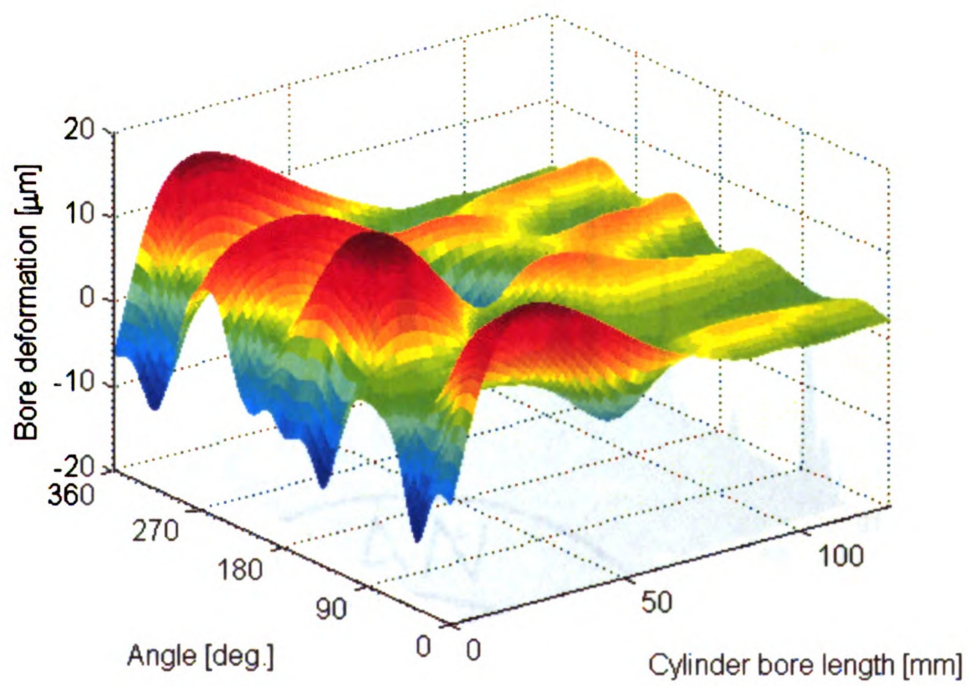


Figure 8.20: Cylinder bore distortion

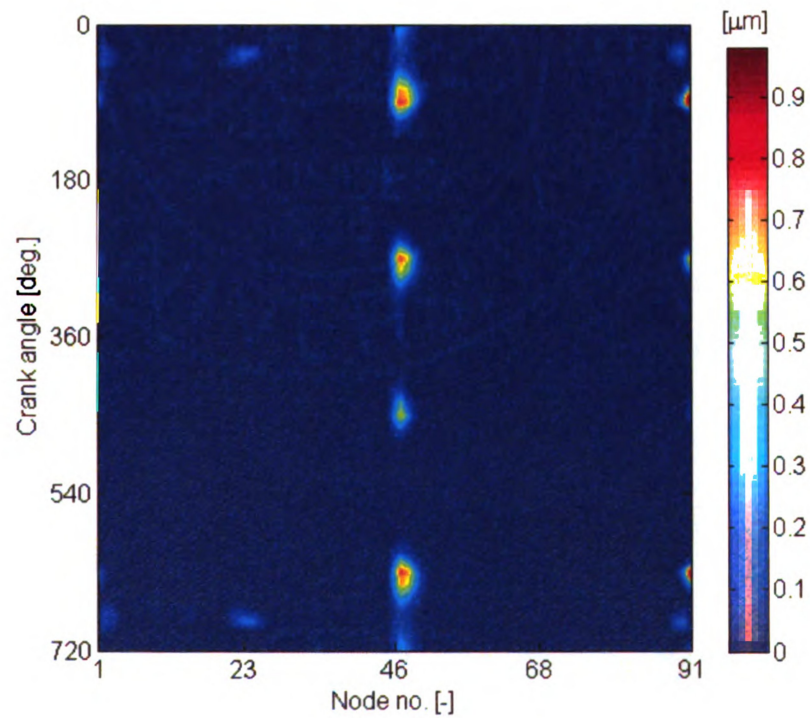
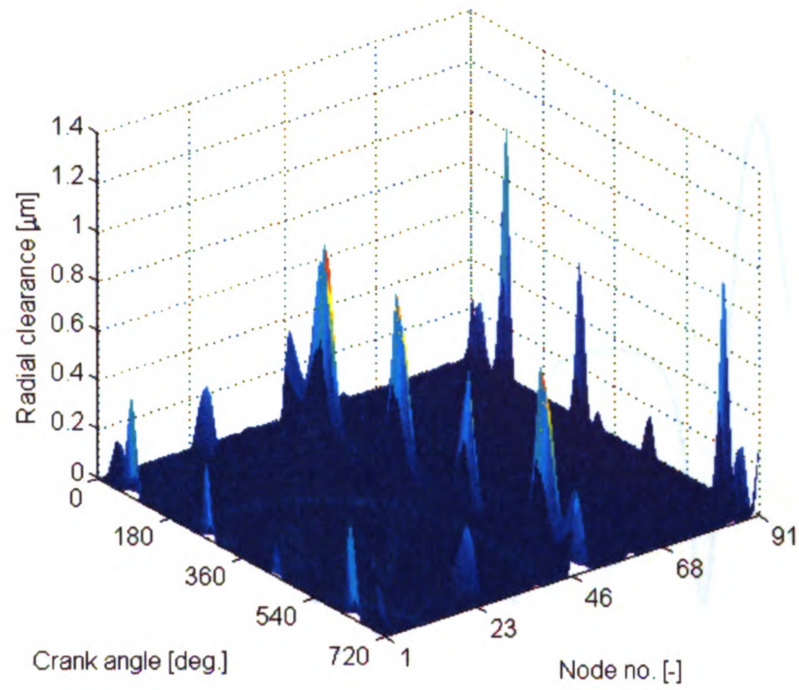


Figure 8.21: Ring-bore conformability – top ring

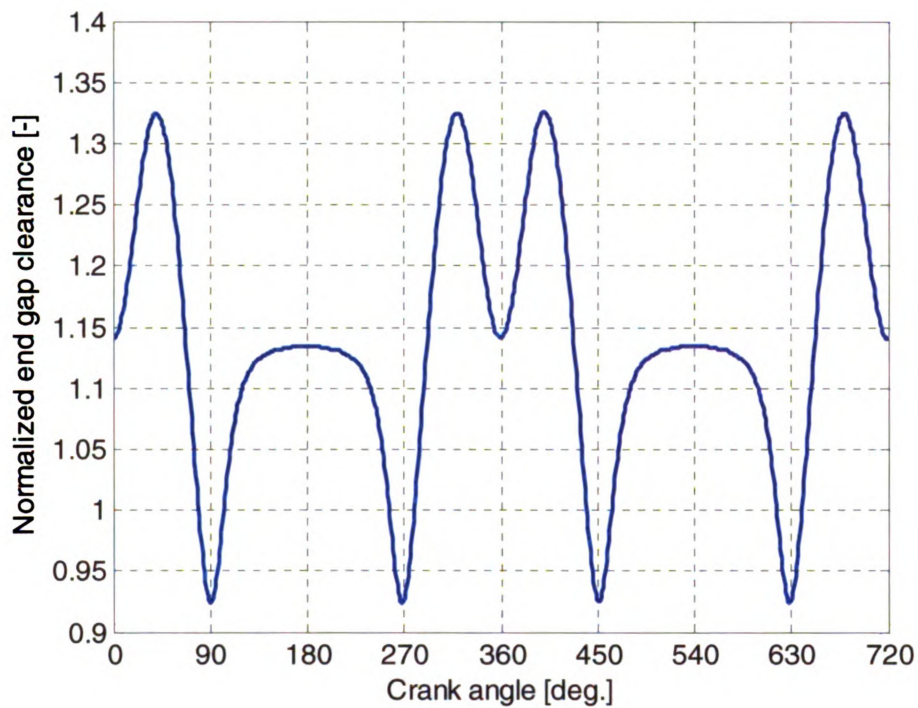


Figure 8.22: End gap clearance – top ring

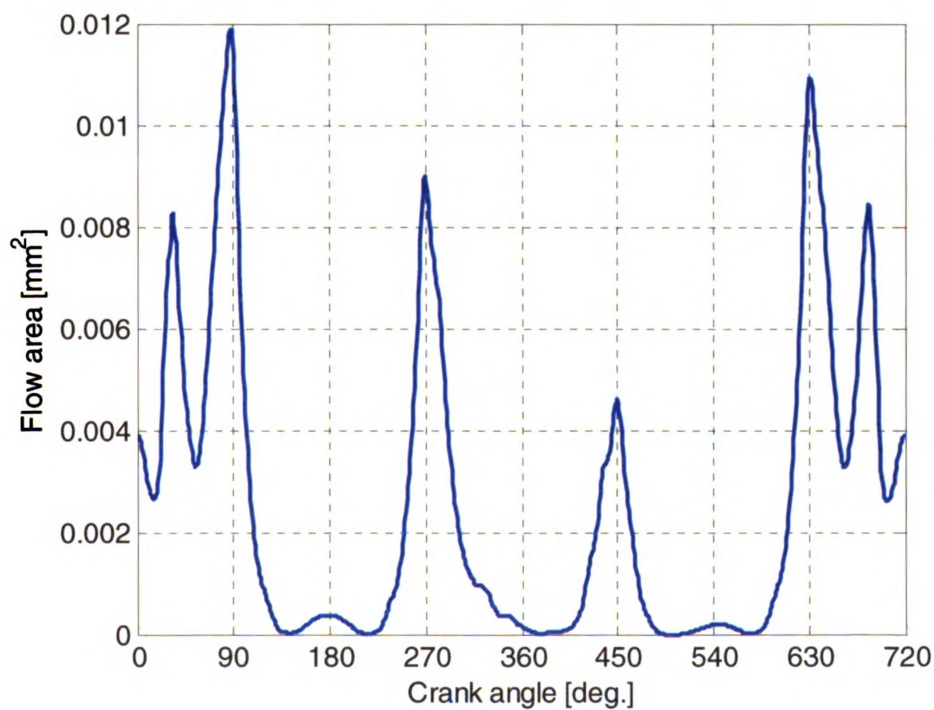


Figure 8.23: Flow area – top ring

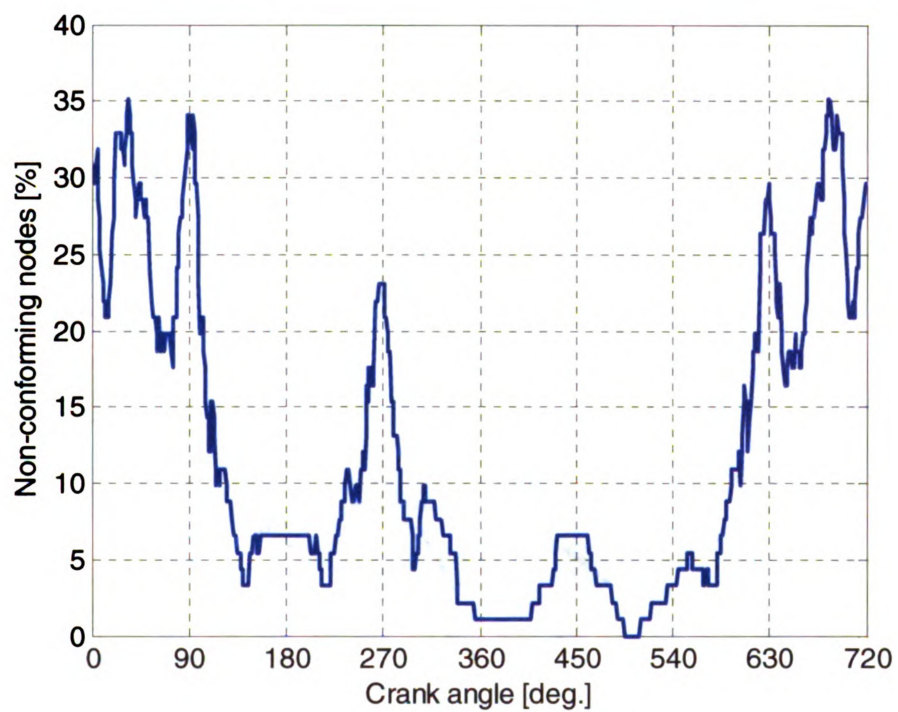


Figure 8.24: Non-conforming node – top ring

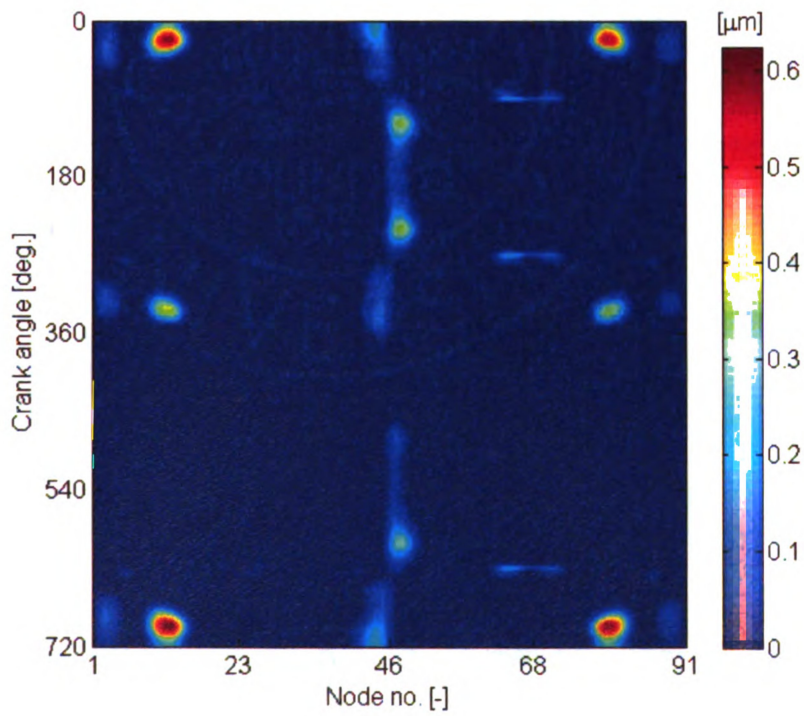
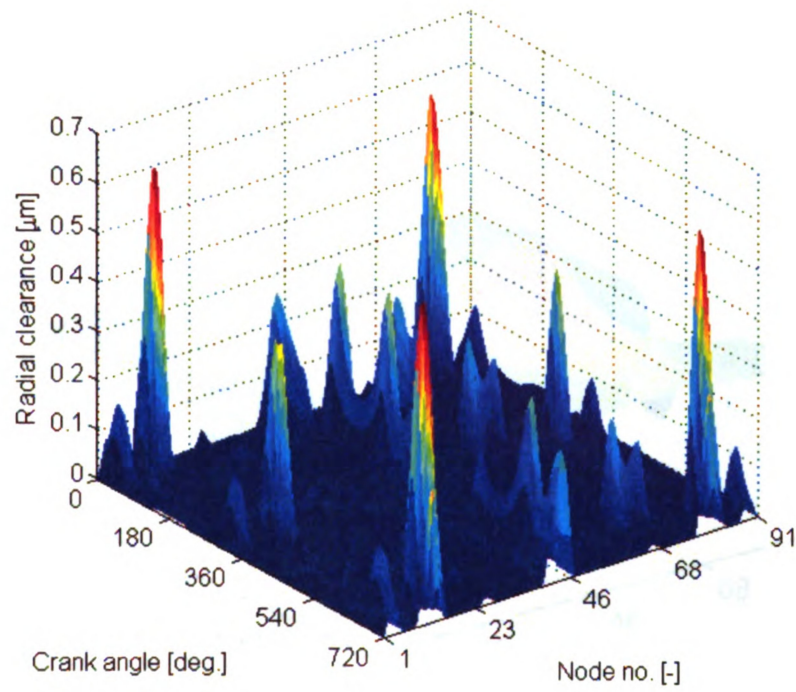


Figure 8.25: Ring-bore conformability – second ring

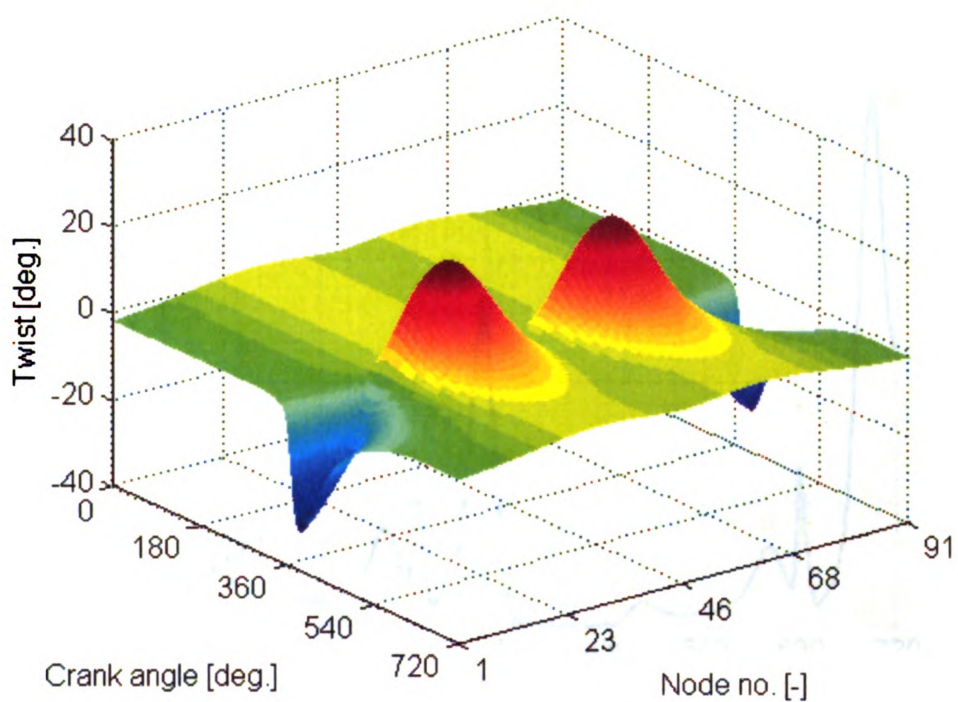


Figure 8.26: Ring twist – second ring

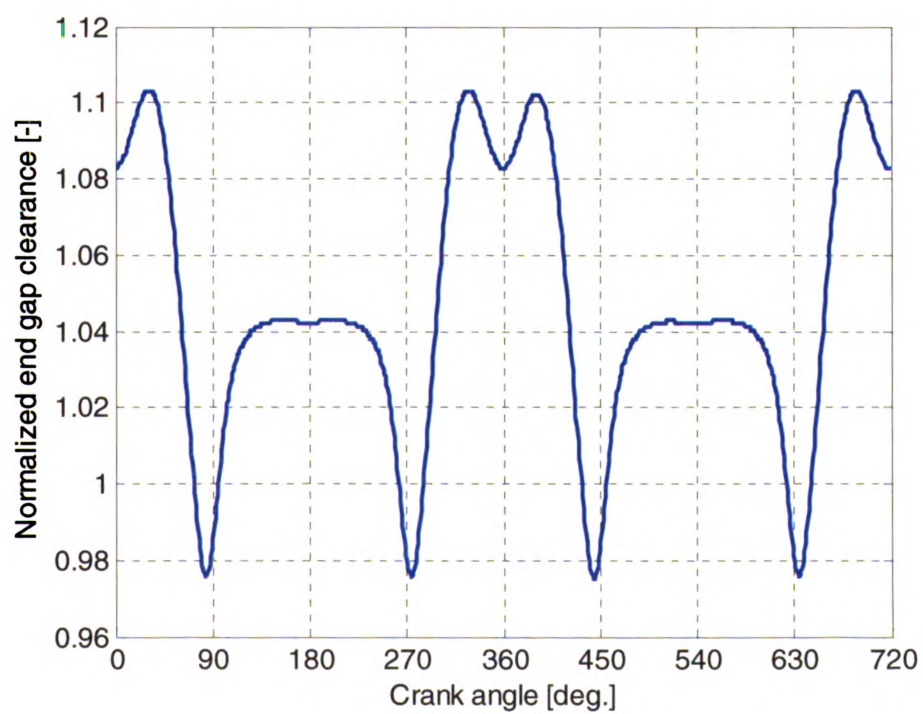


Figure 8.27: End gap clearance – second ring

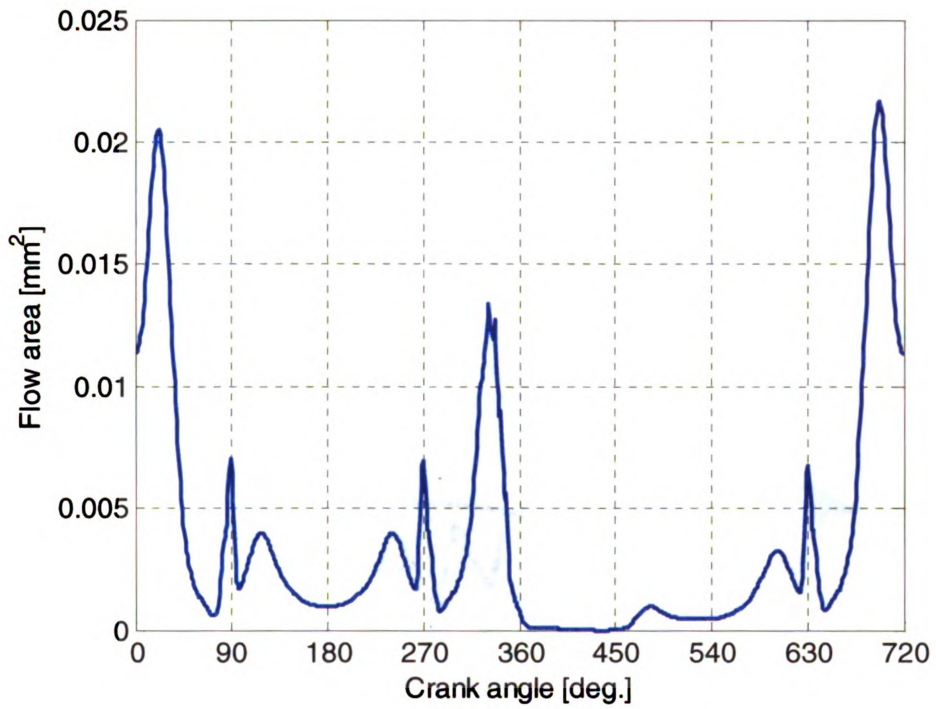


Figure 8.28: Flow area – second ring

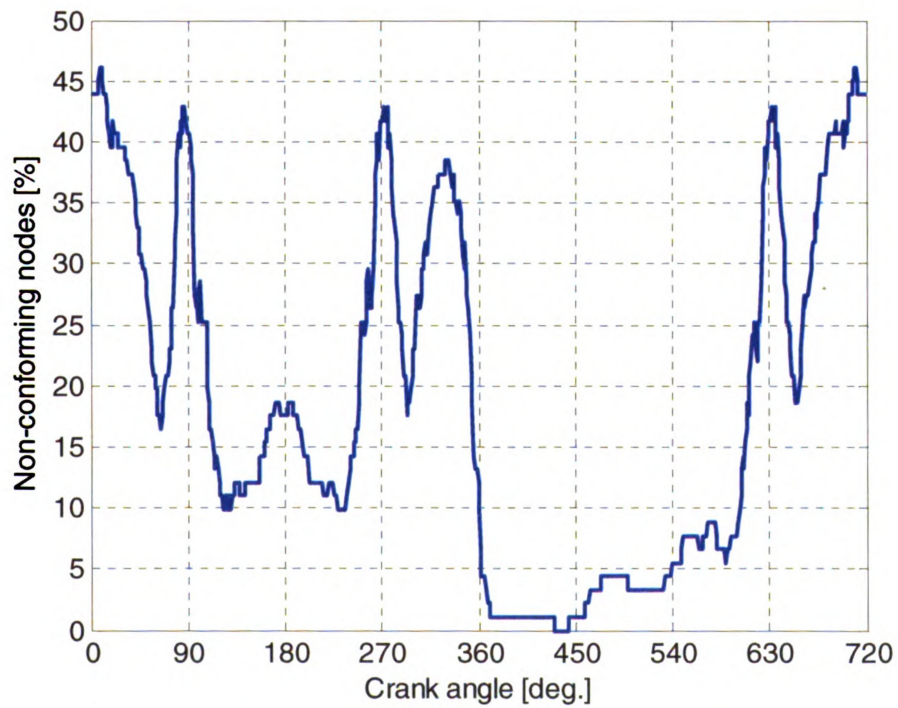


Figure 8.29: Non-conforming nodes – second ring

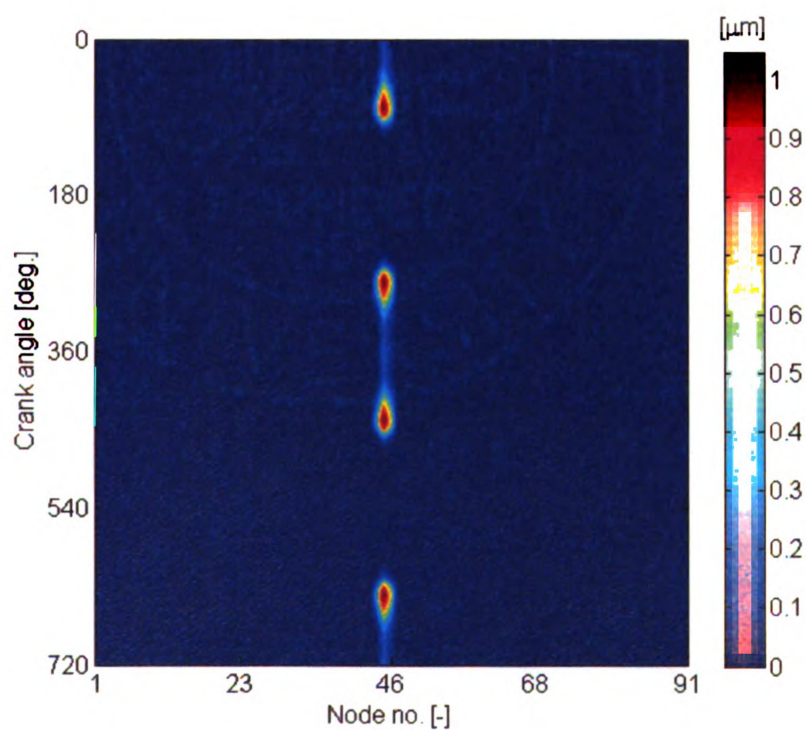
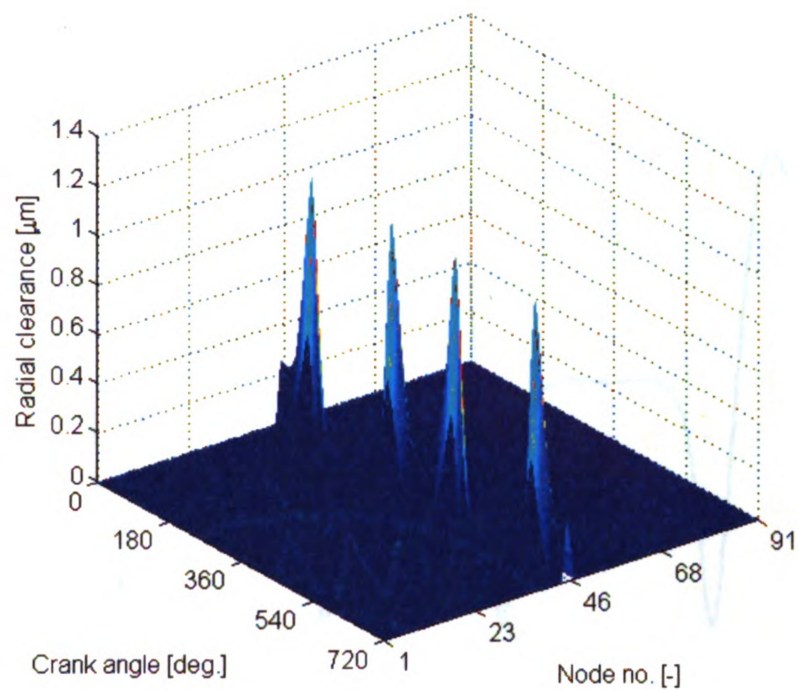


Figure 8.30: Ring-bore conformability – oil ring segment

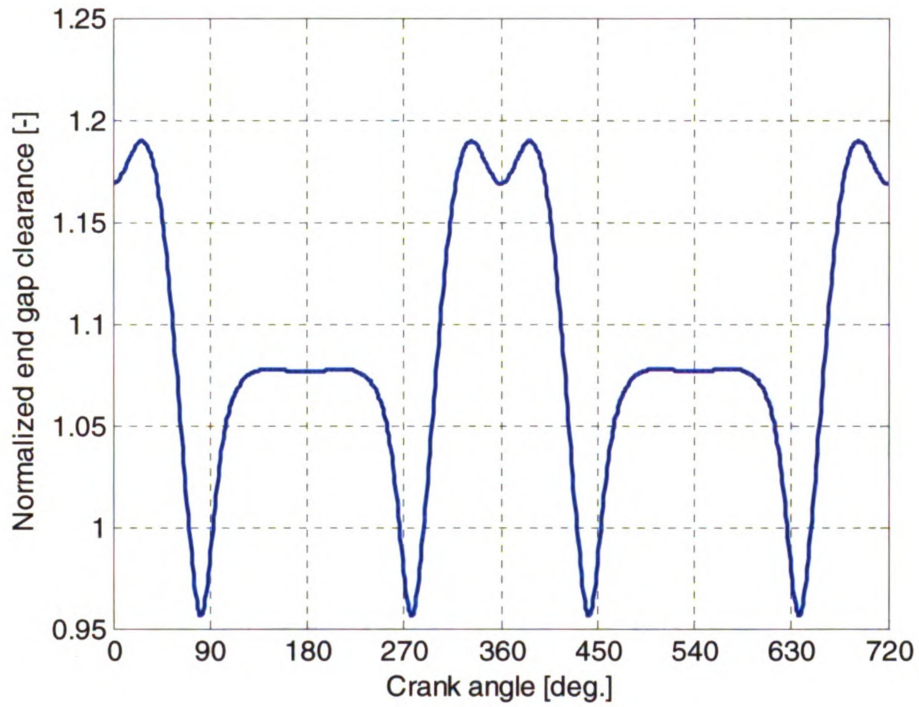


Figure 8.31: End gap clearance – oil ring segment

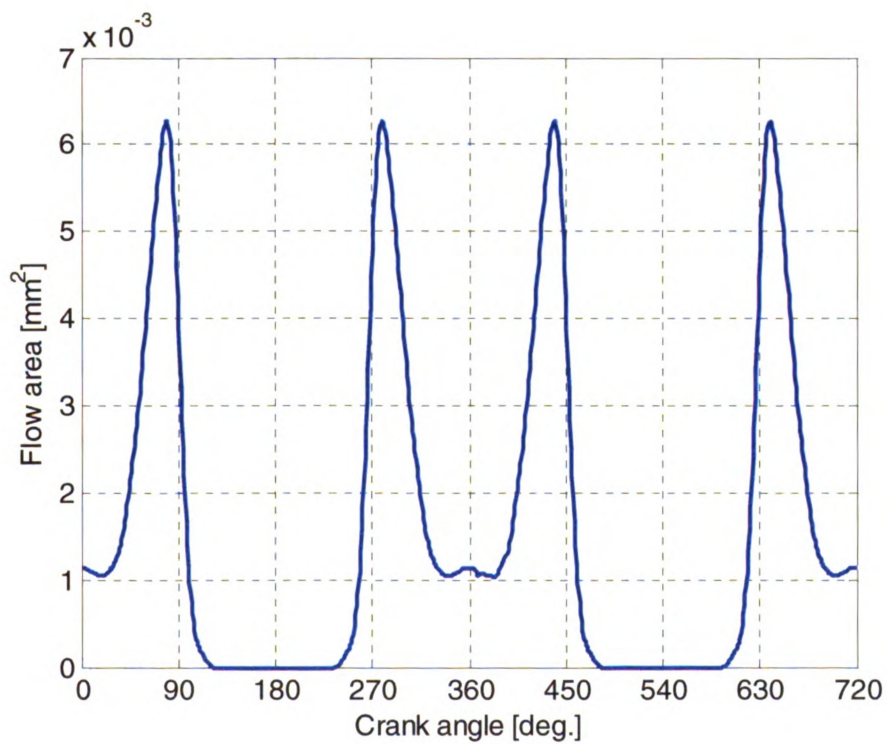


Figure 8.32: Flow area – oil ring segment

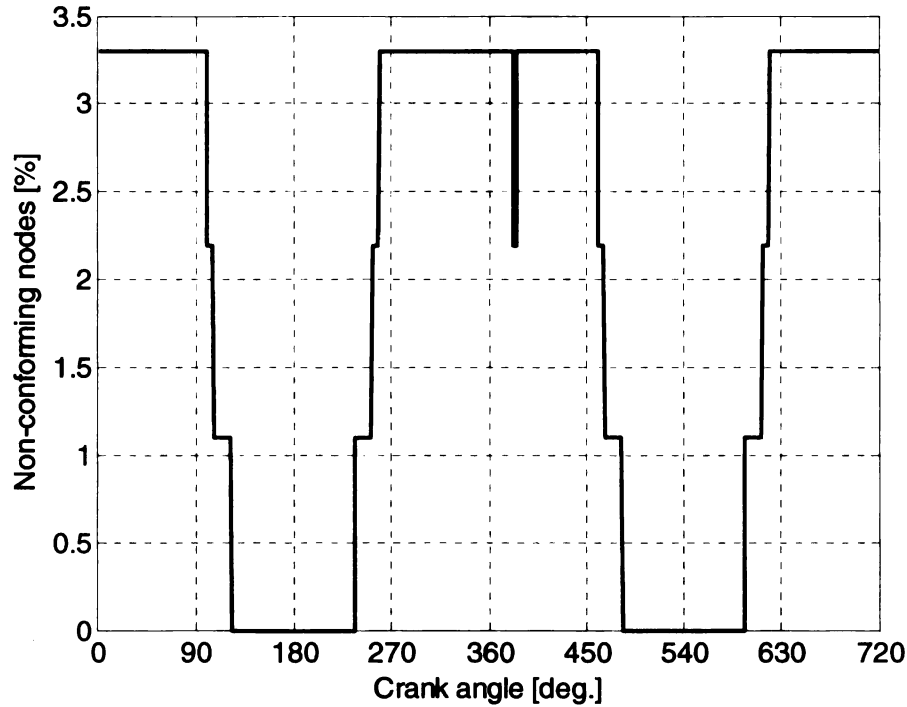


Figure 8.33: Non-conforming nodes – oil ring segment

8.12 Incorporating the Groove

The methodology described so far assumed that the groove was large enough that it would not interfere with the ring. In reality, though, as the ring twists it will come in contact with the groove. In order to constrain the ring in the groove, a coordinate system ξ - η is defined at the center of the groove (Figure 8.34) and the coordinates for the 13 points shown in Figure 8.34 are calculated. It should be noted that points 11 and 12 on the ring are always aligned with points 2 and 3 on the groove. Similarly, points 5 and 6 on the groove are always aligned with points 7 and 10 on the ring. The introduction of the groove introduces an additional four constraints for the i^{th} node,

$$\begin{aligned}
g_{i+1} &= \eta_5 - \eta'_7 \leq 0 \\
g_{i+2} &= \eta_2 - \eta'_{11} \leq 0 \\
g_{i+3} &= \eta'_{12} - \eta_3 \leq 0 \\
g_{i+4} &= \eta'_{10} - \eta_6 \leq 0
\end{aligned}
\tag{8.46}$$

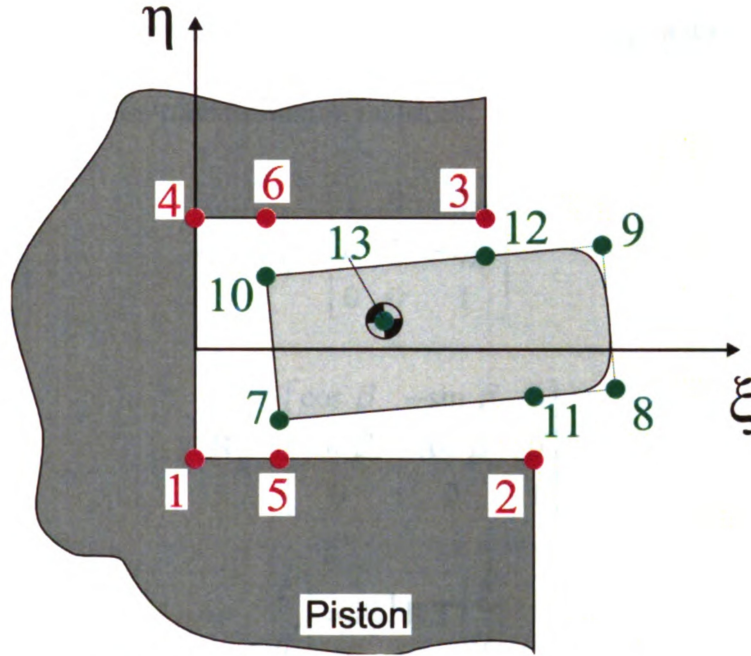


Figure 8.34: Groove coordinate system

The ring-bore-groove conformability problem can then be expressed as,

Find: \mathbf{q}

that minimizes: $\Pi = \frac{1}{2} \mathbf{q}^T \mathbf{K} \mathbf{q} - \mathbf{q}^T \mathbf{f}$

subject to:

$$\begin{aligned}
g_{5i-4} &= \eta_5 - \eta'_7 \leq 0 \\
g_{5i-3} &= \eta_2 - \eta'_{11} \leq 0 \\
g_{5i-2} &= \eta'_{12} - \eta_3 \leq 0 \\
g_{5i-1} &= \eta'_{10} - \eta_6 \leq 0 \\
g_{5i} &= \delta r_i - c_i \leq 0
\end{aligned}$$

The above problem can be solved following the fix-and-release strategy described in Section 8.7.1.

The new coordinates for the ring $\xi' - \eta'$ used in the constraints are calculated by coordinate transformation. Given the location of the ring's center of gravity (ξ_{13}, η_{13}) and the ring twist β , the new coordinates can be calculated using (8.49) where \mathbf{T}_g and \mathbf{R}_g are translation and rotation transformation matrices.

$$\mathbf{T}_g = \begin{bmatrix} 1 & 0 & -\xi_{13} \\ 0 & 1 & -\eta_{13} \\ 0 & 0 & 1 \end{bmatrix} \quad (8.47)$$

$$\mathbf{R}_g = \begin{bmatrix} \cos \beta & -\sin \beta & 0 \\ \sin \beta & \cos \beta & 0 \\ 0 & 0 & 1 \end{bmatrix} \quad (8.48)$$

$$\begin{Bmatrix} \xi' \\ \eta' \end{Bmatrix} = \mathbf{T}_g^{-1} \mathbf{R} \mathbf{T} \begin{Bmatrix} \xi \\ \eta \end{Bmatrix} \quad (8.49)$$

8.12.1 Constrained Ring Results

This section presents some numerical results for the second ring constrained in the groove as described above. Figure 8.35 to Figure 8.39 show the ring-bore conformability, the ring twist, the end gap clearance, the available gas flow area and the percentage of non-conforming nodes over the entire cycle for the second ring with asymmetric cross-section confined within the limits.

Compared with the results presented in the previous section, for the same ring but unconfined, it is observed that the groove confinement improves ring conformability away from the end gap but ring-to-cylinder bore clearance increases by more than 1 μm at the end gap.

Figure 8.36 shows the twist for the ring in the groove. It can be seen that it varies along the circumference and also varies significantly throughout the cycle. This reinforces the necessity of an advanced 3-D ring dynamics model in order to capture all the phenomena around the ring circumference.

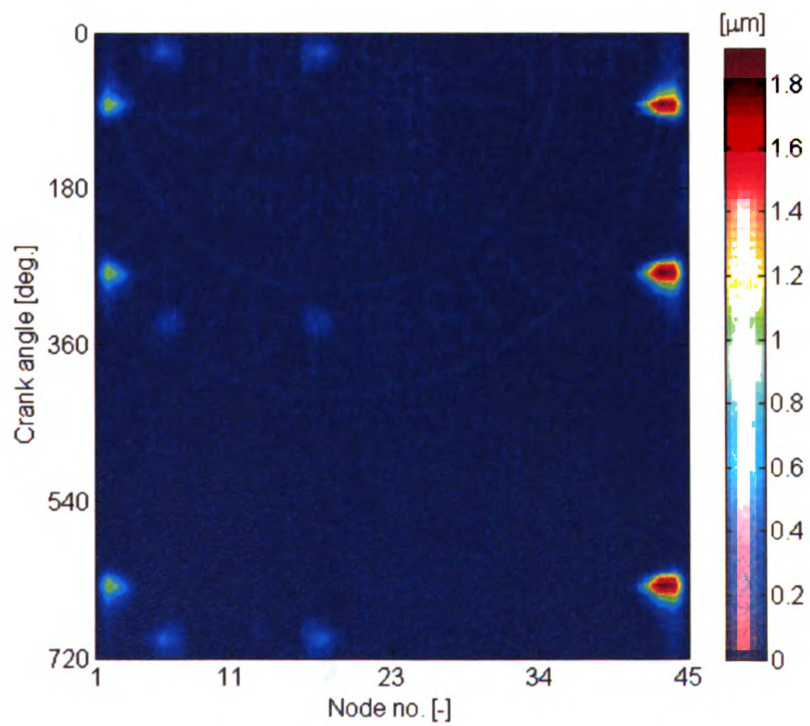
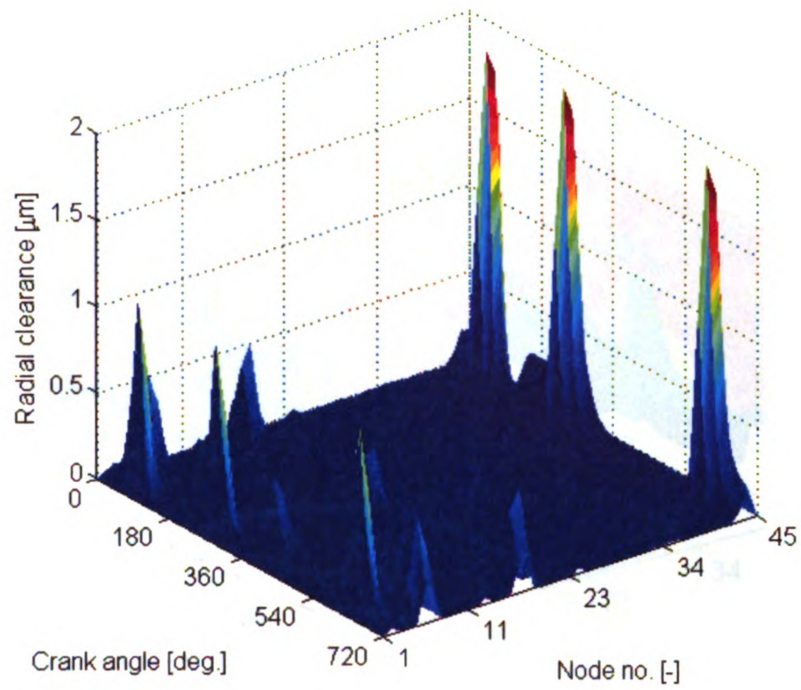


Figure 8.35: Ring-bore conformability – constrained second ring

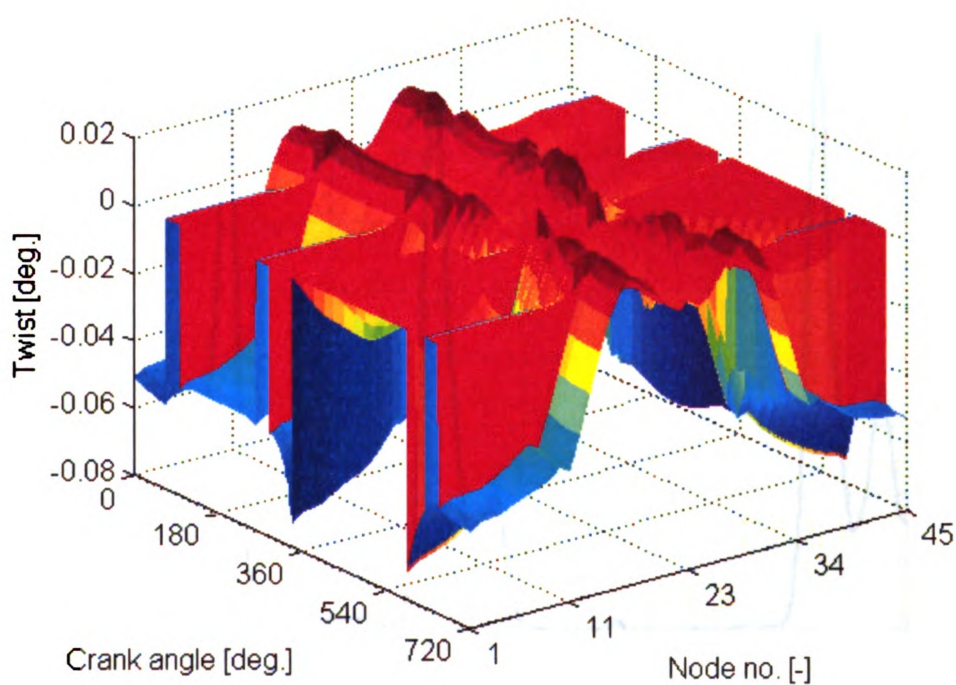


Figure 8.36: Ring twist – constrained second ring

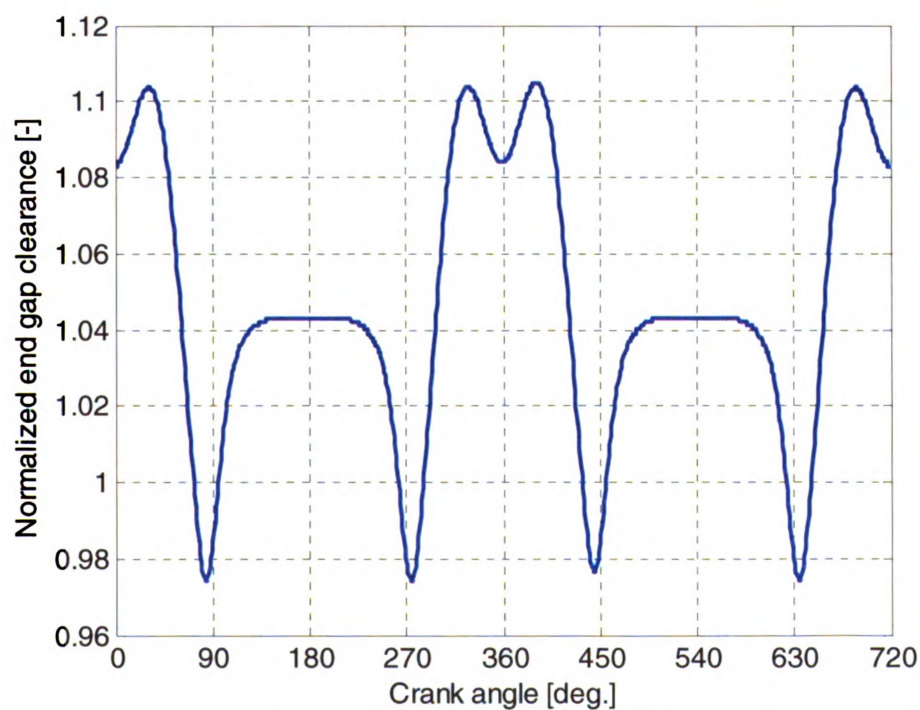


Figure 8.37: End gap clearance – second ring

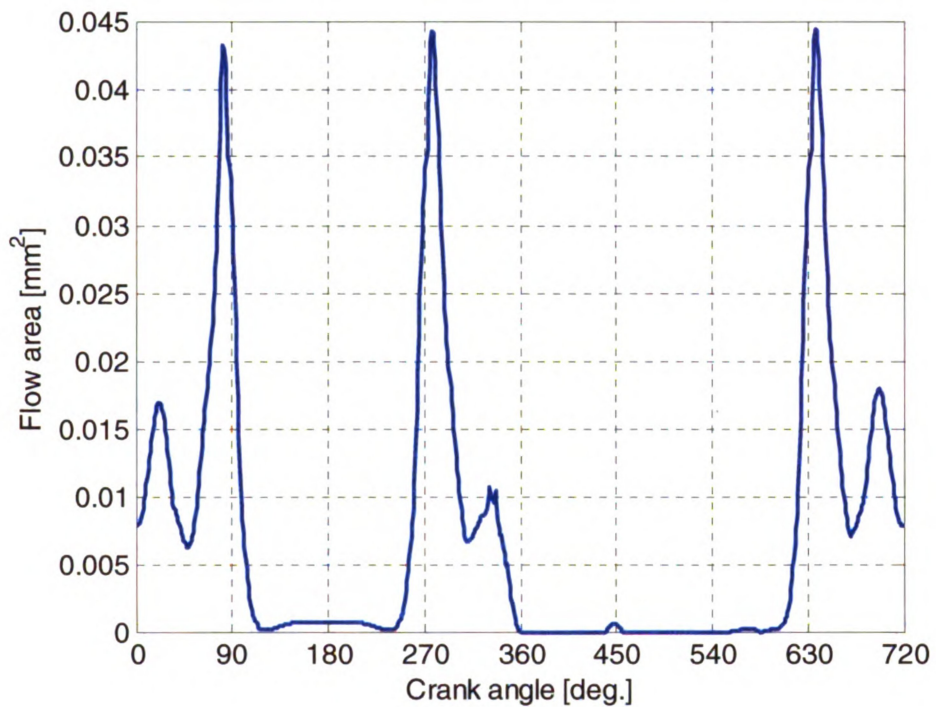


Figure 8.38: Flow area – second ring

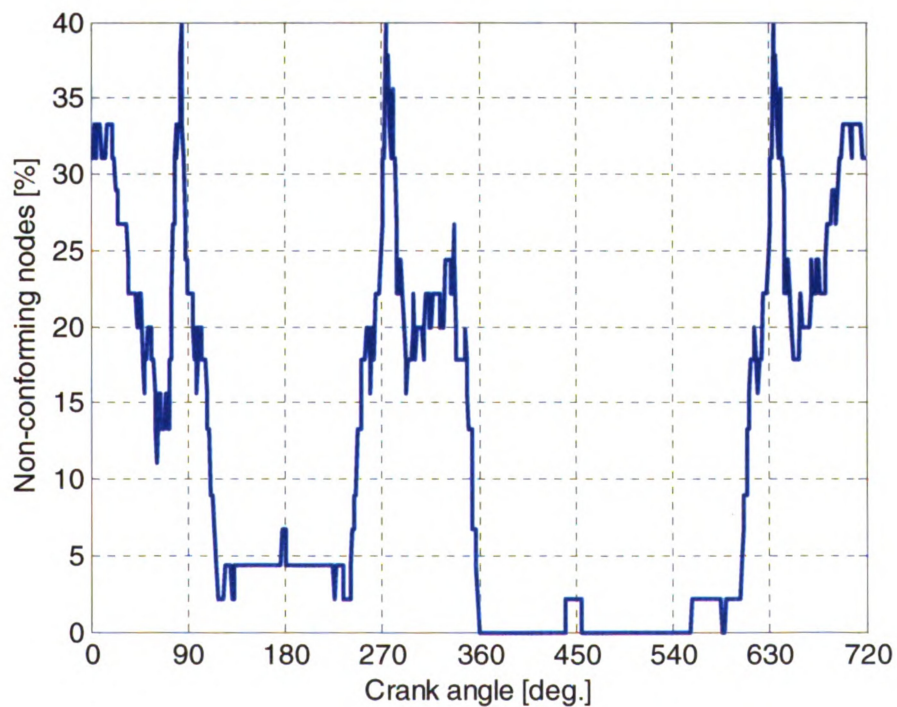


Figure 8.39: Non-conforming nodes – second ring

8.13 Further Developments

Following the above developments it is recommended that a similar direction be pursued in order to solve the full ring dynamics problem. Equation (8.18) should be expanded to account for ring inertia, that is,

$$\mathbf{M}\ddot{\mathbf{q}} + \mathbf{K}\mathbf{q} = \mathbf{f} \quad (8.50)$$

where \mathbf{M} is the mass matrix for the space frame element [59].

Figure 8.40 shows all the loads acting at each cross-section of the ring which corresponds to one node. These loads should be incorporated on the load vector \mathbf{f} . The methodologies for calculating the pressures surrounding the ring are very well documented in [14, 37, 66]. Equation (8.50) can then be solved using standard techniques for second order non-linear problems in order to predict the full dynamic behavior of the ring. One approach would be to use an implicit integration scheme in conjunction with the Newton-Raphson methodology to solve (8.50). Another approach is via the component mode synthesis methodology. The interested reader is referred to [8] for a description of this methodology.

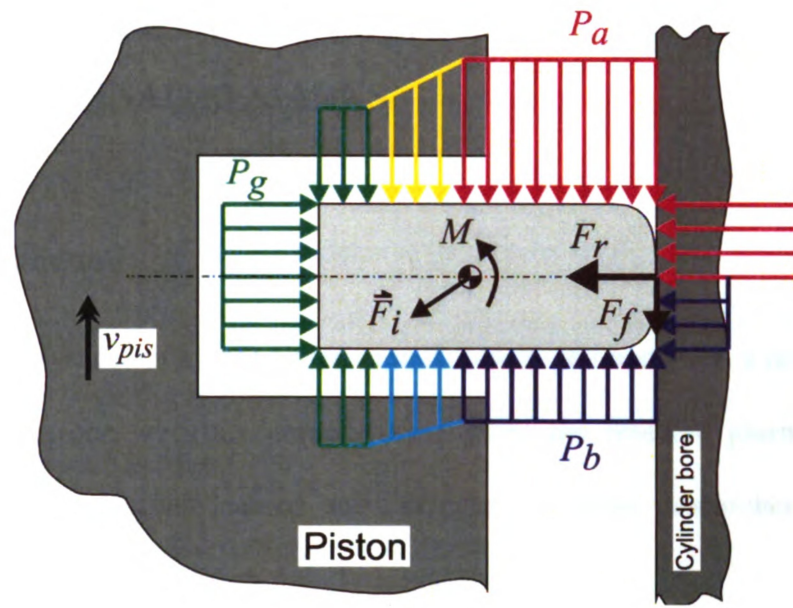


Figure 8.40: Loads on ring at one cross-section

CHAPTER 9. FINAL REMARKS

9.1 Lessons Learned

One of the essences of a PhD dissertation is to help you mature as a researcher. A mature researcher is one who has learned lesson along the research journey. In this section some of those lessons learned are discussed for future researchers to avoid repetition.

The first thing that should be understood in research is *not to reinvent the wheel*. If something has already been developed and is publicly available, use it. In the initial stages of this work, considerable effort was invested in order to develop the finite element (FE) methodology for the piston. The big effort was not to develop the methodology but to implement the programming of it correctly, in order to handle large number of nodes, something that is typical of a piston mesh. Despite these efforts, the capabilities of the model are only limited to linear tetrahedral elements, whereas the industry standard is to use higher order elements. There are numerous commercial finite element software packages that can return all the FE results required by a piston dynamics numerical model. Hence the efforts can be applied in the development of methodologies for piston dynamics, rather than trying to manage computer memory allocation.

Another important lesson is the realization of the usefulness of a methodology. If a methodology is used repeatedly in solving similar problems, it implies that it must possess some advantages. In this work it was chosen to use FE methods to solve the

Reynolds lubrication equation on the skirt domain. This was chosen as it allowed for direct mapping of information from the 3-D piston solid mesh to the 2-D skirt mesh. However, a common practice found in literature is to use finite differences (FD) to solve the Reynolds equation on the skirt domain. The implementation of FD has several advantages over the FE method. The FD mesh is independent from the FE mesh. This allows for a coarse FE mesh and a denser FD mesh. A coarser FE mesh will decrease the computational cost to obtain the skirt compliance. At the same time a dense FD mesh will allow for an accurate calculation of the hydrodynamic pressures. Another advantage of the FD methodology is the implementation of a starvation algorithm for the lubrication analysis. This is very straightforward and has been implemented in many tribological studies. However an implementation of a starvation algorithm is not so straight forward using the FE methodology, nor very well documented.

The message here is to devote the efforts to develop methodologies that are essential to the core of the research and utilize existing well-established methodologies.

9.2 Limitations and Recommendations

In order to continue the improvement of these numerical models, it is important to identify and understand their limitations.

The piston dynamics numerical model can be improved in several areas. First, the finite element results used in the elastohydrodynamic analysis should be obtained via quadratic tetrahedral elements rather than from linear ones. Linear elements tend to be stiffer than quadratic ones. The use of commercial finite element software packages is recommended, adding their results as inputs to the model.

The lubrication model requires improvement in two areas. Currently the standard Reynolds lubrication equation is used. This should be changed to the average Reynolds equation proposed by Patir and Cheng [54] to account for the effects of surface roughness on hydrodynamic pressures. Furthermore, the current model assumes fully flooded lubrication conditions; however, this is not typical under real operating conditions. An oil starvation algorithm [15] should be implemented to account for partially flooded conditions.

The 2-D mesh for the skirt domain should be decoupled from the 3-D solid mesh of the piston. This will allow for a coarser solid mesh to obtain piston deformations and temperatures while allowing for a finer mesh for the solution of the Reynolds lubrication equation. This in turn will reduce computational burden for obtaining the compliance matrix but at the same time maintain accuracy of the solution of the Reynolds equation. In doing so, the Reynolds equation can be solved via finite differences, making it much easier to implement the starvation algorithm.

Currently the pressures on the skirt surface are obtained iteratively via relaxation techniques. The clearances between the skirt and the cylinder bore, though, can be treated as state variables and incorporated in the Newton-Raphson methodology used for the secondary motion evaluations. This will make the computation of the Jacobian matrix more expensive but at the same time it will eliminate the pressure iterative loop in the model and hence make it more robust, since all the unknowns will be calculated with one methodology.

The friction model also needs improvement. Currently the Coulomb friction model is used. It is appropriate for development purposes of the methodology; however,

under operating conditions friction varies with engine speed, loading, and oil temperature. Several models are archived in literature that can account for all these.

Finally, the skirt drop discussed in Section 5.4.3 should be implemented to aid in better prediction of the dynamics at BDC.

The skirt profile optimization methodology requires improvements as well. The different equations defining the skirt profile shape discussed in Section 6.4.2 should be implemented. The most important improvement here, though, is the expansion of the methodology to a multi-objective one in order to be able to optimize a skirt profile for a range of operating conditions and not just one.

9.3 Conclusions

A novel piston dynamics numerical model has been developed. This model is unique as it extends the piston secondary motion calculations in one more dimension, the wrist-pin plane. It was used to evaluate the performance of several pistons.

A numerical experiment was performed using a new generation piston fitted to a cylinder bore with asymmetric deformation and temperature distributions. It was found that the motion along the wrist-pin becomes important when the prediction of piston wear is required.

The model was also used to understand the failure mechanisms of a high-speed piston. The cyclic stress loading was recovered, and it was concluded that failure was occurring due to fatigue. It was deemed that the affected area at the valve pocket edge needed strengthening. Furthermore, during the modeling efforts for this piston a simplified progressive wear model was proposed and tested. This simplified model

appears to predict the trends that are observed in engine break-in. However, the linear extrapolation used for wear progression is inadequate as it highly over-predicts wear.

A comparison was made between the pistons of two similar gasoline engine configurations one production and one under development. It was found that the new engine suffers from higher friction losses at the piston skirt because of higher in-cylinder gas pressure loads. The dynamics of the two pistons were comparable.

The model was employed in the investigations of wear mechanisms on a heavy-duty diesel piston. Several numerical experiments were performed, leading to the conclusion that accurate representations of the cylinder bore deformation and temperature distributions are required for the correct prediction of wear modes under real operating conditions. Some of the predicted results correlate well with test observations.

An optimization methodology was developed for the optimization of piston skirt profiles to complement the above piston dynamics numerical model. The methodology performs very well in addressing the optimization of piston skirt profiles. It has been implemented on a gasoline piston and the numerical results suggest that an optimized profile can lead to a reduction in piston slap while maintaining friction within desirable limits.

A commercial simulation software package for ring dynamics was used to predict interring gas pressures and blow-by for different engines. It was observed that with correct tuning of the model the predicted results can correlate very well with measured ones. It was found that the ring-pack of the newly developed engine performs better than that of the production engine studied, since the higher in-cylinder gas pressures in conjunction with a lighter top ring and heavier second ring demote high blow-by at high

engine speed low engine load conditions. This prevents the top ring from lifting during the compression and expansion strokes, and also second ring flutter is reduced. The model however, has limitations in building blow-by maps. As it is tuned for only one operating condition and also ring twist is considered only in a 2-D space, a predicted blow-by map does not correlate very well with a measured one.

Following these observations an introductory presentation is made for a 3-D ring finite element model. This model accounts for the whole ring, and it can be used for ring-bore conformability and ring twist calculations. Examples are given of cyclic ring-bore conformability and ring twist assuming known gas pressure loading behind the rings. The model is intended to act as a backbone in future development of an advanced 3-D ring dynamics model.

All these methodologies perform well in assessing the cylinder-kit performance of internal combustion engines. However, they need to be continuously improved to account for multiple physical phenomena as engine design requirements become more complicated in search of low cost, high fuel efficiency, long trouble-free life, low emissions and low noise and vibration. The economic crisis of this past year can be demoralizing, but efforts to improve the performance of the internal combustion engine should not be paused. As long as there is oil to be pumped or alternative combustive fuels, there will be pistons and piston rings. And as Governor Arnold Schwarzenegger said at the opening ceremony of the 2009 SAE World Congress,

“The Detroit auto industry is saying I’ll be back!”

APPENDIX A **pARSM - PERFORMANCE MEASURES OF THE SURROGATE MODEL QUALITY**

These are the quantities used to evaluate the quality of the surrogate model in Chapter 6:

(i) The coefficient of determination, R^2 and the adjusted coefficient of determination R_a^2 , where

$$R^2 = 1 - \frac{SS_E}{SS_T} \quad (\text{A.1})$$

and

$$R_a^2 = 1 - \frac{n_d - 1}{n_d - n_b} (1 - R^2) \quad (\text{A.2})$$

In (A.1) and (A.2)

$$SS_E = \sum_{i=1}^{n_d} (y_i - \hat{y}_i)^2 \quad (\text{A.3})$$

is the sum of squares errors and

$$SS_T = \sum_{i=1}^{n_d} (y_i - \bar{y})^2 \quad (\text{A.4})$$

is the total sum of squares errors. \bar{y} is the arithmetic mean of the data values y_i . The R^2 value increases as the number of regression coefficients increases, and R_a^2 provides an estimate which corrects for the number of regression coefficients.

(ii) The standard deviation of the error or data noise $\hat{\sigma}$ and the normalized residual \mathbf{r} , given by

$$\hat{\sigma} = \sqrt{\frac{SS_E}{n_d - n_b}} \quad (\text{A.5})$$

and

$$\mathbf{r} = \frac{1}{\hat{\sigma}} \boldsymbol{\epsilon} \quad (\text{A.6})$$

Myers and Montgomery [44] report that most of the normalized residuals should lie in the interval $-3 \leq r_i \leq 3$. Otherwise this would be an indication that the surrogate model is not a good approximation of the true response surface around the region of the particular design. The maximum and minimum values of the normalized residual vector are defined as

$$r_{\max} = \max_i r_i \quad (\text{A.7})$$

$$r_{\min} = \min_i r_i \quad (\text{A.8})$$

(iii) The estimated standard error. An estimate of the prediction error at each data point is known as the estimated standard error, ϵ_{es} , and is given by,

$$\epsilon_{es}(\mathbf{x}_i) = \hat{\sigma} \sqrt{\boldsymbol{\xi}^T (\mathbf{X}^T \mathbf{X})^{-1} \boldsymbol{\xi}} \quad (\text{A.9})$$

where

$$\boldsymbol{\xi} = \{\xi_1(\mathbf{x}_i) \quad \xi_2(\mathbf{x}_i) \quad \dots \quad \xi_{nb}(\mathbf{x}_i)\}^T \quad (\text{A.10})$$

APPENDIX B pARSM - COEFFICIENTS FOR THE QUARTIC POLYNOMIAL SKIRT PROFILE

These are the coefficients for the quartic polynomial, (6.5), skirt profile in terms of the five design variables, $a_1 - a_5$ and the skirt length, L :

$$C_0 = a_0 \quad (B.1)$$

$$C_1 = a_4 \quad (B.2)$$

$$C_2 = - \left[(a_0 - a_1) a_2^4 + a_2^4 a_4 L - a_2 (4 a_0 - 4 a_3 + 3 a_2 a_4) L^3 + (3 a_0 - 3 a_3 + 2 a_2 a_4) L^4 \right] / \left[a_2^2 (a_2 - L)^2 L^2 \right] \quad (B.3)$$

$$C_3 = \left[2(a_0 - a_1) a_2^4 + 2 a_2^4 a_4 L - a_2^2 (4 a_0 - 4 a_3 + 3 a_2 a_4) L^2 + (2 a_0 - 2 a_3 + a_2 a_4) L^4 \right] / \left[a_2^3 (a_2 - L)^2 L^2 \right] \quad (B.4)$$

$$C_4 = - \left[(a_0 - a_1) a_2^3 + a_2^3 a_4 L - a_2 (3 a_0 - 3 a_3 + 2 a_2 a_4) L^2 + (2 a_0 - 2 a_3 + a_2 a_4) L^3 \right] / \left[a_2^3 (a_2 - L)^2 L^2 \right] \quad (B.5)$$

BIBLIOGRAPHY

1. Akalin, O., Newaz, G. M., 2001, "Piston Ring-Cylinder Bore Friction Modeling in Mixed Lubrication Regime: Part I – Analytical Results," *Journal of Tribology*, Vol. 123, pp. 211-218
2. Annand, W. J. D., 1963, "Heat Transfer in the Cylinders of Reciprocating Internal Combustion Engines," *Proceedings of the Institution of Mechanical Engineers*, Vol. 177, pp. 973-990
3. Archard, J. F., 1953, "Contact and Rubbing of Flat Surfaces," *Journal of Applied Physics*, Vol. 24, pp. 981-988
4. Arcoumanis, C., Ostovar, P., Mortier, R., 1997, "Mixed Lubrication Modeling of Newtonian and Shear Thinning Liquids in a Piston-Ring Configuration," SAE paper 972924
5. Beaton A. E., Tukey J. W., 1974, "The Fitting of Power Series, Meaning Polynomials, Illustrated on Band-Spectroscopic Data," *Technometrics* Vol 16, pp. 147-185
6. CASE, 2007, Mid Michigan Research LLC, <http://www.mmrlc.com>
7. Chui, B-K., *Elastohydrodynamic Modeling and Measurement of Cylinder-kit Assembly Tribological Performance*, PhD Dissertation, Michigan State University, East Lansing, MI, 1998
8. Craig, R. R., Kurdila, A. J., *Fundamentals of Structural Dynamics*, John Wiley & Sons, Inc., Hoboken, NJ, 2006
9. Dursunkaya, Z., Keribar, R., 1992, "Simulation of Secondary Dynamics of Articulated and Conventional Piston Assemblies," SAE Paper 920484
10. Dursunkaya, Z., Keribar, R., Ganapathy, V., 1994, "A Model of Piston Secondary Motion and Elastohydrodynamic Skirt Lubrication," *Journal of Tribology*, Vol. 116, pp. 777-785
11. Duyar, M., Bell, D., Perchanok, M., 2005, "A Comprehensive Piston Skirt Lubrication Model Using a Mass Conserving EHL Algorithm," SAE Paper 2005-01-1640
12. Ejakov, M. A., 2001, "Modeling of Axial and Circumferential Ring Pack Lubrication," ASME paper 2001-ICE-433

13. Ejakov, M. A., Schock, H. J., Brombolich, L. J., Carlstrom, C. M., Williams R. L., 1997, "Simulation Analysis of Interring Gas Pressure and ring Dynamics and their Effect on Blow-by," *ASME ICE* Vol. 29(2), pp. 107-123
14. Ejakov, M., *Ring Pack Behavior and Oil Consumption Modeling in IC Engines*, PhD Dissertation, Michigan State University, East Lansing, MI, 1998
15. Elrod, H.G., 1981, "A Cavitation Algorithm," *ASME Jour. of Lubr. Tech.*, Vol. 103(3), pp. 350-354
16. EXCITE, 2007, Anstalt für Verbrennungskraftmaschinen List, <http://www.avl.com>
17. Goenka, P. K. and Meemik, P. R., 1992, "Lubrication Analysis of Piston Skirts," SAE Paper 920490
18. Greenwood, J. A., Tripp, J. H., 1970-1971, "The Contact of Two Nominally Flat Rough Surfaces," *Proc. Instn. Mech. Engrs*, Vol. 185, pp. 625-634
19. Greenwood, J. A., Tripp, J. H., 1971, "The Contact of Two Nominally Flat Rough Surfaces," *Proceedings of the Institution of Mechanical Engineers*, Vol. 185, pp. 625-633
20. Greenwood, J. A., Williamson, J. B. P., 1966, "Contact of Nominally Flat Surfaces," *Proc. R. Soc. London, Series A, Mathematical and Physical Sciences*, Vol. 295 (1442), pp. 300-319
21. Guyan, R. J., 1965, "Reduction of Stiffness and Mass Matrices," *AIAA Journal*, Vol. 3(2), p. 380
22. Heywood, J. B., *Internal Combustion Engine Fundamentals*, McGraw-Hill, Inc., New York, 1988.
23. Hu, Y., Cheng, H. S., Arai, T., Kobayashi, Y., Aoyama, S., "Numerical Simulation of Piston Ring in Mixed Lubrication – A Nonaxisymmetrical Analysis," 1994, *Journal of Tribology*, Vol. 116, pp. 470-478
24. *Internal Combustion Engines - Piston Rings – General Specifications*, SAE Piston and Ring Standards Committee, SAE J1591, 2008
25. *Internal Combustion Engines - Piston Rings – Oil Control Rings*, SAE Piston and Ring Standards Committee, SAE J2002, 2008
26. *Internal Combustion Engines - Piston Rings - Vocabulary*, SAE Piston and Ring Standards Committee, SAE J1588, 2008
27. *Internal Combustion Engines - Piston Vocabulary*, SAE Piston and Ring Standards Committee, SAE J2612, 2002

28. Jones, D. R., Schonlau, M., Welch, W. J., 1998, "Efficient Global Optimization of Expensive Black-Box Function," *Journal of Global Optimization*, Vol. 13, pp. 455-492
29. Keribar R., Dursunkaya Z., Ganapathy V., 1993, "An Integrated Design Analysis Methodology to Address Piston Tribological Issues," SAE Paper 930793
30. Keribar, R., Dursunkaya, Z., Ganapathy, V., 1993, "An Integrated Design Analysis Methodology to Address Piston Tribological Issues," SAE Paper 930793
31. Li, C. H., 1982, "Piston Thermal Deformation and Friction Considerations," SAE Paper 820086
32. Li, C. H., 1982, "Piston Thermal Deformation and Friction Considerations," SAE Paper 820086
33. Li, C. H., 1986, "Thermoelastic Behavior of an Aluminum Diesel Engine Piston," SAE Paper 860136
34. Li, D. F., Rohde, S. M., Ezzat, H. A., 1982, "An Automotive Piston Lubrication Model," *ASLE Transactions*, Vol. 26, pp. 151-160
35. Li, G., Azarm, S., Farhang-Mehr, A., Diaz, A. R., 2006, "Approximation of Multiresponse Deterministic Engineering Simulations: a Dependent Metamodeling Approach," *Structural and Multidisciplinary Optimization*, Vol. 31, pp. 260-269
36. Liu G. R. and Quek S. S., *The Finite Element Method: A Practical Course*, Butterworth-Heinemann, Boston, MA, 2003
37. Liu, L., *Modeling the Performance of the Piston Ring-Pack with Consideration of Non-Axisymmetric Characteristics of the Power Cylinder System in Internal Combustion Engines*, PhD Dissertation, Massachusetts Institute of Technology, Cambridge, MA, 2005
38. Liu, L., Tian, T., 2004, "A Three-Dimensional Model for Piston Ring-Pack Dynamics and Blow-by Gas Flow," ASME Paper ICEF2004-968
39. Liu, L., Tian, T., 2005, "Modeling Piston Ring-Pack Lubrication with Considerations of Ring Structural Response," SAE Paper 2005-01-1641
40. Liu, L., Tian, T., Rabute, R., 2003, "Development and Applications of an Analytical Tool for Piston Ring Design," SAE Paper 2003-01-3112
41. McClure, F., *Numerical Modeling of Piston Secondary Motion and Skirt Lubrication in Internal Combustion Engines*, PhD Dissertation, Massachusetts Institute of Technology, Cambridge, MA, 2007

42. McClure, F., Tian, T., 2008, "A Simplified Piston Secondary Motion Model Considering the Dynamic and Static Deformation of Piston Skirt and Cylinder Bore in Internal Combustion Engines", SAE Paper 2008-01-1612
43. Mid-Michigan Research, *CASE Theoretical Manual*, Mid-Michigan Research, LLC, Okemos, MI, 2003
44. Myers R. H., Montgomery D. C., *Response Surface Methodology, Process and Product Optimization Using Designed Experiments*. John Wiley & Sons Inc., New York, 1995
45. Nickalls, W. D. R., Dye, H. R., 1996, "The Geometry of the Discriminant of a Polynomial," *The Mathematical Gazette*, Vol. 80 pp. 279-285
46. Oh, K. P., Goenka, P. K., 1985, "The Elastohydrodynamic Solution of Journal Bearing Under Dynamic Loading," *Journal of Tribology*, Vol. 107, pp. 389-395
47. Oh, K. P., Li, C. H., Goenka, P. K., 1987, "Elastohydrodynamic Lubrication of Piston Skirts," *Journal of Tribology*, Vol. 109, pp. 356-362
48. Panayi A. P., Schock, H. J., "Investigations on Piston Secondary Dynamics: A Model that Considers Translation Along the Wrist-pin and Second Land Interactions with the Cylinder Bore," ASME Paper IMECE2007-41264
49. Panayi, A. P., *Piston Design and Analysis: Parameterized and Complete Finite Element Analysis Approach for the Assessment of Piston Performance*, Master's Thesis, Michigan State University, East Lansing, Michigan, 2006
50. Panayi, A. P., Schock, H. J., "Piston Finite Element Modeling for the Estimation of Hydrodynamic and Contact Forces and Moments," *ASME Proceedings of ICEF2006*, Paper No. ICEF2006-1587
51. Panayi, A., Schock, H., Chui, B.K., Ejakov, M., 2006, "Parameterization and FEA Approach for the Assessment of Piston Characteristics," SAE Paper 2006-01-429
52. Papila M., Haftka T. R., 2000, "Response Surface Approximation: Noise, Error, Repair, and Modeling Errors," *AIAA Journal*, Vol. 38, pp. 2336-2343
53. Patel P., Mourelatos P. Z., Shah P., 2007, "A Comprehensive Method for Piston Secondary Dynamics and Piston-Bore Contact," SAE Paper 2007-01-1249
54. Patir, N., Cheng, H. S., 1978, "An Average Flow Model for Determining Effects of Three-Dimensional Roughness on Partial Hydrodynamic Lubrication," *Journal of Lubrication Technology*, Vol. 100, pp. 12-17
55. Perchanok, M., 2000, "Modeling of Piston-Cylinder Lubrication with a Flexible Skirt and Cylinder Wall," SAE Paper 2000-01-2804

56. Piegls, L., Tiller, W., *The NURBS Book*, Springer, Heidelberg, Germany, 1997
57. PISDYN, 2007, Ricardo PLC, <http://www.ricardo.com>
58. Press, W. H., Teukolsky, S. A., Vetterling, W. T., Flannery, B. P., *Numerical Recipes in Fortran 77, The Art of Scientific Computing*, Cambridge University Press, New York, NY, 1992
59. Rao, S. S., *The Finite Element Method in Engineering*, Butterworth-Heinemann, Boston, 1999
60. Richardson, D. E., 2000, "Review of Power Cylinder Friction for Diesel Engines," *Journal of Engineering for Gas Turbines and Power*, Vol. 122, pp. 506-519
61. Richardson, D., 1996, "Comparison of Measured and Theoretical Interring Gas Pressure on a Diesel Engine," SAE Paper 961909
62. Ruddy, B. L., Dowson, D., Economou, P. N., and Baker, A. J. S., 1979, "Piston Ring Lubrication – Part III, The Influence of Ring Dynamics and Ring Twist," *Energy Conservation through Fluid Film Lubrication Technology: Frontiers in Research and Design*, ASME Winter Meeting, 1979, pp. 191-215
63. Sacks, J. Welch, W. J., Mitchell, T. J., Wynn, H. P., 1989, "Design and Analysis of Computer Experiments," *Statistical Science*, Vol. 4, pp. 409-435
64. Simpson W. T., Peplinski D. J., Koch. N. P., Allen K. J., 2001, "Metamodels for Computer-Based Engineering Design: Survey and Recommendations," *Engineering with Computers*, Vol. 17, pp. 129-150
65. Stinstra E., Stehouwer P., den Hertog D., Vestjens A., 2003, "Constrained Maximin Designs for Computer Experiments," *Technometrics*, Vol. 45, pp. 340-346
66. Tian, T., *Modeling the Performance of the Piston Ring-Pack in Internal Combustion Engines*, PhD Dissertation, Massachusetts Institute of Technology, Cambridge, MA, 1997
67. Tsujiuchi, N., Koizumi, T., Hamada, K., Okamura, M., Tsukijima, H., 2004, "Optimization of Profile for Reduction of Piston Slip Excitation," SAE 2004-32-0022
68. Ugural, A. C., Fenster, S. K., *Advanced Strength and Applied Elasticity*, Prentice Hall PTR, Englewood Cliffs, 2003
69. Vogel, H., 1921, "The Law of the Relation Between the Viscosity of Liquids and the Temperature," *Physik Zeitschrift*, Vol. 22, pp. 645-646
70. Wang G. G., 2003, "Adaptive Response Surface Method Using Inherited Latin Hypercube Design Points," *Journal of Mechanical Design*, Vol. 125, pp. 210-220

71. Wang G. G., Dong Z., Aitchison P., 2001, "Adaptive Response Surface Method – A Global Optimization Scheme for Computation-intensive Design Problems," *Journal of Engineering Optimization*, Vol. 33, pp. 707–734
72. Wang G. G., Shan S., 2007, "Review of Metamodeling Techniques in Support of Engineering Optimization," *Journal of Mechanical Design*, Vol. 129, pp. 370-380
73. Wilson, C. E., Sadler P. J., *Kinematics and Dynamics of Machinery*, Prentice Hall, Upper Saddle Valley, NJ, 2003
74. Wong V. W., Tian T., Lang H., Ryan J. P., Sekiya Y., Kobayashi Y., Aoyama S., 1994, "A Numerical Model of Piston Secondary Motion and Piston Slap in Partially Flooded Elastohydrodynamic Skirt Lubrication," SAE Paper 940696
75. Woschni, G., 1967, "Universally Applicable Equation for the Instantaneous Heat Transfer Coefficient in the Internal Combustion Engine," SAE Paper 670931
76. Woschni, G., 1979, "Determination of Local Heat Transfer Coefficients at the Piston of a High Speed Diesel Engine by Evaluation of Measured Temperature Distribution," SAE Paper 790834
77. Wriggers, P., *Computational Contact Mechanics*, Springer-Verlag, Berlin, 2006
78. Wu, H., Chiu, C., 1986, "A Study of Temperature Distribution in a Diesel Piston – Comparison of Analytical and Experimental Results," SAE Paper 861278
79. Wu, H., Chiu, C., 1986, "A Study of Temperature Distribution in a Diesel Piston – Comparison of Analytical and Experimental Results," SAE Paper 861278
80. Wujek, B. A., Renaud, J. E., 1998, "New Adaptive Move-Limit Management Strategy for Approximate Optimization, Part 2," *AIAA Journal*, Vol. 36, pp. 1922-1934
81. Zhu D., Cheng H. S., Arai T., Hamai K., 1992, "A Numerical Analysis for Piston Skirts in Mixed Lubrication - Part I: Basic Modeling," *Journal of Tribology*, Vol. 114, pp. 553-562
82. Zhu D., Hu Y., Cheng H. S., Arai T., Hamai K., 1993, "A Numerical Analysis for Piston Skirts in Mixed Lubrication - Part II: Deformation Considerations," *Journal of Tribology*, Vol. 115, pp. 125-133
83. Zottin, W., Peixoto, V. J. M., 2003, "Numerical Simulation of Piston Rings Instability," SAE 2003-01-0981

MICHIGAN STATE UNIVERSITY LIBRARIES



3 1293 03062 7289